In-Situ Generation and Dissolution of Nano Structures by Liquid and Dry Electron Irradiation Method

Thesis by

Muhammad Sajid Ali Asghar

Department of Materials Science and Engineering

The University of Sheffield

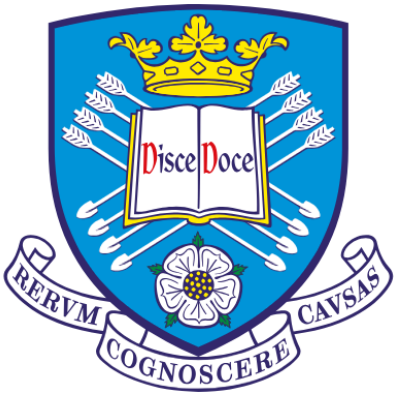

The University Of Sheffield.

This thesis is submitted in partial fulfilment of the requirements for the degree of Doctor of Philosophy in Materials Science and Engineering

Thesis Supervisors

Dr. Günter Möbus
Dr. Beverley Inkson

July 2018

ABSTRACT

Ceria nanostructure synthesis and dissolution has been achieved by using the dry and liquid electron beam irradiation method in transmission electron microscope (TEM). Traditionally used methods for synthesis of ceria nanostructures are chemical precipitation and for dissolution of ceria are based on strong acid with high temperature.

Ceria nanoparticles and nanorods immersed in deionised water were irradiated with different intensity of electron beam using special liquid cell holder in TEM. For this purpose, transmission electron microscopes operating at 200 and 300 kV was used. Upon irradiation, various novel, unknown and known phenomena have been observed live such as, chain formation, new phase formation including (1D needle, multiple spiky needle, star shape needle and nanoparticles) and dissolution. Live in-situ observation of fast and giant dissolution of functional ceramic nanostructure at room temperature without external supply of acid is one of the main novel finding which is never observed before. We quantitatively measure and report the ceramic dissolution of ceria nanoparticles and nanorods in this work and our calculated dissolution rate is 5 orders of magnitude higher than the previous ex-situ calculated dissolution. On the other hand, two types of hydrated cerium salt were irradiated using electron beam of different intensity with or without condenser aperture. Upon direct dry irradiation of hydrated cerium precursors we have successfully explored the amorphous to crystalline transformation and formation of ceria and cerium chloride nanoparticles and nanorods in TEM. During the irradiation of cerium nitrate hexahydrate (CNH) in TEM at 200 kV we have explored the redox transformation and observed the internal precipitation of precursor causes the formation of nanoparticles on precursor. Furthermore, we have also explored the synthesis of ceria nanoparticles, nano rods and ceria nano-tubes by using the wet-chemical precipitation method at room temperature with different molar ratios of CNH and sodium hydroxide.

ACKNOWLEDGEMENTS

“In the name of ALLAH who is most Gracious, and merciful”. “ALLAH’s harmony and kindness be upon the last and final messenger and Prophet Muhammad (SAW)”. ALLAH has blessed me with the patience and strength guided me to follow a straight path in order to complete my PhD study. My utmost thanks to Allah Subanahutalah for His perpetual kindness and support during my research.

First of all, I would like to express my sincere and profound cheers to my esteemed supervisor Dr. Günter Möbus for his generous guidance and the help which he has provided in completion of my PhD research. I am truly obliged to him for his sound expertise, technical advice, assistance and encouragement. He is a good advisor as well as a great teacher and an entrepreneur; it has been a great honor for me to doing study and research under his supervision.

I am also thankful to my second supervisor Prof. Dr. Beverly Inkson for her technical advice and valuable help in high resolution electron microscopy and liquid cell experiments.

I would like to thanks to my current and past colleagues of the Nano-Lab (University of Sheffield) for their support during my PhD research. I would also like to thank Dr. Ian Ross, Dr. Peter Korgel, Dr. Alfonce Chamisa, Dr. Peng Zeng, and Dr. Le Ma for their technical assistance and training in transmission electron microscopy (TEM) and scanning electron microscopy (SEM) at Koroto centre (Sorby Centre). Thanks also go to all Materials Science and Engineering Department general, technical staff and office staff who have facilitated and helped me during my research.

I am immensely grateful to my loving wife Mrs. Rabia Sajid for her valuable help, care, tolerance and support not only spiritually but mentally, and providing me emotional stability which I indeed required during my research. My deep thanks to my loving and princess daughter Anumta Sajid and lovely son Muhammad Shaheer Sajid. Thanks to my loving mother

Sanjeeda Bano and my father Muhammad Asghar Ali for their support, and my late grand-mothers and grand-fathers they were wishing to see this day, my lovely sister Sajida Rizwan and brothers, uncles, aunts, my mother and father-in-law for their mammoth help and encouragement, relatives and my all friends for their support and help.

Finally, I would also like to acknowledge the NED University of Engineering and Technology, Karachi, Pakistan, The University of Sheffield, Sheffield, UK and EPSRC, UK (EP/J021199/1) for funding parts of this PhD research.

Muhammad Sajid Ali Asghar

LIST OF CONTENTS

ABBREVIATIONS

AR: Aspect Ratio

BSE: Backscattered Electrons

CA: Condenser Aperture

CCD: Charge Couple Device

CCL: Cerium Chloride Heptahydrate

Ceria: CeO_2

CNH: Cerium Nitrate Hexahydrate

CNPs: Ceria Nanoparticles

CNR: Ceria Nanorods

CTEM: Conventional Transmission Electron Microscope

DP: Diffraction Patterns

EDX: Energy Dispersive X-ray Spectroscopy

EELS: Electron Energy Loss Spectroscopy

FEG: Field Emission Gun

FFT: Fast Fourier Transformation

HRTEM: High Resolution Transmission Electron Microscopes

JEOL: Japanese Electron Optics Laboratory

LC: Liquid Cell

LCTEM: Liquid Cell Transmission Electron Microscope

LaB_6: Lanthanum Hexaboride

NS: Nanostructure

NP: Nanoparticle

NPs: Nanoparticles

NR: Nanorods

NRs: Nanorods

NCs: Nano Cubes

OA: Oriented Attachment

STEM: Scanning Transmission Electron Microscope

SiN: Silicon Nitride (Si_3N_4)

SAD: Selected Area Diffraction

SH: Sodium Hydroxide

SAED: Selected Area Electron Diffraction

SEM: Scanning Electron Microscopy

SE: Secondary Electron

TEM: Transmission Electron Microscope

W: Tungsten

LIST OF FIGURES

LIST OF APPENDIX FIGURES

LIST OF TABLES

LIST OF PUBLICATIONS AND CONFERENCES

Reviewed journal publications

1. Asghar, M.S.A.; Inkson, B.; Möbus, G. Giant radiolytic dissolution rates of aqueous ceria observed in-situ by liquid-cell TEM. *ChemPhysChem* **2017**, 18, 1-6.
2. Muhammad Sajid Ali Asghar[1], Beverley Inkson[1], Sudipta Seal[2], Marco Molinari[3], Dean Sayle[4], Günter Möbus[1], In-situ observation of radiation chemistry of nanostructured cerium oxide in water. Mater. Res. Express 6 (2019) 015032 (https://doi.org/10.1088/2053-1591/aae634).
3. Asghar, M.S.A.; Inkson, B.; Möbus, In-situ formation of one-dimensional nanostructures from ceria nanoparticle dispersions by liquid cell transmission electron microscopy irradiation. (Submitted for Publication)

Refereed conference proceeding

1. Asghar, M.S.A.; Sabri, M. Mohammad; Tian, Z. ; and Möbus, G, "In-situ irradiation of cerium precursors in TEM to study nanocrystal formation" Journal of Physics: Conference Series, Volume 902, conference 1.
2. Asghar, M.S.A.; Inkson, B.; Möbus, G. "Ceria-Water-Reactions Studied by Liquid Cell TEM" Journal of Physics: Conference Series, Volume 902, conference 1.

Oral presentation at conferences

1. Asghar, M.S.A.; Inkson, B.; Möbus, G. "In-situ dissolution of ceria nanoparticles in liquid-cell TEM" MMC2017- EMAG, Manchester, UK, 3-6 July 2017.
2. Asghar, M.S.A.; Sabri, M. Mohammad; Tian, Z.; and Möbus, G, "In-situ irradiation of cerium precursors in TEM to study nanocrystal formation" MMC2017- EMAG, Manchester, UK, 3-6 July 2017.
3. Asghar, M.S.A.; Inkson, B.; Möbus, G. "In-situ dissolution study of cerium oxide nanoparticles in liquid-cell TEM". The 11th International Nanoscience Student conference (INASCON), Wills Hall, The University of Bristol, Bristol, UK, 21-24 August 2017.

Poster presentation at conferences

4. Asghar, M.S.A., Inkson, B., Möbus, G. "In-situ generation of nanoparticles by electron irradiation" University of Sheffield Engineering Symposium, Sheffield, UK, 24 June 2015.
5. Asghar, M.S.A., Möbus, G. "In-situ Liquid cell TEM Examination of Ceria Nanoparticles" 5th University of Sheffield, Engineering Researcher Symposium 2017, Sheffield, UK, 30 June 2017.
6. Asghar, M.S.A.; Inkson, B.; Möbus, G. "In-situ dissolution of ceria nanoparticles in liquid-cell TEM". MMC2017- EMAG, Manchester, UK, 3-6 July, 2017.
7. Asghar, M.S.A.; Sabri, M. Mohammad; Tian, Z.; and Möbus, G, "In-situ irradiation of cerium precursors in TEM to study nanocrystal formation" MMC2017- EMAG, Manchester, UK, 3-6 July 2017
8. Asghar, M.S.A.; Inkson, B.; Möbus, G. "In-situ dissolution study of cerium oxide nanoparticles in liquid-cell TEM". The 11th International Nanoscience Student conference (INASCON), Wills Hall, The University of Bristol, Bristol, UK, 21-24 August 2017.
9. Asghar, M.S.A.; Inkson, B.; Möbus, G. "In Situ TEM imaging of ceramics nanoparticles in aqueous environment", Microscopy and Microspectroscopy of nanomaterials in Liquids, Plasma Institute, The University of York, UK, 18 September 2017.

Attended conferences / Symposium

1. 3rd University of Sheffield, Engineering Symposium (USES) on 24th June 2015.
2. 4th University of Sheffield, Engineering Symposium (USES) on 6th June 2016.

THESIS OUTLINE

In this thesis, two types of electron beam irradiation methods (liquid and dry) and wet-chemical laboratory synthesis of cerium oxide nanostructures are presented. The structure of this thesis is as follows. Chapter one is starting with the introduction to the research study, aims and connection or relationship of all results. Chapter two present the complete literature review, starting with the general introduction to nano materials and available synthesis methods and applications in different fields. Then describe the specific previous literature of direct dry irradiation of precursors and liquid cell irradiation in TEM. Chapter three describes the used methods during this research and discusses the background of experimental characterisation techniques have been used throughout this work. Generally, all of experimental work results and findings are starting from the chapter four. Chapter four present the results of liquid cell irradiation of ceria nanoparticles and nanorods in water. Chapter five, presents the results obtained from the direct dry irradiation of hydrated cerium precursors i.e. cerium nitrate hexa-hydrate (CNH) and cerium chloride heptahydrate (CCL) respectively. Chapter six describe the wet-chemical laboratory synthesis of ceria nano structures at room temperature. Finally, chapter seven discusses the main findings and conclusions of the research.

CHAPTER ONE

INTRODUCTION

1.1 Live Electron Beam Irradiation of Ceria (CeO_2) Nanostructure

The study of interaction of radiation with matter and its live observation utilizing transmission electron microscope (TEM) beam is of great value in advanced Materials Science [1]. To explore and understand the live behaviour of electron matter interaction and to develop new technologies, in-situ TEM irradiation is extremely helpful to be able to observe the material microstructural changes of irradiation as they happen [2]. In particular, TEM electron beam has an ability to irradiate glass, metal and ceramics for multipurpose applications e.g. amorphous to crystalline transformation, synthesis of nanostructures (NS), defect formation and phase transformation [3]. The application of irradiation induced transformation is not only a dedicated method for nuclear application but also has application in nanotechnology. This electron beam interaction with matter is responsible for various types of radiation damage, such as atomic displacement, electrostatic charging, sputtering, radiolysis, and knock-on damage [4].

In addition to high-resolution imaging, TEM also allow material characterization due to its unique interaction between the matter and electron beam. This interaction carries qualitative information for example relative densities of the material and their in-homogeneous constituents, as well as analytical analysis by using characteristic X-ray emission with help of

energy dispersive X-ray spectroscopy (EDX) and characteristic electron scattering i.e. electron energy loss spectroscopy (EELS). For all of these reasons, TEM has become a standard tool for nano-engineering and is considered as miniature all in one nano-laboratory for nanomaterials synthesis and characterisation at the same time [5, 6].

The electron beam of TEM can be used to alter the physical and chemical properties, structure and composition of metal and oxides. The modification obtained by electron beam irradiation include, void or cavity formation [7], amorphisation [1], phase transformation [8, 9], defect formation [1], gas bubble formation [1], crystallization, nanopatterning and shape transformation [10, 11], phase separation, precipitation [12] and focused electron beams can be used to form several types of impact craters, including conventional thin holes, ring patterns and dot pattern [10]. Direct dry electron irradiation method can be used to generate fresh nanostructures [13], shape transition and ablation of Li [14], change of oxidation state [15], single crystal to poly crystalline transformation [9] and growth of TiO_2 nanorods [16]. Above mentioned irradiation effects might (in past) also possibly be achieved by laser, ion, or microwave. However, then the ability of TEM to irradiate and simultaneously image is lost, and also irradiation becomes out of focused lacking resolution. Most TEM irradiation in the past concerned metals or salt-to-metal conversion. Little attention has been paid by direct dry TEM electron beam irradiation of salt to oxide transformation. Thus, it is important to explore this effect in various salts.

In this research work ceria nano material is the main concern because ceria is the one of the most extraordinary and versatile multifunctional nano oxide material with numerous applications from catalysis to biomedical fields. Ceria is well-known due to oxygen storage capacity and several applications of ceria are based on the ability to change oxidation state between 3+ and 4+, and a predominantly large range of applications uses the particles in aqueous state. Ceria is easily transform from CeO_2 to CeO_{2-x}. The availability of oxygen

vacancies on the surface of ceria nano structures dramatically modify the surface properties. Thus, redox (oxidation and reduction) properties are likely to be dissimilar on the different surfaces. The shape morphology of CeO_2 is widely recognized as a key to altering its chemical and physical properties due to change of surface effect. The previous studies related to the dry ceria irradiation concluded that ceria is a stable oxide but stability of ceria in water under electron beam is unclear.

1.2 Aims of the research

The main aim of this PhD study is the live synthesis and dissolution of oxide nanostructures by using electron beam of transmission electron microscope (TEM). This research covers three distinct but interrelated subtopics:

(a) Synthesis of CeO_2 nanostructures and their reactivity during electron irradiation and chemically induced methods

(b) High intensity chemical reactions and chemically induced transformation of oxide nanomaterials in aqueous dispersion

(c) Irradiation chemistry and physics of ceria nanostructures during synthesis and dissolution, which are individually well established.

Here we try to combine all three topics in one with the help of special liquid cell (LC) TEM holder which was never achieved before due to the usual vacuum requirements of TEM. The main purpose of the combining of all three effects in one because we want, (i) advanced the experimental research field of colloidal and reactive chemistry of nanoscale oxide, (ii) to provide the experimental data or evidence for theoreticians group or researchers:

- who do modelling, chemical and physical predictions of ceria in water.
- who do modelling of particle-particle forces / interaction for example attachment and chain formation.

The findings of irradiation of ceria in water under electron beam are benefitting a variety of engineering and biomedical applications where water is associated with ceria nanostructures e.g. catalysis, environmental pollution, water treatment, polishing, corrosion, nuclear fuels and waste disposal and cell protection against radiation in radiotherapy.

In this research work we want to study the live in-situ generation and dissolution of nanostructures by using TEM electron beam induced irradiation technique. We are using TEM irradiation method because we can observe the live change in structure induced by electron beam and this opens the possibility of discovering new and innovative phenomena, such as formation of functional oxide nanoparticles and nanorods by using direct dry irradiation of salt precursors and movement, new phase formation and dissolution on nanostructures by using liquid cell irradiation. The detailed objectives of this study are based on the advancing or progress of previous work:

- We have expanded the conventional metallic nanoparticles (Au, Fe, Pd) with the oxide nanoparticles i.e. ceria in liquid cell studies.
- We have expanded the typical studies of nanoparticles growth by studies of dissolution and phase transformation of pre-existing well-defined oxide nanoparticles.
- We have employed LC method to check the durability of oxide in liquid state for long term stability of nanostructures in aqueous or acidic environment (due to radiolysis of electron beam) and successfully quantify the live rate of dissolution.
- We replaced previous dry irradiation of cerium carbonates precursor by cerium nitrate and cerium chloride precursors for the synthesis of ceria nanostructures.

extend the ex-situ wet-chemical synthesis of ceria nanostructures by using hydrated cerium precursor at room temperature for comparison with in-situ work.

1.3 Connection/Relationship of Results Chapters

We have anticipated all of experiments in this thesis i.e. Liquid cell, Dry irradiation and Wet-chemical laboratory synthesis to have a relationship in between them because they have some connection with each other which can be seen in the Figure 1-1.

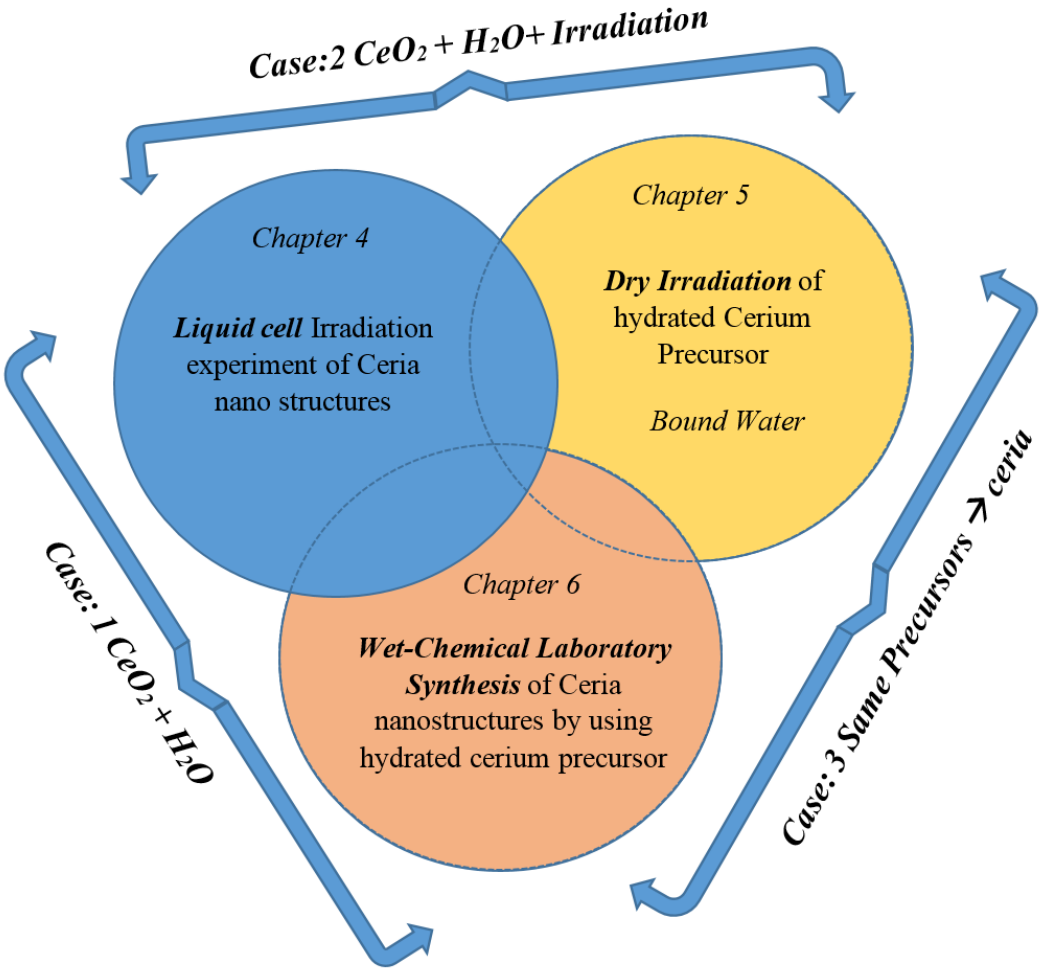

Figure1-1: Diagram shows the relationship between experiments.

During liquid and dry irradiation experiments what type of transformation (i.e. reduction of salt precursor, phase chemical change) we are suspecting. For example in liquid cell we have used ceria nanostructures immersed in water and radiolysis of water occurred due to electron beam

irradiation interaction and causes dissolution and new phase formation. During irradiation of ceria in water electron beam is not directly hitting the ceria because ceria is immersed in water and electron beam is hitting the water first and it generates various water splitting species. Common aspects include in all experiments are:

(i) In all results chapters we study chemical reactions between two cerium-compound (cerium nitrate hexahydrate and cerium chloride hepta hydrate) phases (amorphous or crystalline), either starting from or aiming for CeO_2.

(ii) There are always possible intermediate phases involved, e.g. hydroxides of Cerium, or non-stoichiometric Ce-oxide (CeO_{2-x}).

(iii) Redox reactions are involved in all 3 results chapters, either irradiation (chapter 4 and chapter 5) or chemically induced (chapter 6).

(iv) There is always H_2O available to participate in reactions either as bound water in hydrated salts (chapter 5), or as the water dispersion (chapter 4), or water solution (chapter 6).

There are interesting experimental parameters such as temperature (T), pH, irradiation dose (chapter 4 and chapter 5) to be explored.

CHAPTER TWO

LITERATURE REVIEW

2.1 Introduction

This literature review chapter describes previous research work related to the in-situ irradiation of materials with the electron beam of a Transmission Electron Microscope (TEM). Section 2.2, provides an introduction and definition of nano-materials and types of nano-materials and their applications in different fields. Section 2.3 will gives a brief overview of the synthesis methods for nano-structure materials by using different techniques. Section 2.4 covers the general introduction, chemistry and application of ceria, and Section 2.5 presents the background to in-situ electron irradiation, TEM irradiation, and dry in-situ TEM irradiation. This section also includes the literature related to the effect of an electron beam on matter, and important studies in the irradiation of metallic and ceramic precursor materials using a high energy focused electron beam transmission electron microscope (TEM), for the synthesis of nano-materials. The final section 2.6 provides the literature review related to the introduction of the liquid cell method, liquid irradiation and important studies related to the application of liquid cell irradiation of nano-structures and precursors in different liquids and solvents.

2.2 Introduction to Nano Materials (NM)

Nanostructure materials are known as ultrafine chemical substances that are manufactured at the nanoscale in at least one dimension, of the order of 100 nanometers or less. “Nano” in nanometer is a prefix symbolising the minus 9th power of ten or one millionth of a millimetre.

Nanomaterials are usually defined as materials having size in the range of 1-100 nm that show significantly different properties to that in the same type of conventional or bulk material. Nanostructure materials have a much greater surface area to volume ratio than other conventional materials. To achieve the functional properties of nanomaterials for the majority of biomedical and engineering applications [17-19], they are usually designated as materials with a feature in the range of 5–30nm in size. The performance and properties of electronic components and other devices can be enhanced with nanomaterials by designing and controlling the behaviour of the nanoparticles physical properties (size, shape and surface structure) and chemical properties (chemical composition) [20, 21].

2.2.1 Types of Nano Materials

Nanomaterials can be classified in various forms according to the desired categories which includes crystalline or amorphous phases, metals or ceramics, polymers and composites. Nanostructure materials are also classified by dimensional characteristics such as zero-dimensional, one-dimensional, two-dimensional and three-dimensional [22]. Zero-dimensional nanomaterials are nanoparticles (NPs), and one-dimensional nanostructures are nano rods, wires, whiskers and fibers, and in some cases, nanotubes. Thin films, plates and sheets are considered as two-dimensional nanostructures, and colloids, bearing shapes and super lattices are considered as three-dimensional nanostructures. Table 2- *1* below shows some examples of nanostructure materials of different dimensionalities [23, 24]. Nanostructure materials can exist in single, fused, agglomerated or aggregated forms with different shapes such as spherical, cubic, rod, octahedral, and irregular shapes. Within the remit of the work described here a brief literature is given below of two important and basic types of nano materials i.e. i) metallic and ii) ceramics nanomaterial.

Table 2- 1: Nanostructure material sizes of different dimensionalities [23].

S. No.	Type of Nano-materials	Size (approx.)	Materials
01	Nanocrystals and clusters (quantum dots), Nanoparticles, Nanowires	diameter 1–10 nm	Metals (Co, Ag, Au and Pd), Ceramic oxides (TiO_2, CeO2, SiO_2), magnetic materials, semiconductors, sulfides, and nitrides
02	Nanotubes	diameter 1–100 nm	Metals and Semiconductors carbon nano tubes
03	2-Dimensional (nano plates, sheets, thin films)	several nm^2–μm^2	Various materials, like metals, semiconductors, magnetic materials etc.
04	3-Dimensional structures (super-lattices)	Several nm in all three dimensions	Metals, magnetic materials, and semiconductors

2.2.1.1 Metallic Nanoparticles

Metal nanoparticles are of great interest due to their unusual properties physical, chemical, mechanical, optical, electronic and biomedical. For example physical properties of nanostructure materials depend on the size of their nano scale features in the case of tin and indium, decreasing the diameter of nanoparticles results in a decrease in the melting point [25, 26]. A variety of metallic nano materials have been synthesised in the past in different forms that include as nanoparticles, nanorods, nano plates, nano cubes and nano sheets. These have been fabricated with controlled dimensions and ultrafine purity for applications in various fields such as chemical, electrical and electronic, semiconductor and health care [27]. The most commonly available types of metallic nano materials are silver (Ag), gold (Au), nickel (Ni) and cobalt (Co) [28].

2.2.1.2 Oxides Nanoparticles

Metal-oxide nanomaterials have attracted a lot of interest in recent years due to their unusual physical, chemical, electronic, electrical, optical and magnetic properties[29]. Metal-oxides nanoparticles represent various classes of materials with properties that cover the same range as metals, semiconductors and insulator [30]. These versatile properties have found applications for oxides nanomaterials as a catalyst in fuel cells, as corrosion resistant coatings, as a sensors, piezoelectric devices and in microelectronic circuits [29]. There are also broad classes of ceramics or oxide nanostructures available such as titanium oxide (TiO_2), Iron oxide (FeO_2, Fe_3O_4), ZnO, and ceria (CeO_2) for many other applications such as semiconductor, waste water treatment, glass polishing, sun block cream, coatings and nuclear [31].

2.2.2 Application of Nano Materials

Nanostructure materials have physical and chemical properties such as very high strength, increased diffusivity, low sintering temperatures, valuable catalytic properties, which makes them attractive for many engineering and nanoengineering applications. As science and engineering technology continues to introduce new materials for various applications nanomaterials are at the forefront of these innovations with potential applications in industries that include electronics, information technology, biomedical science , nuclear, marine and energy generation [18, 24]. Iron oxide nanoparticles embedded in zeolites have been deployed in applications in water treatment, remediation and pollution prevention [32]. Given the versatility of these materials and their potential wide range of applications, it is widely believed that nanotechnology will be the next industrial revolution in many science and engineering fields [33].

In conventional bulk polycrystalline metals, grain boundaries are frequently prone to corrosion for example stress corrosion cracking (SCC) and intergranular corrosion. Nano crystalline

materials on the other hand are not prone to these problems thereby offering a superior performance in corrosion resistance [34]. Nano crystalline materials can also provide a much better uniformity in cross-sectional properties in electrical, optoelectronics and electronic fields. Nano based micro-components provide advantages of elastic energy storage capacity (resilience) and are less prone to eddy currents for applications in magnetic components operating at high frequencies [18]. Nanostructured crystalline materials have played a major role in catalysis for the last six or seven decades due to their good catalytic properties. Several catalytic reactions depend on the structural morphology of the catalyst such as particle size and shape, and the amount and types of internal structure defects [35]. Therefore, nano materials are extensively used in many catalytic applications in various industries such as petrochemical production and as a fuel cracking agent, for automobile toxic emission control, and for chemicals synthesis.

Magnetic nanostructure materials have various applications in the field of biomedical science, electrical engineering and electronics, and for data storage. Some magnetic nano materials have been used in magnetic transistors and ferromagnetic semiconductors for spintronic application [36]. The application of nanomaterials in the field of water treatment is cost effective compared with conventional process and an advanced method that removes harmful elements, bacteria and viruses of water contamination. Nanomaterials have been used for water purification effectively in terms of quality and quantity. In recent years various nanomaterials (Ag, ZnO, TiO_2, carbon Nanotubes (CNTs), ceria and ferrous oxide (Fe_3O_4)) have been used for the removal of viruses, natural organic substances, in-organic solutes, complex organic compounds, heavy metals, metallic ions, nitrate, and other dangerous contaminants present in surface water, ground water, and/or industrial water [37].

2.3 Nano Materials Synthesis Methods

Numerous methods have been documented for the preparation of novel nanostructure materials of pure metals, alloys and ceramics. They can be generated by using several preparation methods including physical, chemical and physiochemical methods. Each method has its pros and cons which are described in the next section [22]. The selection of the nano synthesis method depends on the application and a brief description of some useful methods for the synthesis of nano structure materials is as follows:

2.3.1 Physical Methods

The most significant physical methods are gas/vapour evaporation-condensation methods thermochemical/flame methods, and spray pyrolysis [38]. The benefits of physical synthesis methods compared with chemical synthesis processes are ease of performance, uniformity of nanoparticles distribution, and high purity due to the absence of solvent contamination [39]. For example most researchers have used physical synthesis methods for the generation of Ag and lead sulphide (PbS) NPs [39-41].

2.3.2 Chemical Methods

Chemical synthesis of nano structured materials can be conducted in different states like solid, liquid, gas or combination of any two states. Several metallic and functional nano-materials can be synthesised by using aqueous or non-aqueous solutions method. Chemical synthesis is based on three types of general reaction in the aqueous state namely acid/base reaction, precipitation, and redox (reduction/oxidation) [22]. Chemical precipitation methods and the sol-gel processing method are most widely used for the synthesis of ceramic nanoparticles. Nanostructures synthesised by chemical methods contain some residual organics and by-products, depending on the synthesis technique used. This may require a subsequent cleaning

and washing process or heat-treatment for removing of water and controlled crystallisation to form oxides with required crystallite size and structure [18, 29].

2.3.3 Physicochemical Synthesis

Established techniques of physicochemical irradiation methods available for the synthesis of nano materials are a listed below followed by brief description:

- **a)** Microwave-assisted Irradiation Synthesis
- **b)** Laser Irradiation
- **c)** In- Situ Electron Beam Irradiation

2.3.3.1 Microwave-assisted Irradiation Synthesis

This is a promising method for the synthesis of nano materials with smaller nano sizes, uniformly distributed with minor or without agglomeration, and a large degree of crystallisation with shorter reaction time [42, 43]. Control can be gained over the morphology (shape and size) of the nanostructures by the microwave power, the pH of the solution, and with time and temperature [43].

2.3.3.2 Laser Irradiation

The synthesis of nano structure materials by laser irradiation of solids either in vacuum, gas or in water has been widely explored during the last two decades. For example the fabrication of Au, Cu, Ag, Ti, Si, and Au nanoparticles are carried out by laser irradiation [44-46] [47].

2.4 Introduction to Ceria

Ceria (CeO_2) is one of the most important rare earth metal oxides, and the functional properties of ceria nanostructures have attracted attention from a variety of engineering and non-

engineering fields because of their nano size, shape, structure, level of agglomeration and orientation-dependent properties. Due to its great functional properties ceria nano structures are most widely used for catalysis, environmental remediation, biomedical radiation protection, anti-corrosion coatings [23, 27, 48, 49]. Furthermore, ceria is a common non-radioactive analogue for UO_2 and ThO_2, for which irradiation and dissolution are the subjects of study in nuclear fuel disposal. For most ceria applications the distribution of oxygen vacancies, defect structure and the ionic mobility on the nanoparticle (NP) surface is crucial [50]. Ceria nano materials can be synthesised by many wet chemical methods including temperature assisted solution precipitation, hydrothermal/solvothermal process, microemulsion, coprecipitation, coprecipitation, sono-chemical and microwave irradiation [51].

2.4.1 Chemistry of Ceria

Ceria is the one of the most important industrial catalysis oxides. It has several applications due to its chemical properties. Dry Ceria (CeO_2) is a physically and chemically stable oxide and valency of cerium is between +3 and +4 under several redox (reductive or oxidizing) conditions, and electronic configuration for ceria is $4f^2\ 5d^0\ 6S^2$ and intermediate range of transformed stage are Ce_2O_3, CeO_{2-x} and CeO_2 [52]. Current research studies have hypothesised that the concentration of ceria 3+ relative to ceria 4+ rises as particle size decreases, with usually Ceria 3+ at least 6 % in 6nm sized NPs and 1 % in 10nm sized NPs [53]. This double oxidation state of ceria means that these NPs structures contain oxygen vacancies or defects. In a ceria crystal structure, all oxygen atoms are in one plane which permits the fast diffusion as a function of the number of oxygen (O) vacancies [54]. Due to a good redox property in ceria the decrease of oxygen and the reduction of Ceria 4+ to Ceria 3+ is due to the formation of an oxygen vacancy, as shown in equation 2.1 below. The redox property of ceria makes them popular and attractive for energy (catalytic) applications [55].

$$CeO_2 \leftrightarrows CeO_{2-y} + y/2\ O_2 \text{ (Reducing and Oxidizing)} \qquad (2.1)$$

The lattice constant of the cubic ceria unit cell is 0.541 nm, and ceria has a face centre cubic (FCC) fluorite type oxide [51], as shown in Figure 2-1 and similar stoichiometric properties to a calcium fluorite type of crystal structure with a space group of Fm3m [52].

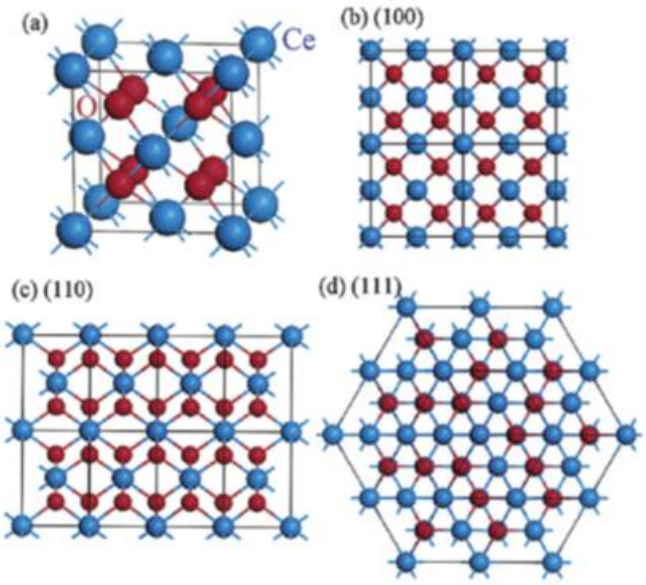

Figure 2-1: The crystal structure of ceria (CeO_2) with a) face-centred crystal structure (FCC) and (b-d) shows the (100) or (200), (110) and (111) planes of ceria [56].

In the FCC crystal structure of ceria each corner cerium (Ce) cation is surrounded by eight neighbouring anion of oxygen atoms while individual oxygen anion is tetrahedrally coordinated by four adjacent cations of Ce. Ceria is formed from a cerium source in which the stoichiometry of the cerium metal is purely based on the temperature and pressure. Cerium is unstable in air, and can react immediately forming Ce_2O_3 and CeO_2 [56]. Previous research studies suggest that there are three low-index lattice planes [(100), (110) and (111)] present on the surface of ceria nano-crystals. As shown in Figure 2-1, the stability of all three planes is different. The general result concerning the stability of the three surfaces of ceria based on density functional theory calculations, are in the order of (111) > (110) > (100), while the surface activity follows the reverse order. The total energy required to form an oxygen vacancy

during the reducibility is approximately 30% less than on the (111) surface in comparison with the bulk [57, 58].

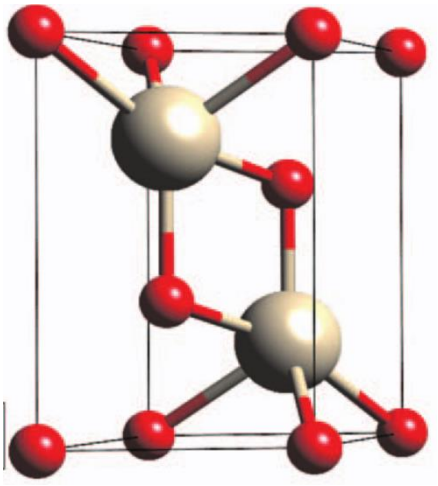

Figure 2-2: The hexagonal crystal structure of Ce_2O_3 [59].

CeO_2 is easily reducible, and this offers an advantage of oxygen storage for use in three way catalysts. At the ambient partial pressure of oxygen, CeO_2 can be form a non-stoichiometric cerium oxide of CeO_{2-x} by absorbing or releasing oxygen without any decomposition [56]. The fully reduced stable form of ceria is Ce_2O_3, it has a hexagonal crystal structure and has a P-3*ml* space group, as shown in

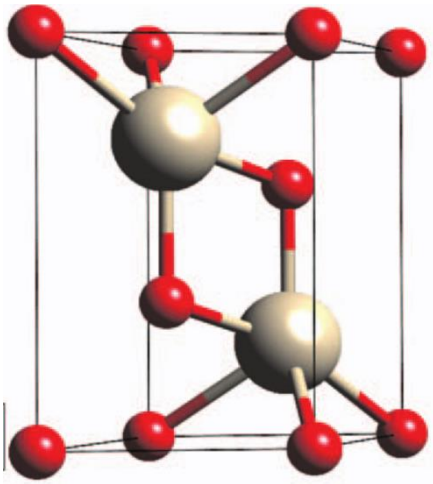

Figure *2-2*. For this hexagonal crystal structure cerium cat-ions are surrounded by oxygen an-ion atoms [59]. However, it is well known that in previous literature the intermediate phase of ceria i.e. CeO_{2-x} with $0.5<x\leq0$ have a FCC fluorite lattice structure depending on the oxygen vacancies. The most popular proto-typical ionic crystal surfaces of ceria are (111), (110), and

(100). The ceria (111) surface has a charge consisting of three repeat planes in a symmetrical atomic configuration with a zero dipole movement perpendicular to the surface. The ceria (110) surface has zero charge because of the stoichiometrically balance between cations and anions in each plane. On the other hand, the ceria (100) surface has an infinite free energy, and alternate charge planes with a repeat unit of two which produces a dipole moment perpendicular to the surface [56, 58, 60, 61].

2.4.2 Application of Ceria

Ceria have a variety of advanced industrial, consumer, environmental and biomedical applications. Ceria are widely used for catalysis as a fuel additive that promotes greater fuel efficiency, and in fuel cells, automotive three-way catalysts and catalysts for large-scale fluid cracking in refineries [62]. Furthermore ceria have found applications in optics, microelectronics devices, glass polishing, environmental cleaning, ultraviolet ray detectors, ultraviolet absorbers, [48, 63, 64] environmentally friendly pigments, gamma radiation dosimetry and gas sensors, (e.g. oxygen sensors) [48, 49, 64]. According to earlier studies, to achieve the best performance of the catalyst materials the size of catalysts particles need to be reduced as small as possible to increase the number of active surface sites for reaction. To achieve the desired properties from ceria, recent studies in materials science and engineering have made it possible to fabricate the ceria nanoparticles with tunable shapes for tailored applications. The advantage of that tunable crystal plane will help to complete the catalytic reaction easily and rapidly. The example of catalytic performance of different shapes of ceria is shown in Figure 2-3. For catalytic performance of ceria, the oxygen storage capacity is important and its dependent on the size and shape of the ceria nanostructures. The oxygen absorbs, and release capacity can happen both at the surfaces of nano rods so nanorods provide better catalytic properties as compare to NPs. Nanorods and nano cube have bulk oxygen

absorb and release capacity and in case of nanoparticles it depends on the size and active surface of NPs. The left side of the figure 2-3 shows the various types of nano rods (needle and rectangular shape) and right side shows the different other shapes of ceria NPs. The pointer on left side on the nano rods indicated that nanorods have better catalytic properties and the performance of ceria on the basis of shapes is going down from left (nanorods) to right side i.e. (NPs or nano cubes).[29, 65].

Figure (Abstract/cover figure) in reference [65]

Figure 2-3: The different shaped geometry of ceria (CeO_2) NPs with respect to the catalytic performance [65].

Figure 2-4 shows the various common shapes of synthesised ceria nano materials for example, octahedron, round, cubes, rods, needle, polyhedron, tube, etc and their application in various engineering, environmental and biomedical fields [66]. Ceria NPs have good catalytic properties (oxygen absorb and release), which makes them proper for use in bio medical treatments and therapy. Nano ceria have been used as an anti-oxidant agent due to the existence of oxygen defects on the surface of ceria, and the auto-generative cycle of its double oxidation states (Ceria 3+ and Ceria 4+). Many disorders in the human body are related with oxidative stress and inflammation and ceria NPs can be used as a tool for the treatment of those problems because they help to reduce the stress and their associated disorder [67, 68]. Ceria nanoparticles have been studied as a means of protecting cells from death due to oxidative stress. Ceria NPs are nontoxic and bio compatible, and the protection of cells from death is because of antioxidant properties of the ceria nanoparticles [55]. Ceria NPs have also been used in cancer treatment and for neuro protection because they have a capability to protect bio cell/tissue from radiation in a cellular liquid environment during cancer treatment [69-71].

Figure (Abstract/cover figure) in reference [66]

Figure 2-4: Applications of nanostructured Ceria materials in different fields [66].

2.5 In-Situ Electron Irradiation

In-situ live transmission electron microscopy (TEM) has been widely applied in studies of the real time observation of radiation effects in various type of precursor materials, such as metals, ceramics and semiconductors inside the sample chambers of transmission electron microscopes. This field of research is now a well established in in-situ electron microscopy [72]. Generally, in TEM the electron beam causes damage of the sample during analysis of any materials. So latterly, the majority of researchers have applied that intentional electron beam damage for the live study of material irradiation and other live observation of chemical changes in structures [3]. The in-situ electron irradiation method is a necessary tool in obtaining a significant understanding of electron beam-matter interactions, damage events, material behaviour under strong radiation environments, and simultaneous morphological changes and crystallographic information during irradiation transformation [4]. Nowadays in-situ TEM electron irradiation microscopy is regarded as a powerful and promising method for the study of real time live structural changes, phase transformation including nucleation and growth transformation at the nanoscale, and also for glass irradiation. In effect researchers have used transmission electron microscope as a 'Nano-laboratory' for conducting experiments on the nano scale [72, 73].

2.5.1 History of TEM irradiation

The TEM electron beam induced irradiation method to produce nanostructures has been in use for more than six decades. A transmission electron microscope (TEM) with live in-situ electron beam irradiation was initially used in 1961 by D.W. Pashley et. al. at the University of Cambridge, in the United Kingdom. They found small spots and dislocation loops in thin film of gold, and their final conclusion is that the defects were generated by the electron beam of the TEM [74]. This TEM irradiation technique is routinely used as ‘‘a powerful means of studying live radiation damage” [74] for the generation of nanostructures without introducing any further contamination especially for metals. The basic applications of in-situ direct electron irradiation have been based on Co, Li and Au in a high voltage TEM [13, 14, 75]. During electron irradiation in TEM, high-energy electrons transfer their energy, and this transfer can lead to a variety of changes, including: chemical composition, single crystal to poly crystalline phase transformation [9], nucleation and growth, precipitation, defect formation, coalescence and diffusion [74], new amorphous and crystalline phase formation, gas bubble formation, radiolysis, and knock-on damage [3].

The results of in-situ electron beam irradiation is generally recorded with the help of a series of still images either captured manually frame by frame, or recorded as a live real time video by using photographic films / TV camera or charge couple device (CCD) cameras. Nowadays, digital CCD cameras with very high sensitivity and low noise have replaced the photographic films or old TV cameras. Digital multi-scan cameras allow the capture of individual frames or digital video sequences of the irradiation experiments in the electron microscope [72].

2.5.2 Dry In-situ TEM e- Irradiation

The irradiation of nanomaterials in this section is labelled “Dry irradiation” to separate from the “liquid cell irradiation” topic described in 2.6.1. To achieve the controlled morphology of

nanostructure (NS) during in-situ e- irradiation, the most important factors are exposure time, thickness of sample, and a fine focus electron beam having appropriate current density and accelerating voltage 200 or 300 kV for the irradiation of samples. Upon the electron-matter interaction of a precursor, the highly intense energetic electron beam of TEM causes the sample to undergo elastic and inelastic scattering phenomena, and as a conclusion there is a transformation of the precursor into a product by damage of the initial sample. Nanostructures formation or other chemical transformations are a result of the beam damage [4]. The continuous irradiation exposure by the direct electron beam causes the knock-on and transfer of kinetic energy from electrons to the precursors, which is the main cause of displacement and rearrangement in the atomic structures [3]. The beam damage is a result of the direct transfer of energy from the electron beam to the sample which produces heating due to electron-phonon scattering. The following expression (2.2) can be used to determine the knock-on displacement energy of atoms. [76].

$$E_t = [(100+AE_d/5)^{1/2} -10]/20 \qquad (2.2)$$

Where E_t is the threshold energy (The energy required to break the atomic bond which represents the how strongly the atoms are bonded to their neighbouring atoms), A is the atomic weight of material or sample and E_d is the displacement energy (the required energy to displace an atom from its atomic position in lattice site called as displacement energy).

2.5.2.1 In-Situ Irradiation in Metallic Particle Research

Following the successful application of in-situ irradiation of metal to metal (in which metal is irradiated in TEM and formed in situ metallic nano structures) transformation of gold thin films into nano particles, researchers have applied this technique for the generation of metallic nanostructures. Because research studies on an in-situ electron irradiation synthesis method for metals has three main advantages. Firstly, it generates high purity of nanostructures materials

because the whole process is in a vacuum and also surfactant free [77, 78]. Secondly, it provides a fresh and on demand bulk yield of nanoparticles. Thirdly, it can provide the formation of different patterned nanostructures [79]. In-situ TEM irradiation has been used for the generation of nanostructures of Au (shown in Figure 2-5) in high voltage TEM [75].

Figure 2(a and b) in reference [75]

Figure 2-5: (a) High-resolution TEM images of Au NPs also showing lattice fringes. (b) Low resolution TEM images of Au NPs [75].

Another example of metal to metal synthesis of Ag nanostructures by using in-situ electron beam irradiation method can be seen in Figure 2-6. In this research they have used calcinated Ag micro particles. In this calcination process they have heated silver ore at high temperatures in the presence of air or oxygen[80].

Figure 3(a and f) in reference [80]

Figure 2-6: (a) TEM images of Ag micro-particles prepared by a calcination method (b) Ag NPs after electron beam irradiation [80].

Similarly, TEM irradiation methods have been used to synthesise metallic nanomaterials of Co, bismuth and Ag from their ceramic (salt) precursors [79, 81]. An example of on demand salt to metal synthesis of ferromagnetic Co nanocrystal hierarchies in various size with shape controlled morphology by using TEM electron irradiation method is shown in Figure 2-7 [13].

Figure 2(a - d) in reference [13]

Figure 2-7: The various shapes and size of Co nanostructures synthesised by In-situ TEM irradiation [13].

2.5.2.2 In-Situ Irradiation of Ceramics

Electron irradiation in the TEM is practical route for producing on-demand oxide nanostructures. The use of ceramic materials in the engineering and biomedical industry has grown within the last few decades due to the availability of unique combinations of chemical and physical properties in ceramic materials to meet a number of demanding applications. The Phase transformation of $CaCO_3$ to CaO (single crystal to poly crystalline) are conducted by direct electron beam irradiation of calcium carbonate precursors as shown in Figure 2-8 [8, 9]. This irradiation method has also been used for the determination of valance charge in various rare earth materials such as cerium (Ceria4+ to Ceria 3+) by using electron energy loss spectroscopy (EELS) [15, 82]. The transformation of a hydrated cerium based sample by electron beam irradiation results in various chemical and physical changes, like inversion of cerium M-edge sub peaks i.e. M5 to M4 ratios, edge effect peak positions and peak separation [15].

Figure 1in reference [9]

Figure 2-8: TEM images and their corresponding FFTs (a-f) show the single crystal to poly crystalline phase transformation of calcite to lime [9].

2.6 Introduction to the Liquid Cell

The basic purpose of TEM is characterisation of materials with high resolution imaging. Originally TEM was not used for the characterisation of liquid samples because they evaporated in vacuum [5, 83], therefore it was limited to only solid or "frozen biological" samples [83]. After the development of environmental TEM technology it became possible to analyse the wet (biological/other) sample with limited resolution. Due to limitations (low resolution, low vacuum) of open environmental chamber, TEM is not suitable for samples in

liquid layers of controlled thickness, or if the experiment needs a continuous flow of fresh liquid.

The solution to that limitation required the design of an enclosed stable hermetically sealed chamber for carrying out controlled characterisation of nano materials, and also for the synthesis of nano materials with known nucleation and growth mechanisms. Previously the synthesis of nano structured materials was possible through an ex-situ method, and the synthesised nano materials were characterised after completion of a whole nucleation and growth process. This kind of post-mortem analysis cannot provide the required information for the optimal synthesis of nano materials because the whole process is not made as a real time observation. After a few years of development in environmental TEM Microscopy, it became possible to enable electron-transparent membranes to form in enclosed uniform liquid chambers [84]. Since then, researchers have used thin carbon foils [85], thin graphene sheets [86] and silicon nitride (Si_3N_4) films as an electron transparent membrane for making a thin enclosed chamber called a "liquid cell" that contains the liquid with the sample. Liquid cells with thin silicon nitride films (20-100nm) are robust and easy to manufacture with homogeneous composition and uniform thickness [87]. Currently in-situ electron microscopy of liquid samples or a liquid /gas environment[88] is possible with a liquid-cell TEM holder in conventional TEM without any modification. The liquid cell TEM holder makes it possible to view the dynamics of live transformation processes of samples in liquid [73, 83]. Figure 2-9 shows schematically the internal dynamics of liquid cell reactions under a live electron beam experiment in TEM [89]. The liquid cell method is the best option for studying the live movement of nanoparticles trajectory, attachment and de-attachment, new phase formation, nano structure formation, nucleation and growth of nano materials, and dissolution [5, 83, 90-92].

Figure (Abstract / cover figure) in reference [89]

Figure 2-9: The schematically internal view of liquid cell irradiation under an electron beam in TEM [89].

Chemical reactions, nucleation and growth process of nano structure materials from ex-situ methods are probably completely blind or unknown. Liquid cell transmission electron microscopy (LCTEM) however, has opened up a brand new approach to overcome the difficulties nanomaterial synthesis by enabling the live observation of nanocrystal formation in a controlled liquid environment. In-situ live synthesis and the characterisation of nanostructure, dissolution, formation and growth of nano structures have been extensively reported in the last few years in diverse areas that include in aqueous chemical solutions [93, 94], nanomaterials diffusion processes [91], self-assembly and attachment of metallic nanoparticles [95] and electron beam-induced dissolution and growth of metallic nanostructures [96].

2.6.1 Liquid irradiation

Liquid in-situ electron irradiation microscopy is a unique and powerful method, that provides an exceptional insight into phenomena in liquid media. Radiolysis of water occurs in different situations, like X-ray radiotherapy, food irradiation, sewage treatment, radio-sterilisation, and also during electron irradiation in liquid cell experiments [97, 98]. In the liquid cell in-situ irradiation process, unintentional radiolysis of water reaction has occurred by TEM electron beam. This causes the formation of electrons, atoms, radicals, ions and molecules (e^-_{aq}, $H^\bullet$, $OH^\bullet$, $HO_2^\bullet$, OH^-, H_3O^+, H_2 and H_2O_2). Water radiolysis is simply the spliting of water molecules by the electron beam of TEM. Generally this ionizing radiation is generated by the decay of radioactive nuclei, beam accelerated particles (electron, protons and neutron), and from the X-ray radiation having a wavelength corresponding to an energy greater than 50-100eV. In the liquid cell experiment, the unintentional radiolysis causes localised changes in

pH from neutral to acidic or basics depends on the formed components of water i.e. $H^{\bullet}$and OH^{-}. The main reason for pH changes is due to water radiolysis generating the different reactive species by water splitting [99, 100] according to the reaction scheme in equation 2.3.

$$H_2O \rightarrow e^-_{aq}, H^{\bullet}, OH^{\bullet}, HO_2^{\bullet}, OH^-, H_2, H_3O^+, H_2O_2 \qquad (2.3)$$

Here, e^-_{aq} denotes the hydrated electron, and species marked ($^{\bullet}$) are radicals and other are ions and molecules accordingly. The first two i.e. (e^-_{aq}, $H^{\bullet}$) have a strong potential to chemically reduce ions in solution or on particle surfaces, while hydroxyl ($OH^{\bullet}$) behaves as an oxidiser [100]. Some reactive products of water splitting are capable of oxide dissolution (e^-_{aq}, $H^{\bullet}$), and are usually short lived. During the time-scales of our dissolution experiments, they are complemented by longer lived products including the final two molecular species of the equation (2.3) [98].

2.6.2 Application of the Liquid Cell

There are several applications of liquid cell TEM holder in different fields of engineering and medical science [101]. Before the introduction of the liquid cell holder, the primary evidence for nucleation and growth processes came from the ex-situ TEM observations. The liquid cell has removed the limitation of post-nucleation mechanism processes [102, 103]. This has raised many new questions related to classical nucleation theories [104] as a result of many new observations and several gaps in knowledge were noticed [105]. The evidence of live nano particle nucleation and growth, self-assembly, and dissolution in different liquid medium are described separately below:

2.6.2.1 In-situ e- Irradiation in Water / NaCl / Water+ Br^- Ions

The radiation chemistry of the liquid is the key factor for all in-situ e- irradiation experiments of the liquid cell process. According to Grogan, et al an increase in the ionic concentration of

irradiated colloidal suspension leads to a reduction in the thickness, induces aggregation, and allow chemical precipitation during the experiments [106]. By using the wet cell TEM method at low, moderate and high electron dose intensity, observations may be made on the dynamic motion trajectory of single nano particles, clusters of nano particles, displacement and rotation of motion of NPs, merging of NPs, and the growth and corrosion. These observations related to the liquid cell TEM of nano particles with pure water, allow a discussion of electron beam effects on the movement, growth and dissolution of nanoparticle clusters.

Electron beam irradiation of aqueous NaCl solution during irradiation experiments may cause the radiolysis of NaCl solutions and generate well known irradiated species such as $HClO^{\bullet-}$ which can change the solutions pH i.e. oxidizing due to the formation of hypochlorite. It is important to understand that during irradiation, the irradiation chemistry of any liquid in the liquid cell should be dependent on the energy of TEM and intensity or dose rate of the electron beam [89, 98]. For example in the case of aqueous NaCl solution, the formation of $HClO^{\bullet-}$ is low when the applied dose rate is low, and it continuously alters or increases with the dose rate of the e- beam during the experiment [107].

Research studies stated that during e- irradiation experiments with the liquid cell with water, various species have been formed, and many chemical reactions are initiated including precipitation, and nucleation reactions, and also the dissolution or corrosion of the precursor or nanoparticles have been observed [98]. For instance the corrosion of Cu and Al nano films in the presence of different molarity of aqueous NaCl have been observed [107]. Some researchers have observed the etching of metallic nano structures during liquid cell experiments. Jiang et. al. revealed the oxidative etching of metallic cubic Pd nano crystals in water in the presence of Br^- ions with a scanning transmission electron microscope (STEM) during liquid cell experiments. They observed the in-situ dissolution of 18nm sized Pd nano cubes (NCs) in STEM in the presence of a dissolving agent (i.e. Potassium bromide (KBr)) as

shown in Figure 2-10 (A). Figure (B) shows the projected area versus time graph for the selected four nano cubes of figure (A) [108].

Figure 2 in reference [108]

Figure 2-10: (A) Time-lapsed colour STEM – HAADF images showing the etching of clusters of Pd NCs, (B) Shows the dissolution plots of time against projected areas for the nominated four NCs shown in A [108].

These authors observed the etching of nano cubes (NCs) from the apexes and edges, rather than from the side facets, which then transformed into a spherical shape nanoparticle. They found the dissolution rate dr/dt increased when the size of the nano cube was reduced in diameter. During liquid cell experiments they have observed that electron beam played a vital role for the dissolution of Palladium NCs due to formation of water splitting products during irradiation. On the other hand, in the absence of STEM electron beam irradiation, Pd NCs remained almost unchanged in the same solution, having the identical concentration of Br^- ions for a few days at normal room temperature. They also observed that when the electron beam intensity increases, the dissolution rate increases, and the electron beam has a directly proportional relationship with the etching. Observations were also made by these authors of a dissolution rate of Pd NCs of three to four orders higher compared with the ex-situ experiments [108].

2.6.2.2 In-situ e- Irradiation in Solvents / Water + Solvents

Recent developments in liquid cell TEM methods provide the opportunity for observing the behaviour of precursors or nano particles in different solutions, like alcohol, ethanol, and mixtures of water and organic solvents. Liao et al. used an organic solvent (i.e. a mixture of penta-decane and oleylamine (7:3 vol/vol) or a combination of pentadecane, oleylamine, and oleic acid (6:3:1 vol/vol/vol)), to explore the colloidal nanocrystal architecture and solution growth of Pt_3Fe nano rods from nanoparticle building blocks [109] as shown in Figure 2-11.

The exact phenomena of growth mechanisms are unclear due to limited research data available regarding the liquid cell. Liao et al. observed that the formation of single crystal nano rods by winding the growth of polycrystalline NP chains through shape oriented nanoparticle attachment. Such types of growth are important for the design and synthesis of hierarchical nano structure materials, and for controlling nano particles self-assembly for functional device applications.

Figure 2 (a) in reference [109]
Figure 2-11: The serial TEM images of the growth of a small Pt_3Fe nanorod [109].

In some other investigations Evans et al. observed the nucleation and growth of lead sulfide (PbS) nanoparticles in a TEM liquid cell experiment by in-situ irradiation of the mixture of a water-based solution containing lead acetate, poly-vinyl alcohol (PVA), isopropyl alcohol and thioacetamide. During the experiment they observed the selective decomposition of thioacetamide and the release of free sulphur by e beam irradiation. This led to the free sulphur reacting with the lead ions to start nucleation and then growth of PbS, where PVA was used as a stabilizing agent [93]. Figure 2-12 (a-d) shows the tracking of live nucleation and growth PbS nano particles in multicomponent solution. The growth occurs homogeneously along all faces, and estimates show that the overall rate of growth increases with volume increase per video frame (i.e. the electron dose). A graph of 5 individual selected NPs of time series shows the NPs size (Area nm^2) verses time (movie frame number) is shown in Figure 2-12 (e). The graph shows the growth of PbS NPs, as grey, blue, red and purple by the use of monomer attachment from the solution as the nanoparticle move out of the field of view as indicated by green line. Furthermore, the plot (e) Figure 2-12 shows a double growth rate as indicated by the blue line of the NP between frames 3 and 4 as great compared to any other nanoparticles following nucleation. The final diameter of NP indicated by the blue line is also double the size of the other PbS nanoparticles [93].

Figure 2 in reference [93]

Figure 2-12: The growth of PbS nanoparticles during LC irradiation experiment (a-d), with (e) showing the plot of growth of NPs size versus time.

2.6.2.3 In-situ e- Irradiation of Precursors (Salts)

In this section we collect earlier research which uses salt as a source for growing particles from salt cations, unlike in 2.6.2.1, where salt was just an additive to the liquid. In the irradiation of a salt precursor of gold in the liquid cell, Nielsen et al. reported live nucleation events of gold nanoparticles from a gold chloride solution containing citric acid as a capping agent. The highlighted rectangular region in Figure 2-13 (a) shows the formation sequence of some nascent nuclei that fail to reach the critical radius for further growth. Nielsen et al. have also observed some fluctuations in sizes, and these fluctuations indicate the true nucleation process in which high density fluctuations are required to complete the nucleation process as shown in Figure 2-13 [104].

Figure 1 in reference [104]

Figure 2-13: The nucleation process of gold nanoparticles. The video sequences (a-d) are of nucleation of Au NPs from a Au-chloride solution in the presence of citric acid. (e-n) is the magnified section of the rectangular area of figure (a) which shows the formation of nuclei (highlighted circle area). These fail to reach the critical radius, and instead fluctuate in size until they entirely disappear [Scale bar (a-d) 500nm and (e-n) 200nm] [104].

Nielsen et al. observed the live growth of ferrihydrite nanoparticles from $FeCl_3$-KH_2PO_4 solution during an in-situ liquid cell experiment. The observed growth was due to movement and co-alignment of the lattice of contacting surface match prior to the attachment of nanoparticles. As a result, these authors obtained a defect-free oblong branched structure due to oriented attachment (OA) as shown in Figure 2-14. In this figure (a-b) dumbbell shape ferihydrite particles approach the large crystal and then they are subject to some attractive forces that drive OA, and it undergoes a clockwise rotation before attachment [104].

Figure 2 in reference [104]

Figure 2-14: The live growth of ferrihydrite nanoparticles via OA. The sequence (a-f) shows the dumbbell shaped ferryhidrite nanoparticles formed during the oriented attachment event. (scale bar 10nm) [104].

Similarly, Woehl et al. used solutions of salt silver nitrate ($AgNO_3$) for liquid cell electron irradiation experiments with a TEM. They observed the controlled growth of silver nano crystals during liquid cell electron irradiation experiment of silver nitrate, as shown in Figure 2-15 [110].

Figure 2 in reference [110]

Figure 2-15: The growth and tracking of silver (Ag) crystals, (e) shows the plot of growth of NP size versus time and (f) shows the plot of NP radius versus time (T) [110].

Woehl et al. suggested that the nucleation proceeds according to classical theory, and the growth rate is dependent on the dose rate of irradiation. Figure 2-16 illustrates the step by step process of radiolysis, the reduction of silver precursors, the formation of controlled nuclei, and the growth mechanism of silver crystals through a liquid cell electron irradiation method in TEM [110].

Figure (abstract figure) in reference [110]

Figure 2-16: The schematic of the radiolysis, reduction of precursor, Nuclei and seed formation and growths of Ag nanoparticles via reaction or diffusion limited method [110].

Abellan et al. conducted experiments using the liquid cell with cerium nitrate as a precursor, and discovered the formation of irregular sized ($Ce(OH)_3$) nanoparticles, as shown in Figure 2-17. Initial experiments by these authors showed that under acidic conditions, the formed cerium oxide was thermodynamically unstable and that it is only stable if the conditions are alkaline. However, they have suggested that the growth of $Ce(OH)_3$ has been observed due to an increase

in pH. They suggested that the pH is increased due to a cascade of radiolytic and chemical reactions induced by a high energy TEM electron beam [111].

Figure 1(a) in reference [111]

Figure 2-17: Dark field Scanning TEM images showing the growth of Cerium-oxide ($Ce(OH)_3$) nanoparticles in LC [111].

Nielsen et al. have described observations of the nucleation and growth, dissolution and re-precipitation of $CaCO_3$. They used $CaCl_2$ and $NaHCO_3$ solutions of variable concentrations in a dual inlet liquid flow cell. They also noticed the live nucleation of both metastable and stable phases in liquid, with amorphous calcium carbonate (ACC) and their dissolution. In the liquid cell experiments they observed a thinning of ACC. Some ACC particles underwent uniform and non-uniform (slow or fast) shrinking until their complete disappearance, as shown in Figure 2-18. They mentioned the observed shrinkage was due to a discharge of water molecule from the amorphous ACC nanoparticle or a sudden reduction in concentration leading to partial dissolution [112].

Figure 4 (a-f) in reference [112]

Figure 2-18: Dissolution behaviour of ACC. Here the ACC nanoparticles undergo liquid-like dissolution and complete disappearance (A - F). (Scale bars are 500nm) [112].

Similarly, Nielsen et al. have also observed the dissolution of a small round shape ferrihydrite nanoparticle with positive curvature near the big ferrihydrite surface with negative curvature, as shown in Figure 2-19. These authors mentioned that the dissolution of ferrihydrite nanoparticles is due to Ostwald ripening controlled by volume diffusion of ionic species in a radiolytic solution, instead of aggregation [104].

Figure 4 in reference [104]

Figure 2-19: (a to f) shows the sequence dissolution of small round ferrihydrite nanoparticle with positive curvature near a big ferrihydrite nanoparticle (Scale bar is 5 nm) [104].

2.6.2.4 In-situ Irradiation Induced NP Movement and Attachment

In-situ electron irradiation of the liquid cell TEM (LCTEM) can also give us a direct observation of nanoscale structure movement of NP aggregates in liquid. Liu et al. have observed the fast repeatedly random movement of small nanoparticle aggregates under electron beam irradiation in TEM in water before attachment. They also reported on observations in NaCl solution where small NPs aggregates moved directly towards large NPs aggregates before attachment, as shown in Figure 2-20. The observed movement has been attributed to the charging of hematite NPs and the Si_3N_4 membrane due to the electron beam. These authors also mentioned that the fast movement of hematite NPs aggregates were due to the electrostatic repulsion forces between the charged NPs and the Si_3N_4 membrane during the irradiation experiment. On the contrary, the presence of the NaCl in the solution during the irradiation experiment exhibited and increase of conductivity in the liquid cell solution and a reduction of the charging effect [113].

Figure 4 (a-d) in reference [113]

Figure 2-20: Cluster-cluster aggregation of hematite NPs in water (A & B) and in NaCl (C & D) solution [113].

Verch et al. observed the movement of Au nanoparticles in liquid during liquid cell electron irradiation experiment, as shown in Figure2-21. They observed a reduction in movement by three orders of magnitude than predicted for the movement in a bulk liquid through Brownian motion. These authors mentioned that the reduction in movement was not due to hydrodynamic interruption near a wall. Which is actually due to the presence of a layer of ordered liquid having a viscosity 5 orders of magnitude higher than a bulk liquid. The observed high viscosity

causes the dramatic reduction of Brownian movement. The layer was formed around Au NPs as a result of the surface charge due to the electron beam [114].

Figure 2 (b-d) in reference [114]

Figure 2-21: The LC irradiation experiment of nanoparticles in liquid a-c) shows the NPs movement, attachment and chain formation [114].

2.7 C*rystal Growth and Dissolution*

Nucleation and growth are the key mechanisms of the phase transition in which nucleation representing initial transformation of amorphous phase into crystalline one. In nucleation and growth process, nucleation represents the initial formation of stable small particles (nuclei) of new phase and growth represents the growth of those new phase. During nucleation process a new phase has formed from an old phase. The surface free energy of old phase is higher than that of the growing new phase. The change in the free energy per molecule of the bulk and that of the surface is referred to as the interfacial free energy or surface free energy [115].

During growth a nucleus with smaller radius has larger relative surface energy, as the radius increases in size its free energy decreases. There is a critical size at which the free energy of a nucleus is at its maxima, and the free energy will always decrease whether the nucleus grows or dissolves. Dissolution is the opposite of growth process in which size of particles is decreasing with time, an increase in relative surface free energy. Crystal growth and dissolution takes place due to changes in surface energy, temperature, pressure, concentration and TEM electron beam intensity from their equilibrium values [115, 116].

2.8 Summary

The dry and liquid TEM in-situ electron beam irradiation method is a powerful experimental technique for studying the live synthesis and dissolution of nano structures. The review of liquid cell irradiation of nano structures and salts indicated that the liquid cell method is the

most promising technique for studying the dynamics of nucleation and growth, chemical reactions kinetics, different new phase formation, single crystal to poly crystalline transformation, movement trajectory of nano particles and particles dissolution. The liquid cell is the only real-time method in which we can produce and characterise the nanostructure in liquid simultaneously.

CHAPTER THREE

METHODS

3.1 Introduction

This chapter will describe in depth all the experimental methods which were used during the research of in-situ irradiation of materials. Section 3.1 will describe the experimental characterisation methods, which include the transmission electron microscope (TEM), with the operational principle of TEM, electron matter interaction and the electron beam sources used in this research. This section also includes brief information related to the use of TEMs in this research. Section 3.2 will start with the sample preparation methods of liquid cell TEM irradiation by using a Protochip P500 liquid cell holder and sample preparation for direct dry irradiation of precursors in the TEM. This section also includes some information related to the elementary parts of the liquid cell holder and all the basic steps of liquid cell holder preparation, before going on to TEM irradiation experiments and finally some limitations of the liquid cell method. The next section (3.3) presents the dry irradiation method and sample preparation methods for dry irradiation of samples in TEM. Section 3.4 presents the working principle of using chemical analysis methods in this work: for example, energy dispersive spectroscopy (EDX) and electron energy loss spectroscopy (EELS). The last section, 3.6, provides a brief description of the working principle of scanning electron microscopy (SEM).

The aim of the experimental methods used is the live synthesis of nano structures, new phase formation and dissolution of nanostructures, and their live characterisation in TEM. I have selected two hydrated cerium precursors and ceria nano structures for the live in-situ electron

irradiation induced synthesis of nanostructures and their dissolution by using high resolution transmission electron microscopes (HRTEMs) at 200 and 300kV. Because TEM irradiation has many advantages and inspirations such as live observation, characterisation of precursor or samples (so there is no need for sample transportation for characterisation purposes) and chemical analysis during experiments is also possible.

3.2 Experimental Characterisation Method / Equipment

Many characterisation methods are available, but every researcher has used different available characterisation methods with respect to their needs and the limitations of either samples or equipment. The most important characterisation tools for nano materials are TEM and SEM. Research studies are based on an assortment of methods, which directly rely on the selection of equipment for the desired experiments and their characterisation. In my case, regarding the selection of equipment to study the in-situ / real time irradiation of materials we have selected two types of high resolution TEM i.e. JEOL 2010-F and JEOL 3010. For the direct dry in-situ irradiation experiments we have selected “standard TEM holder” and for the irradiation of nanostructures in liquid we have used a special “liquid cell holder”. During the irradiation experiments (dry and liquid-cell) we have observed the live changes in structure, new phase formation, formation of 1D needles, movement of nanoparticles, chain formation, attachment of nanoparticles, and dissolution.

For the electron irradiation experiments of materials in TEM, it is very important to understand the working principles of transmission electron microscope and sources of electrons. Because we have used different sizes of electron beams with varying intensities to study the effect of electron beams on the precursors or sample during the irradiation experiments, the next section will describe the TEM and its working principles in detail.

3.2.1 Transmission Electron Microscope

The transmission electron microscope (TEM) is the essential instrument for comprehensive characterization of nano structure materials and nano-devices. Nowadays various types and categories of TEM are available and described by various acronyms, such as conventional transmission electron microscope (CTEM), high resolution transmission electron microscope (HRTEM) and scanning transmission electron microscope (STEM).

3.2.1.1 History of TEM

After the discovery by Louis de Broglie in 1925 that electrons have wave-like characteristics, and successful electron-diffraction experiments by research groups independently (such as Davisson and Germer and Thomson and Reid), two German scientists, Max Knoll and Ernst Ruska, proposed the idea of an electron microscope in 1932. They developed this idea and the working principle of electron lenses in reality, obtaining the electron image for the first time and using it in their paper [117]. The first commercial transmission electron microscope, which was the Metropolitan Vickers EM1 in the UK, was developed in 1936, exactly four years after Knoll and Ruska first proposed their idea. After the end of the Second World War, electron microscope technology became worldwide, and various commercial manufacturers started producing commercial TEMs such as JEOL, HITACHI and PHILIPS. Today's transmission electron microscope is very advanced version of the old ones because they have the capability to analyse samples at a very high resolution and some are able to achieve ultra-high resolution without aberration, and are known as aberration-corrected TEMs. Usually TEMs are available with different attachments like energy dispersive spectroscopy (EDX) and electron energy loss spectroscopy (EELS) for chemical analysis.

3.2.1.2 TEM Structure and Parts

Every transmission electron microscope has a vertical column shaped body structure which contains three main parts: i) illumination part ii) specimen stage, and iii) imaging part, as shown in Figure 3-1. The illumination system of the transmission electron microscope consists of two things (a) an electron gun, which is the main source of electrons, and (b) Condenser lenses either one or two or three in number. In the sample stage area of transmission electron microscope, the sample is loaded for analysis. The third part i.e. imaging system consists of objective and projector lenses that are used to acquire the high-resolution magnified sample images. The images can be obtained on a fluorescent screen, and these images can be recorded by using photographic film, or on a digital screen by using a charge-coupled device (CCD) camera system.

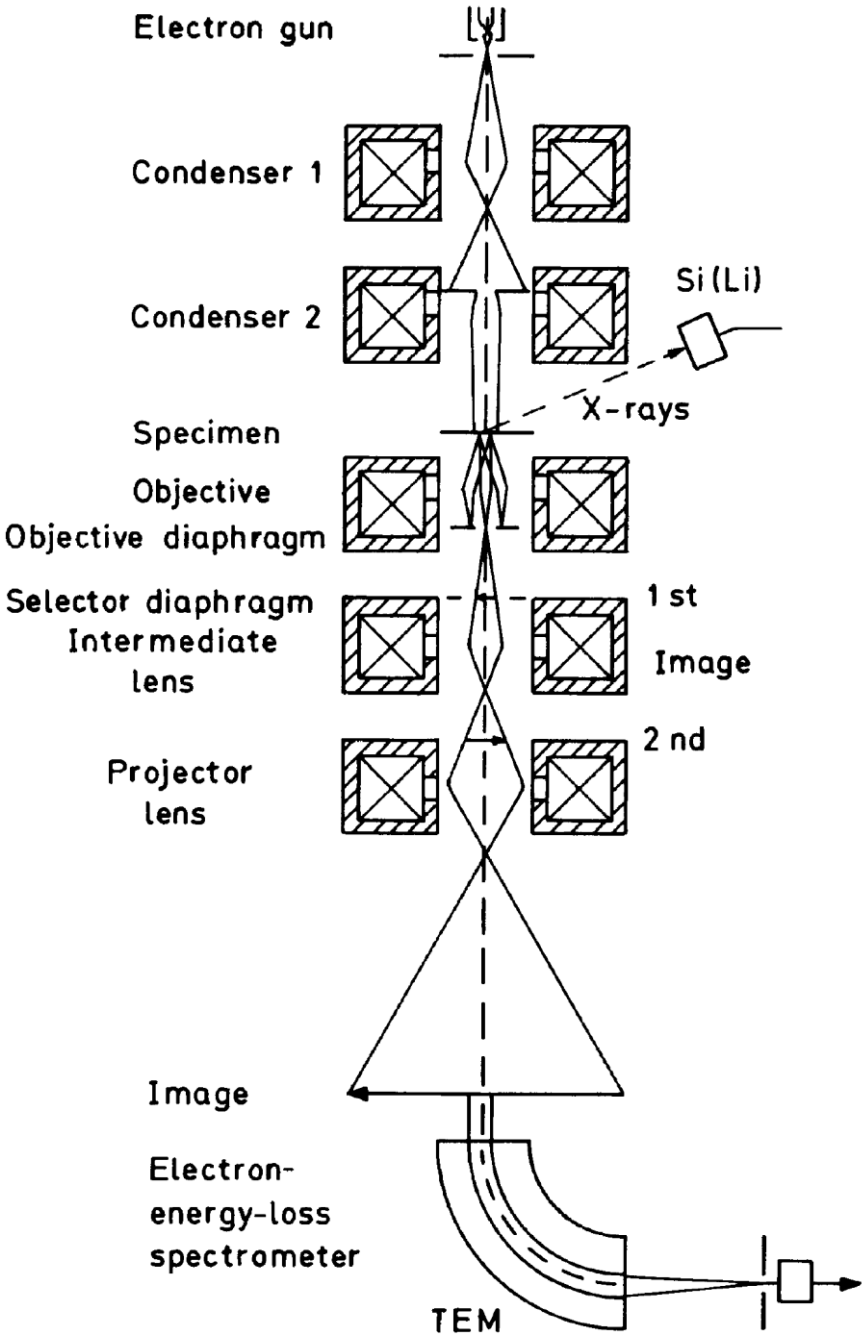

Figure 3-1: Schematic ray diagram of a transmission electron microscope (TEM) equipped with EDX and EELS [76].

3.2.1.2.1 Source of Electron (Electron Guns)

All electron microscopes need a source of electrons to illuminates the sample. There are typically two types of electron sources available: a) thermionic source and b) field emission

sources. Thermionic guns usually contain a tungsten filament (W) or lanthanum hexaboride (LaB_6) and field emission guns contains fine (ZrO/W) needles.

a) Thermionic Emission Gun

In a thermionic gun, electrons will be generated when heated. The working principle of a thermionic emission gun is as follows:

When a cathode (source of electrons) is heated up to a specified temperature (T) and gives the electrons adequate energy to overcome the natural barrier that stops the electron from emitting, the natural barrier is called a work function (∅) and the work function of W metal is 4.5 eV. The Richardson's law describes the physics of the thermionic emission gun and this law relates the current density (*J*) from the source of electron to the operating temperature (T), as can be seen in equation 3.1 [76].

$$J = AT^2 e^{-\emptyset/kT} \qquad (3.1)$$

Where "*k"* is Boltzmann's constant ($k=8.6\times10^{-5}$ eV/K) and *A* is Richardson's constant ($A/m^2 K^2$). In this study, we have used the maximum current intensity and high acceleration voltage i.e. 300kV of TEM comprising thermionic LaB_6 filament. Sometimes we have used intentionally low / high electron beam intensity for irradiation experiments in a dry or liquid state for the formation of nano structures, movement, attachment, new phases, and dissolution of NPs.

b) Field Emission Gun (FEG)

In a field emission gun, the electrons will be generated when an extremely high electric field ($> 10^9$ V /m) is applied to them. The working principle of the field emission source is fundamentally different form that of the thermionic gun. The tunnel of electrons emitted when the strength of an electric field "E" is significantly increased at the sharp points of the source with applied voltage (V) to a spherical point of radius (r) is given below in equation 3.2 [76]:

$$E=V/r \qquad (3.2)$$

In this field emission source there is a high possibility that an electron can easily leave the surface without requiring the high amount of energy represented by the work function. This decrease in work function is because of quantum mechanics and is well known as the tunnelling effect, and as a consequence of this effect many more electrons can be drawn from a piece of tungsten source as compared to using thermionic emission. The brightness can be increased by a factor of a thousand or more to a value in excess of 10^{13} Am $^{-2}$ sr $^{-1}$. The FEG guns can be further split into cold field emission and Schottky guns. The working temperature of the Schottky gun is lower than that of the thermionic gun but the emission current is higher in the Schottky gun as compared to the thermionic gun. However, the working temperature of the cold field emission gun is significantly lower than that of the Schottky and thermionic guns.

We can obtain the fine intensity of an electron beam by using a field emission gun. The electrons from a cold field emission source have a much lower energy spread, typically less than 0.5 eV, but the electrons produced from a thermionic emission source certainly have an high energy spread of 1-2 e V. This is particularly important for both analytical (EDX & EELS) and high-resolution electron microscopy imaging. Field emission guns are important because they deliver a high brightness of beam due to the clean monochromatic supply of electrons. This will make FEG guns more attractive to researchers for application in the irradiation of materials [76, 118]. We have used a 2010-F FEG gun with (W) filaments for our in-situ electron irradiation of dry precursors and liquid cell samples at 200kV with analytical analysis such as EDX and EELS during the experiments.

3.2.1.2.2 Condenser Lenses and Condenser Aperture

Condenser lenses are part of the illumination system of an electron microscope. TEMs have one, two or more condenser lens configurations for the manipulation of electrons. The purpose of condenser lenses is to control and de-magnify the beam emitted by the gun until it hits the

sample. The purpose of the two condenser lenses system is very useful because the first condenser lens C1 (situated immediately below the Wehnelt cylinder), called a spot size, sets the demagnification of the gun crossover, while the second condenser lens C2 is a weak lens that is used to illuminate the sample with an adjustable physical spot size and an angle of convergence. Further control over the angle of convergence can be achieved by adjusting the apertures. The illumination obtained by the condenser system depends upon the user or application: for instance, a small aperture is used for high magnification imaging and a medium one for diffraction patterns. A hole in a disk is called an aperture and diaphragm is the surrounding the aperture. Condenser aperture is used to allow a certain quantity of electrons to pass through the lens and stop extra electrons by using the diaphragm. In other words, the condenser aperture controls the intensity of illumination by controlling the size area of the beam and the convergence angle hitting the sample. We have used a condenser aperture to control the intensity and angle of beam convergence hitting the sample during the irradiation experiment. If we require more intense electron beams for irradiation we do not need the aperture to stop the electrons. In my direct dry irradiation experiments I used the electron beam with an aperture and without an aperture for the synthesis of round and irregular-shaped nano particles and nano rods from hydrated cerium salt precursors [76].

3.2.1.2.3 Objective lenses

In a TEM, the objective lens is the most important lens, because it forms the intermediate image and then the projector lens enlarges the image, which is displayed on the fluorescent viewing screen. There is more than one projector lens available for magnifying the size of images. Several types of objective lens are available, depending upon the need or application. The best-known objective lens has separate upper and lower pole pieces. With this type of pole piece, the X-ray spectrometer in the TEM can easily be installed for chemical analysis. Furthermore,

different tasks can be performed in the TEM, such as irradiation, tilting, rotating, cooling, heating and straining. The objective lens aperture can exclude the high angle scattered electrons from the image or aperture, thus protecting the sample from stray radiation. By using an objective lens aperture we can control the resolution of the specimen image produced by the lens, as well as the depth of field and depth of focus of image, image contrast, collection angle of electron for EELS and EDX, and the angular resolution of the diffraction patterns (DP) [76].

3.2.2 Electron Matter Interaction

Principally, electrons are ionising radiations and they have enough energy to remove the tightly bonded inner shell electrons by transferring some energy to the individual atoms of the samples. The main purpose of using electrons is that they produce a various secondary signals from the sample after electron matter interaction. Some of these signals are summarised in Figure 3-2 below.

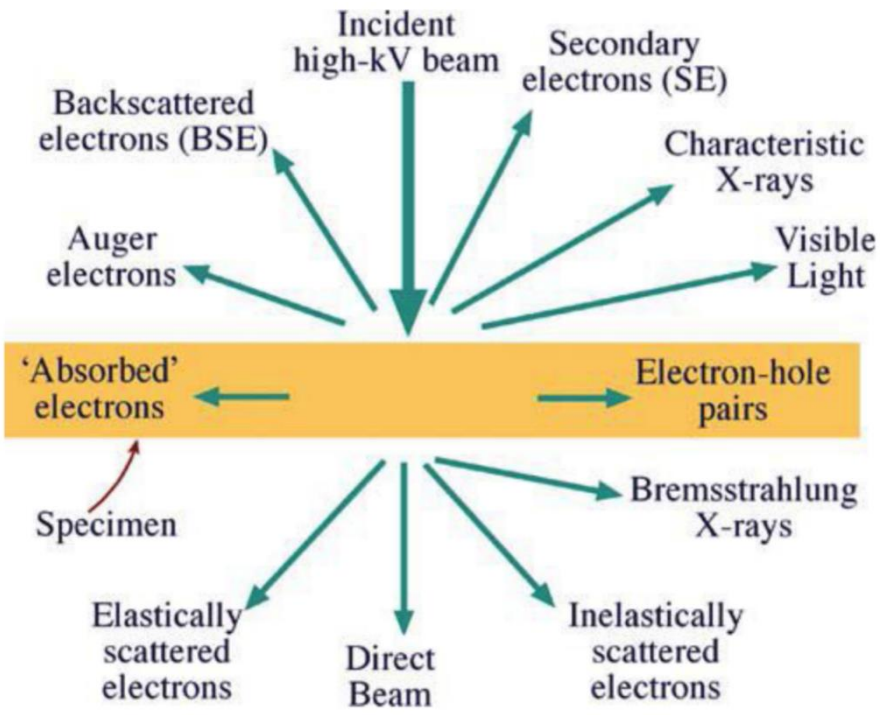

Figure 3-2: The various signals produced by electron matter interaction for both TEM and SEM [119].

This interaction can be divided into two different kinds: i) elastic interaction, and ii) in-elastic interaction.

3.2.2.1 Elastic Interactions

In this interaction, there was no transfer of energy to the sample from the electron. Because of this the electron leaving the sample has their original energy E_0: ($E_{el} = E_0$).

3.2.2.2 Inelastic Interactions

In this interaction, the sample receives some energy from the incident electrons and thus the electron energy after interaction with the matter is reduced: ($E_{el} < E_0$). The transformation of energy from the electron to the matter can causes the formation of different signals like Auger or secondary electrons, plasmons, phonons, cathodoluminescence and some characteristic X-rays. Every signal has its own characteristics and information, and we have processed the required signal by using other devices and made it useful information for characterisation purposes [119]. For example, characteristic X-rays have been used for chemical analysis information, while secondary electrons have been used for high magnification and high resolution imaging of topographical purpose, and back scatter electrons have been used for analytical contrast imaging.

This electron matter interaction causes four types of radiation damage: a) knock-on interaction damage, (b) radiolysis, (c) generation of phonons, and (d) charging.

3.2.2.2.1 Knock-on interaction damage

This is where the incoming electron transfers a large amount of kinetic energy and momentum to an atom in a crystal lattice, causing the formation of defects. If the

kinetic-energy produced by an atom is greater than its displacement threshold energy or surface binding energy, the atom may be displaced from its site to an interstice or vacancy, creating a Frenkel pair in the bulk (this phenomenon frequently happens in metals), or simply sputtered away from surfaces into a vacuum [3].

3.2.2.2.2 Radiolysis

Due to the ionising nature of electrons, the ionisation of samples through inelastic scattering occurs, and causes the breaking of chemical bonds, which is known as a radiolysis process. The radiolysis in the TEM/STEM produces atomic displacement because the excitation needs to be localized for a long enough time for the atoms to counter instinctively, and the kinetic energy acquired by the excited atom must be transferable into a momentum. This process occurs in halides, where the kinetic energy leads to the generation of a metal and the gaseous halogen. For example, common reaction happens in a photographic process in which the metallic Ag is generated from Ag-Br through light irradiation, and also for the amorphisation of crystalline SiO_2 and silicates. Hence electron beam damage due to a radiolysis process may happen in insulating materials such as ceramics and other precursors.

3.2.2.2.3 Generation of Phonons

The collective lattice vibrations are called phonons and these are produced by the up-take of various amounts of kinetic energy from the incident electron beam of the TEM. These phonons directly correspond to heating up the sample in the TEM during an experiment. Therefore, electron sensitive materials decompose easily, amorphous or crystalline, result in precipitation or re-precipitation, or even melt. Sample drift can also be observed during experiments due to the generation of phonons.

3.2.2.2.4 Charging

The charging of materials occurs through incident beams. Charging in TEMs or STEMs is mainly initiated by the emission of secondary and Auger electrons into a vacuum (except SEM) [3, 6, 120].

Electron beam effects can depend completely on some essential parameters such as the energy of the beam, the current density of incident electron beams, exposure time, temperature during imaging, thickness of the sample, and the presence of water and oxygen in the sample. We have used these parameters to explore the effect of electron beam during our irradiation experiment. We have also used the characteristic X-rays and inelastic scattered electrons for the study of the chemical analysis (EDX and EELS) of precursors and for synthesised nano structures. Secondary and backscattered electrons (BSE) also contain useful information related to high-resolution imaging and analytical imaging respectively. Secondary electrons escaping from the few nanometres of the surface of the sample have low energy (<50 eV) as compared to the backscattered electrons. I have used secondary electrons for SEM imaging of dry precursors.

3.2.3 TEMs Used in the Research

There are various types of TEM available for the analysis of materials with different attachments, but I have used two types of high resolution transmission electron microscope having 200 and 300 kV operating voltages respectively for irradiation of materials, as follows:

3.2.3.1 JEOL 2010-F Transmission Electron Microscope

The high resolution JEOL JEM 2010-F is equipped with a field emission gun working at an accelerating voltage of 200 kV, as shown in Figure 3-3, and this was used throughout the research. The main advantage of the 2010-F TEM is that a fine and focused electron beam of

smaller than 1 nm in size can be approximately achieved. 2010-F TEM provides a high intensity of electron beam for irradiation with an image resolution of about 0.19nm. This high resolution TEM 2010-F instrument was equipped with an Oxford Instrument ultra-thin energy dispersive EDX system, a Gatan spectrometer for EELS and a Gatan CCD camera for a digital imaging system.

This high resolution TEM is one of the main type of equipment which was used in this research for the purpose of live irradiation induced synthesis and the characterisation of resulting new chemical phases and nano structures of dry and liquid samples. Throughout the research, during experiments analytical methods like EDX and EELS were also used for the purpose of chemical analysis.

Figure 3-3: JEOL JEM 2010-F TEM Microscope equipped with 200kV FEG gun.

3.2.3.2 JEOL 3010 Transmission Electron Microscope

As can be seen in Figure 3-4 below, the JEOL JEM 3010 is a LaB_6 thermal filament high voltage transmission microscope operating at a maximum voltage of 300kV. So when a high operating voltage (300kV) was needed, we used the JEOL 3010 TEM. This electron microscope allows the irradiation of samples with higher beam current density and with a higher accelerating voltage (i.e. 300 kV). However, the beam has slightly less focus as compared to the FEG-JEOL 2010-F, due to thermal emission from the filament. This microscope has a TVIPS CCD digital imaging camera system for electronic imaging and for video recording purposes, and the image resolution obtained is about 0.17 nm. We used this microscope for the study of electron induced irradiation at high voltage i.e. 300 kV of dry and liquid samples for the synthesis and dissolution of precursors and nanoparticles.

Figure 3-4: JEOL JEM 3010 Transmission electron microscope equipped with 300kV (LaB_6) thermionic gun.

3.3 Sample Preparation Methods

Different sample preparation methods were used during this research project. I have divided sample preparation into two segments, based on dry and liquid samples. In this section some more details will be included regarding the instrumentation of live in-situ irradiation of samples in liquid in TEM.

3.3.1 Liquid Cell TEM

Liquid cell (LC) TEM is the one and only available method which allows the liquid samples to be analysed in a conventional TEM without any modification except the dedicated holder. By using this method, we can observe live nanoparticles (NPs) movement, changes in structure morphology and chemistry, nucleation and growth process, new phase formation and dissolution of structures. We used this liquid cell TEM method throughout our all liquid cell experiments for the study of in-situ movements, dissolution precipitation and new phase formation of nano structures in liquids phase. In a liquid cell we made an electron transparent compact sealed sandwich of silicon nitride (Si_3N_4) membranes as schematically shown in the Figure 3-5.

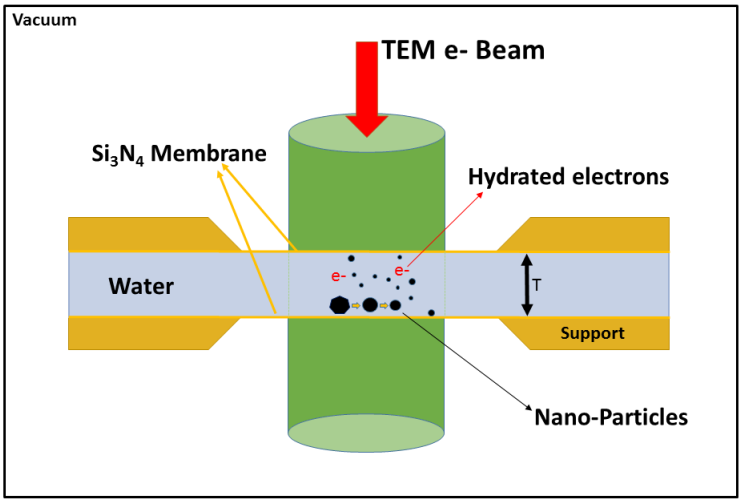

Figure 3-5: Schematic representation of a liquid cell.

3.3.1.1 Protochips Poseidon P500 Liquid Cell Holder

I have used a Poseidon P500 TEM Liquid cell holder in all of my liquid cell experiments. Figure 3-6 shows the complete setup of the Sheffield University Nano-lab liquid cell holder. The P500 is designed for use both as a standard flow or static liquid cell and for electrochemistry based liquid cell experiments. It is comprised of two electron transparent semiconductor based small and large E-chips (made by Protochips Inc. USA) which make a microfluidic silicon nitride (Si_3N_4) liquid cell inside the TEM chamber. These small and large chips are fitted within the tip recesses of the TEM Liquid cell holder with the help of two O-rings, which provide a vacuum tight seal, and are secured by a metal lid with three screws. A typical glass syringe is used in order to flow liquid medium through polyether ether ketone (PEEK) tubing into the LCTEM holder.

Figure 3-6: Nano Lab (Materials Science & Engineering UoS) LCH Setup.

3.3.1.2 Sample Preparation for liquid Irradiation

This section describes the sample preparation of the liquid cell holder for live in-situ electron beam irradiation associated with the procedure of the cleaning and loading of the Si_3N_4 E-chips. Before describing the sample preparation of the liquid cell, an explanation related to the parts and required accessories is given below to help in understanding the sample preparation method. The liquid cell is a combination of different parts: for instance, some parts are as follows:

1. Polymer coated small and large *E-chips* of electron transparent silicon nitride (Si_3N_4) membranes.
2. *O-rings* – small and large
3. Manual *syringe* for injection of fresh water into the PEEK tubing

3.3.1.2.1 E-chips

Each liquid cell experiment requires a pair of E-chips which form the microfluidic cell and serve as the sample support. There are generally two types of chips available: one for standard static or flow liquid cell experiments and another for electrochemistry experiments. Figure3-7 shows the large and small E-chips, and every E-chip is integrated with a durable electron transparent silicon nitride window which provides a strong barrier for liquid samples with minimum beam scatter. There are various type of chips available to accommodate the diversity of samples in order to enhance the performance of liquid cell experiments, and there are some parameters which should be considered during the selection of the appropriate type of E-chip before the start of every experiment, as follows: (1) Si_3N_4 window size and orientation, (2) spacer height and material, (3) flow or static liquid system, and (4) electrode geometries and composition. The volume of a liquid cell can be calculated by multiplying the area of the spacer with nominal spacer thickness, plus any additional volume introduced by the bowing of the silicon nitride window. We have used static and flow large E-chip and small E-chip with 500 nm gold spacer in our all experiment.

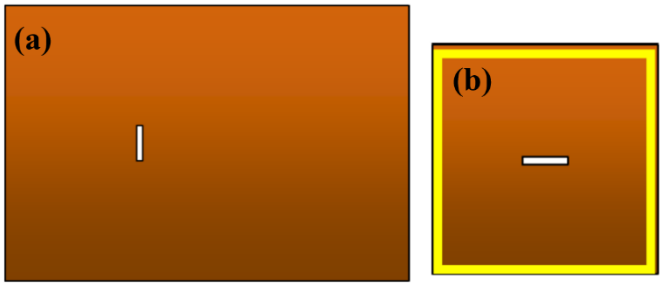

Figure 3- 7: E-chips – a) large chip and b) small chip with 500 nm gold spacer [121].

3.3.1.2.2 O-Rings

In the liquid cell experiments we used two (small and one large) Viton O-rings. These O-rings play an important role in relation to the liquid cell because they provide a vacuum seal around the holder inside the electron microscope. Therefore, without the proper fitting of O-rings, liquid cell experiments are not possible because leaking of cells inside the electron microscope could occur.

3.3.1.2.3 Syringe and Tubing

For static (non-flow) experiments, syringes and tubing are not mandatory. The nanoparticles can be flowed when we inject liquid into the liquid cells by using a syringe and PEEK tubing during the experiment. However, we used a syringe only for pouring deionized water into the liquid cell chamber for the mobilization of nanoparticles.

3.3.1.3 Liquid Cell Holder Preparation Steps

The complete liquid cell assembly is simply a sandwich of small and large silicon-nitride (Si_3N_4) based chips with or without a spacer and vacuum O-rings, as seen in Figure 3.6. A few preparatory steps are required before making the samples, as follows:

i. Removal of protective polymeric film
ii. Plasma treatment
iii. Sample holder preparation
iv. Leak check
v. Final stereo check

3.3.1.3.1 Removal of Protective Polymeric films

The commercial chips are coated with polymer to ensure safety and protection against any contamination, as shown in Figure 3-8 (a). The polymer-coated silicon nitride electron transparent E-chips are first cleaned for two minutes with acetone (99.5% purity, Sigma Aldrich) and for another two minutes with ethanol (100% purity Sigma Aldrich) in order to remove the polymer safety coating on the Si_3N_4 membrane surface. Figure 3-8 (b) shows the cleaned silicon nitride electron transparent chips.

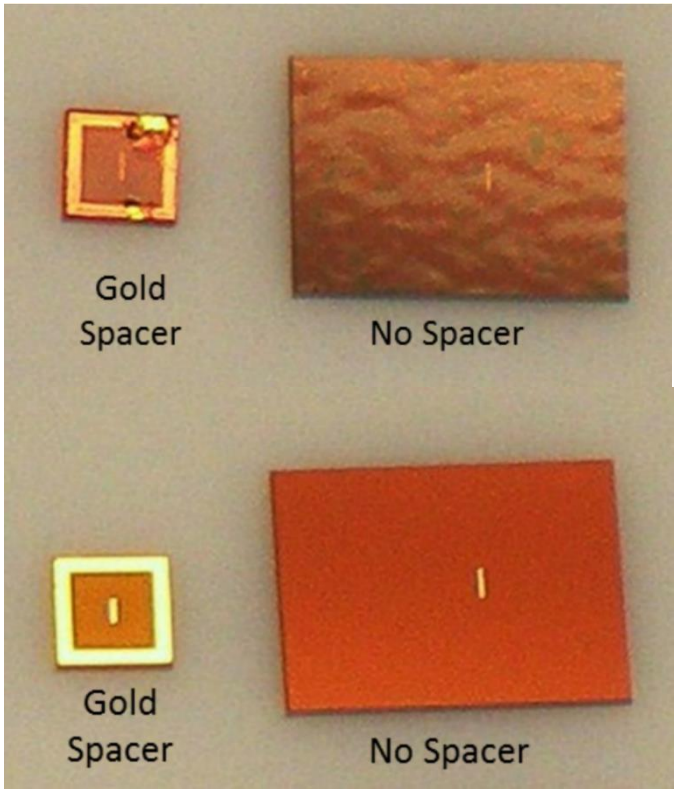

Figure 3-8: Small chips with polymer and gold spacer and large chip without spacer (A) chips before removal of polymeric safety film; (B) cleaned chips [121].

3.3.1.3.2 Plasma Treatment

The cleaned surface of a silicon nitride membrane is hydrophobic in nature, so it was necessary to make the membrane hydrophilic. For that purpose, we have used a plasma generator unit (as seen in Figure 3-9) for 20 seconds of plasma treatment to make it a hydrophilic surface. The application of plasma treatment is not mandatory for every liquid cell experiment: for instance,

if we wished to use a continuous flow system, it would not be necessary to make it hydrophilic because the sample could be injected manually by using a syringe or automatically by using a pump.

Figure 3-9: Plasma generator.

3.3.1.3.3 Sample Holder Preparation

For electron irradiation or imaging in TEMs of nanoparticles in liquid it is necessary to prepare a sample holder after the cleaning and plasma treatment of chips. The sample holder preparation for every sample is different and usually depends upon the nature of the sample and its condition. The simple method for sample holder preparation of liquid cells is as schematically shown in Figure 3-10.

1. First, the small O-ring is placed into the groove of the holder, as seen in Figure 3-10 (a).
2. The small chip on the top of the small O-ring is placed in the available recesses.
3. Less than 0.5 µL of nanoparticles immersed in water is injected onto the cleaned small chip by using a pipet or syringe.
4. The cleaned large chip is placed on top of the small E-chip and the liquid cell is closed as soon as possible, before allowing the solution to dry.

5. After the large chip is in place, a metal lid is placed on top of the large chip and secured to the top by using three screws, as shown in Figure 3-10 (b).

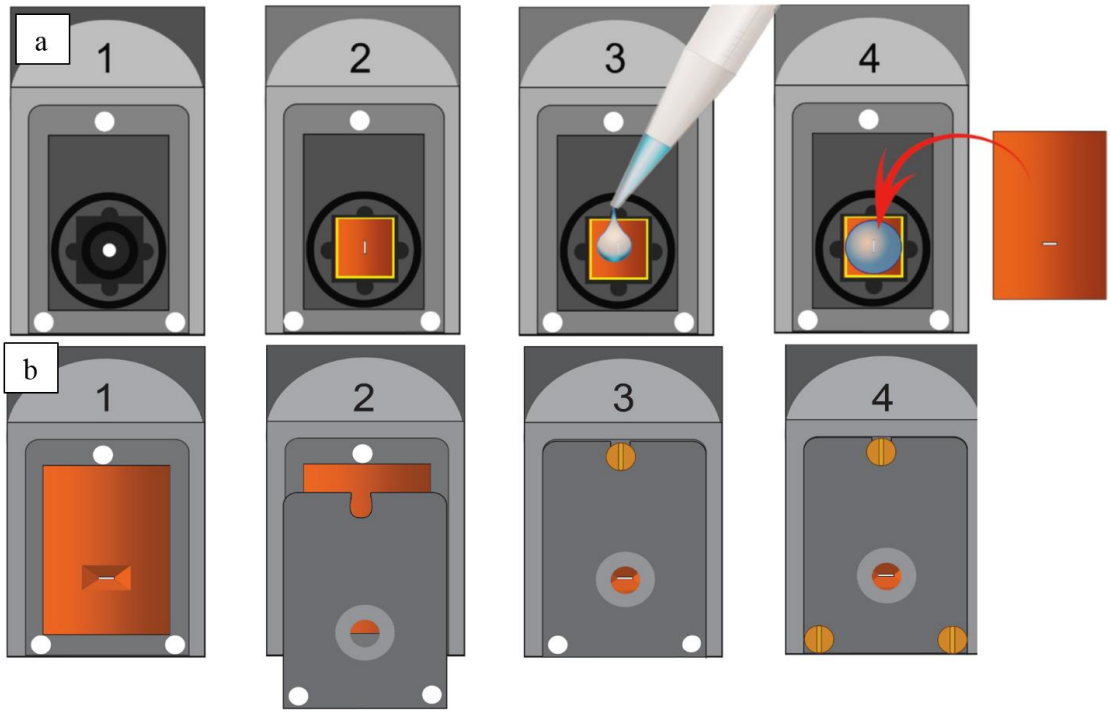

Figure 3-10: Schematic presentation of a) loading of sample onto E-chips; and b) securing of liquid cell chips by metallic lid with the help of three screws [121].

3.3.1.3.4 Leak Check

It is essential to check for any leakage of the assembled liquid cell system before placing the holder in the TEM. This is because without this step, a leak from the sample inside the microscope may cause contamination of the microscope chamber. To conduct the leak check a dry desktop vacuum pump station is used, as seen in Figure 3-11. It is necessary to pre-test the holder in the desktop vacuum because the test will remove all residual liquid during the sample loading process. During the leak check the vacuum needs to be maintained for at least 5 to 10 minutes in order to confirm that the system is not leaking before going into the microscope for the experiment.

Figure 3-11: Desktop vacuum pumping station.

3.3.1.3.5 Final Stereo Check

After the leak check it is necessary to ensure that both E-chips are aligned, so a low magnification optical microscope or stereomicroscope is used, as seen in Figure 3-12. During the final stereo check it can be verified that the viewing region from the front of the holder (where the electron transparent windows overlapped) is a see-through one. Rotating the holder 180 degrees and checking the reflection of light verifies that the window is intact. After verification that both windows (top and bottom) are intact, the holder is ready for the experiment.

Figure 3-12: a) stereo microscope; b) optical microscope.

3.3.2 Limitation of Liquid Cells

An in-situ liquid cell TEM holder apparatus has a number of benefits: for example, it provides direct evidence of real time chemical changes including nucleation and growth in liquid state [93], as well as new phase formation, dissolution of materials and chemical reaction kinetics [87]. However, it also has significant challenges and constraints, some of which are the following [98, 104]:

1. High resolution electron microscopy is difficult due to the thickness
2. Availability of small volume of liquid solution
3. Change in solution pH
4. Sticking of NPs with Si_3N_4 membranes
5. Window bulging

3.3.2.1 Resolution Problem

A liquid cell is a sandwich of the two-electron transparent silicon nitride membranes and it contains a solution with a sample for experiment. So due to the thickness of many layers of

Si_3N_4 membrane and sample and liquid it is difficult to achieve high resolution images during an experiment, and also observe a degraded EELS resolution [99]. There are various thicknesses of silicon nitride membranes available in the market, but the most popular thickness is 50nm, as thinner membranes than this are sensitive and can easily be damaged during the sample preparation process or during an experiment in the TEM.

3.3.2.2 Small Volume of Liquid

The size of a liquid cell is very small, so the volume is also small, and the small volume of liquid phase can limit the in-situ experimental study of live observation and the resulting growth mechanism. The mixing of different chemicals and precursors in a liquid cell is also impossible due to its small size.

3.3.2.3 Change in pH

It is well known during liquid cell irradiation experiments, unintentional localised change in the pH of a solution can occur due to electron beam interaction. This change in pH is due to the radiolysis of the water or solution which produces many reactive species. The change in pH has been observed only near the surrounding area of beam for a temporary period. Many researchers have observed different phenomena, possibly due to a change in pH or other species, formed by water splitting due to the electron beam of the TEM. Such changes include the nucleation and growth process, formation of nano structures, reduction of precursors and dissolution of nanostructures.

3.3.2.4 Particle sticking with Si_3N_4 membranes

Due to the small size of the liquid cell assembly, the sample of nano particles or newly formed nano particles may become stuck to the silicon nitride membrane.

3.3.2.5 Window bulging

The bulging of the electron transparent Si_3N_4 membranes is occur due to the difference in partial pressure between the vacuum sealed liquid cell and the high vacuum in the specimen chamber of the electron microscope. Due to the difference in inner and outer partial pressure of the liquid cell, the liquid path length in the middle of the Si_3N_4 membrane windows and it is grater than the edge of the window [122]. The bulging of windows can be produced multiple artefacts during experiments, such as decreased resolution, microbubble formation and degassing [123].

3.4 Dry Irradiation in TEM

Research studies have shown that dry irradiation of precursors in a TEM is a fast method for achieving fresh nano structures without any transportation problem of further characterisation of nano structures. We have used this method to synthesise nano structures through irradiation of hydrated cerium precursors in HRTEMs at 200 and 300 kV. In this research the purpose of HRTEMs is not only to obtain high resolution images but TEMs focus beams of electron 300 and 200 kV of TEM were used for the reduction of hydrated cerium precursor samples at different exposure times. Figure 3-13 shows schematically the dry irradiation of precursors in the TEM. The nanostructure formation by the electron induced irradiation depends on the electron beam current density and electron dose D ($D=\Phi \times \tau$) [124], where τ is the total irradiation time and Φ is the current density of the beam.

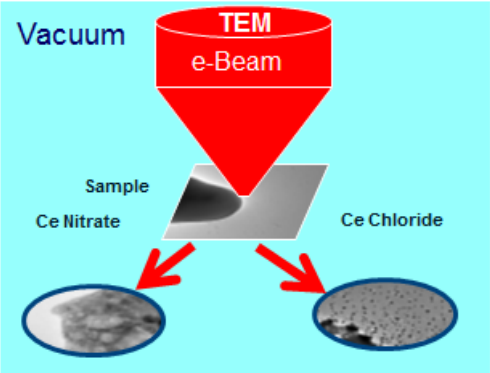

Figure 3-13: Schematic representation of dry irradiation of cerium precursors in TEM.

3.4.1 Sample Preparation for Dry Irradiation

In order to prepare the sample for dry electron irradiation of hydrated cerium precursor in HRTEM, we tried to make the sample as thin as possible, due to the conditions for making electrons transparent. There are two methods we have used for the sample preparation of hydrated cerium precursors. For both methods the small quantity of precursor sample was first manually ground to a fine powder, using a pestle and mortar.

a) The first method involved placing a small amount of very finely ground powder on the TEM copper grid.
b) For the second method, a solution was made by dissolving the ground powder in pure deionised water. A small amount, in other words a tiny drop of liquid sample, was placed on the TEM copper grid. After that the liquid sample was dried at room temperature before the electron irradiation experiment.

Samples prepared by using the second method (i.e. solution-based) are not good enough to irradiate in TEM due to long drying process in lab causes contamination of sample, so this method was not used during our study. Instead, all our samples for dry irradiation were made by using the first method (i.e. dry powder based).

3.5 Chemical Analysis

Energy dispersive x-ray (EDX) and electron energy loss spectroscopy (EELS) analysers have become very common analytical attachments for modern TEM instruments. The EDX analyser is almost a standard feature for an analytical SEM or TEM. Both two types of chemical analysis were used during our irradiation experiment in HRTEM 2010-F with the help of electron energy loss spectroscopy (EELS) and energy dispersive spectroscopy (EDX) attachments to identify the chemistry of synthesised nano structures or other phases. EDX chemical analysis in SEM was also used for the characterisation of precursors material.

3.5.1 EDX

The EDX method is the most widely used analytical technique for determining quantitative chemical results in SEM and TEM. Figure 3-2 indicates that various signals are generated when electrons interact with matter and every signal can carry useful information. The bombardment of high energy electrons on a material causes the removal of tightly bound inner shell electrons and creates a vacancy. Due to the imbalance of the situation of the electron in the inner shell, immediately an electron from the outer shell jump and fill the gap of the inner shell. This inner shell ionisation of atoms causes the generation of "characteristic" X-rays, as seen in Figure 3-14. The resulting X-rays have useful information of materials chemistry atoms present in the specimen [120]. The working principle of EDX analysis is based on the Silicon or germanium detector.

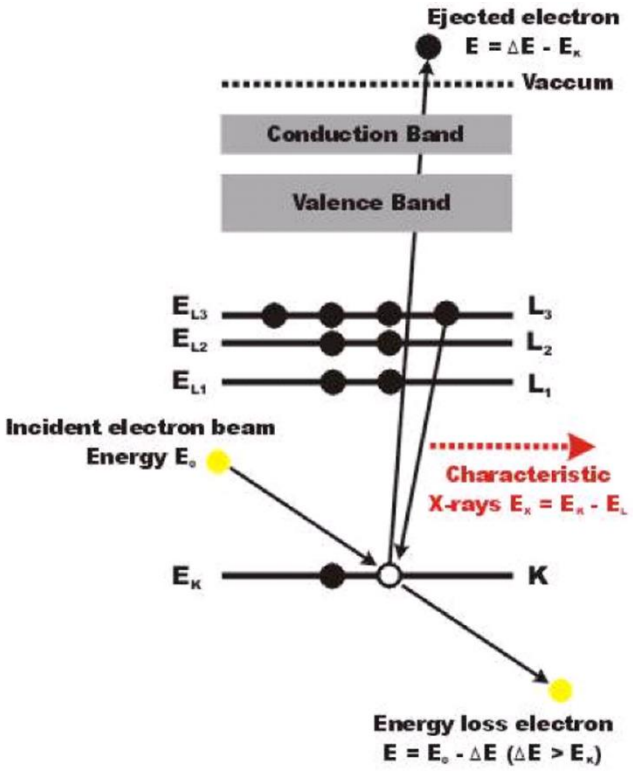

Figure 3-14: Schematic diagram of the ionisation of atoms producing "characteristic" X-rays and energy loss electrons [6].

In this work an Oxford Instruments EDX analyser was used, with an ultra-thin window detector attached to the JEOL JEM 2010-F FEG TEM, for determination of the chemistry of nano structures and phases, and the same type of EDX instrument was also attached to the Inspect-F FEI scanning electron microscope.

3.5.2 Electron Energy Loss Spectroscopy (EELS)

EELS is another important chemical analysis method used in this study. It is used in order to determine the change in chemical and structural information of specimens. EELS is based on a principle that when sample is very thin, and the energy of electron is very high then mostly all of the incident electron is transmitted to EELS spectrum. The basic principle of EELS is that when electron energy is sufficiently high, and the sample is thin enough, almost all of the energy of incident electrons is transmitted to the EELS spectrum analyser and there is no reflection or absorption. A small amount of energy from the transmitted electron will be lost

due to scattering during the interaction and remaining energy of electron carrying the data related sample internal structure can be seen in Figure 3-14 shown above. The EELS signal has the capability to accurately measure light (low Z) as well as heavy (high Z) elements easily, due to the loss of characteristic energy carrying atomic number information during interaction [125].

Therefore, the EELS method is the most important one for checking the chemistry of low-Z elements materials in the TEM during experiments. This method gives more information than EDX, such as data about the electronic configuration structure and the elemental composition of the thin sample [120]. In this research, EELS (Gatan GIF 200) was used in a JEOL 2010-F TEM to identify the chemistry of the dry irradiation product and liquid cell experiments.

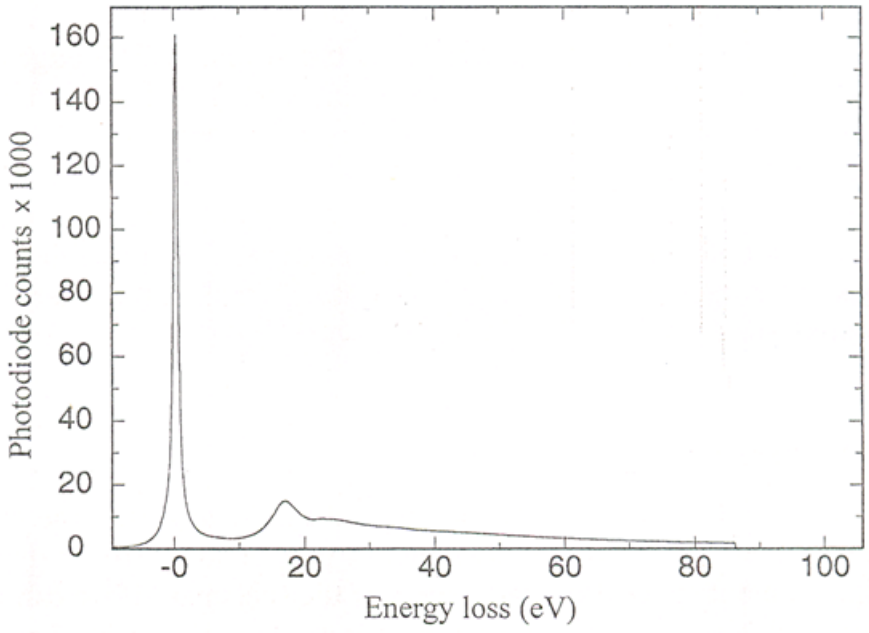

Figure 3-15: A typical EELS spectra showing that zero electron loss peak and low loss (plasmon) regions are evident at energy losses of 0 eV and around 20 eV [118].

Figure 3-15 represents the typical energy-loss spectrum that contains a first dominant zero electron loss peak and low loss region. The initial peak indicates a zero loss peak, which means this peak consists of electrons which do not lose any energy during inelastic scattering. The region consists of peaks below 50 eV, called low loss, and it represents the inelastic scattering

by outer-shell (valence or conduction) electrons in the sample also referred to as plasmon loss. This low loss scattering is the result of the collective oscillation (resonance) of many outer-shell electrons. For chemical analysis of samples, the characteristic edges at higher electron energy losses (core loss) are compulsory. In this region the electrons have suffered high energy losses and the edges represent the inelastic scattering of inner shell electrons. These inelastic excitations of inner-shell electrons have the characteristic energy of particular chemical elements and energy are known for every electron shell, the energy of every ionisation edge shows which chemical elements are present within the thin sample. The qualitative analysis of samples for determining the energies of any edges in this region can usually be seen between 100 and 2000 eV [118, 125].

Electron energy loss spectroscopy (EELS) have superior spatial resolution and energy resolution as compared to EDX, and has well detection capabilities for lanthanides or rare earth elements. Therefore, in this PhD research we have used EELS method to identify the reduction of cerium nitrate to ceria or cerium chloride to ceria. Fortner J.A. and Buck, E.C. et. al. mentioned that electron energy loss spectrometry can be positively used to identify the oxidation or reduction state of rare earth elements [126]. According to them EELS high energy M4 and M5 edges region have absence of overlap with M4 and M5 edges of other trace elements. For rare earths elements, the dependence of M4 and M5 relative peak heights on 4f-shell occupancy is obvious. Therefore, M4 and M5 can be easily used to determine the oxidation state of the multivalent elements like Ce and also for other rare earth elements. They have also revealed that we can straightforwardly use M4 : M5 edge ratio (second derivative or background subtraction method) to extract the chemical oxidation state information or reduction of cerium or rare earth elements. The relative intensities of sharp M4 and M5 edges are characteristic of the 4f-shell occupancy. The two strong features on the M4 and M5 edges

of EELS spectra of the lanthanides indicates the two electronic configurations or transitions i.e. $3d_{3/2} \rightarrow 5f_{5/2}$ and $3d_{5/2} \rightarrow 5f_{7/2}$, respectively[127].

Some group of researchers have used this method to determine the reduction state of Ce4+ in ceria by observing change in shape of the cerium high energy M4 and M5 edges. According to Garvie L. and Buseck P. the energy-loss near-edge structure of the beam-damaged of ceria exhibits cerium M4 and M5 and O K-edge shapes that are constant with reduction to a cerium 3+ oxide. They have also mentioned that during the electron beam reduction the spectrum of ceria changes as follows: (a) decreases in energies of the M5 and M4 peaks (b) changes in shape of peak structure (c) inversion of M5 to M4 ratio and (d) increase in the M5 to M4 area ratio[15].

3.6 Scanning Electron Microscope (SEM)

The scanning electron microscope (SEM) is a type of electron microscope which is principally designed for surface or topographical imaging instead of internal structural analysis, as can be seen schematically in Figure 3-16. The scanning electron microscope is similar to the transmission electron microscope because both have some identical parts, such as the electron gun, condenser lenses, and vacuum system. However, the working principle for image formation is completely different. For instance, the TEM has to provide information about the internal structure of thin specimens, while the SEM provides information about the surface or near surface of bulk samples [118].

The tungsten filament based thermionic emission gun is the one most widely used in SEMs. The electrons are accelerated to an energy that is usually in the range of 0.2keV to 30keV, which is considerably lower than typical TEM energies (100-300 keV). In the SEM, images are produced by raster scanning of electron beam to the sample while displaying the signal

from an electron detector on a computer screen. By choosing the proper detection mode it is possible to obtain a topographic or compositional contrast image. The scanning microscope provides a spatial resolution better than 10nm in SE imaging mode and 100nm in BS imaging or compositional mode with 100 times greater than large depth of field as compared to an optical microscope. Scanning electron microscopes may comprise an X-ray spectrometer attached (i.e. EDX detector) for chemical analysis. we used an FEI inspect-F scanning electron microscope (SEM) for the characterisation of dry precursors before the start of irradiation experiments in a TEM.

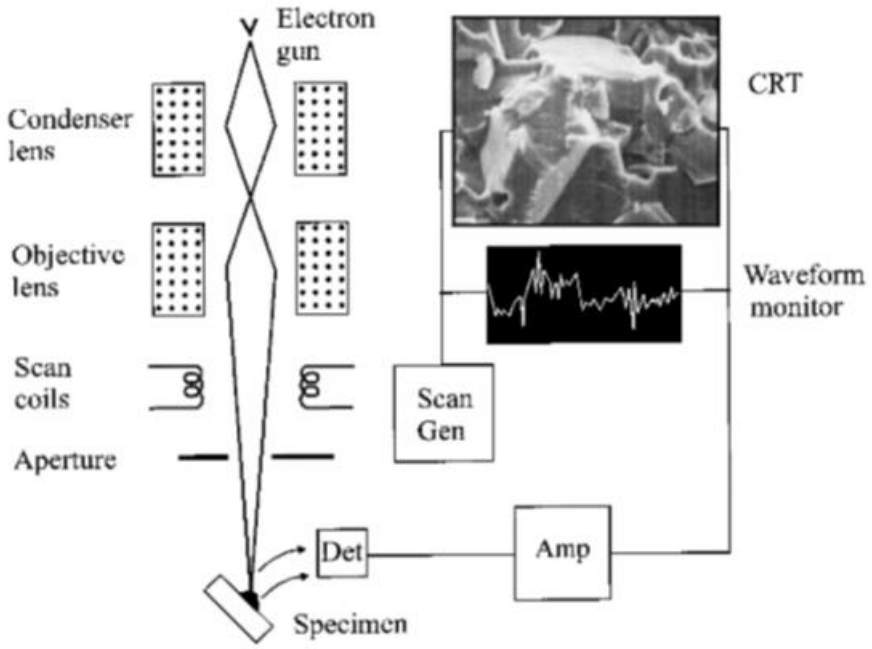

Figure 3-16: Schematic diagram of SEM showing the main components [118].

CHAPTER FOUR

RESULTS & DISCUSSION OF "LIQUID CELL" EXPERIMENTS

4.1 Introduction

This chapter discusses the results of electron (e-) irradiation of ceria nanoparticles (CNPs) immersed in water in a liquid cell (LC) in TEM. Ceria nanoparticles and ceria nanorods were selected for the purpose of electron induced irradiation in liquid (i.e. de-ionised water). The ceria nanoparticles and nanorods were labelled as CNPs and CNRs, respectively. Commercial CNPs from sourced from Sigma Aldrich having a size range of 10-40 nm in diameter, and CNRs were supplied by our USA collaborators and these were 150-200 nm in length. The chemical composition and other detail of CNPs and CNRs are listed in Table 4-1.

Table 4-1: Table provides information on the purity, source and size of the ceria nanoparticles and nanorods.

S. No.	Materials	Source	Geometry	Size nm
01	CNPs	Sigma Aldrich UK	Irregular shape, but predominantly octahedral	10-40
02	CNRs	UCF*	Regular and Irregular top surface rods	150-200

* University of Central Florida, Advanced Materials Processing Analysis Center (AMPAC) and Nanoscience Technology Center (NSTC), Material Science and Engineering, College of Medicine, Florida 32816, United States [7, 128].

The main aim of this study was to explore the live effect of electron beam on nano structures immersed in water by irradiating 10-40 nm diameter ceria nanoparticles (NPs) and 150-200 nm ceria nanorods (NRs) with an electron beam of TEM. The second aim was to record high

resolution images and live video recordings in real-time during the process of deliberate irradiation experiment in TEMs of JEOL JEM 3010 LaB6 thermal filament and JEOL JEM 2010-F field emission gun, operating at 300 and 200 kV respectively. Furthermore, energy dispersive X-ray spectroscopy (EDX) and electron energy loss spectroscopy (EELS) analytical techniques have been applied with the use of the JEOL JEM 2010-F TEM operated at 200 kV. Both TEM devices have been used for low intensity, high resolution imaging and deliberately focussed and high intensity electron beam irradiation during the LC experiments. The electron beam irradiation in both electron microscopes was applied with the biggest condenser aperture (CA) and spot size (1).

This study with the liquid cell has identified questions related to the application of ceria materials with water. These questions include stability of ceria in water, formation of new phases and fast dissolution without any chemicals. To find answers to these questions, different electron beam diameters were used to apply for irradiation with different dose levels in order to explore their influence on ceria in liquid. As reported in the literature review, ceria is the most stable oxide in air, but the stability of ceria in liquid under electron beam irradiation is now open to question. In summary then the aim was to explore the real time behaviour of ceramics in water under electron irradiation with greater precision than before. During these irradiation experiments of ceria in water, older observations were approximately confirmed, and new observations made which add to the knowledge base of these materials.

The following sections describe experiments on the electron irradiation dissolution of ceria NPs and NRs and also formation of new phases, chains and attachment of nanostructures (NS).

4.2 Results in Dissolution of Ceria NS

Multiple in-situ electron irradiation experiments in a liquid cell were conducted at different locations (contain un-irradiated Ceria NPs) and under different conditions, in order to study the

effects of electron beams on ceria NPs and NRs in liquid. This section, discusses the LC irradiation experimental results obtained with ceria nano structures.

Liquid cell experiments with ceria NPs in water using TEM irradiation was applied in order to study the movement of NPs and the behaviour of their trajectories. Earlier in this experimental work on the imaging of a liquid cell containing ceria NPs immersed in de-ionised water, observations were made of the occasional movement of NPs in water from the left to the right side of the cell. On increasing the intensity of the electron beam in these experiments unexpected shrinkage in the diameter of the ceria NPs in water was observed. This had not been reported earlier in the published literature related to ceria, and the first observation in the studies in ceramics described here, were made in 2015. In order to understand this phenomenon of dissolution of ceria nano structures irradiation experiments were carried out at higher electron intensity in TEM and observations were made of a very rapid dissolution of ceria NPs and NRs in liquid.

After multiple electron irradiation experiments a threshold electron beam intensity was identified above which there is a marked difference in the characteristics of ceria NPs and NRs in the liquid phase. Below this electron threshold intensity ($\approx$ 1 nA/μm^2) the appearance of a water front and movement of nano NPs and NRs were observed in the liquid cell. Above the electron threshold intensity ($\approx$3 nA/μm^2), using a highly focused TEM electron beam, high intensity reactions were observed. These consisted of a chain formation of nanoparticles and an instantaneous dissolution of ceria nano structures (NS), where the dissolution of ceria NS could be controlled by different aperture sizes which controls the converged intensity of the electron beam. Furthermore, observations of bubble formation were made when the intensity was increased to much higher levels that were seven times greater than the threshold intensity. It has been assumed that this dissolution behaviour of ceria nano structures in water will need

to be accounted for in any water related applications of ceria. The new observations made with these irradiation experiments of ceria in water are described separately below:

The most significant observation is the dissolution of the ceria NS during irradiation at above the threshold intensity. The bulk dissolution of ceria NPs in de-ionised water under electron beam irradiation at low magnification is shown in Figure 4-1. This figure shows the complete dissolution of the all sizes 10-40 nm of ceria NPs that occurred during irradiation over a period of time. In all cases, somewhat predictably, the smaller particles dissolve first and at the fastest rate compared with the larger nanoparticles.

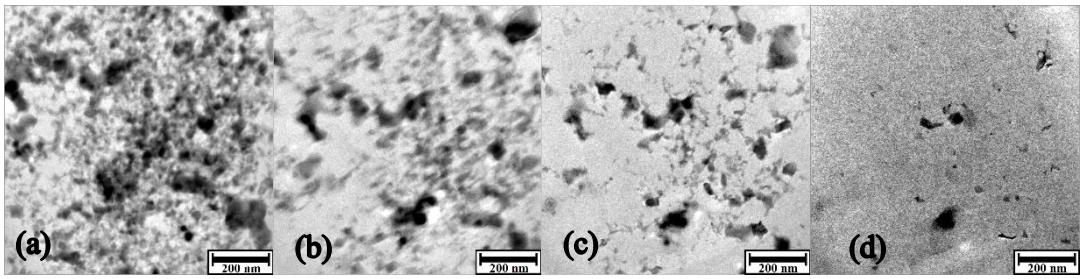

Figure 4-1: Overview of the dissolution of ceria NPs in di-ionized water at low magnification.

Following the observations on the dissolution of ceria NPs from one location in the liquid cell, experiments were then imaging at a reduced magnification in order to observe the beam impact zones of dissolution and the surrounding area. Some interesting results of localised dissolution that occurred during irradiation are shown in the low magnification image i.e. Figure 4-2 (b). This figure explains the sharply boarded regions of irradiated zone and unirradiated zone which shows the both dissolution of nanoparticles and undissolved nanoparticles. Figure 4-2 (a & b) highlights the separation of irradiated (bottom right) and non-irradiated (top left) areas. This Figure 4-2 verifies that the dissolution was only specific to the beam interacting volume zone due to change in the localised pH (acidic in nature) in the internal surrounding area of beam.

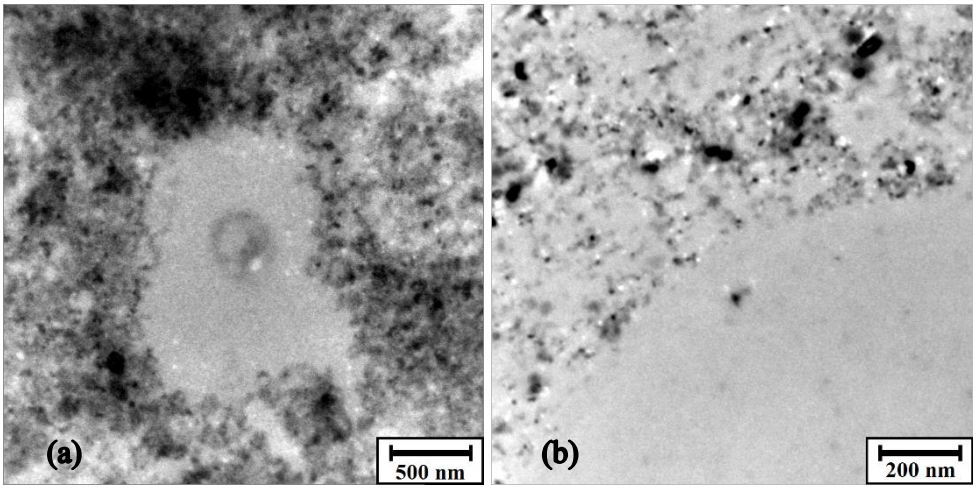

Figure 4-2: Comparison of the sample before and after irradiation dissolution: (a) The low magnification area highlighting the irradiation volume of the beam impact zone. (b) Sudden horizontal movement of the electron beam, highlighting a separation boundary between pre-irradiated (bottom right) and non-irradiated areas (top left).

4.2.1 Dissolution of Ceria Nano Particles

The results of electron (e-) irradiation of ceria NPs immersed in liquid using a large condenser aperture (CA), for the 'above-threshold' intensity e- beam (≈3 nA/μm^2), exhibits a massive dissolution of NPs. This phenomenon of dissolution was captured on a video, recorded through the help of a JEOL JSM 3010 transmission electron microscope equipped with a TVIPS digital camera. In all the experiments of irradiation of ceria it was observed that the dissolution of the ceria NPs was very fast, as shown in Figure 4-3 (a) to (d), and this was without any catalyst or concentrated acid. The dissolution of irregular shaped or sharp edges on the Ceria NPs was faster than that for round particles. The calculated dissolution time of irregular sharp edges was about 1.6 seconds, and to completely transform into pear-shaped nanoparticles took about 4.8 seconds.

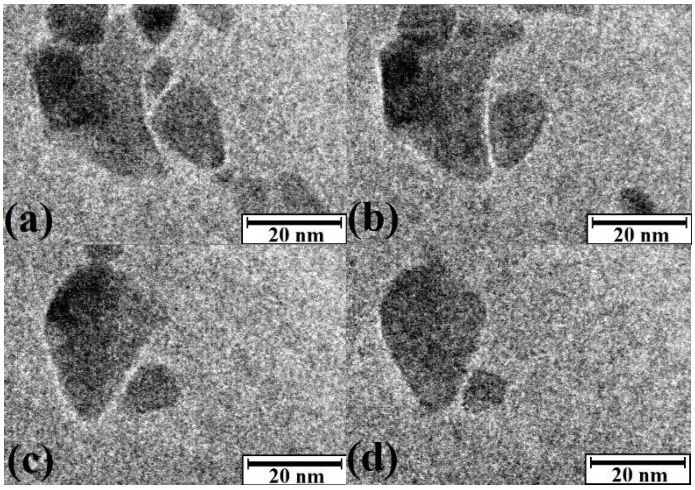

Figure 4-3: Figures (a) to (d) shows the fast dissolution of octahedral shape ceria NPs (scale bar of 20nm), where (a) 0 s (b) 1.6 s (c) 1.6 s and (d) 1.6 s apart.

4.2.1.1 Quantification of Ceria NPs

Comparisons of the dissolution rate in these experiments were made with ex-situ chemical-based dissolution of ceria NPs. To this end quantification of the dissolution rate (R) was made as function of different geometries of the nanoparticles. The calculated dissolution rate (R) in $g/m^2/day$ was used to enable direct comparisons with earlier ex-situ literature. The dissolution rate (R) calculations were made using time differences in the volume normalised to the initial surface area of NPs at the start of the time interval. In the equations (4.1) and (4.2) below m_D is the dissolved mass, ρ density of ceria, V_{SNP} the volume of NPs, and A_{SNP} the surface area of the spherical nanoparticle (approximation respectively) for a time interval t_n.

$$m_D = \rho\,(V_{SNP}(t_n) - V_{SNP}(t_{n-1})) \qquad (4.1)$$

$$R\,(t_n) = m_D / A_{SNP}(t_{n-1}) / (t_n - t_{n-1}) \qquad (4.2)$$

The dissolution rate R is a function of both radius and time for any non-flat shape. For flat surfaces owing to the change in particle size (i.e. the radius during dissolution), a different expression is required. The exponential fit for non-flat shapes can be approximated well as by exponential increase with NP radius and a decrease with time, where α,β,γ are fitting constants and r_0 is the initial nanoparticle radius:

$$R(r,t) = \alpha \exp(-\beta r(t)) \quad (4.3)$$

$$r = r_0 - \gamma t \quad (4.4)$$

$$R(t) = \alpha \exp(-\beta (r_0 - \gamma t)) = const \,.\, exp(\beta\gamma t) \quad (4.5)$$

The shape of the ceria NPs are originally irregular or octahedral, and the dissolution is shown Figure 4-3 where time t=0 is a selected sequence from a video recording. In fact, dissolution appeared earlier on, but it was necessary to wait for particles turning round shape to smoothly fit the sphere formula otherwise we can't use the formula of sphere to calculate the dissolution rate of nanoparticles. At the time of this relative t=0 measurements began of the diameter of the NPs for quantification of dissolution were made. The initial size of the particles (nanoparticle 1 (NP-1) and nanoparticle 2 (NP-2)) at the time of measurement was 35nm in size, and the particle diameter shrank from 35nm to 6 nm in the water during electron irradiation. This shrinkage corresponds to an exponent $\beta = 0.069$ in eq. 3, and the speed of radial shrinkage yields a $\gamma = 0.91$ nm/s, and the relationship between diameter and dissolution / shrinkage was found to be linear.

Tracking of the continuous dissolution of different shape geometries of the NPs (i.e. NP1 and NP2) are shown in Figures 4-4 and Figure 4-5. Further tracking studies were made for particles having projected shapes that were ellipsoid, octahedral and spherical, and the results for these particles are described in Tables 4-2 to Table 4-7. In order to obtain more accurate data, the diameters of nanostructures at the same positions were measured many times (five times) for all quantifications of dissolution, and the standard deviation calculated. The highlighted circles and points in the figures correspond to the selected particles under study. For every quantification of dissolution calculation of the NPs, the t0 is the time where we were started measuring the diameter of nanoparticles. So, for time t1, we have used the surface area of nanoparticle at time t0 to calculate the dissolution value of t1, and for time t2 we have used surface area of time t1 to calculate the dissolution values of time t2 of nanoparticle similarly

for every next nanoparticles. In order to obtain accurate data for quantification, the diameters of NPs at the same positions were measured 5 times. The standard deviation in the table also correspond to the range of 5 multiple measurements, respectively.

4.2.1.1.1 Dissolution Calculations of Nanoparticle 1 (NP-1)

One octahedral nanoparticle was selected for the dissolution calculation of ceria from the video sequences. Continuous irradiation causes dissolution of the edges of the octahedral NP, and this particle turned into a spherical shape (the yellow highlighted circle represents the NP-1 in Figure 4-4) and then the diameter measurement commences at (t=0) for the spherical NP-1 until it completely disappears as shown in Figure 4-4. A spherical approximation was assumed and the formula for a sphere was used for calculations of the surface area ($4\ \pi\ r^2$) and the volume ($4/3\ \pi\ r^3$) during quantification of dissolution calculations where the area and volumes are based on estimates from projections. Table 4.2 shows the diameter of NP-1, and its calculated dissolution rate in $g/m^2/day$ along with the calculated standard deviation.

Table 4-2: The diameter of ceria NP-1 and their dissolution values in $g/m^2/day$ with standard deviation.

NP-1 Diameter nm	**Dissolution (R) $g/m^2/day$**	**Standard Deviation**
34.8	234.9	56.1
33.1	42.7	19.4
26.9	136.4	23.8

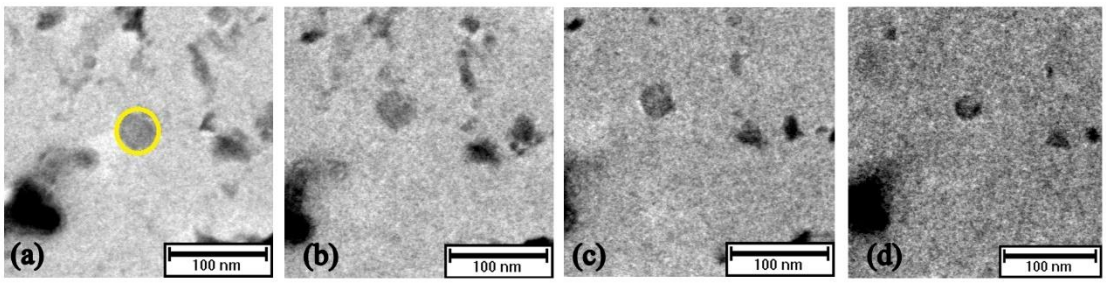

Figure 4-4: The dissolution of CNPs and the yellow circle indicates the NP-1 for the dissolution calculation.

4.2.1.1.2 Dissolution Calculations of Nanoparticle 2 (NP-2)

Figure 4-5 shows the selected images of ceria NPs obtained from the video which shows the dissolution behaviour of NP-2 during liquid cell irradiation experiment. Figure 4-5 (a) indicates the t=0 where the diameter measurement of the spherical NP was made for the dissolution calculation. As before, dissolution was observed before, t=0 because it was necessary to wait for the octahedral NP to transform into a round shape due to easily apply sphere formulae of surface area and volume. A spherical approximation (i.e. surface area ($4\ \pi\ r^2$) and volume ($4/3\ \pi\ r^3$) were used for the quantification of the dissolution of the NP-2. Table 4-3 shows the diameter of the NP-2 and their calculated dissolution rates in g/m^2/day along with the calculated standard deviation.

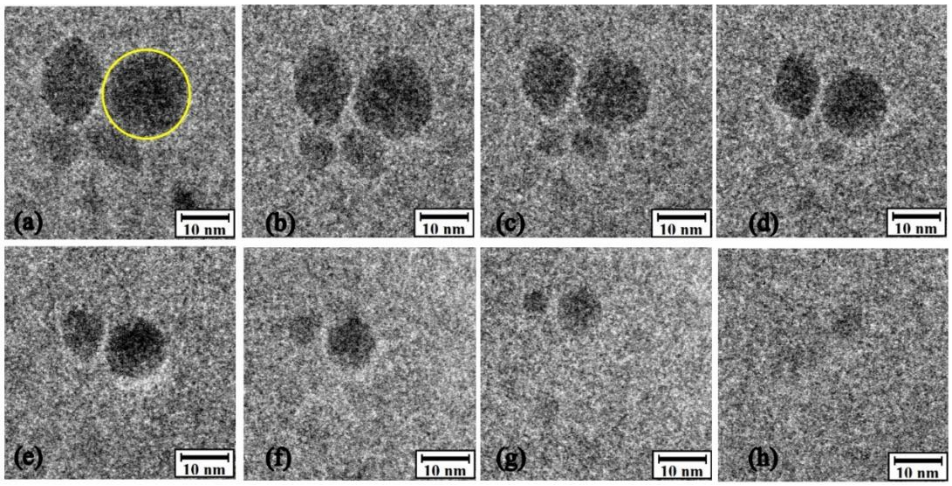

Figure 4-5: The dissolution of CNPs and the yellow circle indicates the NP-2 for the dissolution calculation.

Table 4-3: The diameter of NP-2 and their dissolution values in g/m^2/day with standard deviation.

NP-2 Diameter nm	Dissolution (R) g/m^2/day	Standard Deviation
16.2	283.0	34.0
14.9	444.2	53.4
13.6	420.7	16.9
12.1	497.6	31.5
9.7	617.6	26.0
8.8	378.2	74.7
6.7	731.1	110.4

4.2.1.1.3 Dissolution Calculations of Nanoparticle 3 (NP-3)

NP-3 is octahedral in shape as shown in Figure 4-6 though it was necessary to use the spherical approximation because the orientation of the octahedron of ceria nanoparticle is not known so we cannot apply octahedral formula for calculation of area and volume. To apply the spherical approximation an envelope is estimated such that the octahedral NP is sometime outside, and sometime inside the assumed sphere size so that the total volume is approximately the same. Table 4.4 shows the diameter of NP-3 and its calculated dissolution rate in g/m^2/day along with the calculated standard deviation.

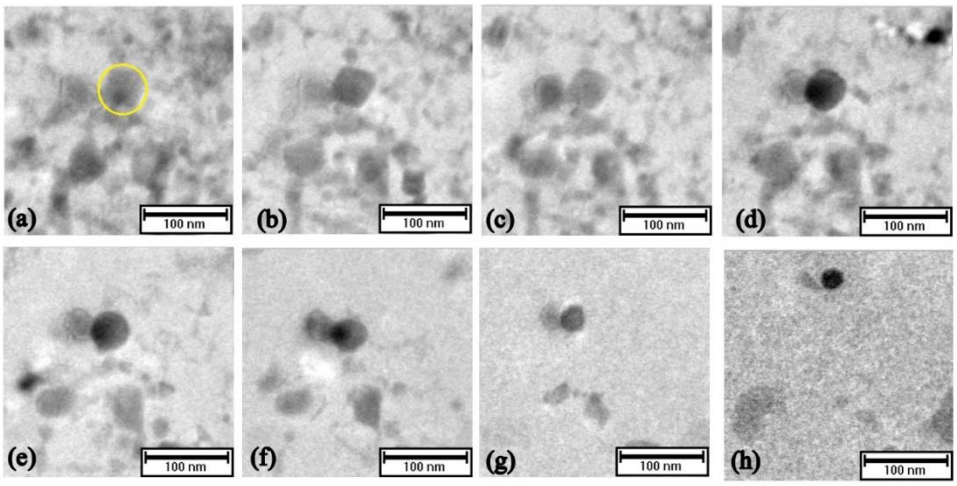

Figure 4-6: The dissolution of octahedral shape NP and yellow circle indicates the NP-3 for dissolution calculation.

Table 4-4: The diameter of NP-3 and their dissolution values in g/m^2/day and the standard deviation.

NP-3 Diameter nm	Dissolution (R) g/m^2/day	Standard Deviation
51.1	143.0	66.5
50.0	157.6	73.3
48.2	144.3	67.1
47.2	55.2	25.7
46.5	28.5	13.2
42.7	102.7	47.8
32.8	125.5	58.4
30.1	107.0	49.8
28.1	128.3	59.7

4.2.1.1.4 Dissolution Calculations of Nanoparticle 4 (NP-4)

The dissolution behaviour of an ellipsoid shaped nanoparticle during irradiation is shown in Figure 4-8. The original shape of NP-4 was octahedral, and irradiation initiates dissolution at the edges resulting in a transformation to an elliptical shape. Following the transformation measurements were made of the projected surface area and volume by considering it as an approximation of an ellipsoid of revolution in which (a=b) shown schematically in Figure 4-7. The formulae 2.6 and 2.7 shown below were used to perform these geometrical calculations and the results shown in Table 4-5. This Table 4-5 give the surface area calculation, the dissolution rate in g/m^2/day along with the with calculated standard deviation.

The surface area of an Ellipsoid = $4 \times \pi \times [((a^2)^{1.6} + 2(ac)^{1.6})/3]^{0.625}$ (2.6)

The volume of an Ellipsoid = $4/3\ \pi\ a^2c$ (2.7)

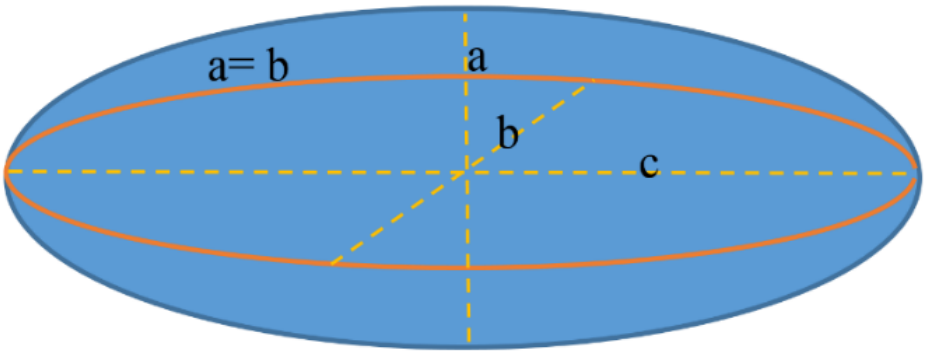

Figure 4-7: Schematic figure of an ellipsoid in which (a=b).

Table 4-5: NP-4 and their dissolution values in g/m^2/day with standard deviation.

NP-4 a (nm)	**C (nm)**	**Dissolution (R) g/m^2/day**	**Standard Deviation**
17.5	28.5	98.1	30.9
15.9	26.9	31.1	25.3
14.5	28.4	26.1	4.2
15.3	27.4	94.1	20.7
13.7	25.5	59.4	9.1
12.9	24.3	29.9	15.2
12.6	22.7	72.9	12.3
11.8	20.8	18.8	22.0
11.6	19.7	121.2	81.5

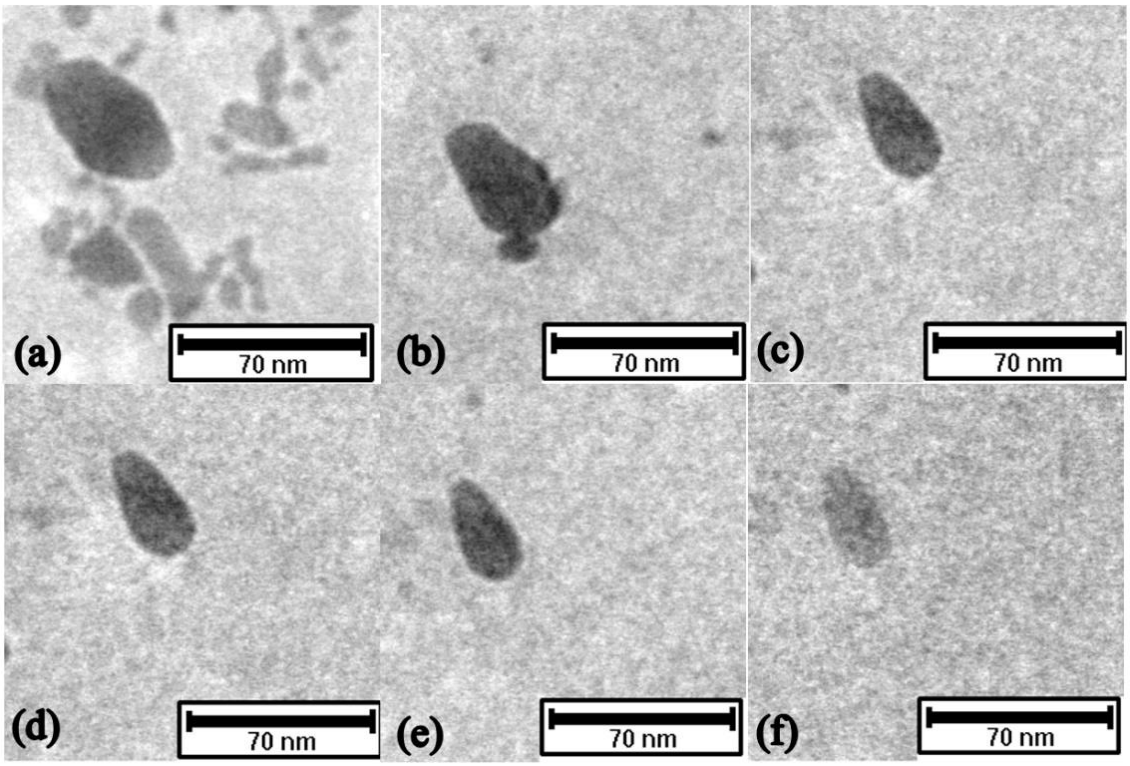

Figure 4-8: Figures (a) to (f) shows the effect of dissolution of an ellipsoid shape NP (scale bar of 70 nm) where (a) to (h) are snapshots 16.6 s apart.

4.2.1.1.5 Dissolution Calculations of Nanoparticle 5 (NP-5)

NP-5 is also an octahedral shape nanoparticle shown in Figure 4-9. As shown in the figure the dissolution started from the corner or edges, and then the particle turned into a round or spherical in shaped nanoparticle under continuous irradiation. The spherical approximation was used for the calculation of the surface area and volume during dissolution of the ceria NP by using the same envelope method that was used with NP-3. Table 4-6 shows the diameter of NP-5 and their calculated dissolution rate in $g/m^2/day$ with standard deviation.

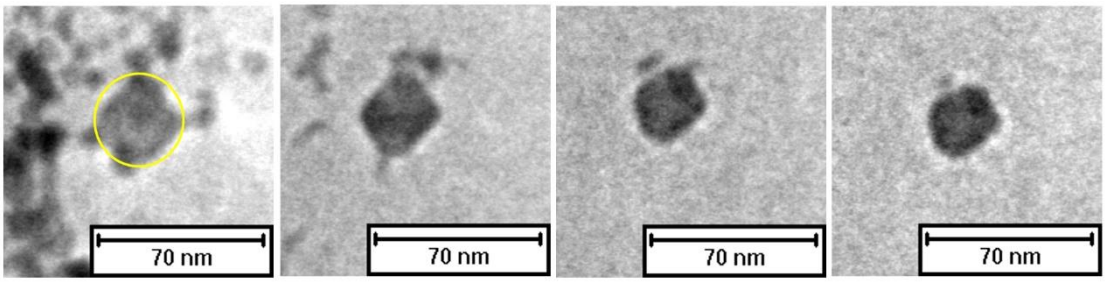

Figure 4-9: The dissolution of an octahedral shape NP and the yellow motif indicates the NP-5 for dissolution calculation.

Table 4-6: The diameter of NP-5 and their dissolution values in g/m^2/day along with standard deviation.

NP-5 Diameter nm	Dissolution (R) g/m^2/day	Standard Deviation
42.9	130.8	17.2
41.6	52.8	15.2
37.8	114.9	16.6
34.1	81.7	14.5
33.0	25.8	7.2
32.9	7.4	2.9

4.2.1.1.6 Dissolution Calculations of Nanoparticle 6 (NP-6)

NP-6 is a round shaped nanoparticle as shown in Figure 4-12. This Figure 4-12 also shows the dissolution behaviour of ceria nanorods for which the observations were made of the dissolution of one nanoparticle. In order to quantify the dissolution of ceria NP-6 a spherical approximation was assumed as described in the dissolution calculations of NP-1. Table 4.7 gives the diameter of NP-6 and the calculated dissolution rates in g/m^2/day along with the calculated standard deviation.

Table 4-7: The diameter of NP-6, and their dissolution values in g/m^2/day along with the standard deviation.

NP-6 Diameter nm	Dissolution (R) g/m^2/day	Standard Deviation
16.6	8.9	1.5
13.8	48.2	8.6
13.0	23.0	2.8
12.0	29.2	8.7

Comparisons have been made of the dissolution rate of ceria NPs in water in this study, with the previously published work related to ex-situ chemically dissolved measurements of ceria and these are summarised in Table 4.8. In this Table 4.8 the dissolution rate of nano and macro sized ceria particles are given in the presence of other NPs, chemicals and ultrasonic excitation. The results electron irradiation indicates that the dissolution rates in this study are found to vary from ~ 10 – 730 g/m^2/day, and this is at least 5 orders of magnitude greater than those reported earlier. Table 4.8 also compares the dissolution rate of different shapes of ceria NPs and it is interesting to note that the particle shape appears to have a minor influence during radiolytic dissolution in water.

Table 4-8: Comparison of ceria NPs dissolution rates from the literature with samples from this work (NP-1 to NP-5).

Ref	Temp (°C)	Dissolution R(CeO_2) (g/m^2/day)	Comments
[129]	40	1.8 x10^{-8}	Ceria NPs, 0.25 M HNO_3 & Pt NPs (2.5 wt%)
[130]	40	2.7 x10^{-9}	Ceria NPs, 0.125 M H_2SO_4 with ultrasound (20kHz) & Pt NPs
[131]	60	2.9 x10^{-5}	Macro-ceria, 2 M HNO_3
[50]	90	4.85 x10^{-4}	Macro-ceria, 0.01 M HNO_3
NP-1	RT	43 - 235	Min – Max rate (Round shape)
NP-2	RT	283 - 730	Min – Max rate (Round shape)
NP-3	RT	28 - 157	Min – max (Octahedral shape)
NP-4	RT	18 - 122	Min – max (Oval shape)
NP-5	RT	7 - 130	Min – max (Octahedral shape)

The combined graph of NP-1 and NP-2 is shown in Figure 4-9. This plot shows the dissolution behaviour of the combined tracking of two nano particles (i.e. NP-1 and NP-2) with error bars based on 5 repeat measurements for each time-step. A graph has also been plotted as shown in Figure 4-9 of nanoparticles size (nm) versus dissolution rate (g/m^2/d), and it was found that the dissolution was a function of both radius and time. The data was fitted with an exponential function for the decrease of radius versus time. The trend of the graph shows that the dissolution

rate of the nanoparticles increases for decreasing diameter and the rate of reduction in radius was found to be linear with time.

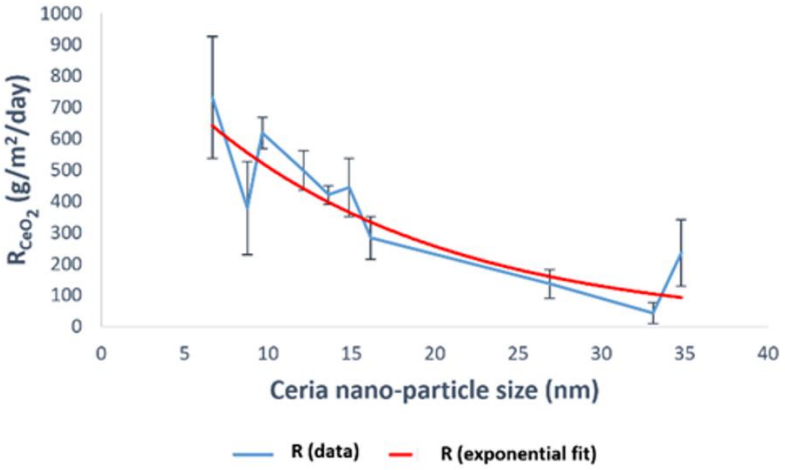

Figure 4-10: Combined graph of NP-1 and NP-2 showing the dissolution behaviour.

A spherical geometry was used for the for the calculation of the dissolution of CNP. To confirm whether or not the NP was spheroidal the TEM image was post processed with image-J photo processing software. The plotted profile shown in Figure 4.11 indicates that sharp edges of sphere and half sine curved which confirm that our NP is solid sphere. The calculated rate of dissolution of spherical ceria NPs given by R_{CeO2} was found to be in the range 10 – 730 g/m^2/day, and the calculated dissolution rate of the ellipsoid shape CNP was 18 - 122 g/m^2/day.

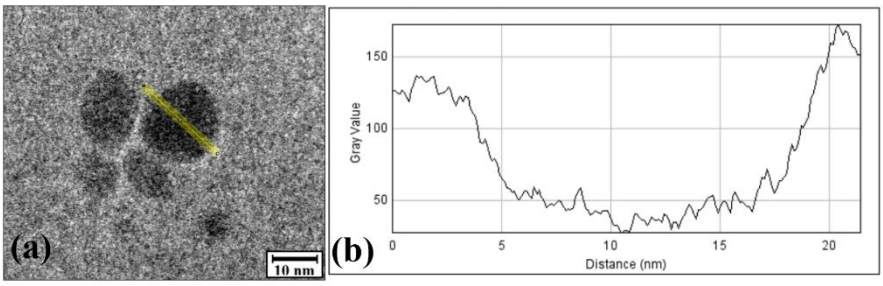

Figure 4-11: (a) shows the crystalline spherical solid NPs during e- irradiation experiment and their plot profile is shown in (b).

4.2.2 Dissolution of Ceria Nanorods (CNRs)

Two types of regular (homogenous) and irregular shaped ceria nanorods (NRs) immersed in deionised water were used in a liquid cell and irradiated at 200kV in 2010-F TEM. The purpose of two types of ceria NS is to compare the behaviour of surface smoothness on the dissolution. The regular or homogenous NRs were 150-200 nm in length and having 5-30 nm in diameter similarly irregular shape NRs have same 150-200 nm in length and having diameter 5-25 nm, but outer surface have irregularities on it. In order to obtain accurate data for quantification, the diameters of NRs at the same positions were measured 5 times. The standard deviation in the table also correspond to the range of 5 multiple measurements, respectively. In common with the earlier dissolution of ceria nanoparticles in liquid cell experiments a similar dissolution behaviour of the CNRs was found above a threshold intensity of the electron beam of TEM. When irradiated with a current density of ≈70 nA/μm^2, the ceria NRs, exhibited a dissolution which was very much similar to that seen in the dissolution of ceria nanoparticles during electron irradiation as shown in Figure 4-12 and Figure 4-13. The average minimum and maximum calculated dissolution rate of the NRs was between 25.5 g/m^2day to 99 g/m^2day. The following observations were made during the dissolution of the CNRs:

1. The corrosion of CNRs started from the surface and resulted in a continuously random thinning of the rod diameter.
2. The dissolution of homogenous rods also started from the surface, and the thinning was very slow compared with the irregular shape ceria nanorods as shown in Figure 4-13.

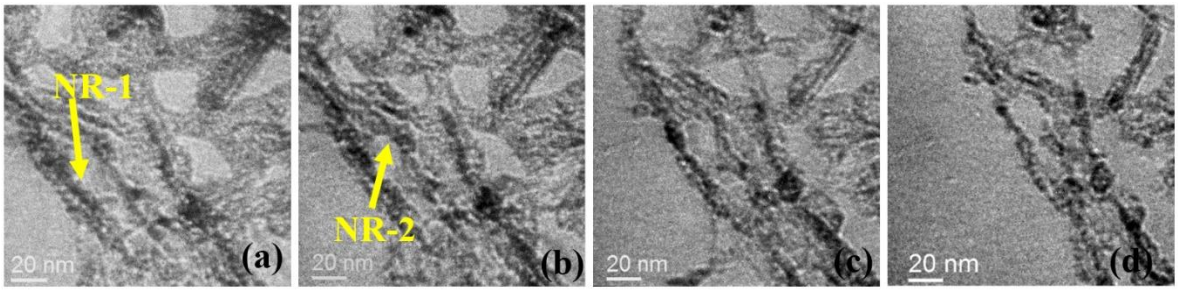

Figure 4-12: (a) to (d) shows the random surface dissolution of ceria NRs.

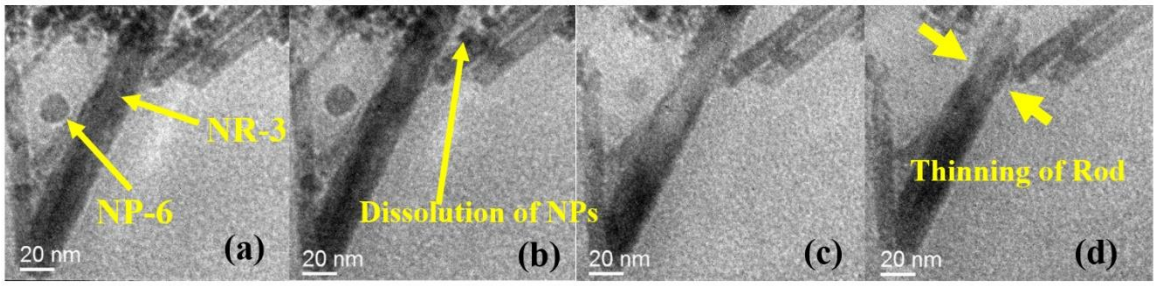

Figure 4-13: (a) to (d) shows the dissolution of ceria NPs and thinning of the NRs.

4.2.2.1 Quantification of the dissolution of Ceria NRs

To quantitatively analyse the dissolution processes of the NRs, the diameters of the NR at nanoscale three locations (highlighted with the yellow arrow) were selected for measurement of diameter of homogeneous and irregular NRs as seen in the Figure 4-12 and Figure 4-13. The dissolution rate (R) was quantified as a function of the homogenous and the irregular surfaces of the nanorods as shown in Figure 4-12 and Figure 4-13, and in Table 4-9 to 4-10 respectively. As before the calculated dissolution rate (R) in units of $g/m^2/day$ was compared with results from the earlier ex-situ literature on ceria nanostructures. It was assumed here the rods were cylindrical and the unit area and volume were determined for calculation purposes. The dissolution rates R were obtained from time differences in the volume normalised to the initial surface area at the start of the interval of NRs. In equations 4.6 and 4.7 below m_D indicates the dissolved mass, ρ density of ceria, V_{SNR} the volume of NRs and A_{SNR} the surface area of the nanorod respectively, at the time interval t_n.

$$m_D = \rho\,(V_{SNR}(t_n) - V_{SNR}(t_{n-1})) \qquad (4.6)$$

$$R\,(t_n) = m_D / A_{SNR}(t_{n-1}) / (t_n - t_{n-1}) \qquad (4.7)$$

4.2.2.1.1 Dissolution Calculations of NRs (1 and 2)

For the quantification of the dissolution of the irregular surfaces of NRs 1 and 2 (as shown in Figure 4-12 with a yellow arrow) in water, a few images of ceria nanorods (NRs) were selected from the still image sequence in the liquid cell dissolution experiments. Figure 4-12 (a) indicates the time t=0 where the measurement was started for the diameters of NR-1 and NR-2 for the dissolution calculation. The ceria NRs are solid, so the surface area and volume of the NRs are based on a solid cylindrical geometry (i.e. [2 π r (h + r)] for the surface area and (π r^2h) for the volume). Table 4-9 and 4-10 shows the diameter of nanorod 1 and 2, and their calculated dissolution rate in g/m^2/day along with the calculated standard deviation.

Table 4-9: The diameter of NR-1 and their dissolution values in g/m^2/day with standard deviation.

NR-1 Diameter nm	**Dissolution (R) g/m^2/day**	**Standard Deviation**
13.2	25.5	1.5
10.6	71.7	1.5
7.8	74.7	0.8
3.4	99.0	0.2

Table 4-10: The diameter of NR-2 and their dissolution values in g/m^2/day with standard deviation.

NR-2 Diameter nm	**Dissolution (R) g/m^2/day**	**Standard Deviation**
14.5	30.9	1.7
12.2	65.0	3.3
9.4	77.4	2.8
6.1	83.4	2.4

4.2.2.1.2 Dissolution Calculation of Nanorod 3 (NR-3)

For the quantification of smooth and homogenous nanorods images of ceria nanorods (NRs) from the still image sequence taken during the irradiation experiment with the TEM 2010-F were used and the results shown in Figure 4-13. Figure 4-13 clearly shows the slow dissolution of the NRs during irradiation. Figure 4-13 (a) indicates the t=0 where the measurement of diameters of for the NR-3 for dissolution calculation started. Again a solid cylindrical approximation was used for the calculation of surface area and volume of NRs. Table 4-11 shows the diameter of nanorod 3 and their calculated dissolution rate in $g/m^2/day$ along with the calculated standard deviation.

Table 4-11: The diameter of NR-3 and their dissolution values in $g/m^2/day$ along with the calculated standard deviation.

NR-3 Diameter nm	**Dissolution (R) $g/m^2/day$**	**Standard Deviation**
11.5	9.8	1.4
11.1	13.0	1.7
10.9	6.4	1.0
10.6	8.4	1.9

4.2.3 Comparison of NPs and NRs:

Two types of regular (homogenous) and irregular shaped ceria nanorods (NRs) immersed in deionised water were used in a liquid cell and irradiated at 200kV in 2010-F TEM. The purpose of two types of ceria NS is to compare the behaviour of surface smoothness on the dissolution. The regular or homogenous NRs were 150-200 nm in length and having 5-30 nm in diameter similarly irregular shape NRs have same 150-200 nm in length and having diameter 5-25 nm, but outer surface have irregularities on it. TEM images (Figure 4-12 and 4-13) reveal the fast reduction of the irregular ceria nano rods grain size and the formation of more irregular

corrosion pits on the surface of the rough NRs during the dissolution experiment in TEM as compared to homogenous NRs.

The combine graph of the dissolution rates of ceria different sized NPs and NRs were measured at different dissolving time and the results are shown in Figure 4-14. It shows that the dissolution rates of different nanostructures i.e NPs of ceria were approximately same. More prominently, the diameter of the irregular shaped CNRs (*d*) reduces roughly with 7 times faster dissolution speed than that for homogenous NRs. It is also interesting to compare nanoparticles with nanorods, and here the dissolution data for the irregular nanorods are found to be within the range of our dissolution data for nanoparticles. On the other hand, homogenous CNR shows an order of magnitude slower dissolution than irregular nanorods or most nanoparticles. The results of in situ dissolution showed that the higher surface curvature of nanoparticles relative to ceria nanorods accelerates dissolution rate in the same way as coarsening of the ceria nanorods.

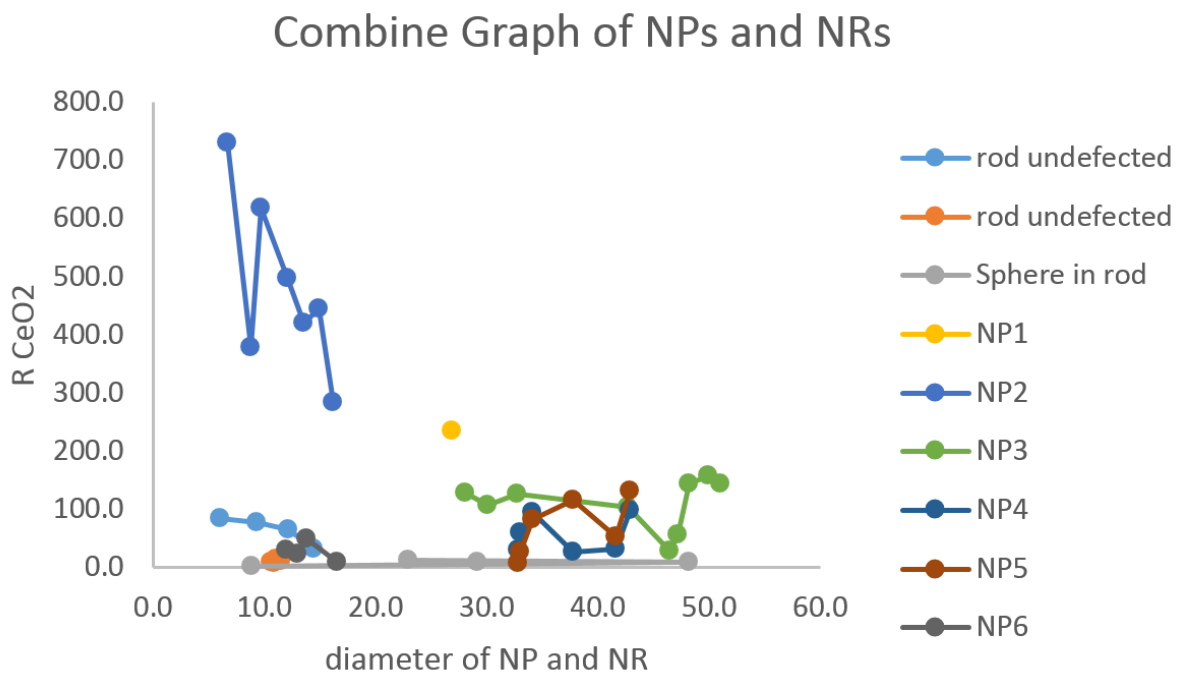

Figure 4-14: Figure shows the combine graph of nanoparticles and nanorods.

4.2.4 Discussion in the dissolution of Ceria NS

A basic observation from low magnification images of irradiation of ceria nanostructures in water under electron beam irradiation shown in Figure 4-1 indicates that irrespective of the initial size and shape of the particle, it will shrink and disappear. For example, the results of predominantly octahedral shape nanoparticles under irradiation with a TEM electron beam shows a rapid dissolution starting from the corners or edges simply because these are the weakest and outer surface and therefore most favourable areas to initiate the shrinking. This shrinking leads to a significant rounding of the irregular or faceted octahedral NPs. The observed speed of dissolution for small nanoparticles is predictably faster than that with larger particles. The continuous monitoring of the overall shrinkage of the NPs diameter indicates a complete disappearance within a few seconds of irradiation. The quantification rate of CNRs was approximately the same as ceria nano particles and the dissolution rates of homogenous

and irregular shape NRs from different positions were different. More importantly, the diameter of the NRs reduces randomly but the speed of dissolution is fast on the surface of irregular shape NRs as compare to homogenous NRs. It was observed that the thinner side started dissolving first, and the surface roughness increased for increasing irradiation time for both types of NRs. Many dissolution sequences of NPs and NRs were observed and almost all types of nanostructures disappeared during irradiation, with calculated dissolution rates in the range 10-730 g/m^2/day. These calculated dissolution rates are five orders of magnitude higher than the laboratory dissolution experiment. Moreover, the NP shape is not critical and has little influence during the dissolution or shrinkage. A more detailed analysis of the quantification of dissolution of individual nanoparticles having precise shapes showed that the shape only had a small effect. The quantification of individual nanoparticles and nanorods can be clearly seen in Figures 4-3 to 4-13 and the octahedral ceria nanoparticles are seen to be undergoing corner-ablation and rounding before dissolution can be seen in Figure 4-4 and Figure 4-6. The quantification results of the ellipsoid shape nanoparticles (Figure 4-8) indicates a dissolution speed that was slightly slower being in-between that of the sphere, octahedra and round shape NPs as shown in Figure 4-5. Referring to the graph of Figure 4-10, the size of the elliptical shape NP can be found out-side of our graph (Figure 4-10). The slow dissolution of the elliptical shaped nanoparticle is due to the relatively large size as compare to the other nanoparticles (i.e. NP-1 to NP-3).

According to Virot et. el. the dissolution rate of ceria can be accelerated or increased by decreasing the size of ceria particles hence it larger specific surface area. In our NPs we have expected the fast dissolution of ceria NPs, but is should be within two order of magnitude as compare to the micro size particles. The results of ceria dissolution experiment of nanoparticle size have been confirmed, as shown in figure 4-10, to be within one order of magnitude (compared to micron size particles i.e. 6-9 micro meter in size), compatible with[129], but

cannot be proceed upto the five orders of magnitude during dissolution. The calculated and literature-based dissolution rate measurements summarized in Table 4-8 comprise a range of ceria NP sizes, from nanoparticles of few tens of nm [129] to high-temperature sintered solid bulk materials[50, 131]. The observed differences related to dissolution are approximately within 2 orders of magnitude of each other, and cannot explain the giant rates of dissolution i.e. 5 order of magnitude higher for nanoparticles.

By comparing the ceria dissolution rates for the two types of irregular and homogenous nanorods, we notice that the average rate of dissolution data of the two rough nanorods NR1 and NR2 is about seven times quicker than the data for the homogenous NR see Figure 4-12. This is due to the roughness of surface which provides an extra enhancement of active surface.

When we compare nanorods with nanoparticles, and the dissolution data for the rough nanorods were found to be within the range of our various findings for nanoparticles. But, the homogenous NR in Figure 4-13 shows one order of magnitude slower shrinkage than most nanoparticles and irregular NRs. We assumed that the higher surface curvature causes the increases of dissolution rate. In our case nano particles relative to nano rods accelerates dissolution rate in the same way as roughening of the rods. We observed that the dissolution rates for nanorods, ellipsoid shape nanoparticles and round nanoparticles were of similar order of magnitude.

Dissolution of ceria NPs and NRs in water were determined by the energy of the TEM, irradiation intensity of the electron beam and the irradiation physics of water under an electron beam. Measurements were performed using both 300 and 200 kV irradiation energy on NPs and NRs using a TEM 3010 and 2010-F electron microscope. The dissolution of ceria NPs occur when we irradiate at 300kV with less current as compare to the irradiate at 200kV. In

this case high energy irradiation possibly causes the formation of more water splitting species such as (e^-_{aq}, $H^\bullet$, $OH^\bullet$, $HO_2^\bullet$, OH^-, H_3O^+, H_2 and H_2O_2).

Similarly, the dissolution of ceria NRs occurs with irradiation at 200kV with a high beam current. In this case the higher beam current causes the formation of more water splitting species. The effect of an e- beam on a sample of water was discussed in [98, 100] and for solutions with dissolved precursor chemicals in [132, 133]. The radiolysis of water causes splitting of the water molecules and the generation of ionic species which are both alkaline and acidic as represented in equation 2.3. The implication of this is that water splitting radicals in the radiolytic water may accelerate the dissolution rate of ceria nanostructures during in-situ liquid cell TEM irradiation experiment. Observation had previously been made of a localised drop in pH during irradiation of the sample in water due to the formation of a water splitting product in which the generation of H_3O^+ dominates [98]. Similarly, in the irradiation experiments of ceria in deionised water described here the dissolution is acidic in nature due to H_3O^+ generation which causes a localised drop in pH down to around 3 near the electron beam i.e. beam impact zone which can be seen in the Figure 4-2. Furthermore, dissolution may be due to the generation of additional electrons (i.e. low-energy secondary electrons present in any solid/liquid, and more specifically bond hydrated electrons in water) and many water splitting radicals as represented in equation 2.3 as well as gases (H_2, O_2) [100] present throughout the interaction volume or surrounding area of the beam as in the Figure 4-2.

The quantified dissolution data in water obtained here have proven that the dissolution rate of ceria nanostructures are five orders of magnitude higher than any earlier rates reported at room temperatures for any shape morphology. Previously reported work demonstrated a dissolution rate 1 to 2 orders of magnitude greater than the ex-situ dissolution rate of ceria due to a number of factors including change in molarity or acidity, temperature, particle size, particle microstructure and reactive water splitting species [98, 129, 131].

We have observed massive dissolution rates of ceria in de-ionised water under TEM electron beam, exceeding any prior reports for laboratory chemical dissolution rates at room temperature by several orders of magnitude. Accelerated dissolution during liquid cell experiment of ceria in TEM were based on the radiolysis of water preceding ceria-attack. Electron-water interaction generates radicals, ions and hydrated electrons, which assist in hydration and reductive dissolution of oxide minerals.

We have started irradiation of ceria immersed in de-ionised water, irradiation causes water splitting and generates ionic species of both alkaline and acidic character. According to the previous research in pure deionised water (as we have used), ultimately H_3O^+ generation dominates, causing a localised drop in pH down to about 3 [16]. The H_3O^+ generation during electron irradiation [98] would move the system rapidly into low pH and therefore a high ionic solution range. Simultaneously, the incident electron beam generates further electrons (low-energy secondary electrons in any solid/liquid and more specifically bound hydrated electrons in water) plus further H_2O-derived radical species and gases (H_2, O_2) [100] throughout the interaction volume. Therefore, we assume that acidic dissolution is the main working mechanism during irradiation of ceria in deionised water under TEM electron beam.

The reasons for giant dissolution rates, which appear to be 5 orders of magnitude higher than any previously reported room temperature rates for ceria in water of any morphology, has to consider 6 key effects: (i) molarity/acidity, (ii) temperature, (iii) particle size, (iv) particle microstructure, and (v) reactive water splitting products.

(i) dissolution of ceria with respect to acidic molarity is unlikely: when extrapolating literature data for 1M and 2M HNO_3 dissolution of ceria [129], as well as from 0.5M - 6M [131], specifies that rate changes are kept to a factor 10 within 12 times higher molarity. Even if there

is no linear relationship hold, 5 orders of magnitude higher R-rates cannot be achieved via such a pure H_3O^+ increase alone.

(ii) As reported earlier water temperature influence with a factor of 2 in ceria dissolution rate for 30º C temperature [131]. In our case we used deionised water so there is no chance of rise in temperature due to electron beam irradiation, therefore we can safely discard this option.

(iii) The results of ceria dissolution experiment of nanoparticle size have been confirmed through figure 4-10 to play a role within one order of magnitude, compatible with [10], but cannot proceed the five orders of magnitude during dissolution.

(iv) Materials morphology and defects can be change the dissolution rate by one order of magnitude. Indeed, in our in-situ experiments confirm primary dissolution of octahedral edges with high surface energy, before dissolution of the spherical remaining core of particles proceeds. As the surface energy is inversely proportional to radius of curvature, accelerated dissolution as of Figure 4-10 is expected.

(v) In the case of previous literature experiments and in our dry irradiation experiments in chapter 5 specially section 5.2 there was less or no water splitting products were available during irradiation. Here in the case of liquid cell experiments irradiation is via a high density of electrons with moderate electron energy (200 kV and 300 kV) of TEM. On the other hand in the case of radioactive decay of UO_2/ThO_2 dissolution studies would depends on lower irradiation dose, but with high particle energies. The additional water splitting reactive species in radiolytic water, which would be absent in standard acidic solutions, include, amongst others [98, 100], hydrogen (the main reducing agent), oxygen, H_2O_2,,hydrated electrons, as well as radicals of hydrogen, water, and hydroxide.

4.3 Formation of New Phases

Some new phase formation during irradiation of ceria NPs in water in liquid cell is reported in this study, and the next section discusses the results of this investigation.

4.3.1 The Formation of Dark Phase NPs

As part of the experimental investigations described here observations were made on the formation of a new dark circular shape nanoparticles apparently larger in size as compare to raw ceria NPs a typical result of which is shown in Figure 4-14. These phases are formed from the irradiation of possibly earlier patches of dissolved ceria nanoparticles samples during the irradiation experiments. All these features have a dark atomic contrast compared with amorphous phase and are either equal or the larger in size (i.e. size > 50 nm) as the raw nanoparticles. This phase consists of approximately round particles, that are monodispersed and having some distance between each other compared with the raw ceria nanoparticles as shown in Figure 4-1. The formation of this round shape particles was observed at the end of the irradiation experiment. We have observed only one time the formation of these dark phase nanoparticles and currently there is no evidence to support a mechanism for their formation because these irradiation patches were left for a long time in the TEM without any irradiation. It may that these patches are a product of dissolved ceria. It was observed that this phase dissolved quickly under irradiation of electron beam within 20 seconds as shown in Figure 4-14 (c).

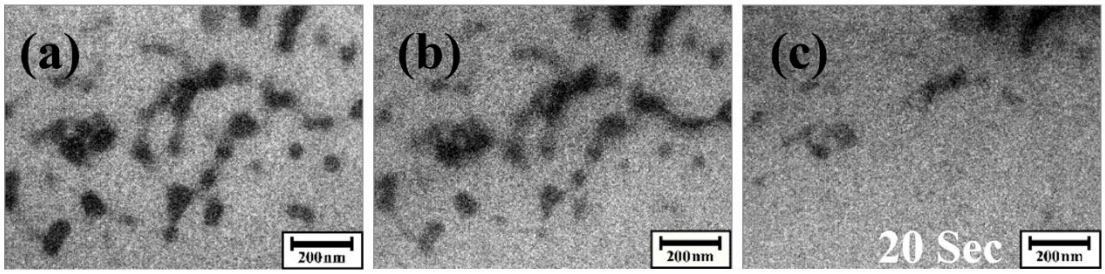

Figure 4-14: Roundish new particles / phase formation having dark contrast and their dissolution under irradiation (scale bar of 200 nm).

4.3.2 The Formation of 1D Free-Standing Needles

The irradiation experiments of ceria NPs in water described here also indicated the formation of 1D free standing needle shaped particles as shown in Figure 4-15. Observations were made of the transformation of ceria NPs into needles in water during irradiation in the TEM. Continuous irradiation of ceria NPs up to 5.4 seconds causes a shrinkage of the surrounding area of NPs as seen in Figure 4-15 (b), and then further irradiation up to 19.5 seconds leads to the formation of needles as shown in Figure 4-15 (c). On further irradiation, after 26.9 seconds it was observed that the needles had a dark atomic contrast similar to raw ceria and also crystalline appearance as shown in Figure 4-15 (d). During this transformation to the needle structures a change of position of the ceria NPs was observed as shown in Figure 4-15 (b) and (c).

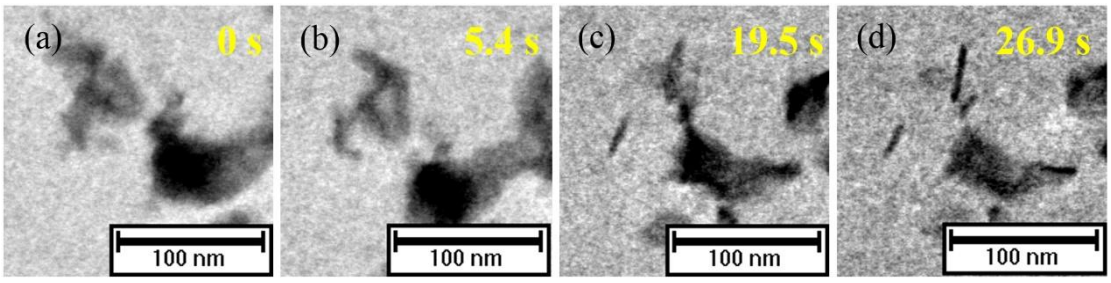

Figure 4-15: The dissolution and formation of newly formed needle-shaped particles from octahedral shaped ceria NPs.

Another similar example of the formation of 1D nano needle from the ceria NPs is seen in Figure 4-16. These needles formed directly during the dissolution processes of ceria NPs that were originally octahedral shape and the mass-thickness atomic contrast of these newly formed needles is similar to raw ceria NPs. The indication of high mass contrast, Bragg scattering, and their flat facets indicated their crystalline nature.

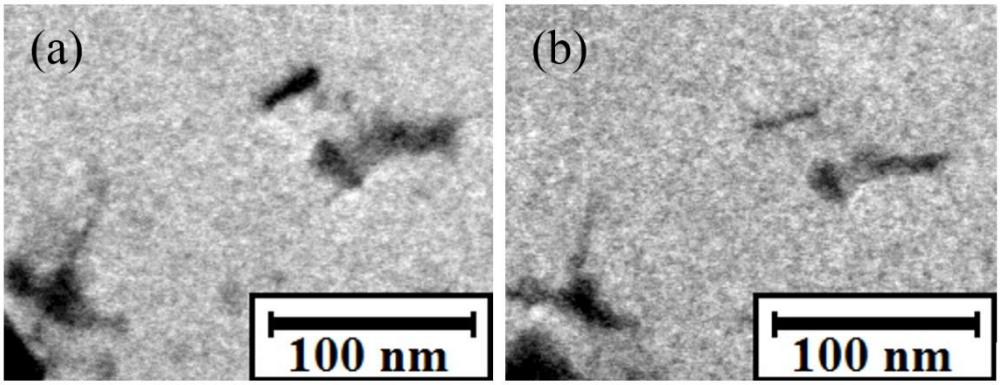

Figure 4-16: Live dissolution and transformation of needles from nanoparticles.

In other related investigations with liquid cell irradiation of ceria NPs needle shape rods were observed to form from an oriented chain of NPs. It was observed on occasion that a chain of oriented attached (OA) NPs in our liquid cell as shown in Figure 4-17. Currently there is no explanation for the assembly of this oriented attachment, and it may be the case that this is form during the hydrothermal synthesis process of ceria nanoparticles. The blue schematic octahedra NPs shows the possible attachment morphology of NPs as shown in the Figure 4-17 (a). During irradiation of the oriented attached chain observations were made of the step by step process formation of needle shape rod through the dissolution of the NPs chain as shown in Figure 4-17 (a) to (d). The continuous irradiation causes the parallel thinning of the CNPs surfaces as shown in Figure 4-17 (b-c) and formation of rods Figure 4-17 (d). The whole process of making needle shape rod via NPs took approximately 29 seconds.

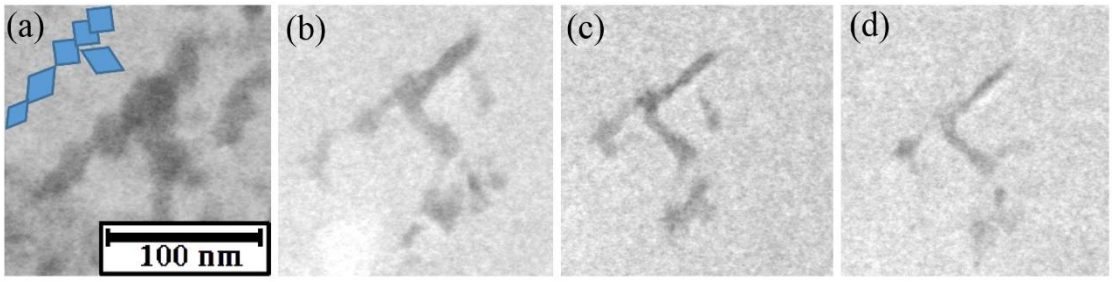

Figure 4-17: Figure shows the formation of needle shape rod from oriented nanoparticles chain (a), oriented attachment of NPs and (c - e) step by step thinning of NPs surfaces and rod formation. (Blue schematic sketches shows the suggested idealised fundamental particle morphologies and crystallographic orientations).

4.3.3 The Formation of Multiple Needles and Spikes Attached to the NP

Further experiments on the irradiation of ceria NPs in water led to the observation of the growth of needles in a well define manner from the octahedra of crystalline raw ceria NPs as shown in Figure 4-18. The growth of these multiple needles starts with relatively broad pyramids shown in Figure 4-18 (a), and after continuous irradiation these become sharper and spikier with an increasing aspect ratio. Such multiple needles appeared during the experiments and they were seen to be formed on a chain of attached nanoparticles. The step by step "life cycle" of the nano needle growth and parallel dissolution of raw ceria NPs is shown in Figure 4-18 (b). The prolonged irradiation causes the growth of many needles as shown in Figure 4-18 (f). The observed dissolution rate of needles is relatively slower than the original ceria NPs and so they dominate the growth during irradiation.

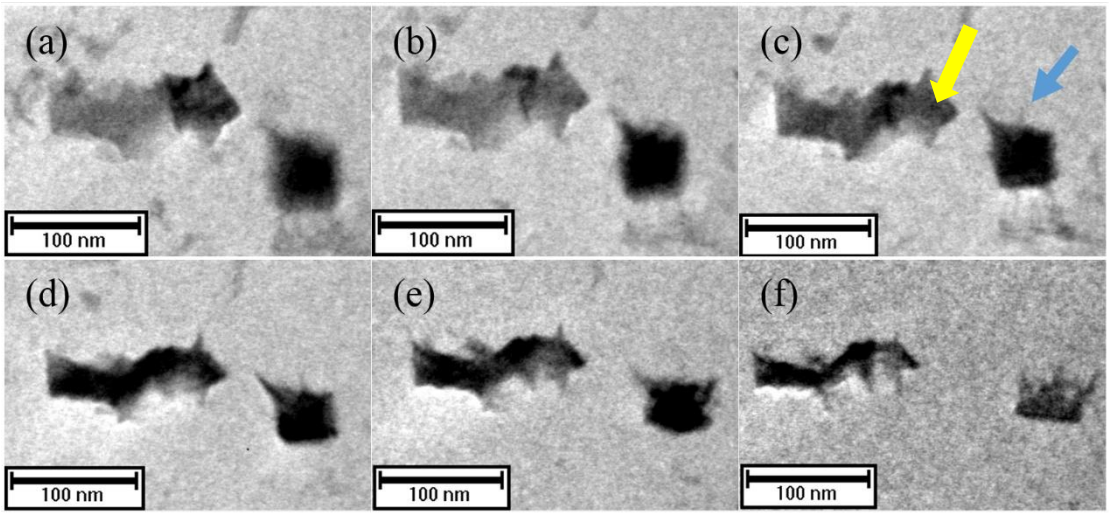

Figure 4-18: Parallel live dissolution and complete step by step "life-cycle" of the growth of nano needles on the facets of ceria octahedra.

Similar nano needle formation and growth was observed on the facets of octahedral of crystalline ceria NPs as shown in Figure 4-19. In this figure (a) shows two attached octahedral ceria NPs which begin shrink due to irradiation, and (c) shows the occurrence of needles at the corners of the octahedra with (d) indicating the clear formation of the needles.

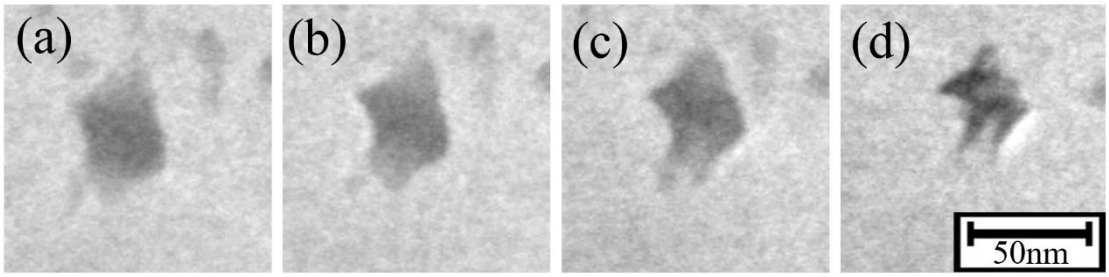

Figure 4-19: Formation and growth of needles on the facets of ceria octahedra.

Another observation in these investigations consisted of the appearance of a "star" shape made from the newly formed nano needles on the facets of the outside of ceria octahedra envelope. All corners of the ceria octahedra facets are the main sites for the development of needles as shown in Figure 4-20 (a) and (b).

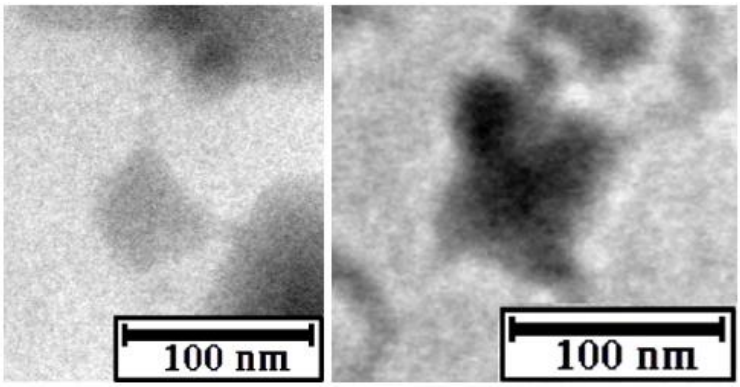

Figure 4-20: The occurrence of needles on the facets of ceria octahedra.

Another example of needle formation during the liquid cell irradiation experiments is illustrated in Figure 4-21. In this figure one small particle joins two large particles from their needles at the corners of the octahedra. Figure 4-21 (c and d) shows that continuous irradiation leads to the fast dissolution of small nanoparticles and the slow dissolution of large particles with parallel thinning of the needles.

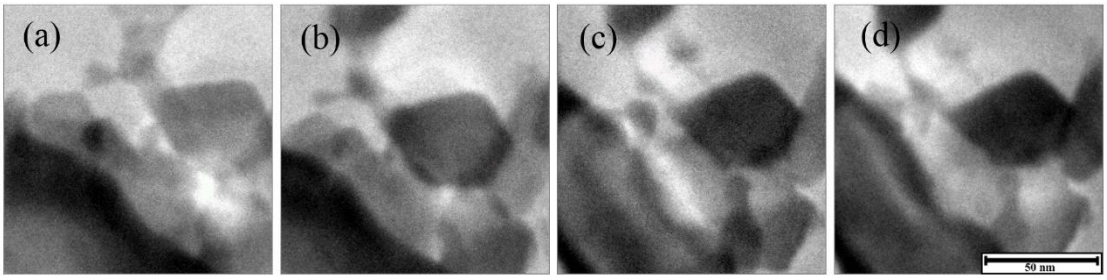

Figure 4-21: (a- d) The growth of needles outside nanoparticle octahedra.

When a new region was irradiated during the experiments it was observed that two nanoparticles can become attached to each other from the corner of the octahedra by needles of one small nanoparticles as shown in Figure 4-22. The high magnification TEM images show that the needles are outside the octahedra of the nanoparticles and continuous irradiation leads to the detachment of nanoparticles due to dissolution in less than 1.5 seconds as shown in Figure 4-22 (b). The needles were found to be sensitive to the electron beam and typically a needle can dissapear within 2 seconds as shown in Figure 4-22 (c). One important observation

is that the dissolution of that needle is very fast compared with to the relatively larger nano particles.

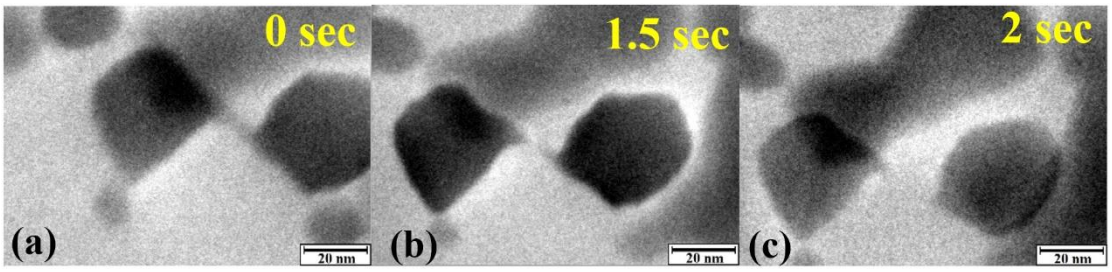

Figure 4-22: The live sequence of needle rupture between two ceria octahedra.

Figure 4-23 shows the formation of star-shaped multi-spike structures growing out of the original raw ceria NPs . These structures were formed very quickly, and last for short period of time during irradiation. All such nanoparticles form spikes an example of which can be seen in Figure 4-23 (b) and (c). The process of transformation and dissolution is very quick and the whole nanoparticle is consumed within 3.9 seconds during the formation of single sharp spikes as shown in Figure 4-23 (d). Further irradiation caases the complete dissolution of all the newly formed star-shaped multi-spike needles.

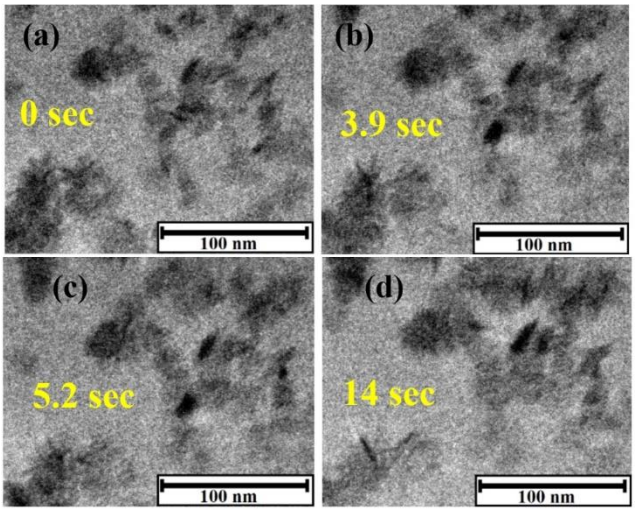

Figure 4-23: Growth of multiple needles per host particle into star shaped objects followed by a narrowing of the needles and dissolution.

4.3.4 Discussion on the New Phase Formation

The new phase formations during irradiation of ceria NPs are listed below followed by proposed mechanism schematically as shown in Figure 4-24 and discussion on each of these observations:

Case a “New phase formation”.

Case a’ “Dissolution of octahedral nanoparticles”

Case b “Formation of 1D needles within the envelope of the original nanoparticle”.

Case c “Formation of multiple spiked needles on chain of multiple nanoparticles”.

Case d “Formation of needles outside the octahedral nanoparticles”.

Case e “Formation of needles from a chain of octahedral nanoparticles”.

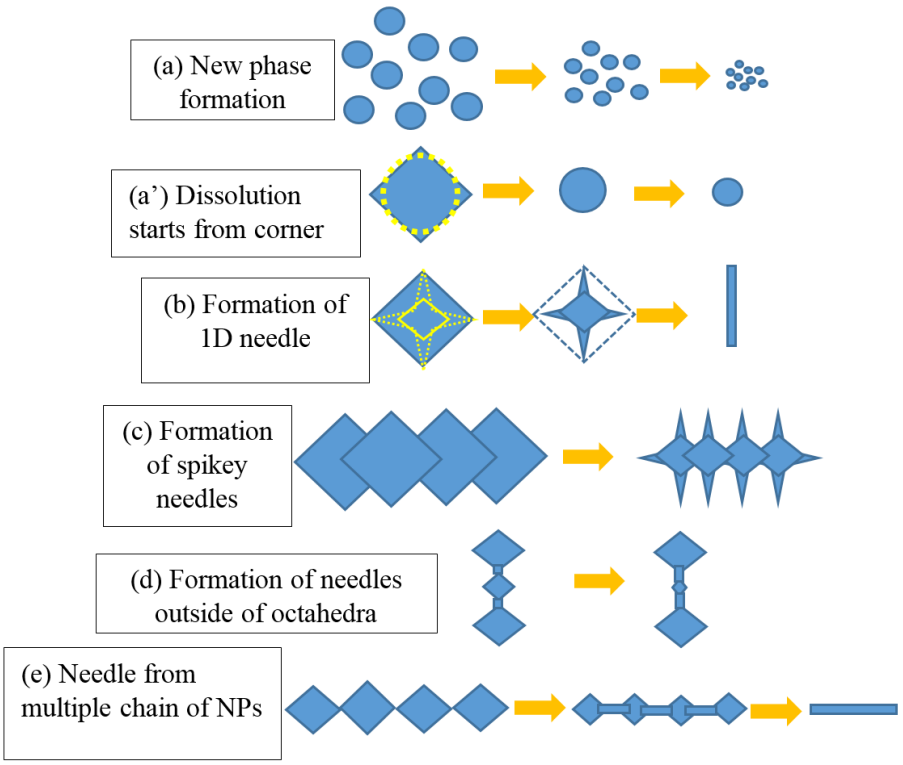

Figure 4-24: Schematic proposed mechanisms for, a) The formation of new round dark phase particles, a’) The dissolution behaviour of the octahedra NP, b) The dissolution of (1 1 1) ðfaces instead of the corner, c) The formation of multiple spikey needles, d) The formation of a needle outside of the NP octahedra and e) The formation of a needle from a chain of oriented NPs.

Case a: It was observed that the new phase has a dark contrast similar to the raw ceria NPs. The new phase showed Bragg diffraction features (dark black particles and their white shadow which can be seen in the figure) during the experiment which implied they had a crystalline structure. The newly formed particles in this phase are roundish in shape and monodispersed as shown in Figure 4-14 and schematically in Figure 4-24 (case a). These newly observed particles dissolved under continuous prolonged irradiation in the same way as raw ceria NPs. It is proposed that these phases are likely to be CeO_x owing to their dark contrast, or it could be a ceria or modified form of cerium oxide. These phases are not identified because 3010 TEM have not analytical attachments, but we assume they are linked to the CeO_2.

Case a': In this case the dissolution of crystalline octahedral ceria NPs started rapidly from the corners as shown in Figures 4-3 and 4-9 and also their proposed mechanism schematically in Figure 4-24 (a') and then it is transformed into a sphere or round shaped nanoparticle. In Figure 4-24 (a') the yellow dashed line indicates the dissolution at the corners first followed transformation into the round shape nanoparticles, and then disappeared due to the continuous irradiation.

Case b: This refers to needle formation at the corners of the octahedra within the envelope of the original raw nanoparticle. In this case it was observed that parallel dissolution of the ceria NP started in an opposite manner from the surface (i.e. possibly the (1 1 1) faces of the NP rather than from the octahedra corner or edges. This irradiation causes the shrinking of surfaces beside the corner, and made a needle like appearance as clearly shown in Figure 4-15 or schematically in Figure 4-24 (b). In Figure 4-24 (case b) the yellow dashed line indicates the dissolution of faces and the transformation of octahedral shapes into the needle shaped spikey particle. The simple analogy is that the removal of materials takes place from both sides of the octahedra corner which leads to the growth of the nano needle-like structure.

Case c: The formation of needles starts from pyramids on more than one particles with likely octahedral shape. Upon continuous irradiation needles become sharper and pointier with increasing aspect ratio. In this case if it is assumed the ceria NPs as {100} capped cubic-octahedral shapes, then needles grow parallel {100} with in the original particle envelope in the orientation of <100 >as shown in the Figure 4-18 (c) (see yellow arrow) and proposed schematic model in the Figure 4-24 (case c). If the growth is perpendicular to planes this can be possibly due to another underlying particle (see blue arrow Figure 4-18 (c)).

Case d: Occasional formation of needles on outside of cube envelope of ceria {100} octahedra facet as show in Figure 4-24 case d. Figure 4-21 (a) shows that both particles were attached to the octahedra at the {100} cube facets, and all the ceria NPs are aligned with common <001> axes. In this Figure 4-21 one small NPs is connecting two large ceria NPs and we observed the parallel dissolution of small NP due to irradiation.

Case e: We noticed the formation of one large needle from the oriented attached chain during irradiation as shown in Figure 4-17 (a) to (d). The continuous irradiation causes the thinning of the CNPs surfaces as shown in Figure 4-17 (b-c) and formation of approximately 80 nm long rods within 29 seconds as seen in Figure 4-17 (d). The mass-thickness contrast of needle is similar to raw ceria NPs. We assumed that the possible oriented attachment is <001> and the mechanism of attachment of NPs can be seen in the Figure 4-24 case d. We believed that the all NPs are bonded atomically on {100} planes in the direction of [001] and forming a singal crystal.

The dissolution of octahedral ceria NPs in water under e- beam irradiation has opened up many questions because during irradiation many types of known anomalous behaviour have been observed. We have no further explanation regarding this behaviour due to limited availability of research data regarding ceria in water but this is hypothesised as this behaviour was observed

due to the formation of different water splitting species or a change of pH of the water during the irradiation experiments. Previous research by Schneider et al. suggested the change of pH by the electron beam of the TEM causes many changes similar to etching in the growth of metallic nanoparticles in a liquid cell [98]. Alternatively, regarding the observed anomalies it has been assumed this may be due to time specific (irradiation dose) or the concentration and size difference of the NPs in the liquid cell. The interesting phenomena of "dissolution" was observed in every irradiation experiment and it was concluded that under continuous irradiation the complete disappearance of all type of ceria nano structures will take place and this includes octahedral or round nanoparticles, nanorods or newly formed spikey needles and free standing needles. For case (a') the octahedral shape NP transformed in to a round shape NP and then disappeared due to dissolution. In another experiment the same octahedral shaped NP transformed into a spikey needle or into free-standing needles first, and then disappeared due to dissolution. It is known from the literature review of ceria energy that $E_{111} < E_{100}$ [58]. The implications of this are that dissolution would start from the corner first, and make it round the octahedral NP. However, in these studies this wasn't always the case and occasionally the reverse was observed. Alternatively, it was assumed that the particle would shrink and the formation of a needle have been happened from solution or from the surrounding of the dissolved atom of cerium. The observed needle existed only for few seconds and then dissolved due to the continuous irradiation.

4.4 Movement, Chain Formation and Attachment

The results of e- irradiation of ceria NPs in water have exhibited many phenomena such as the movement of the NPs, high intensity neck/chain formation, and the attachment of nano particles before complete dissolution due to continuous electron (e-) irradiation. In this section these phenomena will be discussed in detail.

4.4.1 Nano Particle Mobility

The mobility of a group of crystalline raw ceria NPs in water at irradiation levels that are low or below the threshold intensity of electron beam are shown in Figure 4-25. Here it can be seen how a group of original raw nanoparticles randomly move and change location in water. We noticed the various events during the mobility of nanoparticles, such as touching, rotating and de-touching with each other. During the 2D movement we observed that the particles were not self-assembling or making a chain, but were bouncing and moving freely in the liquid, as can be seen in Figure 4-25 (c-d).

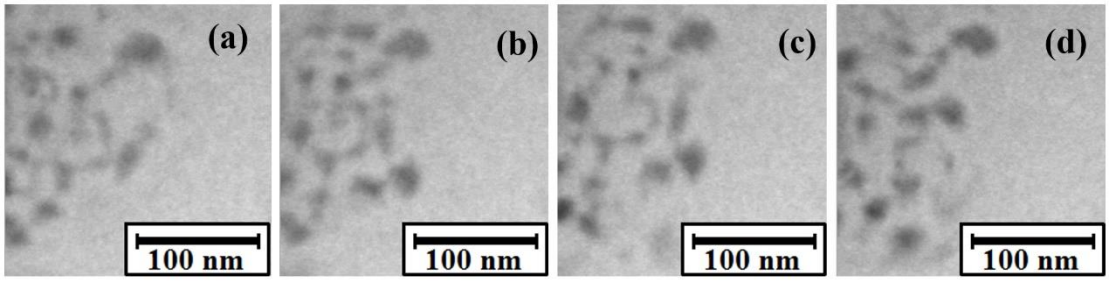

Figure 4-25: (a) and (b) show semi-free “2D” movement of particles suspended in water.

We also observed the water front and movement of ceria NPs in water during the experiment, as seen in Figure 4-26. In this figure the step by step layer of marks of water front can clearly be seen, as shown by the yellow arrow in Figure 4-26 (a). These water fronts were formed due to the introduction of a fresh water supply into the liquid cell system with the help of a manual syringe. We only observed this type of water front during the experiment when we introduced a fresh water supply into the liquid cell in order to boost the movement of the ceria NPs. In Figure 4-26 (d) it can be seen that some empathy spaces indicated by the yellow arrow in Figure 4-26 (c) have been filled by the freshly moved ceria NPs.

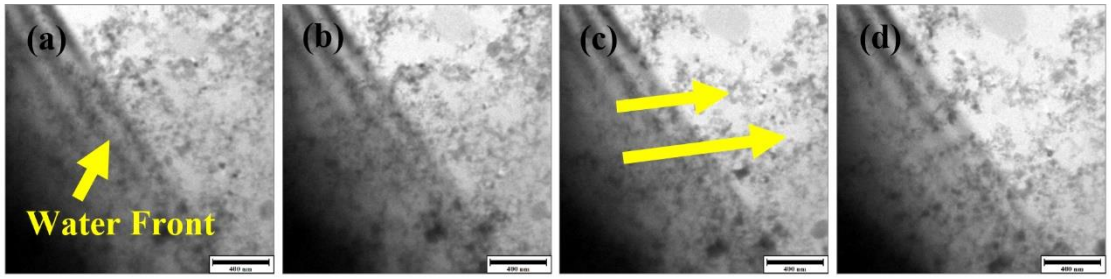

Figure 4-26: (a) to (d) show the water front stability and movement of ceria NPs (scale bar at 400nm).

4.4.2 Nano Particles Chain Formation and Attachment

The results of the electron irradiation of ceria NPs at low and high intensity of electrons in water showed many phenomena, such as particle movement, attachment and detachment during chain formation during the LC experiment. When we started the experiment of electron beam irradiation we made the following types of observation:

1) Case 1: the movement of NPs with slow dissolution and the making of small particles chains with some gaps or without attachment, as clearly seen in Figure 4-27.
2) Case 2: the movement of NPs with slow dissolution and the making of chains with corner to corner attachment, as clearly seen in Figure 4-28.
3) Case 3: the movement of NPs without dissolution and the making of small chains of two or more NPs can be seen in Figure 4-29.

Case 1: In the high magnification images of the irradiation experiment of ceria in water we observed the nice movement sequences of NPs, as seen in Figure 4-27. In Figure 4-27 (a) one large dumbbell-shaped NP attached itself to the small octahedral nanoparticle from the corner. In Figure 4-27 (b) we noticed the shrinkage of the dumbbell-shaped NP and an octahedral-shaped NP and the breaking of the attachment of the dumbbell-shaped NP to the octahedral-shaped NP. We observed that four nanoparticles as seen in the Figure 4-27(b & d) were trying to make a chain without attachment and with some gaps in between them. In this figure one important visible observation was the parallel dissolution and chain formation phenomena

without attachment. So, we observed some continuous thinning of NPs and some particles were dissolved, while some undissolved particles were making a small straight chain with gaps, as seen in Figure 4-27 (c).

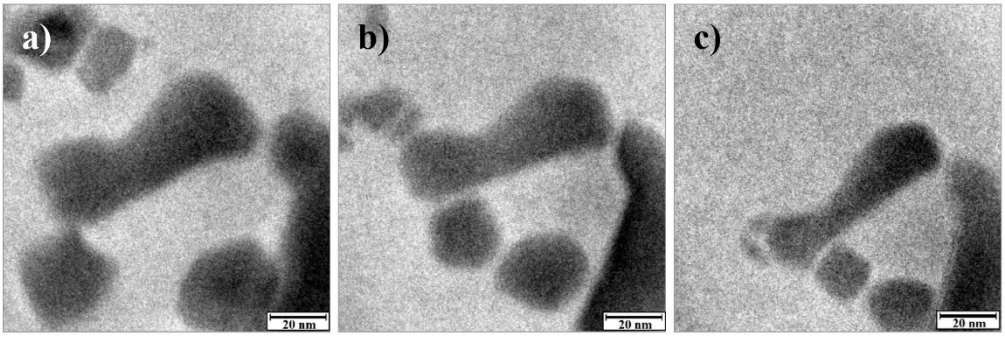

Figure 4-27: The movement of octahedral-shaped ceria NPs and chain formation without attachment before complete dissolution.

Case 2: The high magnification images of the liquid cell experiment also showed the long random movement of NPs in the liquid and forming chains, as seen in Figure 4-28. In this experiment, the octahedral ceria NPs were showing a slow parallel dissolution, moving from one point to another and making tip to tip corner-attached chains. All the nanoparticles were moving freely in the solution (water) of the liquid cell. In Figure 4-28 (a) before any movement occurred we noticed the two pairs of face to face attachment of particles: the first pair was one large and small particles (highlighted by a blue circle) and the second was another pair of small NPs (highlighted by a yellow circle). The pair of small nanoparticles moved a distance of approximately 100 nm from their location to another location of NPs and attached themselves to the octahedra facets of ceria NPs to form a corner to corner chain, as clearly seen inside the yellow circle of Figure 4-28 (b). Figure 4-28 (c) indicates the up and down movement of the ceria nanoparticle chain marked by a red curved arrow line. The clear parallel dissolution of NPs could be observed in Figure 4-28 (d) during the corner to corner attachment.

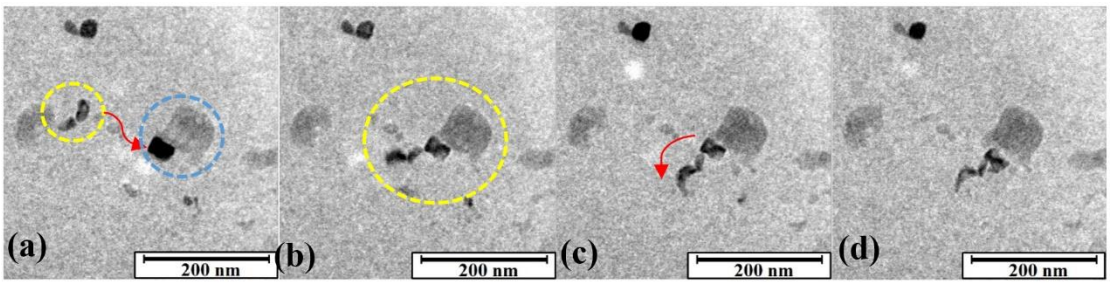

Figure 4-28: Nanoparticle movement and tip to tip chain formation with parallel slow dissolution.

Case 3: In liquid cell irradiation experiment of ceria NPs in water we observed the chain formation of round NPs below the threshold intensity of the electron beam. We noticed that some of the particles attracted each other and formed a chain of two or multiple NPs. The chains that were formed can be seen in Figures 4-29 and 4-30. In Figure 4-29 we observed that six NPs were attracted to each other and formed a straight chain. Initially, all these NPs were moving randomly in the liquid, as can be seen in Figure 4-29 (a). In Figure 4-30 (b) we have observed that six NPs are trying to align in straight line and started to make a chain of multiple NPs that can be seen in Figures 4.26 (c) and (d).

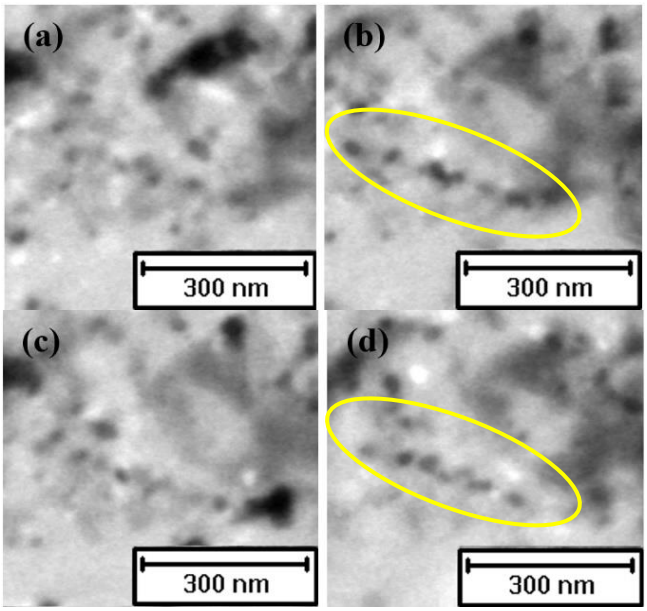

Figure 4-29: Nanoparticle movement and chain formation in water.

Similarly, in another experiment we observed that 3 small chains were formed in the same area of liquid cell irradiation, as seen in Figure 4-30. Figure 4-30 (b) shows the 2 small chains (inside the highlighted yellow circle) containing 3 NPs. We observed that continuous irradiation in liquid caused more NPs to become attracted to each other and to make a long chain containing four or more NPs, as seen in Figure 4-30 (c).

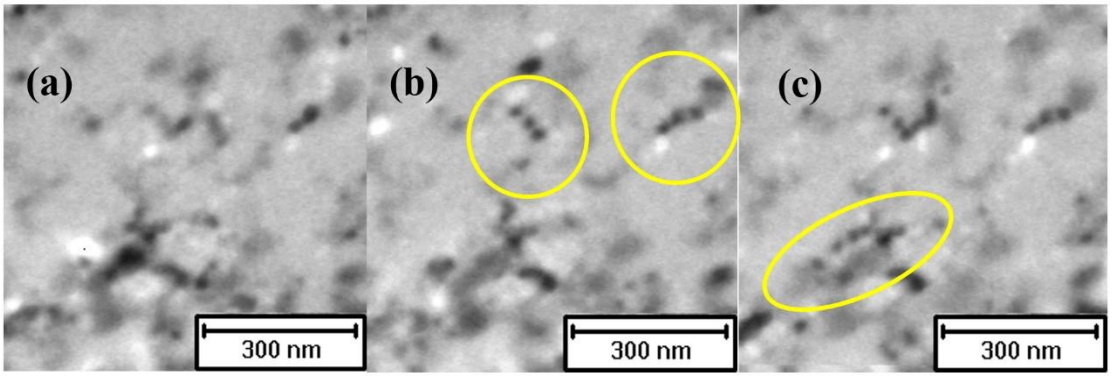

Figure 4-30: (a) to (c) show the movement of the NPs and the small chain formation.

Furthermore, we also observed a long chain containing five NPs, as seen in Figure 4-31. In this figure, step by step all the sequences of chain formation could be observed. In Figure 4-31 (a) 2 NPs initially attracted each other and then these 2 NPs moved from their location to another side and attached themselves to 3 more NPs, making a long chain of 5 NPs within 2.9 seconds, as seen in Figure 4-31 (b). The chain formed was a curved shape, as shown inside the yellow highlighted area of Figure 4-31 (b). We noticed the stability of the chain, which was moving freely in the water under the electron beam, as seen in Figure 4-31 (d). This figure (d) also shows the curved chain moving down from the left corner and making a straight chain. We noticed that the NPs or NP chains were continuously moving up and down, so we observed blurred or slightly out of focus images, which can be seen in Figure 4-31 (a-f).

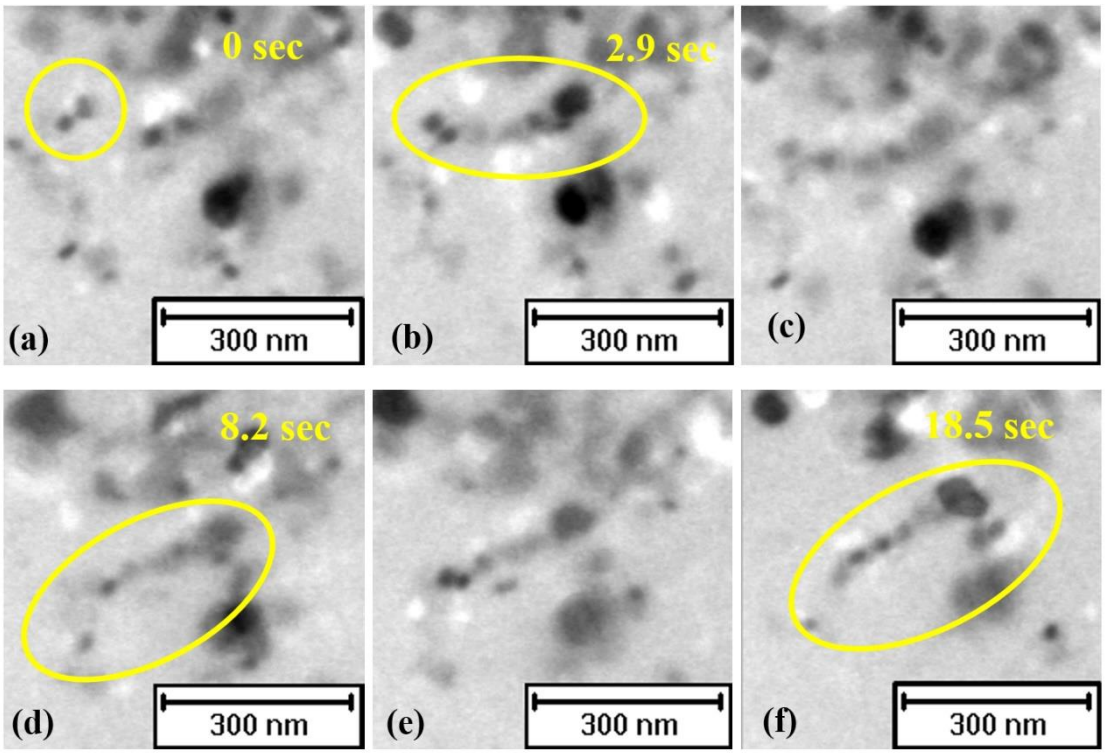

Figure 4-31: Movement of NPs, and their stability and step by step chain formation.

4.4.3 Discussion on Movement, Chain Formation and Attachment

The results of the low and high magnification images of the liquid cell irradiation experiments of ceria NPs in water have revealed the movement, attachment and some more complex and opposite phenomena of movement and attachment during chain formation in the same experiment. The previous research studies related to the liquid cell TEM of different metallic and ceramic NPs also showed oriented attachment, agglomeration and de-agglomeration [94, 109] but in our case we observed some similar and some opposite results.

The results of low intensity irradiation of ceria NPs indicate the usual mobility of NPs in water, as can be seen in Figure 4-25. This figure show that the particles are bouncing, moving away from each other and making spaces in between them. According to the previous research studies this type of movement of NPs may be due to the electrostatic force or may be due to the same charge, which is why they were repelling each other.

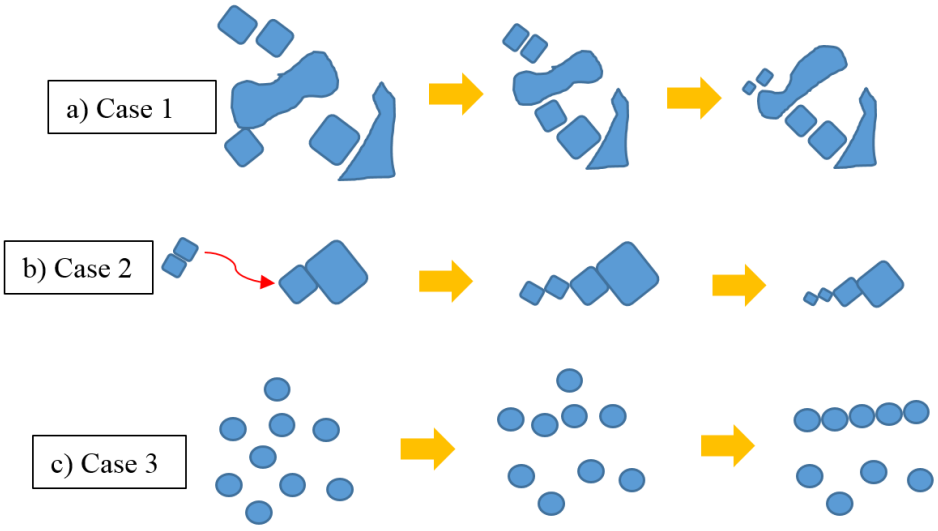

Figure 4-32: This schematic figure shows the proposed mechanisms of movement and chain formation: (a) particle movement and chain formation with some gaps with parallel dissolution; (b) large displacement and movement with corner to corner attachment with parallel dissolution; and (c) movement and chain formation without dissolution.

In our liquid cell experiments of ceria NPs in water we observed three different types of movement and chain formation which were opposite in nature. The proposed mechanisms can be seen schematically in Figure 4-32. When we increased the intensity of the electron beam we observed the movement of NPs involved slow dissolution and the making of small nanoparticles chain with some gaps, as clearly seen in Case 1 in Figure 4-32 and also in Figure 4-27. In this case, particles are trying to connect with each other but they are not in fact connecting as they maintain a little gap. The same type of separation or gap has been observed by an earlier team of researchers in relation to metallic Au nanoparticles. According to them, the separation between the nanoparticles in water is due to the mono or bi-layer of hydration on NPs [134]. Alternatively, the gaps observed between the NPs were due to two types of generated forces which may be attractive and repulsive forces in nature. In the case of materials that are identical, they are usually attractive in nature, but it is possible for two dissimilar materials to be repulsive in nature. Generally, previous studies have shown that the interaction between metal, metal oxide and ceramic NPs and NRs during movement, attachment,

agglomeration and de-agglomeration in liquid were probably due to van der Waals forces, hydrophobic attractions, and charge-charge interactions [135]. So, in our Case 1, both attractive and repulsive forces may be present: due to the attractive forces the particles are trying to join together, while at the same time the repulsive forces are causing them to repel each other. It may therefore be due to these forces that our NP chains have some gaps in between them.

Similarly, in Case 2 we observed a long displacement of two NPs and their attachment with other NPs along with a slow parallel dissolution and the making of small corner to corner attached chains, as the mechanism can be seen schematically in Figure 4-32 Case 2 (b) or in Figure 4-28. In this case, our particles were not round but octahedral in shape, so possibly they had some strong dipole forces or strong van der Waals forces for attachment. Those forces had a tendency to aggregate them with each other easily. According to earlier research, the irregular-shaped NPs preferred to attach themselves to each other at their ends, not from the middle, due to the strong positive and negative forces; each NP in liquid has its own distinct point of dipoles; and the free movement of NPs around other NPs or NP chains is due to the small amount of interaction energy [109]. It has also been mentioned in previous research that magnetic NPs have magnetic dipole moments so they have both magnetic dipole and electrostatic dipole movements at the same time [136]. In our Case 2, there was no chance of any sort of magnetic dipole movement because our NPs were non-magnetic in nature. Some researchers have also found that applied convective forces like magnetic and electrostatic forces are also being used to align and control NPs [137]. Possibly we observed these types of forces in between the particles during chain formation due to use of the electron beam.

In our Case 3, we observed the stability of ceria NPs, which formed small and large chains of NPs, as seen the mechanism schematically in Figure 4-32 (Case 3) and in Figure 4-29 and Figure 4-31. In this case we observed that attractive forces were present between the NPs and due to these they attracted each other and made a small or large chain. According to previous

research studies related to our case 3, the round nanoparticles contain some charge effect and due to this they attract each other. Anand et al. have observed the attachment or coalescence of NPs due to the removal of the hydration layer from the surface of Au NPs [134].

4.5 Bubble Formation

The highly focused prolonged electron beam irradiation of the ceria NPs in an aqueous solution (i.e. de-ionised water) has complimentarily led to the generation of nano bubbles in water. We used approximately 7 times greater electron intensity as compared to the dissolution intensity: i.e. 3 nA/μm^2 for the generation of nano bubbles in water. Initially, irradiation causes the dissolution of ceria nanoparticles and then formation of nano bubbles in the liquid and continuous electron irradiation with a highly converged electron beam caused the nano bubbles to grow, as shown in Figure 4-33. Figure 4-33 (a) shows the presence of some ceria NPs at the start of irradiation but the high intensity of the electron beam caused the fast dissolution of NPs, as can be seen in Figure 4-33 (b). Figure 4-33 (c) shows the formation of nano bubbles due to continuous irradiation, while Figure (d) indicates the growth of such bubbles, also due to the irradiation. We observed the formation of bubbles after the complete dissolution of ceria NPs.

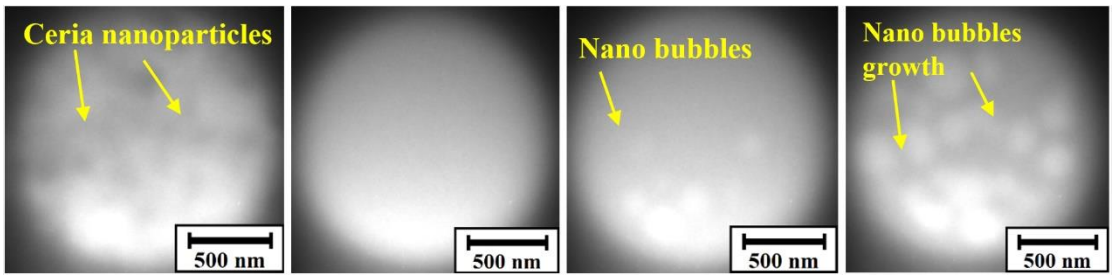

Figure 4-33: Nano bubble formation and their growth at even high intensity of LC electron beam irradiation (scale bar of 500nm) where (a), (b), (c) and (d) are snapshots 40.5 s, 8.3 s, 6.6 s, and 33.33 s apart respectively.

4.5.1 Discussion of Bubble Formation

Low intensity irradiation has not indicated any nano bubble formation inside the liquid cell during the irradiation experiments of ceria NPs. We assumed that the generation of nano bubbles was due to the formation of hydrogen in the liquid cell, as shown in Figure 4-33 (a) to (d). According to research studies, the generation of nano bubbles were due to the formation of hydrogen inside the liquid cell, because of the splitting of water into species through e- irradiation [106]. The formation of hydrogen ions, together with other molecule and radicals species, is a usual phenomenon which occurs when water is irradiated by an e- beam of >200kV. So, we predicted that possibly hydrogen generation to some degree would happen at an early stage in our irradiation experiment and be consumed by secondary reactions. High intensity irradiation only causes the formation of enough hydrogen to be released simultaneously to react into stable molecular H_2 and start visible bubble formation. The continuous irradiation causes the growth of the bubbles, as can be seen in Figure 4-33 (d). We noticed that during the dissolution of ceria NPs, bubbles were absent, even at high intensity irradiation.

4.6 Related Liquid Cell Observations

We also observed some multiple minor allied LC observations, which were as follows:

4.6.1 Fresnel Rings Formation

Furthermore, during the dissolution of solid ceria NPs in the e- irradiation experiment in the liquid cell, we observed some instantaneous appearance and disappearance of rings and core shell patterns, as shown in Figure 4-34. The total time for which the ring phase existed was about 0.3 seconds, as shown in Figure 4-34 and for the core shell it was 1.3 seconds. Actually,

the ring phase appeared during one frame of the image and disappeared in the next frame of the video. So, we assumed that these rings were temporary rings formed due to the up and down movement of particles in water in the liquid cell. For further confirmation that these rings were temporary rings we post-processed some similar rings containing NPs. Our images and results of the plot profile (as shown in Figure 4-35) indicate that these rings are Fresnel rings instead of chemical rings, due to the up and down movement of NPs in water.

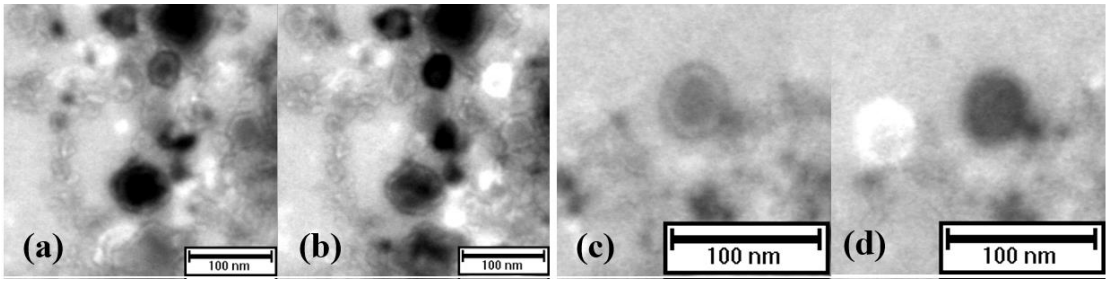

Figure 4-34: Pairs of particles showing jumping/tilting behaviour via Fresnel fringe changes.

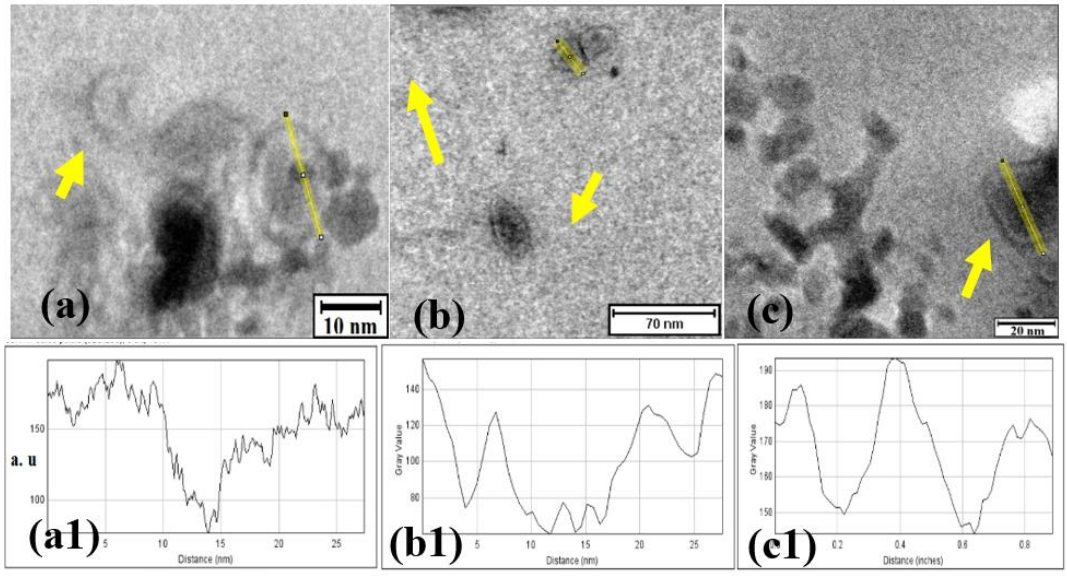

Figure 4-35: Figures (a), (b) & (c) show the formation of Fresnel rings (by arrow) due to the movement of particles, while (a1), (b1) and (c1) are plot profiles of images (a), (b) and (c) respectively.

4.6.2 EELS of H_2O

Through the liquid cell irradiation experiments of ceria NPs we have discovered many live reaction, phase formation, chain formation, attachments and de-attachment in the presence of water. During the experiment in TEM 2010-F we used electron energy loss spectroscopy (EELS) chemical analysis of liquid cell with ceria NPs. We have observed the EELS spectrum of water and ceria NPs and successfully recorded the EELS of plasmon range signals from water and the ceria nano structures. We observed the difference in plasmon scattering results due to changes of water thickness as shown in Figure 4-36. Multiple selected area EELS analysis indicates an increase in water thickness and shows Δz sensitivity through multiple plasmon scattering (Figure 4-36).

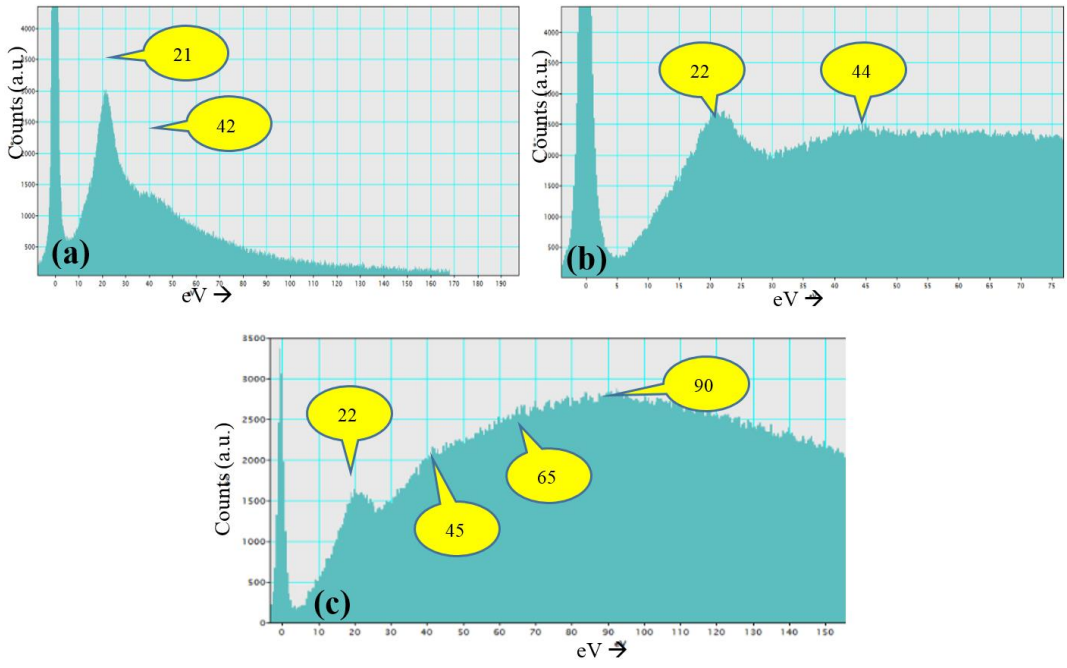

Figure 4-36: (a – c) Low loss EELS of water at 3 thicknesses (on the basis of Δz sensitivity through multiple plasmon scattering). (c) single to 4-fold plasmon peaks (in eV).

Similarly, we recorded the EELS spectra of cerium peaks (i.e. Ce M-edge) as shown in Figure 4.37. The magnified view of the M-edge specifies the presence of Ce^{4+}. The EELS spectra also indicate the oxygen and nitrogen peaks as well.

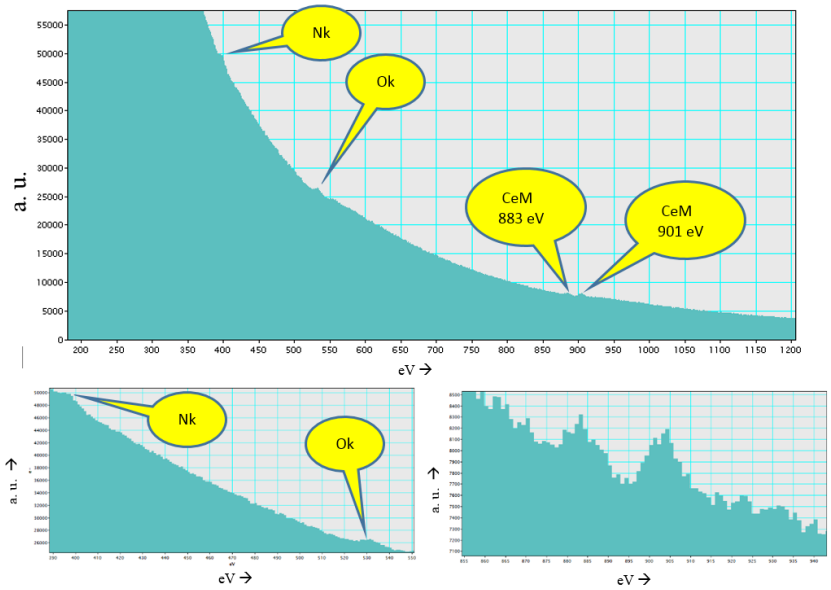

Figure 4-37: (a) EELS spectra of cerium and water; (b) magnified view of spectra containing nitrogen and oxygen; and (c) magnified view reveals the M4 and M5 sub peaks of cerium (in eV).

4.6.3 Post Processing of Liquid Cell Chips

4.6.3.1 Dry Chip Imaging

After the successful liquid cell experiments we post-processed the small chips to further investigate the final product material: for example the morphology of ceria NPs, their size, geometry and chemistry, and any contamination. We selected the small Si_3N_4 chips to analyse in the TEM by using a standard JEOL TEM holder as we were unable to do any post-processing of large chips in a standard TEM holder due to its large restricted size. The results, as seen in Figure 4-38, show that we observed the clusters of NPs having the size range of raw material, which means that the dissolution of NPs in the liquid cell was limited to the localised region of the electron beam impact zone, rather than being in the whole cell.

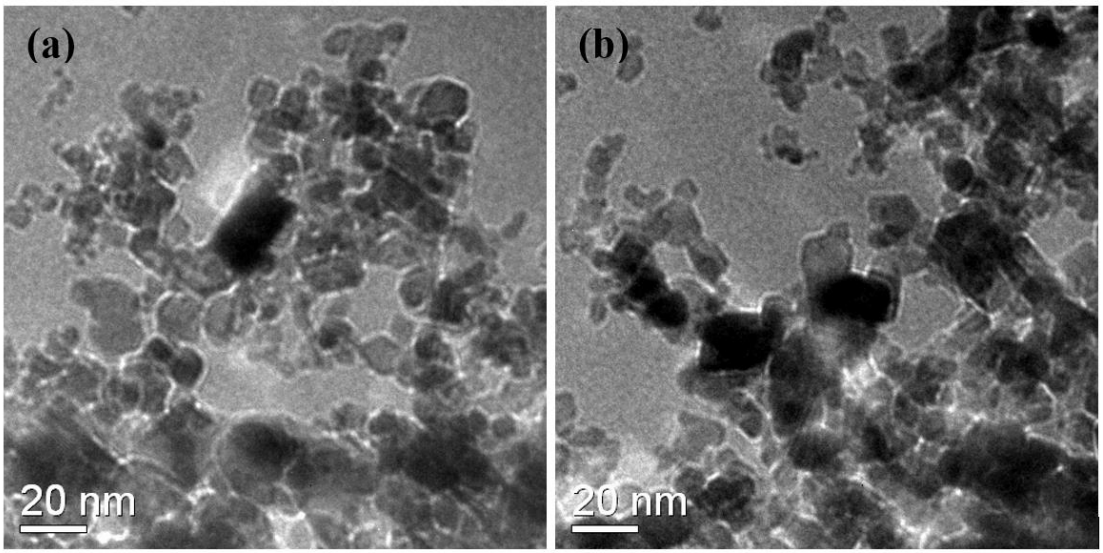

Figure 4-38: (a & b) Unirradiated dry ceria NPs on small Si_3N_4 chip.

4.6.3.2 Dry Chip EELS

Furthermore, we did some EELS spectroscopy of our dry chips samples and the EELS spectra indicated the presence of some nitrogen (which basically came from the silicon nitride membrane), oxygen and cerium (from the ceria). The EELS spectra indicated the presence of two cerium peaks, of M4 and M5 respectively, and the M4 peak was larger than the M5 one, which meant this belonged to Ce4+. The EELS results also indicated that no carbon contamination happened in our case, as we did not observe any carbon edge in the spectrum, as seen in Figure 4.39 (a & b). Initially we suspected and assumed that we were facing some carbon contamination, which is usually formed during irradiation experiments, but the EELS spectrum results clearly showed that there was no carbon k-edge present. This meant, therefore, that as carbon was absent there was no chance of carbon contamination in our experiment.

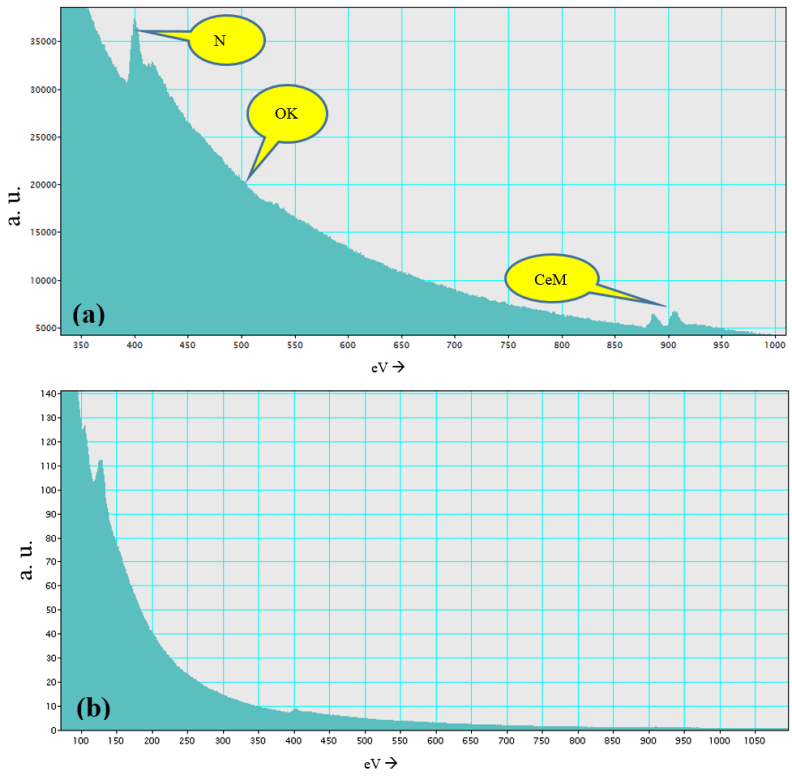

Figure 4-39: EELS spectra of small chips containing ceria NPs: (a) shows the presence of nitrogen, oxygen and cerium M-edge with two sub peaks; and (b) indicates that no carbon peak is present.

CHAPTER FIVE

DIRECT DRY IRRADIATION OF PRECURSORS

5.1 Introduction

In this direct dry irradiation method, cerium salts – cerium nitrate hexahydrate (CNH) and cerium chloride heptahydrate (CCL) were used, and these salts are referred to as 'precursor' throughout this chapter. Direct dry irradiation of salts or compounds has rarely been studied and the formation of nano structures (NS) by this method has become a topic of great interest. Ceria nano structures are the most studied ceramic nano materials due to the high number of applications in different fields of catalysis and biomedics. Research studies have shown that many ex-situ laboratory based synthesis methods are available such as chemical precipitation and sol-gel for the synthesis of ceria nano structures. Although some studies have been conducted on the synthesis of metallic nano structures by in situ electron beam induced irradiation, to the best of our information there is no research to date on the synthesis of ceria nano structures by using cerium nitrate hexahydrate as a precursor through the method of direct electron induced irradiation.

The aim of this study therefore is to fill the gap in the ceria literature by attempting the in-situ irradiation of hydrated cerium precursors and the formation of ceria or cerium chloride nano structures through electron beam irradiation in TEM. Two hydrated cerium precursors cerium nitrate hexahydrate ($(CeNO_3)_3\ 6H_2O$) and cerium chloride hepta hydrate ($CeCl_3\ 7H_2O$) were chosen for the purpose of exploring the electron irradiation induced nanostructure formation.

We used 99.9 % pure water soluble salts of the cerium nitrate hexahydrate precursor and 99.9 % pure water soluble salts of the cerium chloride heptahydrate precursor during the dry irradiation experiments. The CNH and CCL were purchased from Sigma Aldrich UK. In this research the production of nanostructures (i.e. nanoparticles and nanorods from cerium precursors) was carried out in a JEOL JEM 2010-F and JEOL JEM 3010 TEMs at acceleration voltages of 200 kV and 300kV respectively. We used converged electron beams of different intensities with and without condenser apertures for different doses during the experiment.

After successful liquid cell irradiation of the nano structures in water we started the irradiation experiment of dry precursors of hydrated cerium. We think newly formed 1D rod by liquid cell method and rods formed by dry irradiation could have a relationship. In both liquid cell and dry experiment irradiation, water and ceria are common. Hence we are interested in studying those hydrated cerium precursor materials and the said connection is our motivation because our intention is to explore the interconnected phenomena of the synthesis of functional oxide through the TEM electron beam irradiation induced method.

In this work our main aim is the synthesis of nanostructures but in addition to this we have tried to explore the effect of electron beams by varying the size and intensity on the cerium precursor salts. We started dry irradiation experiments with the CNH and then we switched to CCL for the synthesis of nanostructures. So, in this chapter, section 5.2 starts with the results of the CNH and the section will present the irradiation results of TEM and the electron energy loss spectroscopy (EELS) chemical analysis results. Section 5.3 presents the irradiation results of CCL at 200kV and 300kV, and includes the formation of nano rods and irregular and round shaped nanoparticles (NPs) with or without condenser apertures (CA).

5.2 Results of Electron Irradiation of CNH

The results of this CNH study differ slightly in one respect from all the previous reported studies related to the change of oxidation state of cerium during irradiation, because we did not observe the ceria 3+ to 4+ transformation. However, upon irradiation of CNH we observed the following results: First, the irradiation of CNH precursor was achieved by an electron beam of TEM. Second, nanostructures 3-6 nm in size were formed through internal precipitation on the precursor material. Third, we observed the amorphous to crystalline transformation of amorphous CNH and formation of crystalline nano precipitates or nanoparticles.

We were interested in the transformation of the amorphous CNH precursor to the crystalline phase with the aid of electron beam induced irradiation in TEM. We were exploring the redox transformation of CNH and this was assumed to be an amorphous to crystalline transformation. The majority of the literature indicates that reduction takes place during the electron irradiation of precursors for example the reduction of metal halides (LiF and CoF_2) to metal (Li and Co) [13, 138, 139], reduction of cerium 4+ to 3+ [15] and reduction of TiO_2 to Ti [16] metal. On the other hand, some groups of researchers have observed that occasionally an redox neutral reaction in which there is no reduction has occurred for example during the irradiation of calcium carbonate to lime transformation [8, 9].

5.2.1 TEM Results

Figure 5-1 (a and b) shows the TEM images of a CNH sample from different locations before irradiation, while (c) shows the selected area diffraction (SAD) of the CNH precursor before irradiation from a different region. It can be seen from Figure 5-1 (a & b) that the initial CNH precursor is clean and homogenous, while Figure 5-1 (c) indicates that our raw materials are amorphous in nature because the selected area diffraction (SAD) image only shows the

amorphous rings or halo rings without any peaks of crystallinity.

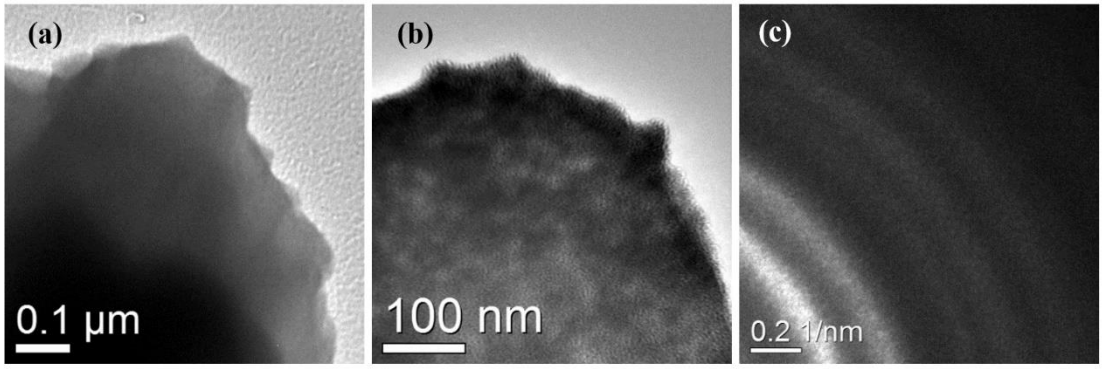

Figure 5-1: (a) and (b) show the TEM images of CNH before irradiation and (c) shows the selected area diffraction (SAD) before irradiation.

We irradiated our CNH sample many times from many new locations with variable electron intensity with or without a condenser aperture (CA), but every time we found that our CNH was a very tough material from which to form individual ceria nano structures on the holey carbon grid or adjacent to precursor materials. During the electron irradiation we observed the formation of nano precipitates or nanoparticles in our CNH sample through the internal precipitation method. Figure 5-2 (a & b) shows the TEM images of the CNH precursor after 1 and 2 minutes irradiation while (c) presents a selected area diffraction after irradiation from a different location. Figure 5-2 (a) shows that 1-minute irradiation causes the formation of internal precipitation of the precursor and shows the lattice fringes in the TEM image. When the sample was irradiated for another minute, we observed the formation of clear lattice fringes inside the precursor through the internal precipitation method, as can be seen in Figure 5-2 (b). The measured size of precipitates or nanoparticles formed on the precursor were in the range of 3-6 nm. The d-spacing measured between the lattice fringes on the newly formed precipitates was d=3.15 nm. The results of the d-spacing measured by the lattice fringes can be seen in Table 5-1. Furthermore, Figure 5-2 (c) shows the small magnification of the SAD image of the CNH sample after irradiation from a different location. This SAD shows the peak on it which indicates that our final irradiated product is crystalline in nature. This is because the peaks on

the SAD image represent the formation of some crystalline precipitates or phases on the precursor material due to irradiation.

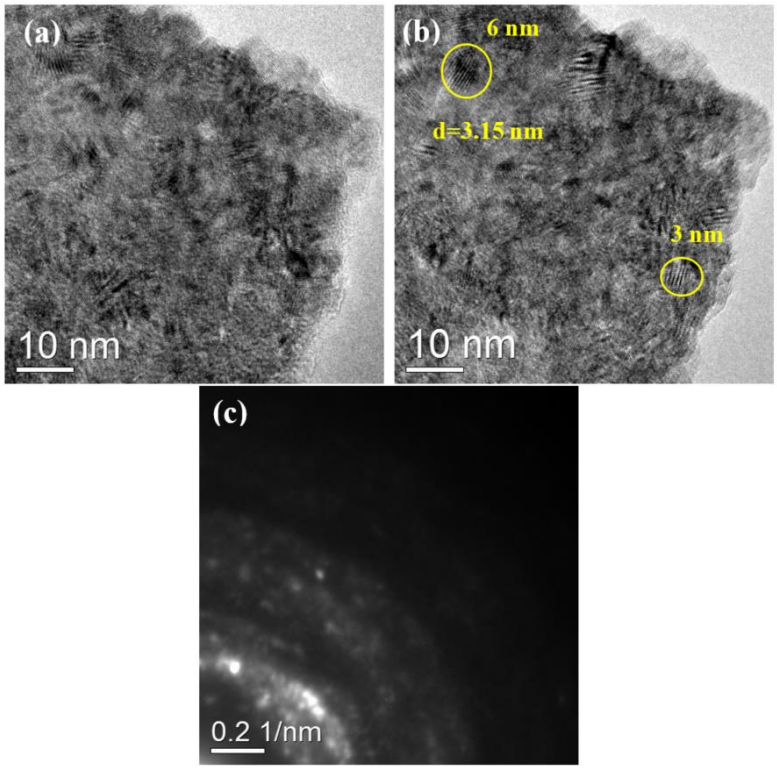

Figure 5-2: (a) and (b) show the presence of freshly formed nanoparticles with lattice fringes having d111 =0.315nm after electron irradiation: in (a) after irradiation of 1 minute; in (b) after 2 minutes irradiation. (c) shows the selected area diffraction (SAD after irradiation).

5.2.2 Post-Processing of TEM Results

We have post-processed our TEM result by using Image-J and Gatan digital micrograph 3.9 software to confirm the amorphous to crystalline transformation of the CNH precursor. In the past, researchers have used the fast Fourier transform (FFT) to show the single crystal to poly crystalline transformation of $CaCO_3$ to CaO after irradiation [8, 9]. Similarly, we have used the TEM images and their corresponding FFT, to show the amorphous to crystalline transformation of the CNH precursor, to calculate the d-spacing, as can be seen in Figure 5-3 (a & b). After irradiation of CNH precursor as seen in Figure 5-3 (a) represents the internal precipitation and their corresponding FFT shows the ring with solid peaks of crystalline materials as seen in Figure 5-3 (b).

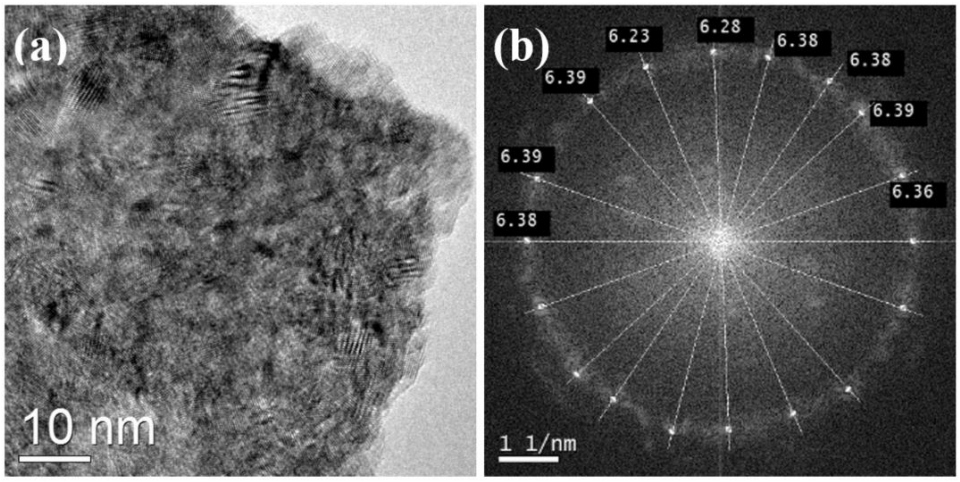

Figure 5-3: Figure (a, b, c and d) shows the TEM images of before and after irradiation of CNH from different location and their corresponding FFTs.

We used the FFT of the TEM images of 'after irradiation' to calculate the d-spacing. The results of the calculations of the d-spacing from the FFT can be seen in the

Table *5-1* This table also presents the value of the reciprocal of the d-spacing and lattice parameter. We have compared the results of the d-spacing and the reciprocal of the d-spacing and lattice parameter, measured by the lattice fringes and FFT of TEM images, with the literature-based calculated value of the d-spacing, reciprocal of the d-spacing and lattice parameter of nano crystalline ceria for the (111) plane, as can be seen in

Table *5-1* [140]. The calculated values of the d-spacing and lattice parameter by FFT of TEM images are <d>= 0.314 nm with a deviation +.001 and a = 0.5453 nm with a deviation (+0.0026) respectively. Similarly, the calculated values of the d-spacing and lattice parameter by lattice fringes (as seen in Figure 5-2 (b), highlighted by yellow circles) are <d>= 0.315 nm with a deviation +.002 and a = 0.5455 nm with a deviation +.0028.

Table 5-1:Literature based calculated value and calculated values of ceria lattice parameter, d-spacing and reciprocal of d-spacing from TEM images and their corresponding FFT.

Parameter / Method	a (nm) [Deviation]	d_{111}(nm) [Deviation]	$1/d_{111}$ (1/nm)	$2x1/d_{111}$ (1/nm)
Literature Value	0.5427	0.313	3.191	6.383
Calculated value by FFT	0.5453 [+0.0026]	0.314 [+0.001]	3.176	6.35
Calculated value by lattice fringe	0.5455 [+0.0028]	0.315 [+0.002]	3.174	6.349

5.2.3 EELS Results

The EELS results of irradiation of CNH precursors under electron beams show some significantly different phenomena in many respects. Firstly, we did not observe the first transformation of Ce^{3+} to Ce^{4+} by the help of EELS. It is believed that this transformation is very sensitive to electron beams and so possibly this transformation occurred for a very short duration or in the early stage of focusing and preparing the electron beam for irradiation. Second, we observed the second transformation of CNH (i.e. Ce^{4+} to Ce^{3+}) with the help of EELS spectra as shown in Figure 5-4 (a - c). We used EELS method because it has better detection capabilities of rare earth elements for example cerium for the transformation of Ce^{3+} to Ce^{4+} to Ce^{3+} [15, 126]. Figure 5-4 (a - c) shows the effect of electron beam irradiation at different times of t1 and t2 (1 and 2 minutes irradiation) of the CNH sample at view point 1 and similarly t3 for 1 minute at view point 2. At the time zero irradiation we was unable to record the EELS spectra due to stage preparation and focusing. The EELS spectrum in Figure 5-4 shows the presence of a cerium M-edge with two sub-peaks and an oxygen edge. These spectra also show that the influence of electron beams on CNH causes the inversion of the

cerium M-edge peaks and effects a change in the charge valences by the electron irradiation of cerium samples.

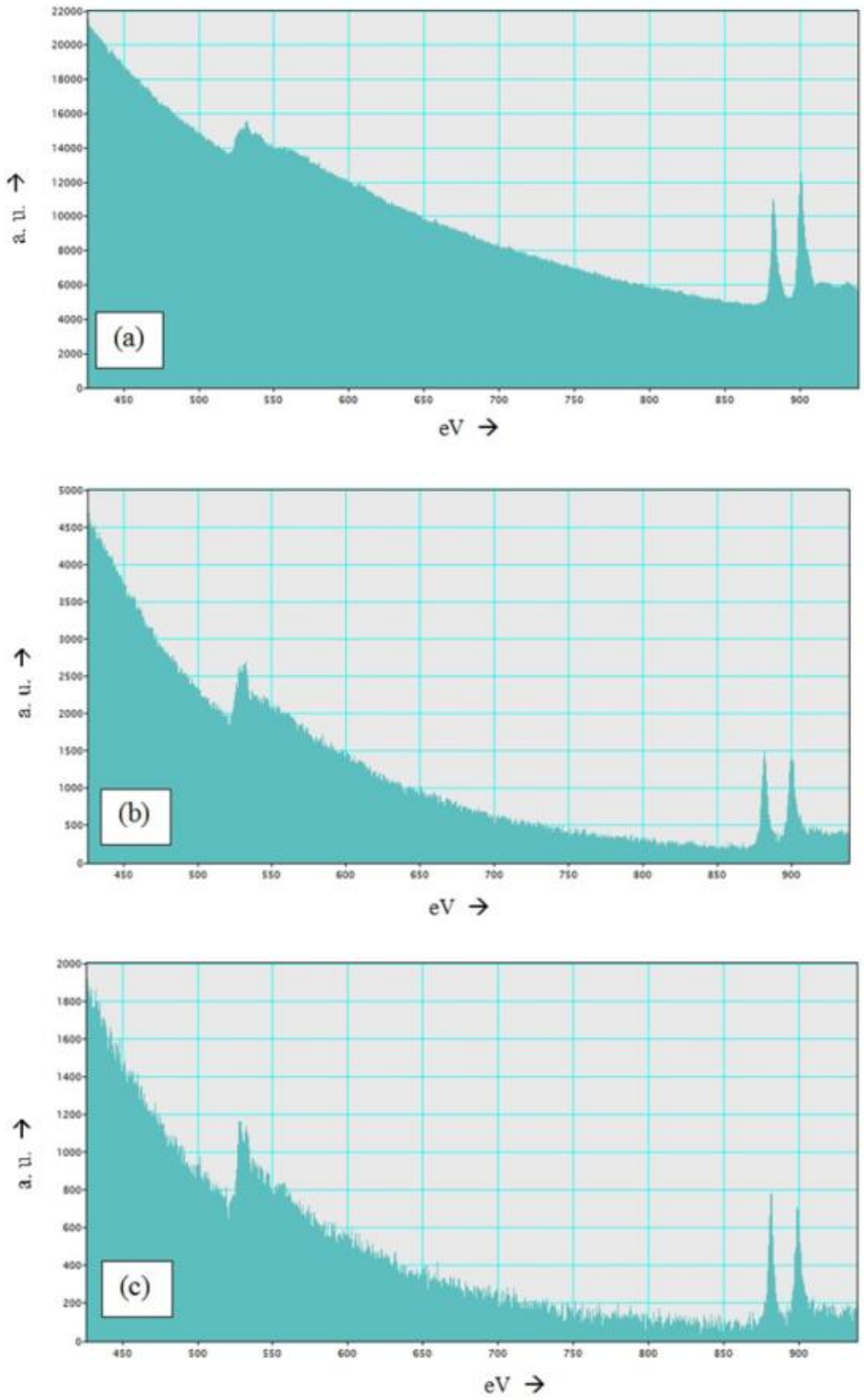

Figure 5-4: Figure (a, b and c) shows the EELS spectra of CNH irradiation at different times, showing the inversion of the Ce M-edge sub-peaks and the presence of oxygen.

Figure 5-4 (a) indicates the EELS spectrum of the CNH precursor at the time of the start of irradiation and the spectrum shows the cerium M-edge with their two sub-peaks (i.e. M5 and M4). In this spectrum we observed that the cerium M5 peak was smaller than the M4 peak at the time of start of irradiation. After the 1-minute irradiation, modification in this region under the electron beam occurred, possibly due to internal precipitation and we observed the two approximately equal sub-peaks of cerium M-edge on the EELS spectra in Figure 5-4 (b). Additionally, more electron irradiation of CNH at view point 2 for 1-minute shows the cerium M-edge with two sub peaks in which the M5 peak is slightly larger than the M4 one. We assumed that this inversion of peaks was due to the continuous electron irradiation of CNH.

5.2.4 Post-Processing of EELS Results

The EELS results, as shown in Figure 5-4 (a - c), have been post-processed by two different methods: 1) second derivative method; and 2) background subtraction method, by the help of digital micrograph software. The EELS spectra were acquired, after the pre-calibration using zero loss peak (ZLP), by using Gatan 200 EELS spectrometer attached to a TEM JEOL 2010-F [82]. The post-processing of the EELS spectra by the second derivative method of the CNH sample is shown in Figure 5-5 (a - c). The experimental calculated relative white line area ratio, of cerium M-edge sub peaks (M5/M4), was estimated to be 0.8801, 1.165 and 1.1308 respectively and the experimental calculated change of charge valency of cerium by electron irradiation is shown in Figure 5-5 [141]. The calculated peak ratio and change of valency of cerium by the post-processing of the EELS spectra using the second derivative method is shown in Table 5-2.

Table 5-2: Peak ratios of M5 and M4 and calculated charges of Ce by using second derivative method.

S. No.	Sample Name	Time	2nd Derivative			Calculated Charge of Ce
01	CNH	t1	Left peak, M5 580.7	Right peak, M4 659.7	Ratio M5:M4 0.8801	4.05
02	CNH	t2	Left peak, M5 121.0	Right peak, M4 103.8	Ratio M5:M4 1.165	3.35
03	CNH	t3	Left peak, M5 64.2	Right peak, M4 49.1	Ratio M5:M4 1.3088	3.0

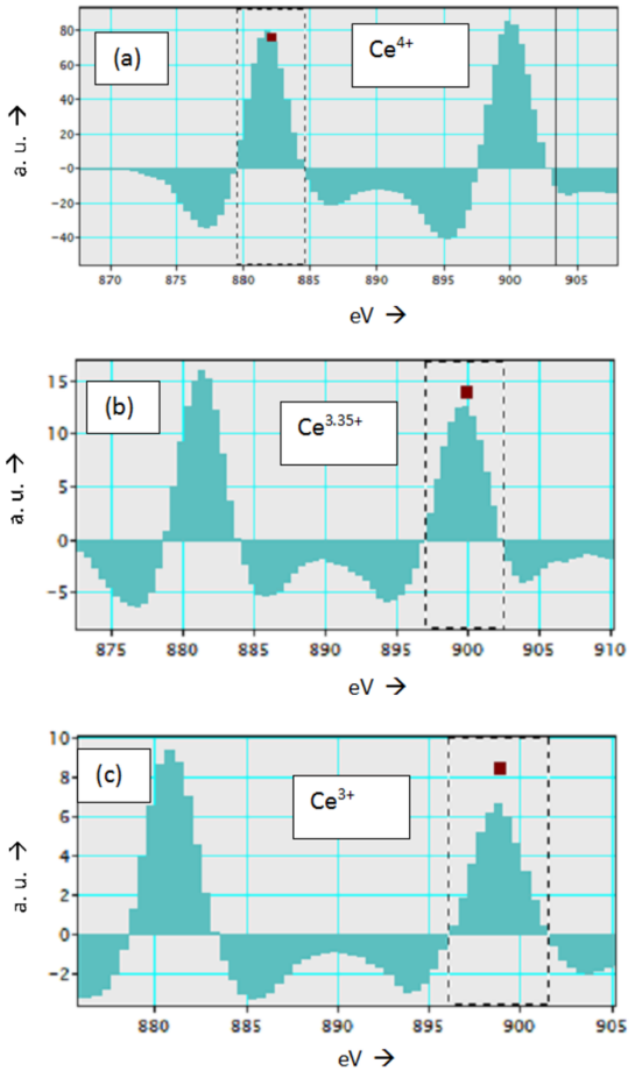

Figure 5-5:(a), (b) and (c) show the second derivative of EELS spectra of Figure 5.4 (a - c) with calculated change of charges of cerium (Ce4+, Ce3.35+, and Ce3+) after electron irradiation.

Similarly, the post-processing of EELS results, by the background subtraction process, of M5 and M4 subpeaks of cerium is shown in Figure 5-6 (a, b and c). The background subtracted EELS spectra of electrons irradiated at time t1 showed a small shoulder of Ce after the M4 peak but after continuous exposure of electron irradiation (i.e. t2 and t3), the small shoulder of Ce disappeared completely, as can be seen in Figure 5-6 (b and c) [15]. The calculated peak ratio and charge of valency of cerium by the post-processing of EELS spectra using the background subtraction method is shown in Table 5-3.

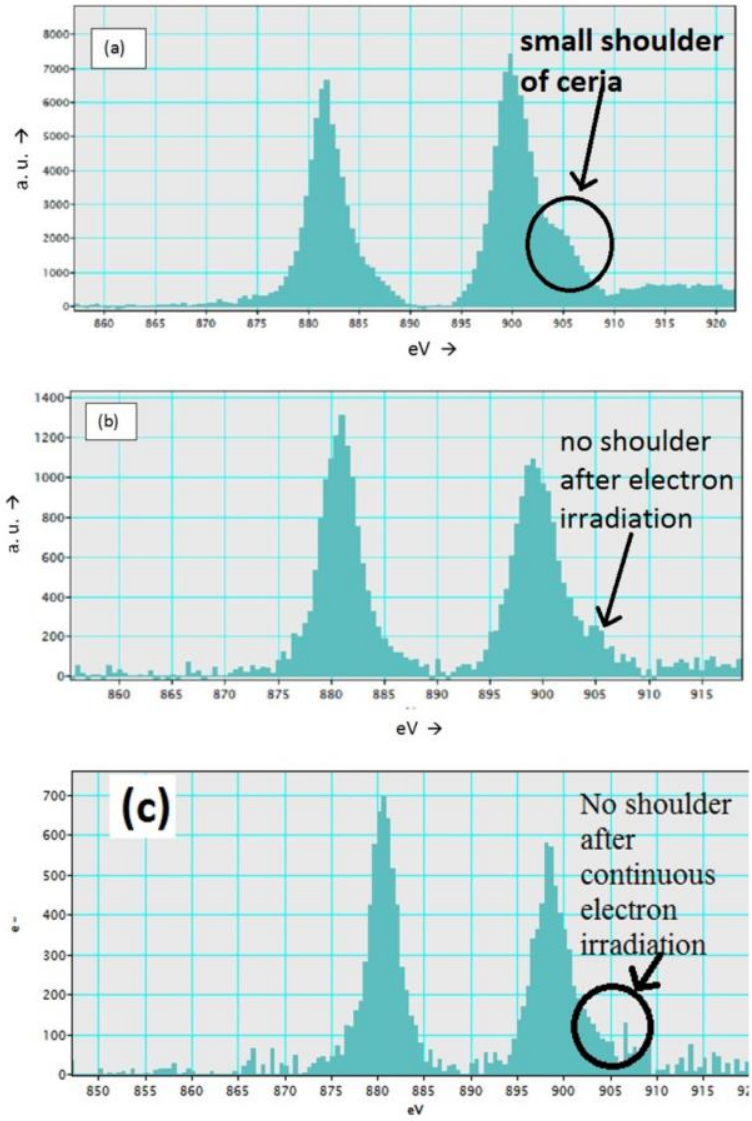

Figure 5-6: (a), (b) and c) show the back ground subtracted EELS spectra of Figure 5.4 (a - c): (a) shows small shoulder of Ce, figure (b) and (c) shows the absence of shoulder of Ce after electron irradiation.

Table 5-3: Peak ratios of M5:M4 and calculated charges of Ce by using background subtraction method.

S. No.	Sample Name	Time	Background Subtraction Method			Calculated Charge of Ce
01	CNH	t1	Left peak, M5 580.8	Right peak, M4 656.5	Ratio M5:M4 0.8847	4.04
02	CNH	t2	Left peak, M5 122.6	Right peak, M4 103.0	Ratio M5:M4 1.190	3.29
03	CNH	t3	Left peak, M5 64.3	Right peak, M4 49.1	Ratio M5:M4 1.309	3.002

The EELS results of the e- irradiation of the CNH sample in TEM shows the ablation of nitrogen percentage, as shown in Figure 5-7 (a) and (b), and in Table 5-4. Figure 5-7 (a) shows the EELS spectra of the CNH sample at the start of irradiation: it shows that a high percentage of nitrogen was present in our material and remaining oxygen. Similarly, in Figure 5-7 (b), the EELS spectra of CNH sample after irradiation shows the clear decrease in the percentage of nitrogen and increase in the percentage of oxygen.

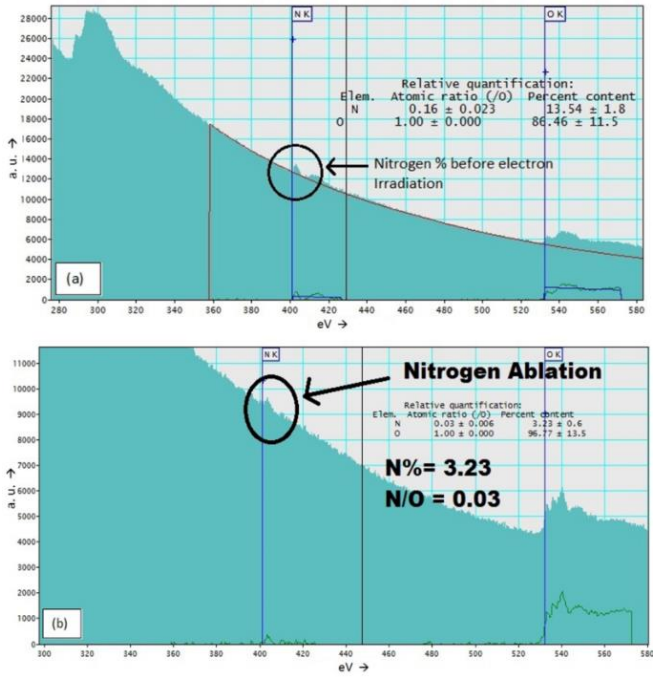

Figure 5-7: EELS spectra in (a) and (b) show the ablation of nitrogen after electron irradiation.

Table 5-4: Percentages of nitrogen and oxygen.

S. No.	Element / Method	% of N	% of O
01	Before irradiation	13.54 (±1.8)	86.46 (±11.5)
02	After irradiation	3.23 (±0.6)	96.77 (±13.5)

5.2.5 Discussion of CNH

The TEM results of the cerium nitrate hexahydrate show the presence of a beam impact zone and de-homogenisation during irradiation. The TEM images also show the progress of transformation from an amorphous precursor to nanocrystalline particles, starting the formation of crystals at the edge or thin area of the precursor, due to irradiation. This crystallisation inside the precursor indicates that the internal precipitation of the CNH precursor occurred during irradiation. In the past a group of researchers used FFT to show the single crystal to poly crystalline transformation of $CaCO_3$ to CaO by irradiation [8, 9]. The high resolution images show that newly formed precipitates have lattice fringes and the d-spacing measured of those lattice fringes is d=3.15nm, which matches the literature value of the d-spacing of the ceria [140]. The calculated results of d-spacing from the FFT of TEM images after irradiation also matches the d-spacing of the ceria. The results of the d-spacing from the FFT confirmed that internal precipitation had occurred, and that the precipitates which were formed belonged to the ceria. Finally, on the basis of the TEM results it can be said that electron irradiation causes the amorphous to crystalline transformation of CNH and the formation of crystalline precipitates of ceria through in-situ electron irradiation in TEM.

Similarly, our interpretation is based on EELS spectra and their post-processing by using second derivatives of Ce-M as inset at three consecutive time steps (t1-t3), and upon irradiation we observed thinning, oxygen enhancement and unexpected Ce^{3+} enhancement. We observed

the thinning after electron irradiation at t3, as seen in Figure 5.4 (c). This was possibly due to the irradiation, which causes the reduction of material, and we observed the cerium 3+ was possibly coming from a thin surface. The same type of thinning has been observe in the past, during the irradiation of ceria nanorods [142]. The results of the calculated charge of cerium by using EELS spectra through the second derivative (as seen in Table 5.2) showed that at time t1 the calculated charge was 4.05, at time t2 charge of Ce it was 3.35, and at time t3 the charge was 3. Similarly, the results of the calculated charge of cerium by the background subtraction method (as seen in Table 5.3) were approximately same as the results calculated by the second derivative method. Based on the change of charge valency of the cerium in the CNH sample during irradiation, the material formed at time t1 was equal to the ceria, at time t2 it was approximately equal to CeO_{2-x} and at time t3 it was probably equal to Ce_2O_3 or another form of cerium oxide. However, we have observed a reverse redox reaction (i.e. transformation from Ce^{4+} to Ce^{3+}), which was possibly masking an earlier 3+ to 4+ fast transformation to ceria, followed by a secondary beam-induced reduction to CeO_{2-x}, known to exist for this material, and for many other forms of oxide [143]. Furthermore, the EELS results also show the nitrogen ablation during irradation experiment, due to the reduction of the CNH precursor, which indicates the formation of CeO_2.

5.3 Results of Cerium Chloride Heptahydrate (CCL)

The cerium chloride hepta hydrate was found to respond much faster to irradiation as compared to the cerium nitrate hexahydrate. The differences we observed were as follows. First, irradiation of the precursor was achieved, and as result, a high number of fresh free-standing nanostructures were immediately formed on the adjacent carbon-support film or near to the precursor material. Second, we observed that nano particles (with different shapes) and nanorods were growing rapidly out of the precursor fragment. Finally, we also observed that the nano rods, in the form of needles, super thin needles and rods, were formed and then grew on the precursor before finally becoming detached from the precursor.

5.3.1 Formation of Nanorods (NRs)

The electron irradiation of the CCL precursor at 200 kV and 300kV showed the formation of different types of NRs. We observed free standing NRs and the formation and growth of NRs on the precursor at both 200 and 300 kV. We performed multiple experiments from different new and unirradiated locations with different levels of electron intensity, in order to explore the formation phenomena of NRs. In this section, the results of NR formation will be split into types: freestanding NRs and the ones growing on the precursor.

5.3.1.1 Free Standing NRs

Electron irradiation of the raw powder of CCL fragments (as shown in Figure 5-8) in TEM 2010-F at 200kV caused the formation of a huge number of free standing NRs with some NPs. We observed that there was no change during the e-irradiation of the CCL precursor with a condenser aperture (CA). On the other hand, when we started the electron beam irradiation of the CCL precursor without a condenser aperture we observed a high number of freshly formed

NRs, as shown in Figure 5-9. During the generation of freshly formed nanorods and some nanoparticles, the shape may have been controlled by the intensity of the electron beam.

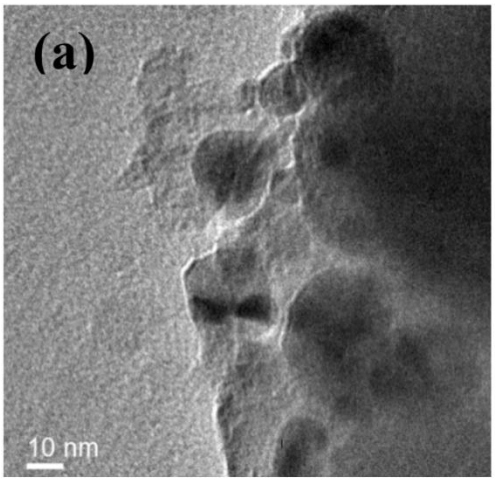

Figure 5-8: Cerium chloride hepta hydrate precursor before e- irradiation.

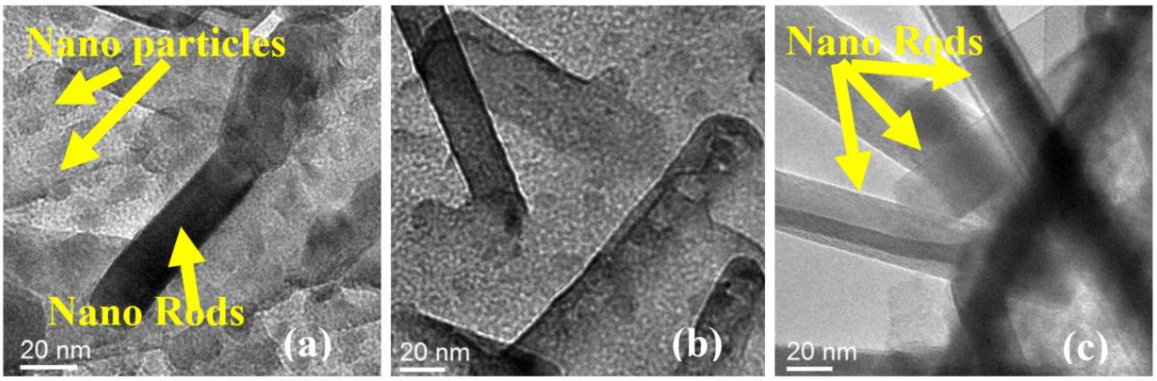

Figure 5-9: Figure (a) to (c) show the freshly formed nano rods with some nano particles after open aperture e- irradiation.

The results of the electron irradiation of CCL showed that formation of fine distributed nano rods with a diameter between approximately 15-35 nm and length between approximately 70-200 nm, as seen in Figure 5-9, after continuous e- irradiation of the precursor on carbon-supported film adjacent to the powder fragment without a condenser aperture. We also noticed that some of nano rods were surrounded by non-uniform nanoparticles with a size range of 5 to 30 nm.

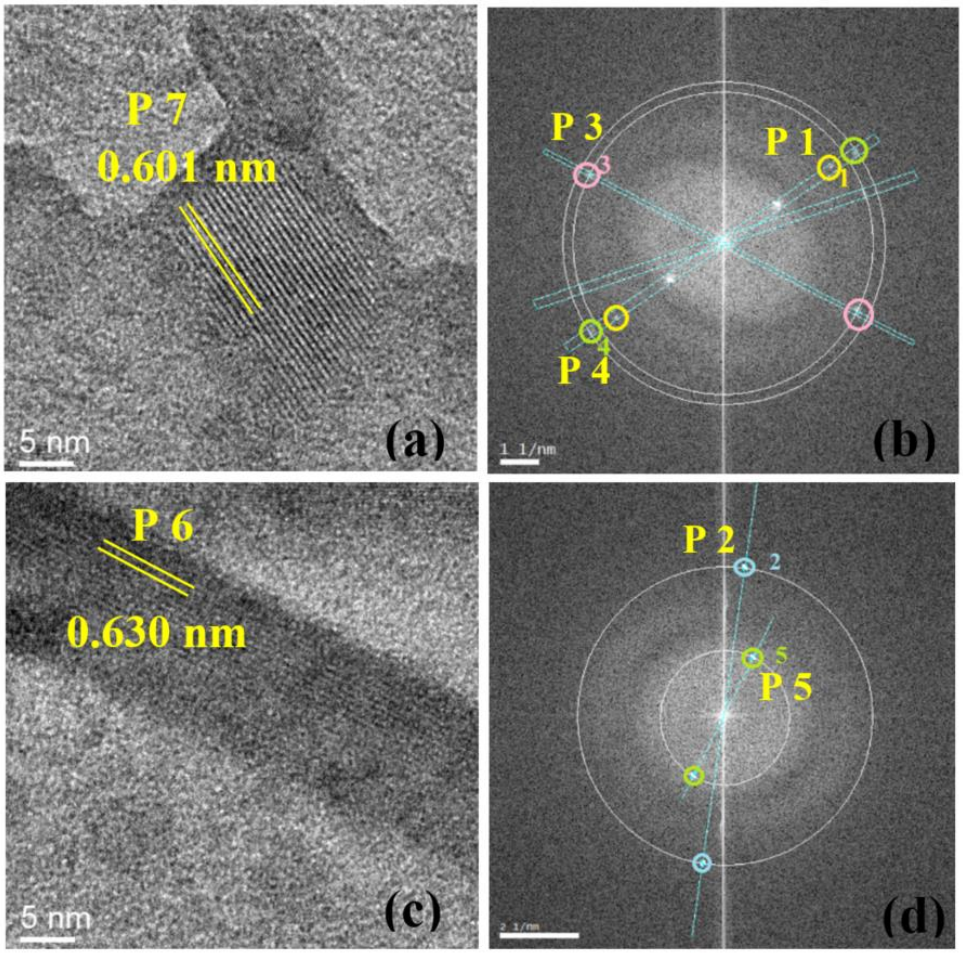

Figure 5-10: (a) and (c) show the high resolution TEM images: (a) shows the lattice fringes of the nanoparticles, while (c) shows the lattice fringes of nanorods; (b) and (d) show the crossponding FFT of (a) and (c).

Figure 5-10 presents high resolution TEM images in which the lattice fringes of the nanoparticles and nanorods can be seen. We post-processed our high resolution TEM images with lattice fringes by using the ImageJ software to calculate the d-spacing of the nanoparticles and nanorods formed. For that purpose, we first measured the d-spacing of NP and NR by using Figure 5-10 (a & c), which were 0.601 nm and .630 nm respectively. As an alternative, we used the corresponding FFT of TEM images of Figure 5-10 (b & d) to calculate the d-spacing of synthesised NP and NR. The calculated values of d-spacing can be found in Table 5-5.

Table 5-5: Literature (Lit.) based (cerium chloride and CeO_2) [[13] [14], Appendix-C] and calculated values of d-spacing from lattice fringes and FFT of TEM images.

	Plane	Lit. based Ceria d-spacing (nm)	Lit. based $CeCl_3$ d-spacing (nm)	Calculated d-spacing (nm) from lattice fringes	Calculated d-spacing (nm) from FFT
P 1	111	0.31 [144]	--	--	0.315 -0.004
P 2	200	0.27 [145]	--	--	0.268 +0.002
P 3	201	--	0.2586	--	0.259 -0.001
P 4	210	--	0.2438	--	0.245 -0.002
P 5	100	--	0.647	--	0.646 +0.001
P 6	100	--	0.647	0.639 +0.008	--
P 7	100	--	0.647	0.640 +0.007	--

The post-processing results, related to the irradiation induced transformation of the CCL precursor material into crystalline nano structures, were evaluated by means of d-spacing measurement by using TEM images and their corresponding FFT, as shown in Table 5.5, with the help of ImageJ and Gatan digital-micrograph 3.9 software. We noticed that the FFTs contained various peaks, which were possibly coming from different planes. We assumed that the different peaks observed were due to the presence of our raw material near NPs or NRs as can be seen in Figure 5.10 (a and c). The result of d-spacing of point 1, as seen in Figure 5.10 (b) was d=0.316 nm, which was closer to the (111) planes of ceria [144], with a deviation of -0.005. The result of d-spacing of point 2, as seen in Figure 5.10 (d), was d=0.267 nm, which was closer to the (200) planes of ceria [144] with a deviation of +0.003. The results of d-spacing of point 3 in Figure 5.10 (b) was d=0.2638, which was closer to the (201) cerium chloride plane with a deviation of -0.005. The result of d-spacing of point 4 in Figure 5.10 (b) was d=0.2495 nm, which was closer to the (210) plane of cerium chloride with a deviation of -0.005, while d-spacing of point 5 on Figure 5.10 (d) was d=0.601 nm, which was closer to the (100) plane of cerium chloride.

5.3.1.2 Growth of NRs on Precursor

During the electron irradiation of the CCL precursor in TEM at 200kV and 300kV we observed the formation of different shapes of nanorods. We noticed that the irradiation caused the formation and growth of NRs at the edge of the precursor. The results of the electron irradiation of the CCL precursor fragments (as seen in Figure 5-11(a)) at 200kV show the formation and growth of the rods. We observed the live growth of NRs which contain the NPs on top of the rod, as can be seen in Figure 5-11 (c). We assumed that these NP was formed initially and caused the formation of the rods, and then the growth of the rods occurred due to continuous irradiation, which can be seen in Figure 5-11 (d). The measured average diameter of observed NPs was approximately 16 nm and the average length of freshly formed NR was about 45 nm.

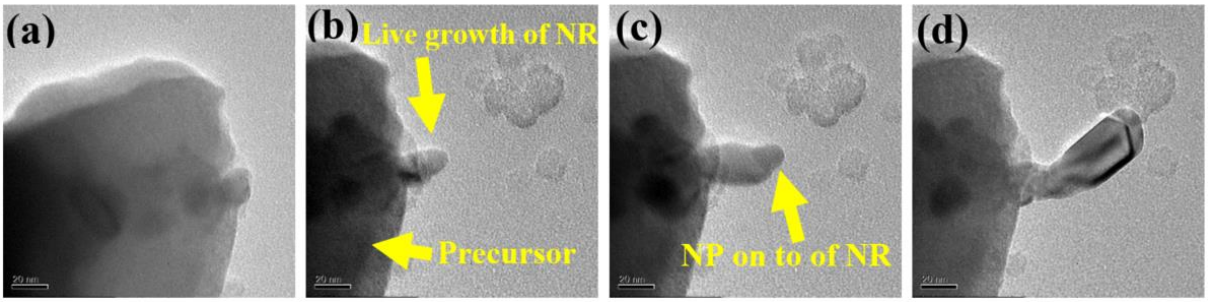

Figure 5-11: (a) to (d) show the formation and growth of nanorods in TEM through irradiation at 200kV with open condenser aperture.

Similarly, the irradiation results of the CCL precursor at 300kV show the formation of NRs on the edge of the precursor. Multiple irradiation experiments were performed at the new location of the precursor. We saw the presence of NPs on the surface of the precursor before e-irradiation, as can be seen in Figure 5-12 (a) with the help of the yellow arrow. We have assumed that these NPs were formed in the early stage of irradiation of the surrounding area or because of adjustment or focusing of the beam. We observed that continuous electron beam irradiation caused the formation and growth of NRs. The bottom right hand corner of Figure 5-12 (b) shows the formation and growth of the rods due to continuous irradiation (highlighted

by the yellow arrow). Figure 5-12 (c) shows the growth of rods having particles on top (indicated by the yellow arrow). We noticed that the NRs had a dark contrast and the Bragg Scattering (dark black particles and their parallel white shadow)can be seen in Figure 5-12 (a) to (c).

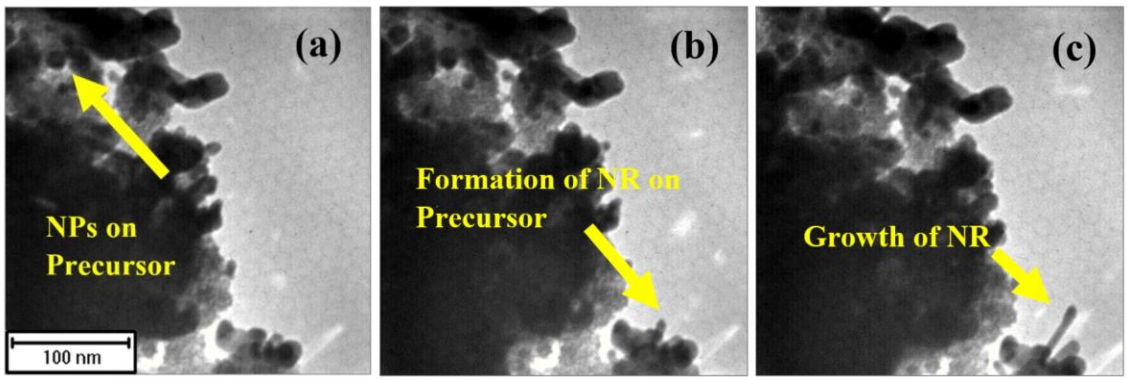

Figure 5-12: Video sequence (a-c) showing the presence of NPs on the precursor and also the formation and growth of nanorods.

Figure 5-13 (a) shows the presence of some NPs (indicated by blue arrow) and growth of rods. Occasionally, we noticed the formation and growth of more than one rod on the same area of the precursor. In Figure 5-13 (c) the formation of another NR can be seen (highlighted by the yellow arrow). Figure 5-13 (d) shows that the freshly formed NR and its growth is thicker than the other two neighbouring rods (indicated by the yellow arrow).

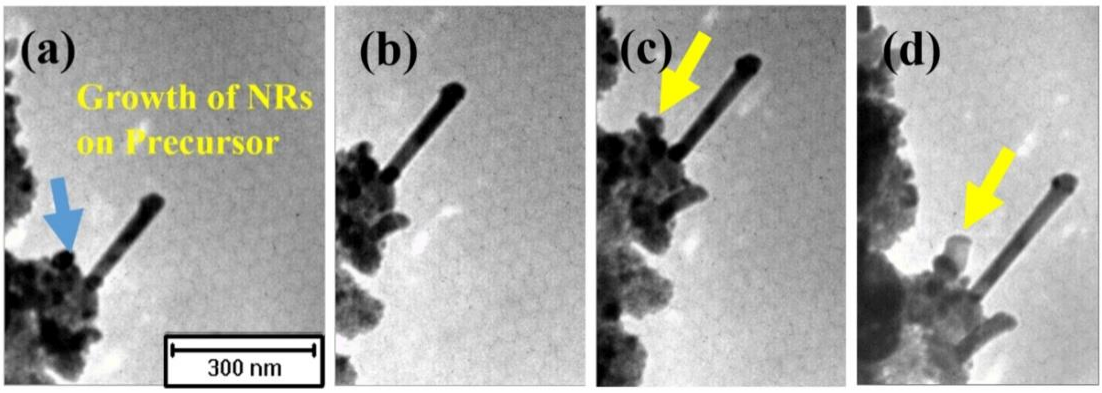

Figure 5-13: Video sequence (a-d) shows the formation and growth of rods on the precursor.

Figure 5-14 shows that the formation and growth of rods are in both vertical and horizontal directions. It was noticed that some NPs existed on the precusor before the start of irradiation (indicated by the blue arrow), as seen in Figure 5-14 (b). When the electron irradiation started, we noticed the vertical formation and growth of NRs, as seen in Figure 5-14 (a to c). We observed that continious irradiation causes the growth of rods and then at a certain length the rod becomes detached from the precursor and disappears into the vacumm or the copper grid. The continuous electron irradiation of the same area causes the horizontal formation and growth of NRs, as seen in Figure 5-14 (d to f).

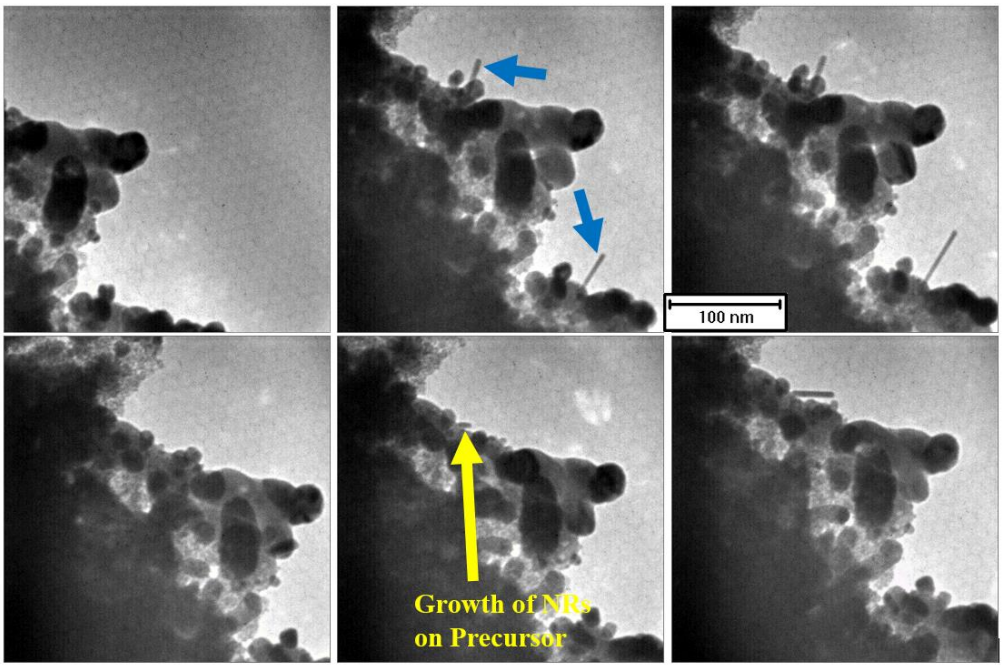

Figure 5-14: Video sequences (a-c) and (d-f) from the same location: (a-c) show the vertical formation and growth of rods, while (d-f) show the horizontal formation and growth of rods on the precursor (scale bar at 100nm).

The results of irradiation at 300 kV show the formation and growth of thin and thick (10-50 nm size in diameter) rod and super thin needles (≤ less than 4nm) during the experiment as shown in Figure 5-15 (a to d). We observed that the rods were continuously growing in a vertical direction to a certain length, then noticed that the rods became detached from their origin. Figure 5-15 (c and f) show that the formed rods are dark in contrast to the raw materials

and it also shows the Bragg Scattering. Figure 5-15 (f) shows the formation of multiple super thin needles at the same time from different regions.

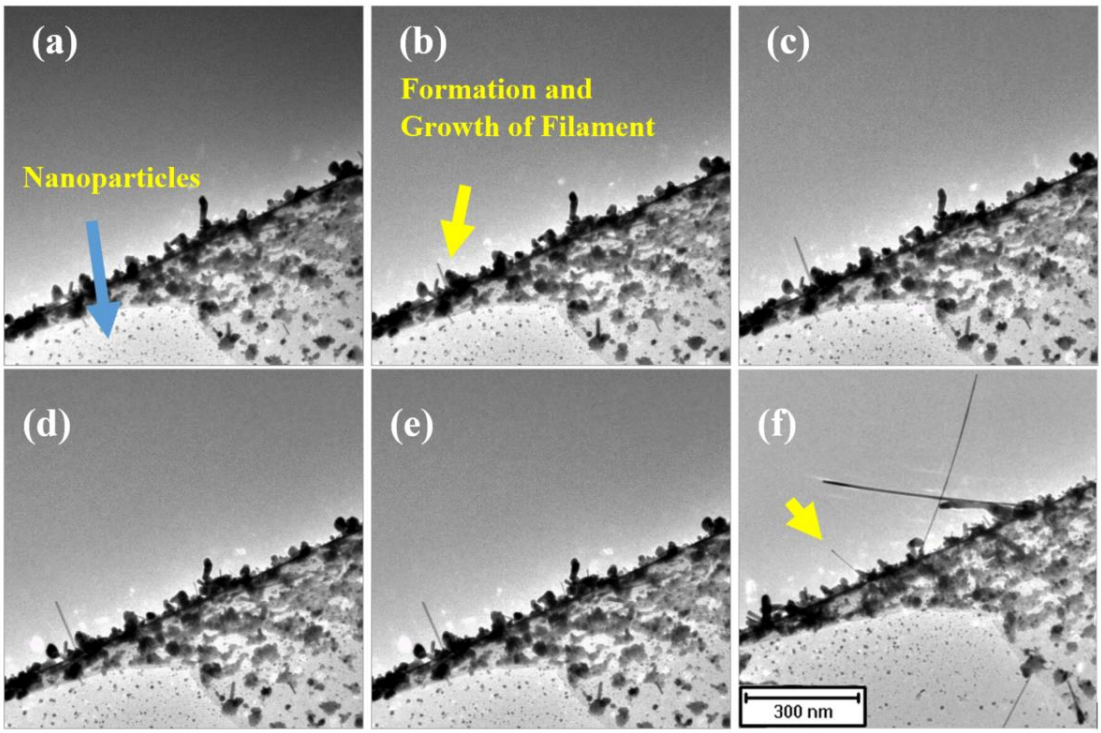

Figure 5-15: Video sequence (a to f) shows the formation and growth of thin rods on the precursor.

We also observed that irradiation of the CCL precursor at 300 kV caused the formation of thick rods having diameter $\leq$ 50 nm, as seen in Figure 5-16 (a-i). The series of images shows the formation and growth of multiple thick rods in the same area during irradiation. This figure shows that the central area or inner surface of rods are dark in contrast to the outer surface and it also shows the Bragg Scattering. Figure 5-16 (a & b) indicates the formation and growth of rod 1 (R1), which became detached from the precursor after few seconds of irradiation. In Figure 5-16 (c) we observed the formation of another thick rod 2 (R2) just next to rod R1. Figure 5-16 (d) shows the formation and growth of rod 3 (R3), which also became detached from the precursor due to continuous irradiation. Similarly, we observed the formation of rod 4 (R4) in Figure 5-16 (e). We noticed that continious irradiation caused the growth of R4 and

touched R2, as seen in Figure 5-16 (f). Prolonged irradiation caused a slight movement of R4 from the upside direction and further growth of R4, as seen in Figure 5-16 (h to i).

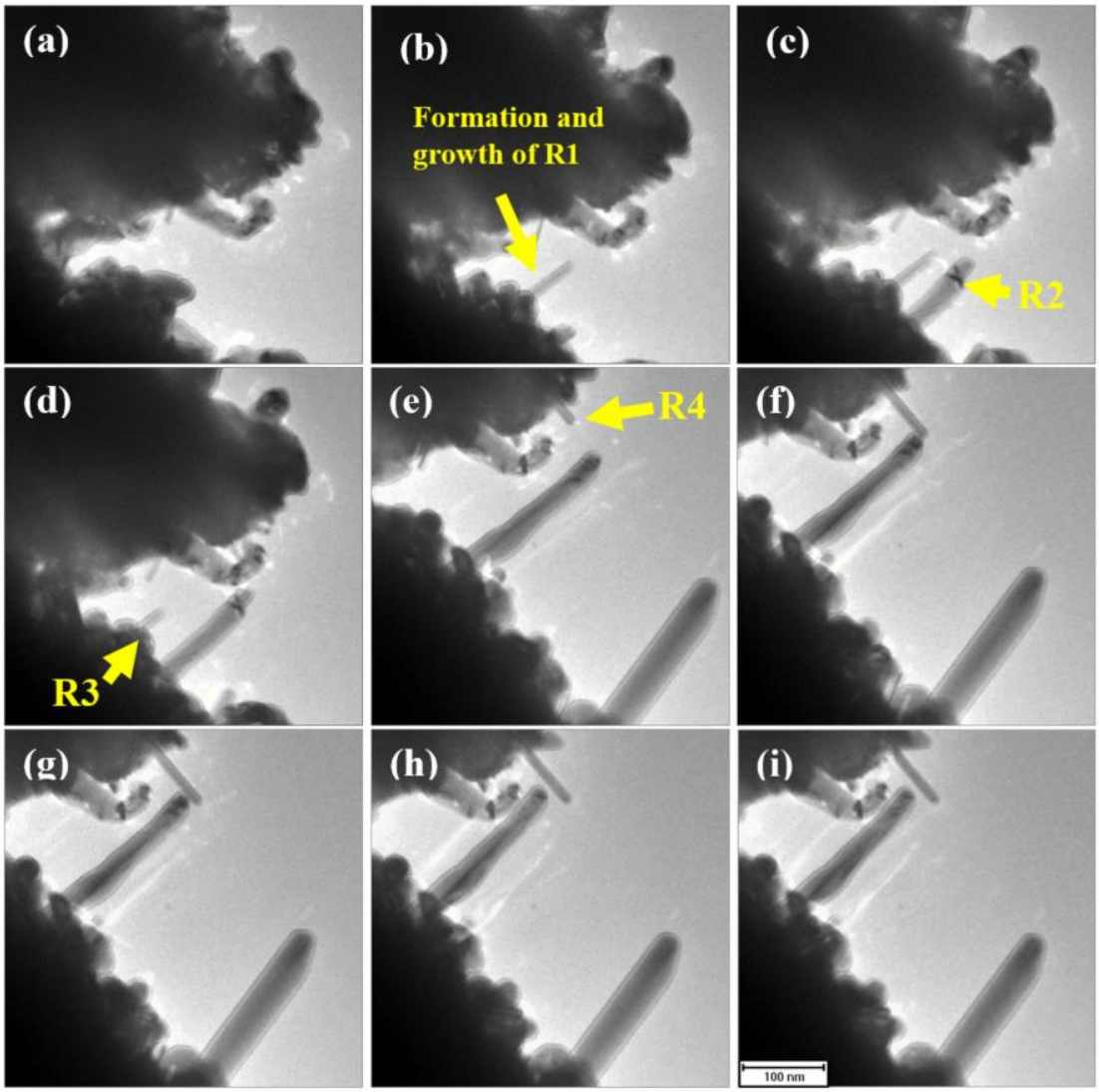

Figure 5-16: Video sequence (a - i) shows the formation and growth of different rods on the Ce-Chloride precursor.

5.3.3 Formation of Nanoparticles (NPs)

Electron beam irradiation of the raw powder of the CCL fragment (as seen in Figure 5-17) in TEM 3010 at 300 kV with and without an condenser aperture has produced a high number of free-standing NPs just adjacent to the surroundings of the precursor fragment on carbon-support film, as shown in Figure 5-18.

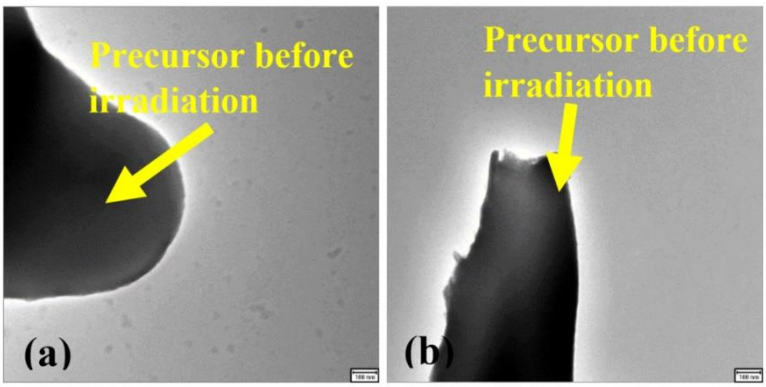

Figure 5-17: (a) and (b) show the cerium chloride hepta hydrate precursor before e-irradiation (scale bar at 100 nm).

The electron irradiation of the CCL precursor with the current density on the specimen (i.e. ≈ 2.45nA/ μm^2) with a condenser aperture caused the formation of a vast number of free-standing coarse NPs of irregular size and shape near the precursor, as seen in Figure 5-18 (a) to (f). The continuous highly focused e-beam irradiation with the current density on the sample (i.e. ≈ 7 nA/$\mu m^{2)}$ caused the formation of freshly formed irregular shaped NPs (as shown in Figure 5-18 (f)). Upon continuous irradiation of same area having coarse NPs can lead to further transformation through internal precipitation into round-shaped NPs which were relatively dark in contrast to the coarse NPs (as indicated by the yellow arrow in Figure 5-18 (f)).

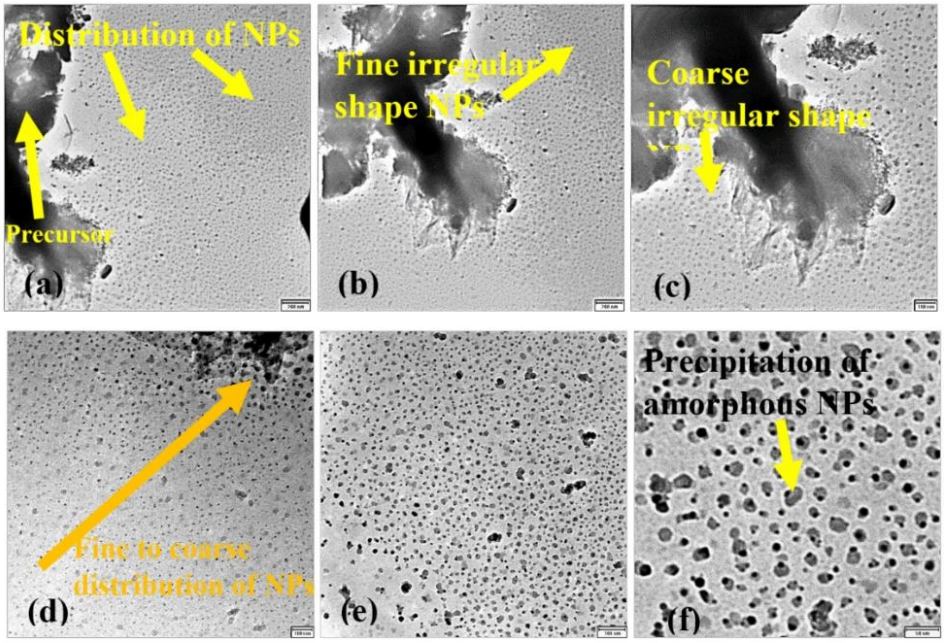

Figure 5-18: (a), (b) and (c) show the freshly formed NPs after e-irradiation with condenser aperture; (d), (e) and (f) show the irregular size and fine to coarse distribution of NPs formed.

When the CCL precursor fragment was irradiated with an open aperture, we observed the freshly formed round-shaped NPs, as shown in Figure 5-19. The high magnification TEM images of the same irradiated area show that the round NPs which were formed are relatively dark in contrast to the coarse or irregular shape NPs, as can be seen in Figure 5-20. The irradiation results of CCL without an aperture showed that the synthesised NPs were more uniform size and well-distributed near the surroundings of the precursor fragments on the copper grid, as shown in Figure 5-19 (a). In Figure 5-19 (c), some irregular-shaped nanoparticles can be seen, with the help of the yellow arrow. It was noticed that the size distribution of freshly-formed NPs near to the precursor was coarse, whereas away from the precursor it was very fine, as clearly seen in Figure 5-20 (a). The calculated diameter of freshly formed NPs was in the range of 10-40 nm in size.

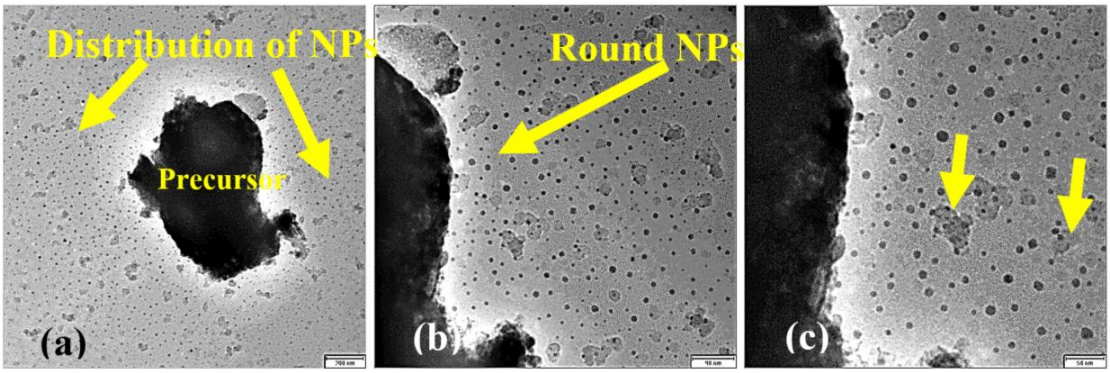

Figure 5-19: (a), (b) and (c) show the freshly formed nano particles after e-irradiation with open aperture.

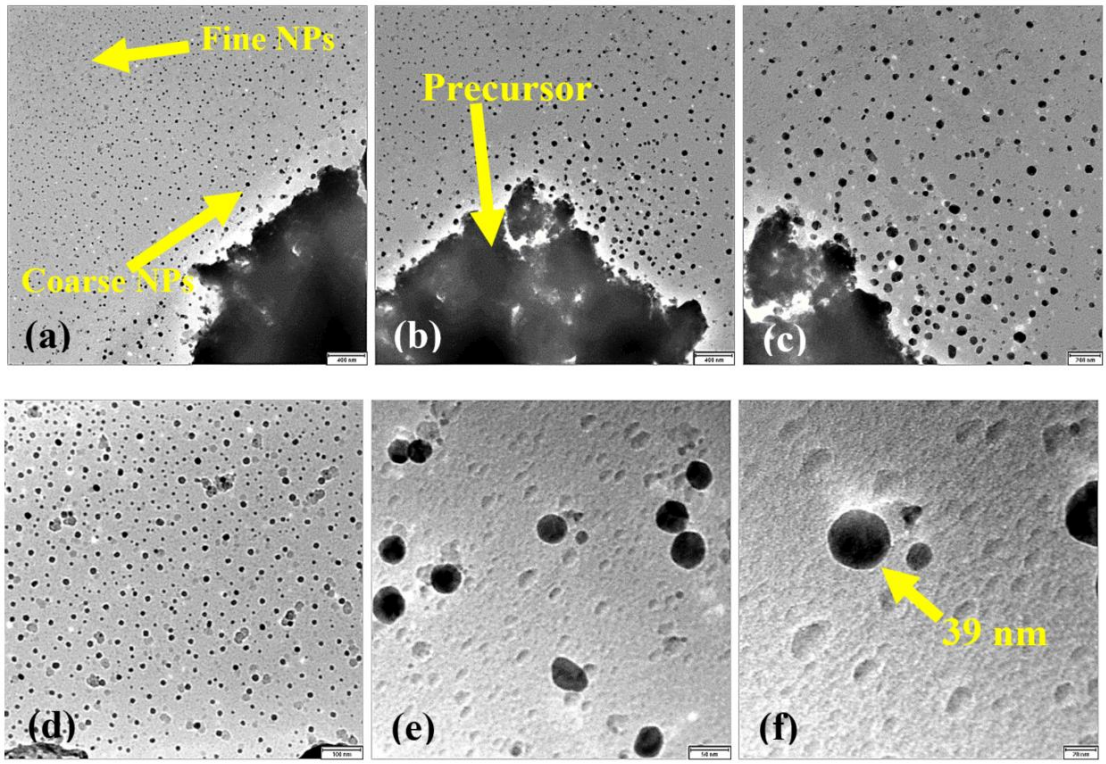

Figure 5-20: (a) to (f) show the low to high magnification images of freshly formed nanoparticles after e-irradiation with an open aperture.

5.3.3.1 EELS Results

Figure 5-21 shows the EELS spectra of the CCL before irradiation, and corresponds to Figure 5.8 which shows the cerium M-edge with two sub-peaks (i.e. M5 and M4) and oxygen K-edge. This EELS spectrum shows that the cerium M4 peak is smaller than the M5 one, as clearly seen in Figure 5-21 which indicates that the Ce is in a Ce^{3+} state.

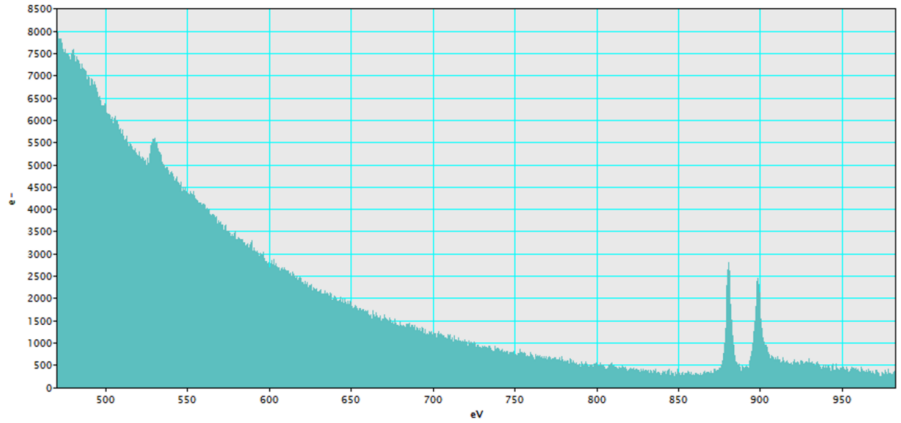

Figure 5-21: EELS spectra of CCL before irradiation.

Figure 5-22 shows the EELS spectra of CCL after irradiation near a synthesised nanostructure which shows the cerium M-edge and oxygen K-edge. The two sub-peaks indicate the same weight, possibly between cerium 3+ and 4+. In this spectrum it is very clear that the percentage of oxygen is boosted, which mean our final product of irradiation has oxide, possibly CeO_{2-x}.

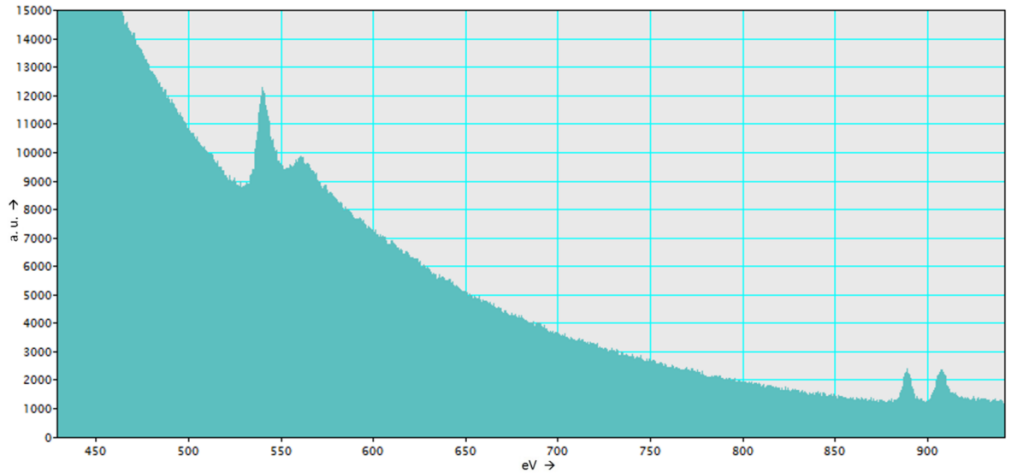

Figure 5-22: EELS spectra shows the enhancement of O K-edge after electron irradiation.

5.3.3.2 EDX Results

The EDX results corresponding to Figure 5-8 show that our precursor materials had cerium, oxygen and chlorine. The atomic percentage of EDX results can be found in Table 5-6. The results of the table show that the percentage of chlorine was approximately 50 percent and cerium was 15 percent near the rod area. The EDX results of Figure 5-9 near the round nanoparticles show that the percentage of chlorine was approximately 7.87 percent and cerium was 52 percent. These EDX results indicate a decrease in chlorine and increase in cerium percentage near many round NPs (as seen in Figure 5-9). So, the irradiation of the CCL precursor causes a decrease in percentage of chloride which means our raw materials were possibly becoming transformed into the ceria, another form of cerium oxide or cerium chloride. However, some of the EDX results show a mixture of chloride and oxygen, as seen in Figure

5-23. In this EDX spectrum, approximately equal peaks of Oxygen, cerium and chlorine were observed, which indicates that this analysis contains our raw material (i.e. CCL). Our measured results of d-spacing through lattice fringes and the FFT of TEM images also show the formation of the mixture of chloride and oxide NRs and NPs respectively during the irradiation of the CCL in TEM.

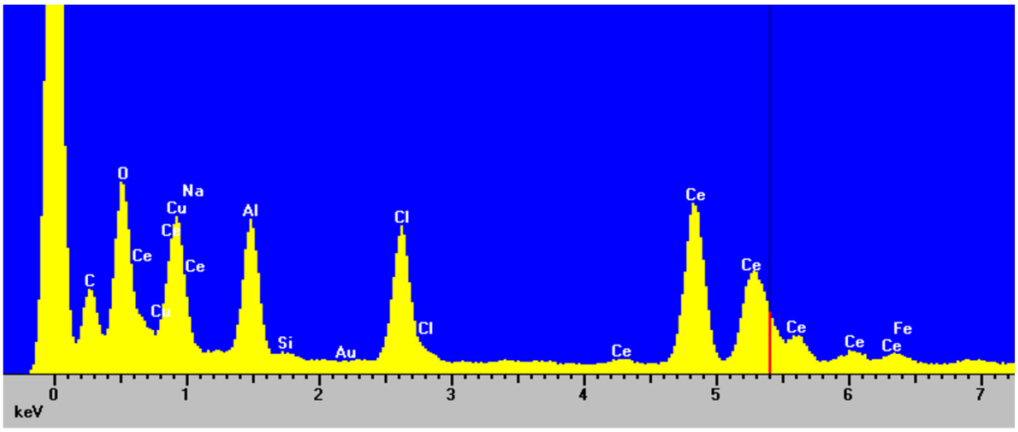

Figure 5-23: EDX results of mixture of cerium, oxygen and chloride.

Table 5-6: EDX analysis results of atomic percentages of cerium, oxygen and chlorine.

S. No.	Element	Ce	O	Cl
01	Irradiation near rods	14.24	35.56	50.20
02	Irradiation (at round nano-particles)	52	40.13	7.87

5.3.4 Discussion of CCL

The irradiation results of cerium chloride hepta hydrate (CCL) indicates that CCL is very sensitive to electron beams. It was observed that irradiation causes the formation of huge number of fresh free-standing nanostructures near adjacent carbon support film and nanorods are growing out at the edge of precursor fragments. This type of nanostructure formation corresponds to an evaporation-condensation mechanism reported earlier in the case of Ag and metal halides [80, 138]. We observed that the results of electron irradiation of cerium chloride

at 300keV show the impact of electron beam intensity on the shape of freshly formed nanoparticles: moderate intensity leads to irregular or coarse shaped nanoparticles and high intensity leads to round-shaped nanoparticles, possibly through ripening by secondary irradiation and quasi-melting.

Results have not shown the presence of the redox process during the irradiation of CCL and the final crystalline nanoparticles and nanorods contain high cerium and oxygen, and cerium and chlorine as elements respectively, as evidenced by EELS, and Ce is in a Ce^3 state. Due to this, we assumed that Ce-chloride rods and ceria particles might both form in parallel. We did not observe the formation of cerium metal during the irradiation experiment because our d-spacing data did not correspond to the d-spacing of the cerium metal. The irradiation caused the growth of thin or thick nanorods at the edge of the original precursor fragment. The same type of TiO_2 nanorods were observed by other researchers [16]. In their work they observed the reduction of TiO_2 and formation of Ti metal and then re-oxidation caused the growth of TiO_2 nanorods. However, in our case, we started with CCL and did not observe the formation of cerium metal during irradiation because our precursor contained water so there was no possibility of formation of cerium metal, so we discarded this option permanently. Alternatively, in relation to the irradiation of ceria, in the past researchers have found ceria is extremely stable and they do not find the same type of TiO_2 reaction is produced, which means ceria must behave differently when compared to TiO_2 [146]. Our thin long rods showed Bragg scattering, which means they are crystalline in nature, and for the thick rods the Bragg scattering came from the centre of each rod, which means the core area of thick rods is crystalline.

The results of high resolution images of synthesised nanostructures showed that the lattice fringes and the d-spacing measured by lattice fringes and corresponding FFT of high-resolution TEM images (as shown in Figure 5.10 and Table 5.5) matched either the planes of ceria (111)

and (200) or cerium chloride (210), (201) and (100). The results of the calculated d-spacing of nanoparticles matched the ceria and the calculated d-spacing results of rods matched cerium chloride. So, we assumed that our irradiation caused the transformation of amorphous CCL into a mixture of crystalline NPs and NRs of ceria or cerium chloride respectively. However, the EELS and EDX results confirm that chlorine still persists in the new particles, which can be round or rod-shaped. We have assumed that our EELS and EDX results may have contained some residual raw CCL material, so we observed a high percentage of chloride in our results. Furthermore, the EDX results show the reduction in the chlorine percentage near the freshly formed nanostructures with an increase of oxygen content, as well as showing a mixture of oxide and cerium chloride nanostructures. Our EDX results also shows the formation of oxide nanoparticles and cerium chloride nanorods during irradiation. This is in agreement with the d-spacing calculation from the lattice fringes and FFT of TEM images of CCL irradiation.

5.3.5 Live Irradiation-induced Shape Change

We observed that the Ce-chloride precursor was unstable under the electron beam irradiation and showed the formation of NPs and NRs and upon continuous irradiation caused the nanoparticles to change into various shapes. The same type of shape changes were observed by a group of researchers during the irradiation of LiF and CoF_2 [13, 138, 139]. Upon the irradiation of halides they observed the live formation and different shape changes of metallic Li or Co nanoparticles. Unfortunately, we did not observe the formation of freshly formed NPs, as possibly the formation process was very fast or sensitive to electron beam or it formed during the focusing of the beam. We noticed that continuous electron irradiation causes the shape changes of these NPs. We managed to successfully record the video sequence of shape changes from an NP shape whose area footprint projected volume is equal to cube, triangle and hexagon shape, as seen in Figure 5-21. Figure 5-21 (a) shows the presence of a few NPs on the top of

precursors at the start of irradiation, and continuous e- irradiation of that area containing those NPs shows the following behaviours: 1) Prolonged continuous irradiation causes small movements and a shrinkage in the diameter of NP1 and the growth of NP2 (as marked by the blue arrow in Figure 5-21 (a)). 2) More continuous irradiation causes the transformation of NP1 and NP2 into the shape whose area footprint projected volume is equal to cubic and triangle shape respectively as shown in Figure 5-21 (d). Unfortunately, during the electron irradiation of the CCL precursor in TEM 3010 we were unable to perform any chemical analysis test due to the limitations of the microscope (i.e. absence of any EDX or EELS attachments). So, we do not know the chemistry of the synthesised nano structures. The contrast between the NPs and other shapes are dark we assumed that these NPs or other shapes could be a ceria or cerium chloride.

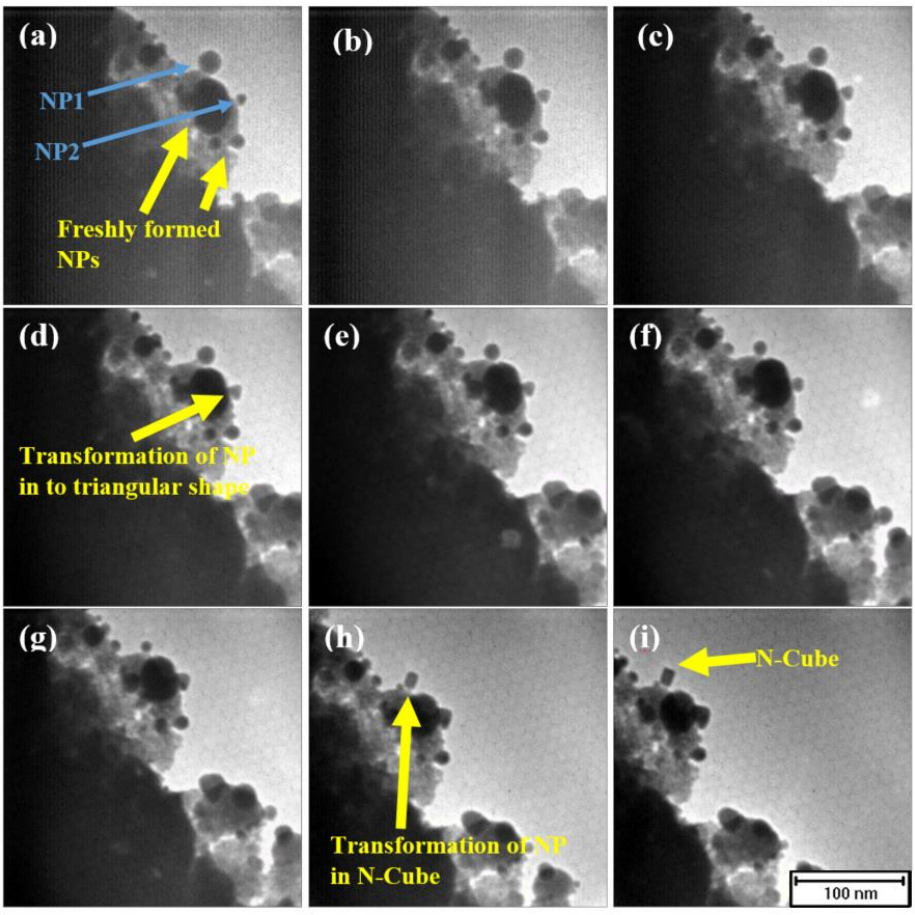

Figure 5-24: video sequence (a to i) show the shrinkage and growth of particles into shapes whose projected areas are equal to the cube of a triangle.

CHAPTER SIX

WET-CHEMICAL SYNTHESIS OF CERIA NANO STRUCTURES

6.1 Introduction

There are a variety of chemical and physicochemical synthesis methods for ceria available at high or room temperature (RT), such as chemical precipitation, hydrothermal / solvothermal process, microemulsion, sono-chemical and irradiation with laser and microwave. Yet even so, a room temperature synthesis of nano ceria has been insufficiently studied and not well understood in the literature. The synthesis of ceria nanostructures by the chemical precipitation method at room temperature has been reported superficially by one group of researchers in the past. So, in this research, our aim is to achieve a new insight into room temperature synthesis of ceria nanostructures, expanding on the work of Du et al.[144] in depth with different molarity and temperatures. The main aim is to obtain a better understanding of room temperature synthesis of ceria, as this is important for room temperature liquid cell studies of cerium compounds, and also because it includes the intermediate hydroxide phases during the synthesis process of ceria in a liquid cell. Basically, the intention is to explore the connection or relationship between the laboratory synthesis of ceria nanostructures with liquid cell and dry irradiation of cerium precursor because in all our experiments – i.e. liquid cell, dry irradiation or laboratory synthesis – water and ceria are common substances and possibly they have similar intermediate phases. Thus, the aim is to discover the relationship between water and ceria, ceria and irradiation, and cerium precursor and water. In our liquid cells we are dissolving crystalline

ceria which possibly forms an intermediate cerium hydroxide phase, and in the case of dry irradiation and laboratory synthesis we have started with amorphous material to transform this into crystalline ceria, so logically there should be a connection between them.

In this chapter, I will discuss the laboratory based chemical precipitation synthesis method of ceria nano structure at 75°C and at room temperature (i.e. 25°C) with different molarities of cerium nitrate hexahydrate and Sodium hydroide. In this synthesis method I have used the commercial hydrated salts of cerium nitrate hexahydrate purchased from Sigma-Aldrich UK, with a purity of 99.9% and sodium hydroxide, also from Sigma-Aldrich, UK, having a purity of 99.9%. In this research we have used JEOL JEM 2010-F and JEOL JEM 3010 TEMs at an acceleration voltage of 200 kV and 300kV respectively for the purpose of characterisation.

6.2 Experimental Work

6.2.1 Methods

We have selected the two temperatures (the first at 25 °C and the second at 75 °C) and two different molar ratios (1:1 and 3:1) of cerium nitrate hexa hydrate (CNH) and sodium hydroxide (SH) for the synthesis of ceria nanostructures by using a wet-chemical precipitation method [144]. To achieve the desired molar ratio, we have mixed 0.43 grams of CNH in 10 ml of water and 0.04 grams of sodium hydroxide in 10 ml of deionised water. All parameters used for the experiments are mentioned in Table 6.1.

Table 6-1: Experimental parameters for laboratory-based wet-chemical synthesis of ceria nano structures.

S. No.	Ratio Ce^{3+}: OH^-	Temperature (°C)	g- value of CNH	g- value of SH
01	1:1	25	0.43	0.04
02	1:1	75	0.43	0.04
03	3:1	25	1.30	0.04
04	3:1	75	1.30	0.04

6.2.1 Procedure

The ceria nanostructures were fabricated by the reaction of $Ce(NO_3)_3$ 6 H_2O and NaOH at 25°C and 75°C in an aqueous solution. In this method we added sodium hydroxide one drop by drop at a time into a stirred solution of cerium nitrate. The ratios used of CNH and SH were 1:1 and 3:1 at two temperatures (25 °C and 75 °C). We observed the whole stirring process of the chemical precipitation reactions and recorded the phenomenon of colour changes during the experiment, as seen in Figure 6-1. First, we started the experiment at 25 °C with a 1:1 molar ratio by adding an aqueous solution of 1M sodium hydroxide solution drop by drop into an aqueous solution of 1M cerium nitrate hexa hydrate. We observed the solution change white colour into purple and black within six minutes and after 10 minutes it had become transformed completely into light purple. After continuous stirring 30 minutes it became transformed into brown and then further transformed into a yellow-brown colour after 40 minutes. Finally, it became transformed into a yellow colour after 60 minutes of continuous stirring. We noticed, however, that a prolonged stirring of the solution until the time reached 100 minutes could not change the yellow colour. We also noticed the presence of white powdery material on the bottom of glass vial after 60 minutes of stirring. The samples of synthesised powder were washed three times with de-ionised water to remove the residual nitrate content and other by-products.

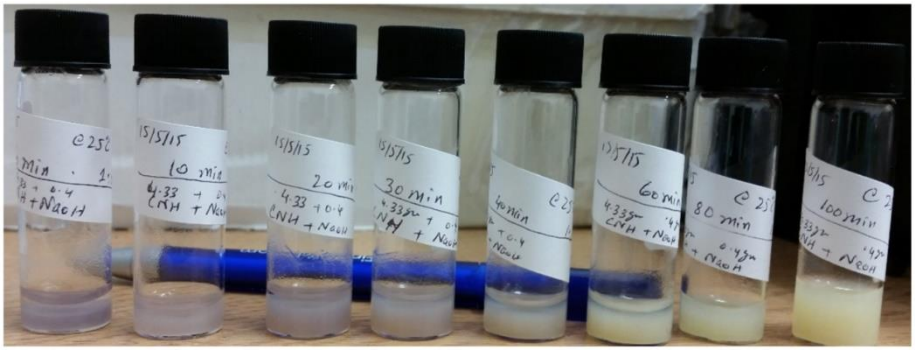

Figure 6-1: This shows the change of colour during the chemical precipitation reaction of cerium nitrate and sodium hydroxide.

We also performed the same procedure for the synthesis of ceria nano structures by using other temperatures and molar ratios of CNH and SH. Unfortunately, we did not have any images of the process of chemical precipitation reactions of colour changes as in the case of 1:1 at 25°C, but the change of colour observed with respect to the pH of the solution with the temperature and ratio during the experiment are as shown in Table 6-2.

Table 6-2: Parameters used and colour change phenomena during laboratory synthesis of Ceria NPs.

S. No.	Time (min)	At 75 °C (1:1) Colour change	At 75 °C (3:1) Colour change	At 25 °C (1:1) Colour change	At 25 °C (3:1) Colour change
01	6	Muddy (black/ brownish shade)	Muddy yellowish (light milky white)	Purple	Muddy yellowish (very light milky white)
02	10	Very light milky white	Milky white	light purple + black	Milky white
03	20	Very light milky white	Milky white	Brown	
04	30	Light milky white	Milky white	Brown + Yellow	
05	40	Milky white	Milky white	Yellow	
06	50	White (light purple shade)	Milky white	Yellow	
07	60	White (purple shade)	Milky white	Yellow	

6.3 Results

The TEM characterisation results of the laboratory-based chemical precipitation of cerium nitrate hexahydrate with sodium hydroxide were divided into four sections with respect to molar ratio and temperature.

6.3.1 Molar ratio 1:1 at 25°C

The TEM results of 1:1 CNH and SH at 25 °C indicate the successful synthesis of 2nm to 10nm size of the nano particles by using a chemical precipitation method. The low magnification TEM images of Figure 6-2 (a & b) indicates some agglomeration in between the synthesised nano particles with irregular chain like structure. These TEM images also shows some areas with weak agglomeration of nanoparticles (NPs). Moreover, the structure of the ceria nanorods is further characterized by high resolution transmission microscope (HRTEM), as shown in Figure 6-2 (c & d) which shows the fine NPs with the lattice fringes of individual particles. As can be seen in HRTEM Figure 6-2 (c & d), the majority of nanoparticles are in the range of 3 to ~5 nm in size with (111) preferred plane orientation. We have also used the FFT of the high resolution TEM images of synthesised nanoparticles to calculate the d-spacing. The results of the calculations of the d-spacing from the FFT can be seen in the Table 6-3. This table also presents the value of the lattice parameter and reciprocal of the d-spacing. We have compared the results of the d-spacing and the reciprocal of the d-spacing and lattice parameter, measured by the lattice fringes and FFT of TEM images, with the literature-based calculated value of the d-spacing, reciprocal of the d-spacing and lattice parameter of synthesised nano crystalline ceria for the (111) plane, as can be seen in Table 6-3. The calculated values of the d-spacing and lattice parameter by FFT of TEM images are <d>= 0.311 nm with a deviation +.002 and a = 0.5387 nm with a deviation (+0.004) respectively. Similarly, the calculated values of the d-spacing and lattice parameter by lattice fringes as seen in Figure 6-2 (b) are <d>= 0.310 nm with a deviation +.003 and a = 0.5370 nm with a deviation +.0057. Figure 6-3 shows the EELS spectra of synthesised nanoparticles which indicate the oxygen K-edge and cerium M-edge with their two-sub peaks, in which the cerium M5 peak is smaller and the cerium M4 peak is larger.

Table 6-3: Literature based calculated value and calculated values of lattice parameter, d-spacing and reciprocal of d-spacing from TEM images and their corresponding FFT.

Parameter / Method	a (nm) [Deviation]	d_{111}(nm) [Deviation]	$1/d_{111}$ (1/nm)	$2x1/d_{111}$ (1/nm)
Literature Value	0.5427	0.313	3.191	6.383
Calculated value by FFT	0.5387 [+0.0040]	0.311 [+0.002]	3.215	6.43
Calculated value by lattice fringe	0.5370 [+0.0057]	0.310 [+0.003]	3.225	6.451

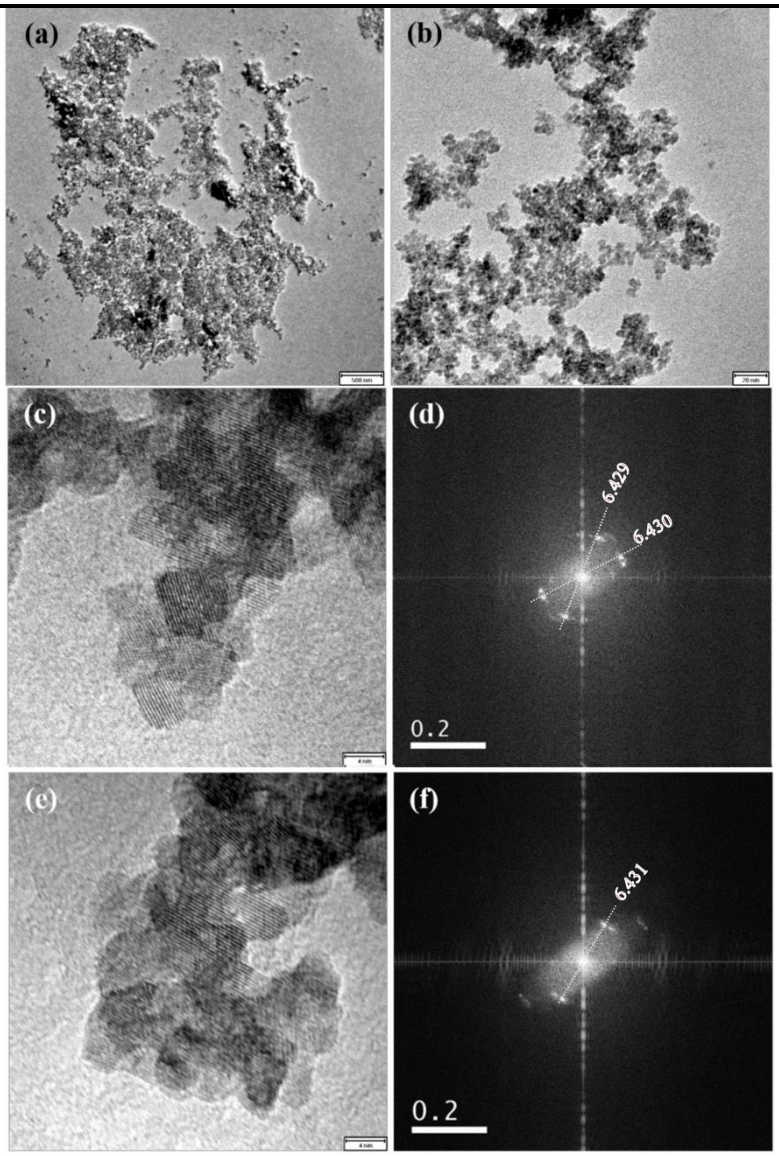

Figure 6-2: (a) and (b) show the TEM images of synthesised nanoparticles by aqueous precipitation method having an ionic ratio CNH:NaOH of 1:1 at room temperature (25 °C); (b) and (e) show the HRTEM images showing lattice fringes and (d) and (f) show the FFT of images (b) and (e). (Scale bar for (a-b) is 500 nm and for (c & e) is 4 nm)

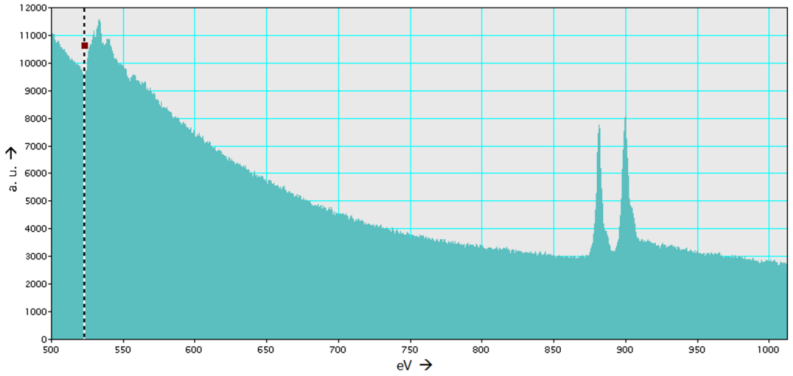

Figure 6-3: EELS spectra of synthesised nanoparticles, showing M-edge with two sub peaks.

6.3.2 Molar ratio 1:1 at 75°C

The results of 1:1 at 75°C indicate the formation of 10-40 nm sized nanoparticles and we did not observe any significant difference rather than size of particles synthesised at 25°C or 75°C, as can be seen in Figure 6-4. The TEM observation indicates that the particles appear as short small chains of 3 or 4 particles, or, significantly, individual well-dispersed particle clusters, as seen in Figure 6-4 (a & b). We noticed the presence of a few nanorods with different aspect ratio having 100 to 500 nm in size in length during characterisation in TEM. we observed that smaller nanorods were rectangular in shape and some of the large nanorods have needle shape morphology. Furthermore, the high resolution TEM images show the lattice fringes of the nano particles and nanorods, as seen in Figure 6-4 (c & d). We have again used the FFT of the high resolution TEM images of synthesised nanoparticles to calculate the d-spacing. The results of the calculations of the d-spacing from the FFT can be seen in the Table 6-4. This table also presents the value of the lattice parameter and reciprocal of the d-spacing. We have compared the results of the d-spacing and the reciprocal of the d-spacing and lattice parameter, measured by the lattice fringes and FFT of TEM images, with the literature-based calculated value of the d-spacing, reciprocal of the d-spacing and lattice parameter of synthesised nano crystalline ceria for the (111) plane, as can be seen in Table 6-4. The calculated values of the d-spacing and lattice parameter by FFT of TEM images are <d>= 0.312 nm with a deviation +.001 and a

= 0.5403 nm with a deviation (+0.0024) respectively. Similarly, the calculated values of the d-spacing and lattice parameter by lattice fringes as seen in Figure 6-2 (b) are <d>= 0.311 nm with a deviation +.002 and a = 0.5387 nm with a deviation +.0040.

Table 6-3: Literature based calculated value and calculated values of lattice parameter, d-spacing and reciprocal of d-spacing from TEM images and their corresponding FFT.

Parameter / **Method**	**a (nm) [Deviation]**	**d_{111}(nm) [Deviation]**	**$1/d_{111}$ (1/nm)**	**$2x1/d_{111}$ (1/nm)**
Literature Value	0.5427	0.313	3.191	6.383
Calculated value by FFT	0.5403 [+0.0024]	0.312 [+0.001]	3.205	6.410
Calculated value by lattice fringe	0.5387 [+0.0040]	0.311 [+0.002]	3.215	6.430

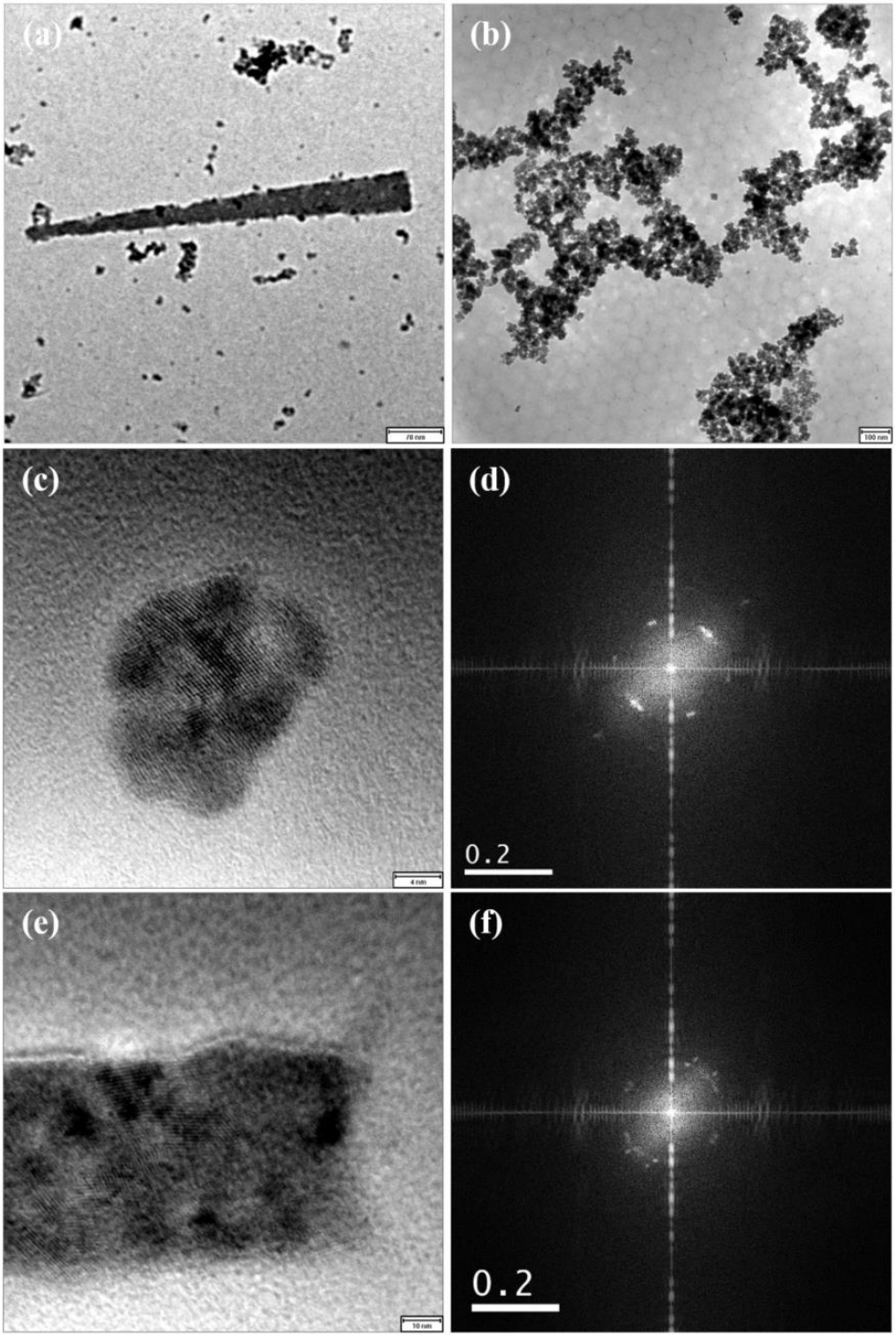

Figure 6-4: (a) and (b) show the ceria NPs with some nanorods by an aqueous precipitation method: ionic ratio (CNH:NaOH of 1:1 at 75 °C); (c) and (d) show the HRTEM image of the nanoparticles with their corresponding FFT; and (e) and (f) show the HRTEM image of the nanorods with their corresponding FFT. (Scale bar for, (a) 70nm, (b) 100 nm, (c) 4nm and (e) 10 nm)

6.3.3 Molar ratio 3:1 at 25°C

The TEM results of molar ratio 3:1 (CNH and SH) at 25°C indicates the formation of nanorods with some residual cerium nitrate, as seen in Figure 6-5. The synthesised nanorods were different aspect ratio having 40 to ∼50 nm in lateral size and 100 to ∼ 700 nm in longitudinal size. Furthermore, the high magnification image as shown in Figure 6-5 (c & d) indicates that some rods have a needle-shaped structure. We observed some residual cerium nitrate, which might be due to incomplete washing of samples, because while taking the images we observed the live changing in the matrices, possibly due to unreacted cerium nitrate. Figure 6-5 (d) shows the porous sponge type matrices indicated by a yellow arrow, and possibly these are the result of the reduction of cerium nitrate and the formation of NO_2 or H_2O or H_2 gas bubbles. The same Figure 6-5 (d) indicates that the long rods indicated by the blue arrow are crystalline from the middle and amorphous from the outer surface because the middle part has a dark contrast and other outer parts have a light contrast.

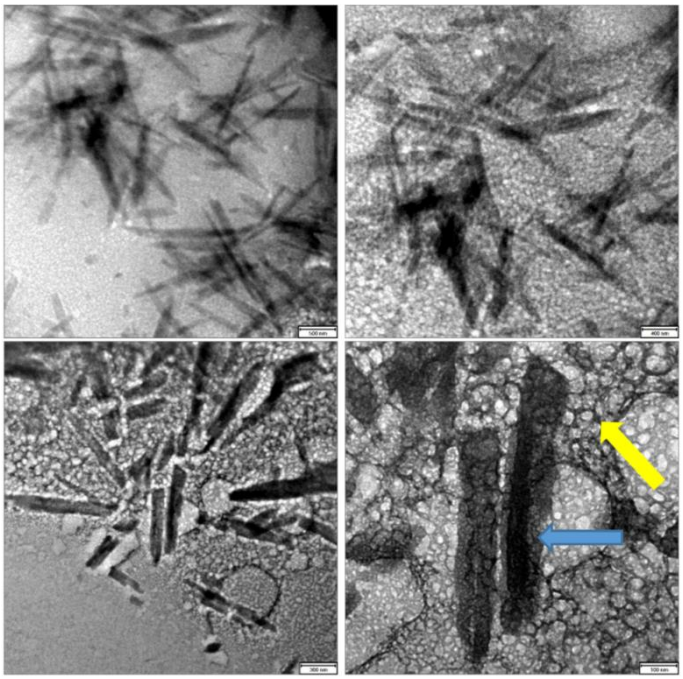

Figure 6-5: This shows the TEM images of nanorods synthesised by using an ionic ratio CNH:NaOH of 3:1 at 25 °C.

6.3.4 Molar ratio 3:1 at 75°C

The TEM results of the of the experiment at 75°C having a molar ratio (i.e. CNH:NaOH of 3:1) indicates the synthesis of the nanorods. We observed that the synthesis of the nanorods by using a molar ratio of CNH:NaOH (3:1) at 75 °C had relatively similar results at 25 °C. The high magnification images of TEM show that our synthesised nano rods were rectangular and needle in shape morphology and possibly our nanorods contain voids or cavity-like features, as shown in Figure 6.5 (d). Figure 6.5 (d) shows the formation of long needle-shaped rods having a diameter 50-200 nm and a length between 600-4000 nm, and one rod has octahedral-shaped voids in a line, mostly in the centre of the rod, highlighted by a yellow arrow. The synthesised rods have voids in the middle of rod and the tip of the rod can show a variety of shapes, including a facetted tip-shape, as well as a rectangular or rounded shape. We assumed that possibly our synthesised products were nanorods and nanotubes. Our general observations related to nanotubes are as follows:

(i) A void contrast is light in colour as compared to the matrices of nanotubes. The variation in contrast between voids and matrices is too prominent and the voids indicate that some material is missing, as compared to the matrices.

(ii) Voids are in a straight line and conform to a perfect projected capped octahedral shape.

(iii) Observed voids are both small and large in size and found at the centre, not on the surface or side face of rods.

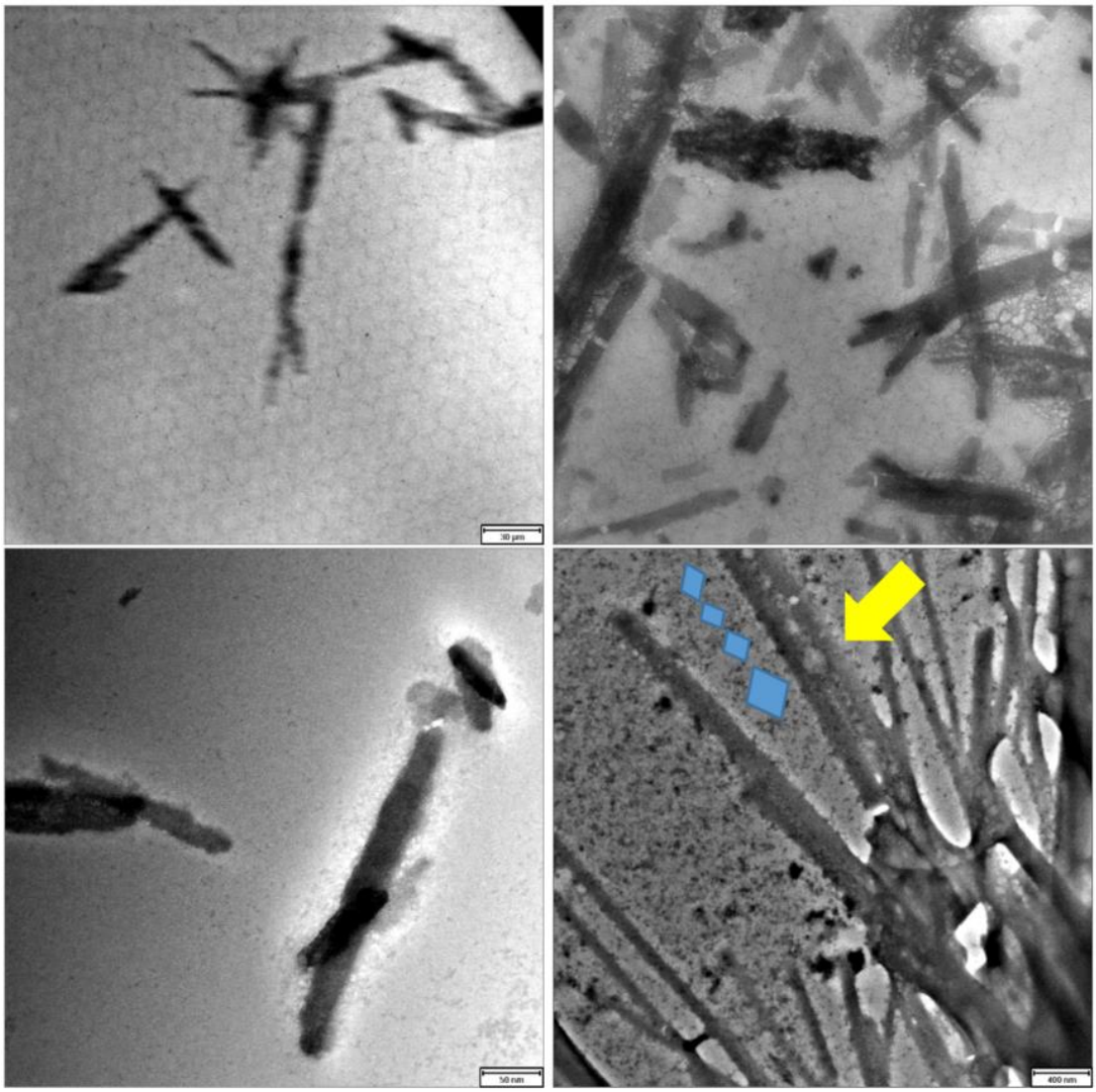

Figure 6-6: (a) to (d) show the ceria or cerium nanorods by an aqueous precipitation method: ionic ratio (CNH:NaOH of 3:1 at 75 °C). (d) indicates the void-like feature in the centre of the rods.

6.4 Discussion

In order to explore the formation mechanism of the ceria nanostructures, by using a chemical precipitation method related to the detailed morphological and structural analysis for the synthesis of nanoparticles and rod formation we were able to record the colour change of chemical precipitation reaction and we performed high resolution TEM imaging. The step by step change of colour during the chemical precipitation reaction indicates the change of pH which is almost as per the literature [147]. In addition, the final yellow colour with some white

powdery materials at the bottom of the glass vial indicates the completion of the chemical precipitation reaction because after that time we did not observe any change of colour. As can be seen from the low and high resolution TEM Figures 6.2 (c-d) and 6.3 (c-d), the synthesised nanoparticles are agglomerated and some of them are individually dispersed on the copper grid. We further characterised the individual synthesised nanoparticles and nanorods by using HRTEM, as shown in Figures 6.2 (c-d) and 6.3 (c-d). These HRTEM images shows the lattice fringes and the measured d-spacing results are matched with the d-spacing of the ceria. As compared to the previous literature, in these images the dominant fringes of the ceria nanocrystals are matched with {111} and {200}. Furthermore, we observed that the molar ratio of Ceria 3+ and hydroxide is a key factor for the synthesis of ceria nanorods and nanoparticles at room temperature. We noticed that when the molar ratio of Ceria 3+ and hydroxide was less than 3, only the agglomerated or individually dispersed nanoparticles were formed, as shown in Figure 6.2 (a-d). When the used molar ratio of Ceria 3+ and hydroxide was 3, the nanorods were formed, as shown in Figure 6.4 (a-d). We also noticed that the effect of temperature has no major influence during the synthesis of nanoparticles or nanorods. For example, at molar ratio1:1 at 25°C we noticed a higher agglomeration of nanoparticles as compared to the molar ratio 1:1 at 75°C. In our case, at both temperature ranges (i.e. 25 and 75°C) we observed a similar size of nanoparticles and nanorods except in the case of 75 °C at 3:1 where we noticed the formation of nanotubes, as seen in Figure 6.5 (d). Earlier, a group of researchers formed CeO_{2-x} nanotubes at 100°C through chemical precipitation of cerium nitrate hexahydrate with ammonium hydroxide [148]. In Figure 6.5 (d) we observed the nanorods with void-like features, some of octahedral and round shapes but rather central, almost resembling, ceria nanotubes. We called them ceria nanotubes because our rods were completely filled with empty spaces i.e. octahedral voids. This is similar to the findings of Shakthivel et al., where they observed the octahedral, roundish, rectangular and oval shaped voids and cavities mainly in

the central grain areas away from surface and grain boundaries in their ceria nanorods during in-situ irradiation at 600-800 ºC [7]. They formed nanotubes from nanorods with random octahedral shaped voids at high temperature, but in our case, we observed the same type of octahedral voids at 75 ºC without any post irradiation at high temperature. Our nanotubes had small and large voids in size, mostly at the center of the rods, as can be seen schematically in Figure 6.5 (d).

The EELS spectra of synthesized ceria NPs shows the cerium M-edge with two sub-peaks in which M4 is larger than M5, and this represents the charge valency of $Ce4^{+}$. The EELS spectra also contain oxygen K-edge which indicates the presence of oxides in our sample. Based on presence of oxygen K-edge and the charge 4+ valency, the synthesized nanoparticles are ceria nanoparticles.

The formation of rods in chapter 5 through electron beam irradiation matched with the cerium chloride instead of ceria possibly due incomplete chemical precipitation reaction. In this direct electron beam irradiation causes the direct transformation of rod via evaporation-condensation mechanism. In case of chapter 6 i.e. chemical precipitation method we have used cerium nitrate and hydroxide. On the other hand, for electron beam irradiation method (chapter 5) contain only cerium nirate or cerium chloride with few molecules of water so we have less or absent of hydroxide during electron beam irradiation which causes the incomplete reaction of precipitation. So, we formed the cerium chloride nanorods during electron beam irradiation experiemnt.

Similarly, in chapter 4 we have observed the formation of NRs from NPs during liquid cell dissolution experiments. The formed NR have dark contrast with sharp external facets. During wet chemical precipitation experiments we can formed hexagonal solid $Ce(OH)_3$ phase but this phase is unstable in air. It is possible in our liquid cell experiments because it prevents air

exposure. In liquid cell due to change of localized pH (reversal of pH near neutral) could favor an elongated ceria structure with 1D shape through oriented attachment. Our formed ceria rods have similar mass thickness as raw ceria NPs which confirm the formation of crystalline ceria NRs.

Therefore, we have assumed that the change of OH^- concentration is causes the formation of ceria nanoparticles: nanorods at 25 ºC and nanotubes at 75 ºC. The above TEM results and EELS spectra related to the synthesis of nanoparticles and the d-spacing measured by lattice fringes indicates the formation of ceria NPs. We can therefore say that in this research experiment, nano ceria and nanotubes were successfully synthesised by a simple chemical precipitation method at room temperature and 75 ºC respectively.

CHAPTER SEVEN

CONCLUSION

In-situ transmission electron microscope (TEM) electron beam induced irradiation has been shown to be a powerful technique to study the synthesis of nano structures in dry TEM and chemical transformations, new phase formation and dissolution of nanostructures in liquid cell TEM.

7.1 Liquid Cell

It has been successfully used to explore the irradiation phenomena of ceria nano structures in water by using liquid cell holder. Here, no precursor salts and no pH change other than by electrons was used. In our live study of ceria nanostructures in water in liquid cell observations were nanoparticles movement, new phase formation, needle formation, attachment and detachment of nanoparticles and dissolution of nanoparticles and nanorods were surmised in figure 7-1. Although this method is new but, previous research study showed the live observations such as nanoparticles movement, nucleation and growth, chemical transformations and dissolution in TEM related to metal.

Our novel liquid cell method was a promising technique to study the dissolution of functional ceramic i.e. ceria and we have discovered the giant dissolution (without strong acids and high temperature) of ceria nano structures were in between 10 -730 g/m^2/day much higher than (5 order) as compare to the bespoke laboratory dissolution. We have observed that there is an influence of electron beam intensity during irradiation of nanostructures in water and there is a threshold value and it depends on the energy of electron microscope and thickness of liquid

for dissolution of nanostructures. We have noted that above the threshold intensity dissolution was observed and below we have observed the movement, attachment, detachment and chain formation.

The comparison of the two type of ceria nanostructure (nanoparticles and nanorods) irradiation in liquid cell was undertaken to find out the influence of electron beam on type, size and shape of nanostructures immersed in water. It was found that the general behaviour of dissolution of nanostructure is common in order of magnitude for any size, shape and type. But if we look in detail at the quantification of dissolution of individual nanoparticle or nanorod in precise shape and size consideration, then shape has an effect. For example, dissolution rate of smaller nanoparticles was fast as compare to large nanoparticles similarly the dissolution rate of irregular shape nanorods was fast as compare to homogeneous nanorods. We have noticed that the dissolution of nanoparticles started from the edges or corners and all shapes of nanoparticles turned into the spherical shape nanoparticles. It was confirmed that the dissolution of all type of ceramic nanostructures is only specific to irradiation volume of beam impact zone and inside the zone all nano structures undergoes dissolution either slow or fast until complete disappearance during irradiation.

Furthermore, our liquid cell electron irradiation was shown to be an innovative method for the formation of new phases including round shape nanoparticles, free standing 1D needles, spikey needles and star shape objects from ceria nanoparticles. We have noticed the formation of dark contrast monodispersed round shape particles having size little bit larger than to raw ceria nanoparticles. We have observed the formation of free standing needles during parallel dissolution of NPs, spikey needles formation within the envelope of original raw nanoparticles or outside of the corner of octahedra and star shaped objects during dissolution of crystalline ceria nanoparticles.

Moreover, our liquid cell irradiation of ceria nanoparticles in water at low intensity was shown to be a promising method to study the 2D movement, attachment and de-attachment and chain formation with and without gap.

We have concluded that this process is a useful and innovative technology which provides a real-time new insight of radiation induced change of chemistry of cerium oxide nanostructure in radiolytic de-ionised water. We can employ this technique:

1. To check the durability of oxides in liquid state e.g.
    a. Long-term stability and durability of nanostructures in acidic environments,
    b. Usage of oxide coatings for nuclear engineering,
    c. Innovative options for rapid & giant room-temperature dissolution of ceria avoiding strong acids and high temperatures.
2. For tracking of NPs e.g.
    a. Chain formation to study the oriented attachment of NPs
    b. Behaviour of NPs interaction forces during movement
3. For formation of different shapes
    a. We can use this technique to study the formation of nanorods from nanoparticles.
    b. Formation of spiky needles and star shape objects from nanoparticles.

The overall conclusions of irradiation of ceria in liquid cell are very useful for science and engineering application disciplines where ceria nanoparticles are functionally employed in water, with or without exposure to radiation for example, i) oxide protective coatings of metals in irradiation environment and for protection against sea water corrosion, ii) catalysis application where dispersion and surface activation for maximum performance with water is important, iii) environmental applications where ceria reactions with water are essential for

water-pollution clean-up, iv) for chemical-mechanical polishing where ceria is an ideal slurry-dispersion element in water for glass and Si polishing, and v) CeO_2 is a non-radioactive analogue for UO_2, and reactions of ceria with water under radiation (including H_2 formation) are important for nuclear engineering.

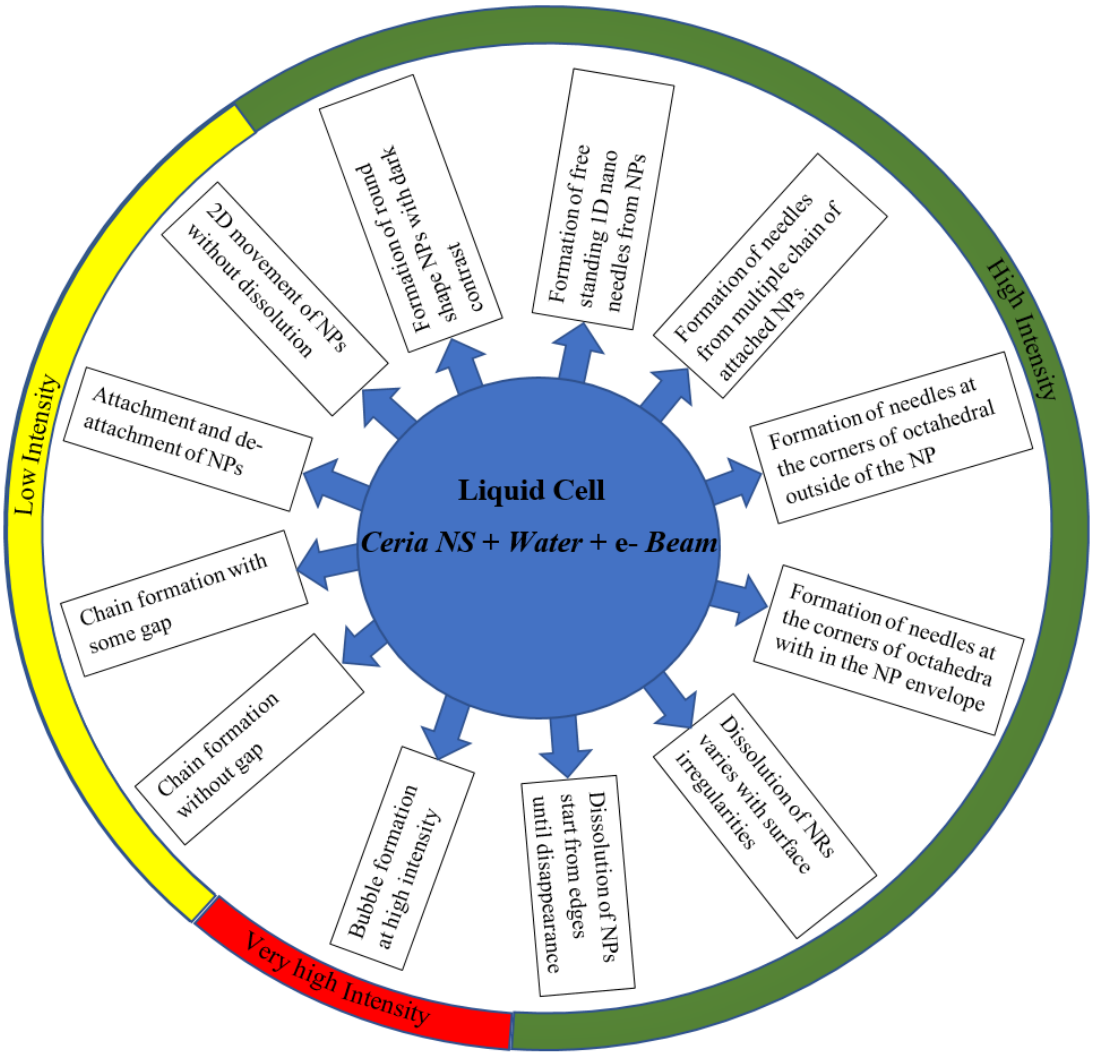

Figure 7-1: Effect of electron beam irradiation at very high, high and low intensity.

7.2 Dry Irradiation of Cerium Precursors

In conclusion, direct electron irradiation of dry cerium precursor compound chemicals has a great potential to explore the insight into redox reactions and for synthesis of nanostructures by "irradiation damage". We concluded that electron beam irradiation is a one-step and fast process to form nanostructures in TEM in comparison with other techniques which are multi step process for example laboratory based chemical precipitation synthesis. In our direct irradiation of dry cerium precursors, the formation of nanostructures i.e. nanoparticles, nanorods, needles and super thin needles was attributed to internal precipitation of precursor or condensation of precursor and growth of nanorods on precursor. Nevertheless, the HRTEM of internally precipitated and condensated nanoparticles exhibited crystalline nature and the evolution of lattice fringes of nanoparticles.

Dry TEM irradiation has overall appeared to be a very rapid but variable transformation, sometimes too fast to be tracked by analytical TEM for example irradiation of CNH samples.

7.3 Wet-Chemical Synthesis

We have successfully synthesised the ceria nanoparticles and rods by using chemical precipitation method at room temperature (RT). In addition to this we have also formed rods that shows the void or cavities like features, some of them are octahedral or round shape but inside the middle of the rod, almost resembling with the ceria nanotubes [7]. We observed that at room temperature the molar ration has major influence during synthesis of nanoparticles and nanorods because at 1:1 we observed the formation of nano particles and at 3:1 we observed the synthesis of nanorods. In conclusion, chemically induced synthesis of ceria nanostructures at RT have great diversity of shapes including round, rods, hallow rods and needles.

7.4 Joint Aspects of all Results Chapters

The following aspects are common across all major experiments, including liquid cell irradiation of ceria nanostructures, direct dry irradiation of hydrated cerium precursors and wet-chemical synthesis of ceria nanostructures at room temperature.

1. Water is playing a diverse role, either as oxygen source or as pH and redox medium during the experiments.
2. Nanorods are crucial for understanding of 1D-growth modes and anisotropies. In all chapter 4-6 we explored 1D-growth of Ce-compounds (needles in LC, nanorods and needles in cerium chloride dry irradiation and nanorods with or without voids in wet-chemical synthesis).
3. Irradiation is used either for direct (chapter 5) or indirect (chapter 4) transformation of materials, for example via radiolysis of water in chapter 4.

We have formed nano rods by different methods in chapter 4, 5 and 6. In case of chapter 6, ceria nano rods were formed due to chemical precipitation reaction of cerium nitrate and hydroxide. The formed NRs were based on the pH of the solution and molar ration of CNH and SH. But in case of chapter 5, we have formed cerium chloride nano rods by evaporation-condensation mechanism through direct electron beam irradiation of precursor. For the case of chapter 4, we have formed crystalline ceria nanorods in liquid cell experiments in TEM possibly by change of pH (down to neutral) through oriented attachment.

Mostly, dissolution rate of ceria nanoparticles and nanorods can be controlled by the dissolution reaction and can be affected by crystal size, surface roughness, crystal aggregation, water thickness, temperature, solution and solution pH.

During high intensity electron beam irradiation of ceria nano structures, the higher surface energy, increased rod tip curvature, irregular NRs and NPs dissolving sites (sharp corner or edge) of smaller nano-particles have showed the higher dissolution rate.

APPENDIX A

In this Appendix A section some results will be included that are related to the liquid cell irradiation of ceria NPs in water and which are completely unidentified and/or unknown, but they have some worthwhile information regarding the irradiation of ceria in water.

A-1 New Unidentified Phase Formation

The e- beam irradiation of ceria NPs above threshold intensity formed some new grey patches of different irregular and blob shapes. The formation of these patches was very quick, so that many times during the irradiation experiment we were not able to observe this process. We observed many times newly formed unknown light grey contrast phases, which are supposed to be an amorphous phase, as shown in Figures A-1 and A-2.

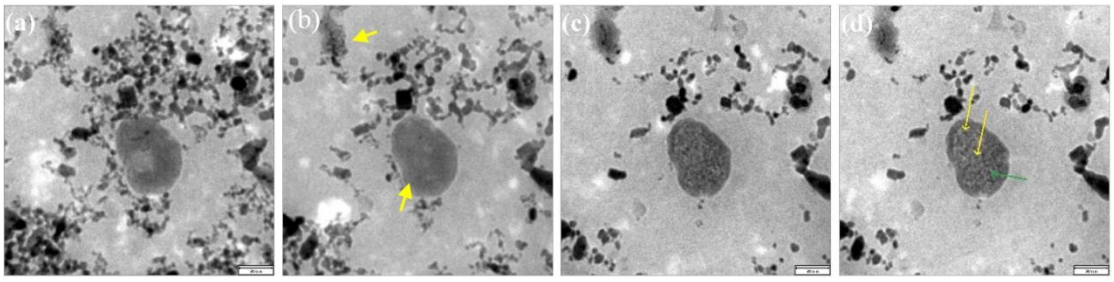

Figure A-1:(a) to (d) show the formation of an amorphous phase (scale bar of 70nm) where (b-d) are snapshots 41.6 s, 4.1 s and 4.1 s apart respectively.

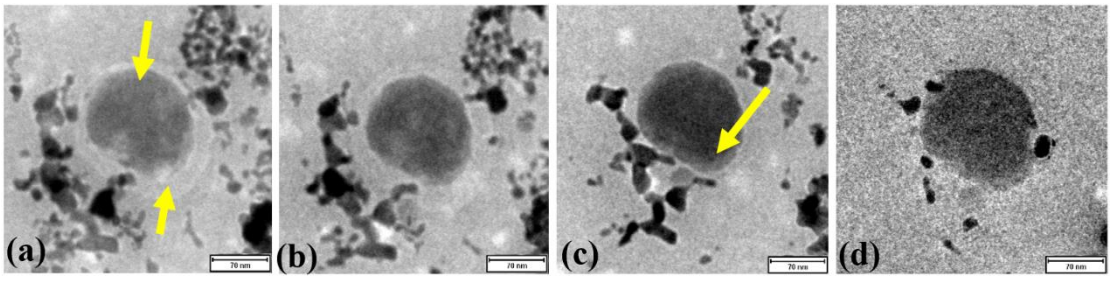

Figure A-2: (a) shows the amorphous round blob with unidentified core shell; (b) and (c) show the dissolution of surrounding NPs; and (d) shows the dissolution of one corner of round blob and two particles sitting on the blob due to movement (scale bar at 70nm) where (b-d) are snapshots 8.3 s, 33.3 s and 102.8 s, apart respectively.

The newly formed grey patches or blobs were stable under the electron beam and did not dissolve during irradiation. We do not know why this phase did not dissolve although the surrounding area did so. Figure A-1 shows the grey blob shape patch in the centre with one ceria nano particle on the top of the grey blob, which was not a precipitate. In fact, this was a Ceria NP which came from the movement of Ceria NPs in the liquid cell chamber. The left corner of Figure A-1 also shows the formation of a freshly formed amorphous grey patch from ceria NPs in the liquid cell. Figure A-2 shows the blob with a mysterious milky ring, and the ring is attached to the core of the amorphous blob. This ring has various diameters being wide from the lower side and narrow from the top of the blob, and does not look like a black and white defocused ring. We assumed these grey patches were carbon contamination formed during irradiation, but the EELS spectrum results indicated that there was no carbon k-edge present. So, we discarded this option and assumed that these amorphous phases may be a form of cerium hydroxide, based on their light atomic contrast.

A-2 Formation of Speckles

We observed that the amorphous blob of ceria had some nano speckles as can be seen in Figure A-3. Unfortunately, we were not able to capture any live sequence or phenomenon of freshly formed nano speckles during the liquid e- irradiation experiment. We assumed that these were speckles freshly formed through irradiation because they had the same dark contrast as raw ceria NPs.

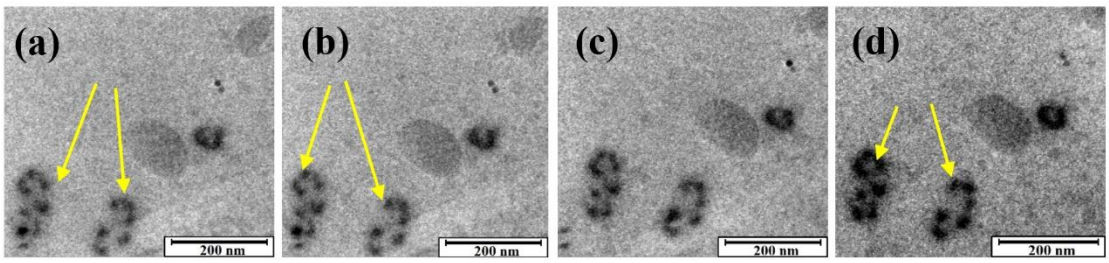

Figure A-3: (a) to (d) show the formation and enlargement of nano speckles (probably ceria) by e- irradiation (scale bar of 200nm) where (a), (b), (c) and (d) are snapshots 1.3 s apart.

A-3 Formation of Amorphous Rings

We attempted many electron irradiation experiments of ceria in water, and fortunately we managed to capture the formation of amorphous patches around the ceria NPs, as seen in Figure A-4. Figure A-4 (a) shows the presence of ceria NPs but when the electron irradiation started we observed the formation of amorphous patches around the NPs. After continuous electron irradiation we also observed the coalescence of all the neighbouring patches of NPs, which made a one bulk amorphous patch, as clearly seen in Figure A-4 (b), within 71 seconds. A prolonged electron irradiation to 150 seconds caused the dissolution of approximately all the crystalline NPs, as seen in Figure A-4 (c). We also recorded the formation of amorphous ring around the octahedral ceria NP, as shown in Figure A-4 (d) to (f). The high magnification image of Figure A-4 (d) indicates the crystalline ceria NPs without any ring or amorphous patch. After 52 seconds of irradiation we observed the formation of ring around the octahedral NP, as seen in Figure A-4 (e). With continuous irradiation of ceria nanoparticle up to 73 seconds we observed a complete circular ring around the ceria nanoparticle, which indicated the formation of a new amorphous phase because that phase shows a low contrast as compared to the crystalline ceria NPs. We assumed these observed rings were chemical rings instead of Fresnel rings (due to the defocus of the NPs).

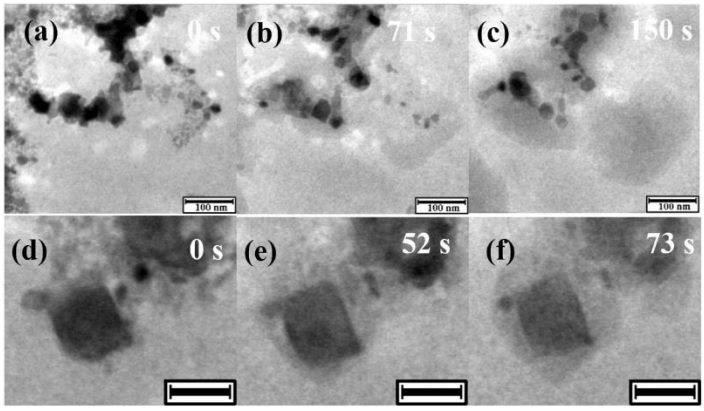

Figure A-4: Formation of a new amorphous phase during the irradiation of crystalline original ceria powder: (a-c): delocalised deposits around particle cluster, and (d-f): formation of amorphous shell around one octahedral particle.

A-4 Nano Speckles Movement

The e- irradiation of the liquid cell at below threshold intensity showed only the movement of some unidentified fine speckles. These speckles were very fine sized, less than 5 nm, and had a dendritic shape morphology, as can be seen in Figure A-5 (a). The speckles were a low contrast grey in colour which means they had a low atomic number as compared to the raw ceria NPs. These speckles were quite exotic and did not look like ceria NPs: we did not know where they came from during the experiment. In this experiment we observed the movement of these nano speckles and their displacement in liquid under electron beam irradiation in TEM, as can be seen in Figure A-5 with the yellow arrow.

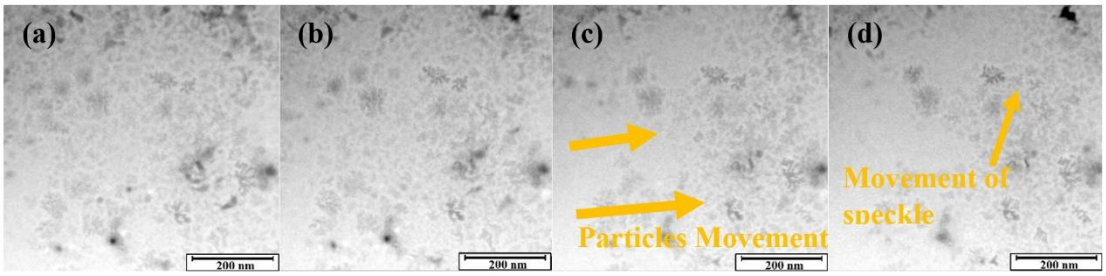

Figure A-5: (a) to (d) show the stability and movement of ceria NPs particles and speckles below threshold $I < I_{th}$ in water.

APPENDIX B

Appendix B summaries some additional results related to chapters 5 that were obtained from direct dry electron beam irradiation of cerium nitrate hexahydrate precursor.

2.1 CNH Dry Irradiation Results

The electron beam irradiation of CNH powder in 3010 TEM electron microscope, we saw the formation of nanoporous which can be seen in Figure B-1 and Figure B-2. Upon irradiation we observed the very tinny round things in Figures B-1 and B-2 on the precursor which may be a nano bubble if they are inside possibly they filled with gas or empty space. In Figure B-1 we noticed the formation of uniform gray ring outside of the precursor fragment. The atomic contrast of the ring is light as compare to the atomic contrast of ceria NPs, so we assumed that this ring is amorphous. We have observed that more irradiation causes the formation of more open empty spaces and we noticed that there is more pore volume than materials volume as seen in Figure B-1 (e).

Our CNH sample contains water molecule so during irradiation of precursor possibly they formed gases such as H_2, O, and may be NO_2. We assumed during irradiation water molecule comes out from the CNH and causes the formation of bubble or porous. It is also possible the formation of H_2 and O due to irradiation of electron beam. Or alternatively upon heating of CNH higher than the water evaporation temperature it transformed into CeO_2 and NO_2. Similarly, in our case during irradiation of CNH NO_2 may be formed, possibly due to this NO_2 we observed the formation nanoporous. Generally, the sponge type structure looks like a nanoporous material formed during irradiation of CNH.

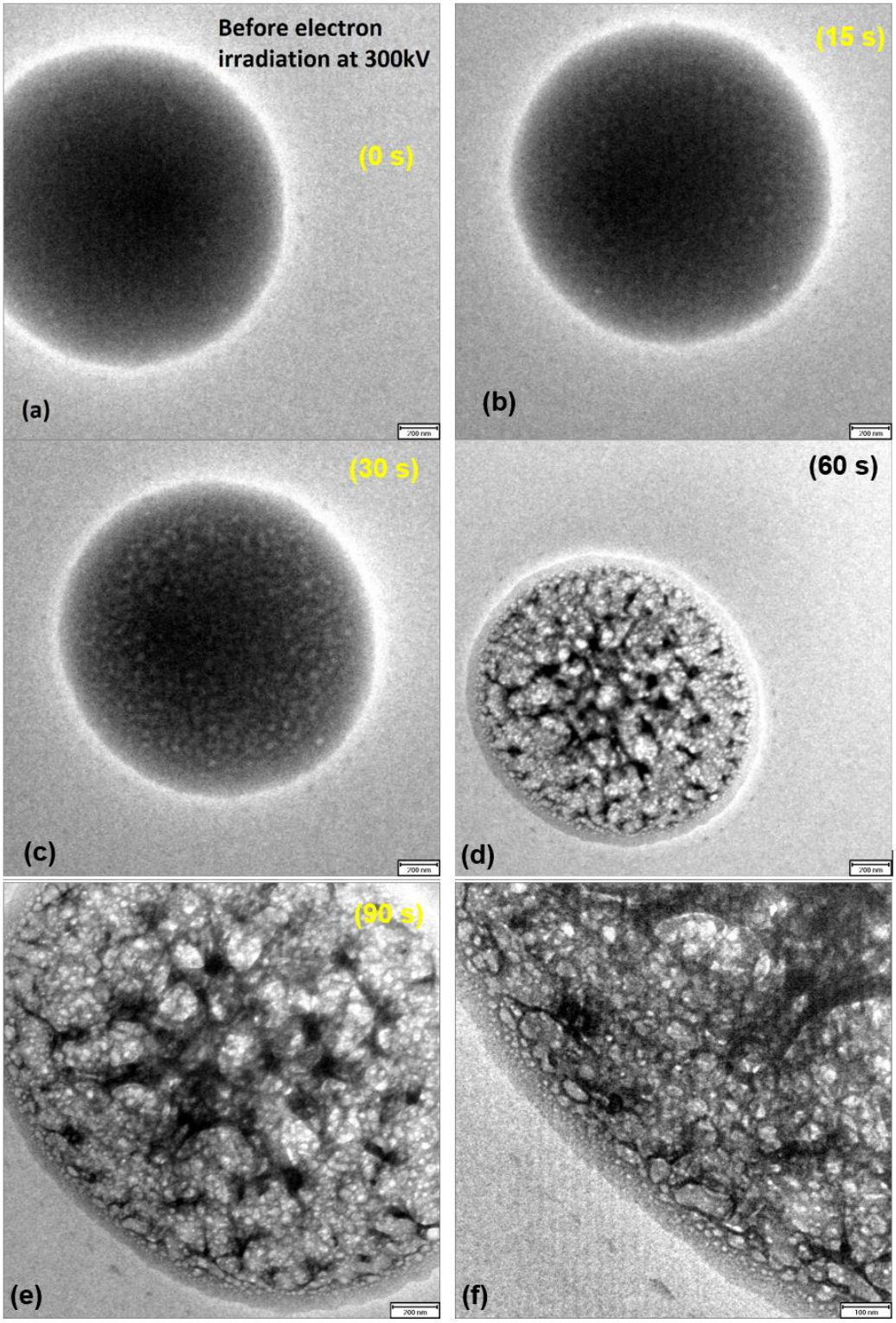

Figure B- 1: (a - f) shows the formation of nanoporous (a) precursor before irradiation (b) shows the start of nano nanoporous formation (c-f) the progressive formation and growth of nanoporous.

We noticed that the edge of CNH sample was homogenous before irradiation as seen in the Figure B-2(a). When we started irradiation, we noticed the formation of nanoporous along the thin corner edge of CNH sample after 30 seconds of electron beam irradiation as shown in Figure B-2 (b). After 60 and 90 seconds of electron irradiation, we noticed the increase in the size and number of nanoporous as shown in Figure B-2 (c) and (d).

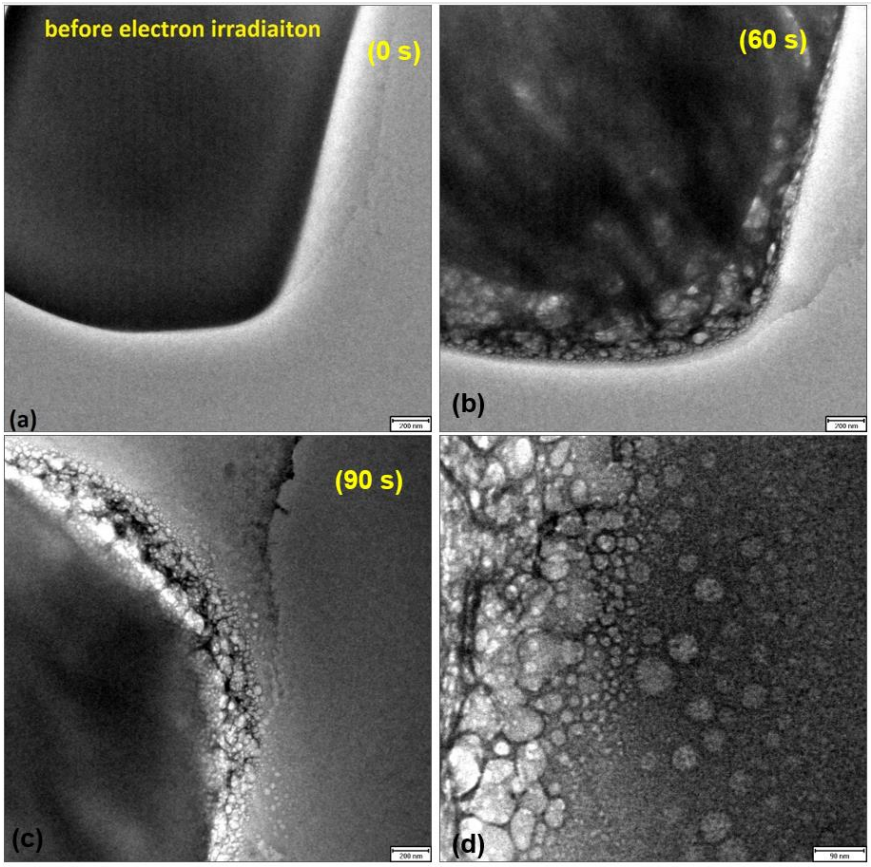

Figure B- 2: (a-d) shows the formation of nanoporous (a) before irradiation (b-d) start of nanoporous formation at the thin edge of sample with progressive growth.

APPENDIX C

UNITED STATES DEPARTMENT OF COMMERCE • Luther H. Hodges, *Secretary*
NATIONAL BUREAU OF STANDARDS • A. V. Astin, *Director*

Howard E. Swanson, M. C. Morris,
Roger P. Stinchfield, and Eloise H. Evans

Standard X-ray Diffraction Powder Patterns

Cerium(III) Chloride, $CeCl_3$ (hexagonal)

ASTM cards

Card number	Index lines	Radiation	Source
9–68	2. 56 2. 11 3. 56	Copper	Zachariasen [1] 1955

Additional published patterns

Source	Radiation
Kojima, Inoue, and Ishiyama [2]	Copper

NBS sample. The sample of cerium chloride was received as a hydrate from Lindsay Chemical Co., West Chicago, Ill. It was dried in a hydrogen chloride atmosphere at 30 mm total pressure and 450 °C for one and one-half hours. It was then transferred in a dry box to a dry atmosphere sample holder used to prepare the patterns. An analysis from Lindsay Chemical Co. showed the following impurities: less than 0.1 percent combined of lanthanum, praseodymium, and neodymium.

The sample was colorless. The indices of refraction could not be determined because the sample was too hygroscopic.

The *d*-values of the three strongest lines are: 2.586, 6.47, and 3.590A.

Structural data. Zachariasen [3] in 1948 determined that cerium chloride has the uranium chloride-type structure, the space group C^2_{6h}-$P6_3/m$ (No. 176) and $2(CeCl_3)$ per unit cell.

Lattice constants

		a	*c*
		A	*A*
1948	Zachariasen [3]	7. 451	4. 313
1951	Kojima, Inoue, and Ishiyama [2].	7. 451	4. 313
1961	National Bureau of Standards.	7. 454	4. 312 at 25 °C.

The density of cerium chloride calculated from the NBS lattice constants is 3.944 g/cm³ at 25 °C.

hkl	1961 National Bureau of Standards Cu, 1.5405 A at 25 °C	
	d	*I*
	A	
100	6. 47	84
110	3. 729	48
101	3. 590	78
200	3. 229	19
111	2. 824	51
201	2. 586	100
210	2. 438	16
002, 300	2. 153	47
211	2. 125	71
102	2. 048	16
112, 220	1. 864	19
202	1. 792	11
311	1. 654	12
212	1. 615	13
302	1. 523	17
320	1. 482	17
410	1. 408	23
321	1. 401	23
312	1. 3776	6
203	1. 3126	9
402	1. 2923	6
500	1. 2912	<1
213	1. 2382	11
412	1. 1790	9
511	1. 1192	8
323	1. 0313	11

References

[1] W. Zachariasen, The crystal structure of trichlorides, tribromides and trihydroxides of uranium and of rare earth elements, U.S. Atomic Energy Comm. TID **5212,** 157–164 (1955).
[2] T. Kojima, T. Inoue, and T. Ishiyama, Crystal structure of cerium compounds II, studies on cerium compounds by X-Ray analysis of crystal structure (Report 2), J. Electrochem. Soc. Japan **19,** 383–386 (1951).
[3] W. Zachariasen, Crystal chemical studies of the 5-f series of elements, Acta Cryst. **1,** 265–268 (1948).

National Bureau of Standards Monograph 25 — Section 1
Issued March 9, 1962

REFERENCES

[1] Birtcher, R.C. and M.A. Kirk, *In situ transmission electron microscopy investigation of radiation effects.* J. Mater. Res., 2005. **20**(7), 1654-1683.

[2] Hinks, J.A., *Transmission electron microscopy with in situ ion irradiation.* J.Mater. Res. , 2015. **30**(9), 1214-1221.

[3] Egerton, R.F., P. Li, and M. Malac, *Radiation damage in the TEM and SEM.* Micron, 2004. **35**(6), 399-409.

[4] Egerton, R.F., *Control of radiation damage in the TEM.* Ultramicroscopy, 2013. **127**, 100-8.

[5] Grogan, J.M. and H.H. Bau, *The Nanoaquarium: A platform for in situ transmission electron microscopy in liquid media.* Journal of Microelectromechanical Systems, 2010. **19**(4), 885-894.

[6] Krumeich, F., *Properties of electrons, their interactions with matter and applications in electron microscopy," Laboratory of Inorganic Chemistry, ETH Zurich, HCI-H1111, CH-8093 Zurich http://www.microscopy.ethz.ch/downloads/Interactions.pdf (Accessed April 25, 2018).* 1-23.

[7] Sakthivel, T.S., D.L. Reid, U.M. Bhatta, G. Möbus, D.C. Sayle, and S. Seal, *Engineering of nanoscale defect patterns in CeO2 nanorods via ex situ and in situ annealing.* Nanoscale, 2015. **7**, 5169-5177.

[8] Golla-Schindler, U., G. Benner, and U. Kaiser, *In situ observation of the phase transformation from calcite to lime by electron-irradiation damage investigated with high and low kV transmission electron microscopy.* 2012.

[9] Golla-Schindler, U., G. Benner, A. Orchowski, and U. Kaiser, *In situ observation of electron beam-induced phase transformation of CaCO3 to CaO via ELNES at low electron beam energies.* Microsc. & Microanal., 2014, 1-8.

[10] Möbus, G., J. Tsai, X.J. Xu, P. Bingham, and G. Yang, *Nanobead formation and nanopatterning in glasses.* Microsc Microanal 2008. **14**(2), 434-435.

[11] Möbus, G., M. Ojovan, S. Cook, J. Tsai, and Y. Guang, *Nano-scale quasi-melting of alkali-borosilicate glasses under electron irradiation* Journal of Nuclear Materials, 2010. **396**, 264-271.

[12] Jiang, N., *Damage mechanisms in electron microscopy of insulating materials.* J. Phys. D: Appl. Phys. 46 (2013) 305502, 2013. **46**(305502), 1-11.

[13] Gnanavel, T. and G. Moebus, *In situ synthesis of cobalt nanocrystal hierarchies in a transmission electron microscope.* J Nanopart Res., 2012. **14**(683), 2-12.

[14] Ghatak, J., W. Guan, and G. Moebus, *In situ TEM observation of lithium nanoparticle growth and morphological cycling.* Nanoscale, 2012, 4, 1754, 2012. **4**, 1754-1759.

[15] Garvie, L.A.J. and P.R. Buseck, *Determination of Ce4+ /Ce3+ in electron-beam-damaged CeO2 by electron energy-loss spectroscopy.* Journal of Physics and Chemistry of Solids 1999. **60**, 1943–1947.

[16] Chee, S.W., S. Sivaramakrishnan, R. Sharma, and J.-M. Zuo, *Electron-Beam-Induced Growth of TiO2 Nanostructures.* Microsc. Microanal. , 2011. **17**, 274-278.

[17] Siegel, R.W., *Nanostructured materials mind over matter.* Nanostructured Materials 1993. **3**, 1-18.

[18] Koch, C.C., *Nanostructured materials: processing, properties and application,* 2nd ed ed. G.E. McGuire. 2007, William Andrew, Inc.

[19] Bandyopadhyay, *Nano Materials* 2008, New Age International (P) Ltd.

[20] Lewis, L.N., *Chemical Catalysis by Colloids and Clusters.* Chemical Reviews, American Chemical Society, 1993. **93**(8), 2693-2730.
[21] Wang, Z.L., *Characterization of nanophase materials*. 2000, Wiley VCH.
[22] Edelstein, A. and R. Cammaratra, *Nanomaterials: synthesis, properties and applications,* ed. A. Edelstein and R. Cammaratra. 1998, Institute of Physics Publishing.
[23] Rao, C.N.R. and A.K. Cheetham, *Science and technology of nanomaterials: current status and future prospects.* J. Mater. Chem., 2011. **11**, 2887–2894.
[24] Rao, C.N.R., A. Muller, and A.K. Cheetham, *The chemistry of nanomaterials synthesis, properties and applications,* ed. C.N.R. Rao, A. Muller, and A.K. Cheetham. 2004, Willey-VCH.
[25] Lai, S.L., J.Y. Guo, V. Petrova, G. Ramanath, and L.H. Allen, *Size-dependent melting properties of small Tin particles: nanocalorimetric measurements.* Physical Review Letters, 1996. **77**(1).
[26] Zhang, M., M.Y. Efremov, F. Schiettekatte, E.A. Olson, A.T. Kwan, S.L. Lai, T. Wisled er, J.E. Greene, and L.H. Allen, *Size-dependent melting point depression of nanostructures: Nanocalorimetric measurements.* Physical Review B, 2000. **62**(15), 548-557.
[27] El-Sayed, M.A., *Some interesting properties of metals confined in time and nanometer space of different shapes.* Accounts of Chemical Research, American Chemical Society, 2001. **34**(4), 257-264.
[28] Fedlheim, D.L. and C.A. Foss, *Metal nanoparticles: synthesis, characterization, and applications*, ed. D.L. Fedlheim and C.A. Foss. 2002, Marcel Dekker, Inc., New York.
[29] Fernandez-Garcıa, M., A. Martınez-Arias, J.C. Hanson, and J.A. Rodriguez, *Nanostructured oxides in chemistry: characterization and properties.* Chem. Rev., 2004. **104**, 4063-4104.
[30] Rodriguez, J.A. and M. Fernandez-Garcıa, *Synthesis, properties, and aplication of oxide nanomaterials*. 2007, John Wiley & Sons, New Jersey.
[31] Zhai, T., X. Fang, M. Liao, X. Xu, H. Zeng, B. Yoshio, and D. Golberg, *A comprehensive review of one-dimensional metal-oxide nanostructure photodetectors.* Sensors 2009. **9**, 6504-6529.
[32] Vaseashta, A., M. Vaclavikova, S. Vaseashta, G. Gallios, P. Roy, and O. Pummakarnchana, *Nanostructures in environmental pollution detection, monitoring, and remediation.* Science and Technology of Advanced Materials, 2007. **8**, 47-59.
[33] Bhushan, B., *Hand book of nano technology* ed. B. Bhushan. 2004, Springer, Springer-Verlag Berlin Heidelberg, Germany.
[34] Saji, V.S. and J. Thomas, *Nanomaterials for corrosion control.* Current Science, 2007. **92**(1), 51-55.
[35] Heiz, U. and W.-D. Schneider, *Nanoassembled model catalysts.* J. Phys. D: Appl. Phys. , 2000. **33**, 85-102.
[36] Lu, A.H., E.L. Salabas, and F. Schüth, *Magnetic nanoparticles: synthesis, protection, functionalization, and application.* Angew. Chem. Int. Ed., 2007. **46**, 1222-1244.
[37] Amin, M.T., A.A. Alazba, and U. Manzoor, *A review of removal of pollutants from water/wastewater using different types of nanomaterials.* Advances in Materials Science and Engineering, 2014. **2014**, 1-24.
[38] Veaux, S.C.D.L. and e. al., *Method of producing nanoparticles using a evaporation-condensation process with a reaction chamber plasma reactor system* in *US Patent*, US, Editor. 2010, E. I. du Pont de Nemours and Company, Wilmington, DE (US): USA.
[39] El-Nour, K.M.M.A., A.a. Eftaiha, A. Al-Warthan, and R.A.A. Ammar, *Synthesis and applications of silver nanoparticles.* Arabian Journal of Chemistry 2010. **3**, 135–140.

[40] Iravani, S., H. Korbekandi, S.V. Mirmohammadi, and B. Zolfaghari, *Synthesis of silver nanoparticles: chemical, physical and biological methods.* Research in Pharmaceutical Sciences, 2014. **9**(6), 385-406.

[41] Kruis, F.E., H. Fissan, and B. Rellinghaus, *Sintering and evaporation characteristics of gas-phase synthesis of size-selected PbS nanoparticles.* Mater Sci Eng B., 2000. **69**, 329-334.

[42] Nadagouda MN, Speth TF, and V. R, *Microwaveassisted green synthesis of silver nanostructures.* Acc Chem Res., 2011. **44**, 469−478.

[43] Zawadzki, M., *Preparation and characterization of ceria nanoparticles by microwave-assisted solvothermal process.* Journal of Alloys and Compounds 2008. **454**, 347–351.

[44] Link, S., C. Burda, B. Nikoobakht, and M.A. El-Sayed, *Laser-Induced shape changes of colloidal gold nanorods using femtosecond and nanosecond laser pulses.* J. Phys. Chem. B, 2000. **104**, 6152-6163.

[45] Takami, A., H. Kurita, and S. Koda, *Laser-induced size reduction of noble metal particles.* J. Phys. Chem. B, 1999. **103**, 1226-1232.

[46] Yeh, M.-S., Y.-S. Yang, Y.-P. Lee, H.-F. Lee, Y.-H. Yeh, and C.-S. Yeh, *Formation and characteristics of Cu colloids from CuO powder by laser irradiation in 2-Propanol.* J. Phys. Chem. B, 1999. **103**, 6851-6857.

[47] Dolgaev, S.I., A.V. Simakin, V.V. Voronov, G.A. Shafeev, and F. Bozon-Verduraz, *Nanoparticles produced by laser ablation of solids in liquid environment.* Applied Surface Science, 2002. **186**, 546-551.

[48] Araujo, V.D., W. Avansi, H.B.d. Carvalho, M.L. Moreira, E. Longo, C. Ribeiro, and M.I.B. Bernardi, *CeO2 nanoparticles synthesized by a microwave-assisted hydrothermal method: evolution from nanospheres to nanorods.* CrystEngComm, , 2012. **14**, 1150–1154.

[49] Wang, Z.L. and X. Feng, *Polyhedral Shapes of CeO2 Nanoparticles.* J. Phys. Chem. B 2003. **107**, 13563-13566.

[50] Stennett, M.C., C.L. Corkhill, L.A. Marshall, and N.C. Hyatt, *Preparation, characterisation and dissolution of a CeO2 analogue for UO2 nuclear fuel.* Journal of Nuclear Materials 2013. **432**, 182–188

[51] Bumajdad, A., J. Eastoe, and A. Mathew, *Cerium oxide nanoparticles prepared in self-assembled systems.* Advances in Colloid and Interface Science, 2009. **147-148**, 56-66.

[52] Mogensen, M., N.M. Sammes, and G.A. Tompsett, *Physical, chemical and electrochemical properties of pure and doped ceria.* M. Mogensen et al. / Solid State Ionics 2000. **129**, 63 –94.

[53] Zhang, F., P. Wang, J. Koberstein, S. Khalid, and S.-W. Chan, *Cerium oxidation state in ceria nanoparticles studied with X-ray photoelectron spectroscopy and absorption near edge spectroscopy.* Surface Science, 2004. **563**(1-3), 74-82.

[54] Esch, F., S. Fabris, L. Zhou, T. Montini, C. Africh, P. Fornasiero, G. Comelli, and R. Rosei, *Electron Localization Determines Defect Formation on Ceria Substrates.* SCIENCE, 2005. **309**(5735), 752-755.

[55] Schubert, D., R. Dargusch, J. Raitano, and S.-W. Chan, *Cerium and yttrium oxide nanoparticles are neuroprotective.* Biochemical and Biophysical Research Communications 2006. **342**, 86–91.

[56] Zhang, D., X. Du, L. Shia, and R. Gao, *Shape-controlled synthesis and catalytic application of ceria nanomaterials.* Dalton Trans., 2012. **41**, 14455-14475.

[57] Sayle, T.X.T., S.C. Parker, and C.R.A. Catlow, *Surface oxygen vacancy formation on CeO2 and its role in the oxidation of carbon monoxide.* J. Chem. Soc., Chem. Commun. , 1992. **0**, 977-978

[58] Jiang, Y., J.B. Adams, and M.v. Schilfgaarde, *Density-functional calculation of CeO2 surfaces and prediction of effects of oxygen partial pressure and temperature on stabilities.* The Journal of Chemical Physics, 2005. **123**, 064701 (1-10).

[59] Fronzi, M., A. Soon, B. Delley, E. Traversa, and C. Stampfl, *Stability and morphology of cerium oxide surfaces in an oxidizing environment: A first-principles investigation.* The Journal of Chemical Physics, 2009. **131**, 104701 (1-16).

[60] Sayle, D.C., S.A. Maicaneanu, and G.W. Watson, *Atomistic models for CeO2(111), (110), and (100) nanoparticles, supported on Yttrium-stabilized Zirconia.* J. Am. Chem. Soc., 2002. **124**(38), 11429-11439.

[61] Jiang, Y., J.B. Adams, and M.v. Schilfgaarde, *Theoretical study of environmental dependence of oxygen vacancy formation in CeO2.* Applied Physics letters, 2005. **87**, 141917 (1-3).

[62] Laha, S.C. and R. Ryoo, *Synthesis of thermally stable mesoporous cerium oxide with nanocrystalline frameworks using mesoporous silica templates.* Chem. Commun. , 2003, 2138–2139.

[63] Wang, H., J.-J. Zhu, J.-M. Zhu, X.-H. Liao, S. Xu, T. Dinga, and H.-Y. Chen, *Preparation of nanocrystalline ceria particles by sonochemical and microwave assisted heating methods.* Phys. Chem. Chem. Phys., 2002. **4**, 3794-3799.

[64] Masui, T., K. Fujiwara, K.-i. Machida, and G.-y. Adachi, *Characterization of Cerium(IV) Oxide Ultrafine Particles Prepared Using Reversed Micelles.* Chem. Mater. , 1997. **9**, 2197-2204.

[65] Na, T., L.J. Jingyue, and S. Wenjie, *Tuning the shape of ceria nanomaterials for catalytic applications.* Chinese Journal of Catalysis, 2013. **34**, 838–850.

[66] Sun, C., H. Liab, and L. Chen, *Nanostructured ceria-based materials: synthesis, properties, and applications.* Energy Environ. Sci., 2012. **5**, 8475-8505.

[67] Celardo, I., E. Traversa, and L. Ghibelli, *Cerium oxide nanoparticles: a promise for applications in therapy.* Journal of Experimental Therapeutics and Oncology, 2011. **9**(1), 47-51.

[68] Karakoti, A.S., N.A. Monteiro-Riviere, R. Aggarwal, J.P. Davis, R.J. Narayan, W.T. Self, J. McGinnis, and S. Seal, *Nanoceria as antioxidant: synthesis and biomedical applications.* Biological Materials Science, JOM, 2008. **60**(3), 33-37.

[69] Das, M., S. Patil, N. Bhargava, J.F. Kang, L.M. Riedel, S. Seal, and J.J. Hickman, *Auto-catalytic ceria nanoparticles offer neuroprotection to adult rat spinal cord neurons.* Biomaterials, 2007. **28**(10), 1918-1925.

[70] Tarnuzzer, R.W., J. Colon, S. Patil, and S. Seal, *Vacancy engineered ceria nanostructures for protection from induced cellular damage.* Nano Letters, 2005. **5**(12), 2573-2577.

[71] Ouyang, Z., M.K. Mainali, N. Sinha, G. Strack, Y. Altundal, Y. Hao, T.A. Winningham, E. Sajo, J. Celli, and W. Ngwa, *Potential of using cerium oxide nanoparticles for protecting healthy tissue during accelerated partial breast irradiation (APBI).* Phys Med, 2016. **32**(4), 631-635.

[72] Florian, B., *In-situ electron microscopy at high resolution*. 2008, World Scientific Publishing Co. Pte. Ltd., Singapore.

[73] Ferreira, P.J., K. Mitsuishi, and E.A. Stach, *In situ transmission electron microscopy.* Mrs Bulletin, 2008. **33**

[74] Hinks, J.A., *A review of transmission electron microscopes with in situ ion irradiation.* Nuclear Instruments and Methods in Physics Research B 2009. **267**, 3652–3662.

[75] Kim, J.U., S.H. Cha, K. Shin, and e. al., *Synthesis of gold nanoparticles from Gold(I)−alkanethiolate complexes with supramolecular structures through electron beam irradiation in TEM* J. Am. Chem. Soc. , 2005. **127**, 9962–9963.

[76] Williams, D.B. and C.B. Carter, *Transmission electron microscopy*. 1996, Plenum Press, New York.

[77] Cho, S.O., H.Y. Jun, and S.K. Ahn, *A novel route to three diensionall ordered macroporous polymers by electron irradiation of polymer colloids.* Adv. Mater., 2005. **17**(01).

[78] Cho, S.O., E.J. Lee, H.M. Lee, J.G. Kim, and Y.J. Kim, *Controlled Synthesis of Abundantly Branched, Hierarchical Nanotrees by Electron Irradiation of Polymers.* Adv. Mater., 2006. **18**, 60–65.

[79] Li, Y., Y.N. Kim, E.J. Lee, W.P. Cai, and S.O. Cho, *Synthesis of silver nanoparticles by electron irradiation of silver acetate.* Nuc. Instru. & Meth. in Phys. Research B, 2006. **251**, 425–428.

[80] Li, K. and F.-S. Zhang, *A novel approach for preparing silver nanoparticles under electron beam irradiation.* J Nanopart Res 2010. **12**, 1423-1428.

[81] Sepulveda-Guzman, S., N. Elizondo-Villarreal, D. Ferrer, and e. al., *In situ formation of bismuth nanoparticles through electron-beam irradiation in a transmission electron microscope.* Nanotechnology 2007. **18**, 335604–335609.

[82] Fortner, J.A. and E.C. Buck, *The chemistry of the light rareearth elements as determined by electron energy loss spectroscopy*. Appl. Phys. Lett. , 1996. **68**(26), 3817-3819.

[83] Grogan, J.M., L. Rotkina, and H.H. Bau1, *In situ liquid-cell electron microscopy of colloid aggregation and growth dynamics.* Physical Review E 2011. **83**(061405), 1-5.

[84] Abrams, I.M. and J.W. McBain, *A closed cell for electron microscopy.* J Appl. Phys. , 1944. **15**, 607–609

[85] Nishijima, K., J. Yamasaki, H. Orihara, and N. Tanaka, *Development of microcapsules for electron microscopy and their application to dynamical observation of liquid crystals in transmission electron microscopy.* Nanotechnology 2004. **15**, S329–S332.

[86] Mohanty, N., M. Fahrenholtz, A. Nagaraja, D. Boyle, and V. Berry, *Impermeable graphenic encasement of bacteria.* Nano Lett., 2011. **11**, 1270–1275.

[87] De Jonge, N. and F.M. Ross, *Electron microscopy of specimens in liquid.* Nature Nanotechnology, 2011. **6**, 695-704.

[88] Alsem, D., R. Unocic, G. Veith, K. More, and N. Salmon, *Transmission electron microscopy of nano-scale materials in liquid and gas environments.* Hummingbird Scientific.

[89] Abellan, P., T.J. Woehl, L.R. Parent, N.D. Browning, J.E. Evansc, and I. Arslan, *Factors influencing quantitative liquid (scanning) transmission electron microscopy.* Chem. Commun., 2014. **50**, 4873-4880.

[90] Williamson, M.J., R.M. Tromp, P.M. Vereecken, R. Hull, and F.M. Ross, *Dynamic microscopy of nanoscale cluster growth at the solid–liquid interface.* Nature Materials 2003. **2**, 532-536.

[91] Zheng, H., S.A. Claridge, A.M. Minor, A.P. Alivisatos, and U. Dahmen, *Nanocrystal diffusion in a liquid thin film observed by in situ transmission electron microscopy.* Nano Letters, 2009. **9**(6), 2460-2465.

[92] Zheng, H., R.K. Smith, Y.-w. Jun, C. Kisielowski, U. Dahmen, and A.P. Alivisatos, *Observation of Single Colloidal Platinum Nanocrystal Growth Trajectories.* Science Reports, 2009. **324**.

[93] Evans, J.E., K.L. Jungjohann, N.D. Browning, and I. Arslan, *Controlled Growth of Nanoparticles from Solution with In Situ Liquid Transmission Electron Microscopy.* Nano Lett. , 2011. **11**, 2809–2813.

[94] Li, D., M.H. Nielsen, J.R.I. Lee, C. Frandsen, J.F. Banfield, and J.J.D. Yoreo, *Direction-Specific Interactions Control Crystal Growth by Oriented Attachment.* Science Reports, 2012. **336**, 1014-1018.

[95] Park, J., H. Zheng, W.C. Lee, P.L. Geissler, E. Rabani, and A.P. Alivisatos, *Direct observation of nanoparticle superlattice formation by using liquid cell transmission electron microscopy.* ACS Nano, 2012. **6**(3), 2078-2085.

[96] Noh, K.W., Y. Liu, L. Sun, and S.J. Dillon, *Challenges associated with in-situ TEM in environmental systems: The case of silver in aqueous solutions.* Ultramicroscopy 2012. **116**, 34–38.

[97] Katayama, T., M. Nakauma, S. Todoriki, G.O. Phillips, and M. Tad, *Radiation-induced polymerization of gum arabic (Acacia senegal) in aqueous solution.* Food Hydrocolloids, 2006. **20**, 983-989.

[98] Schneider, N.M., M.M. Norton, B.J. Mendel, J.M. Grogan, F.M. Ross, and H.H. Bau, *Electron−water interactions and implications for liquid cell electron microscopy.* J. Phys. Chem. C 2014. **118**, 22373-22382.

[99] Woehl, T.J., K.L. Jungjohann, J.E. Evans, I. Arslan, W.D. Ristenpart, and N.D. Browning, *Experimental procedures to mitigate electron beam induced artifacts during in situ fluid imaging of nanomaterials.* Ultramicroscopy, 2013. **127**, 53-63.

[100] Caër, S.L., *Water radiolysis: influence of oxide surfaces on H2 production under ionizing radiation.* Water, 2011. **3**, 235-253.

[101] Poseidon. *In situ Poseidon 210 liquid flow TEM holder*. 2015; Available from: http://www.protochips.com/products/poseidon.html.

[102] Radisic, A., P.M. VEREECKEN, J.B. Hannon, P.C. Searson, and F.M. Ross, *Quantifying electrochemical nucleation and growth of nanoscale clusters using real-time kinetic data.* Nano letters, 2006. **6**(2), 238-242.

[103] Radisic, A., F.M. Ross, and P.C. Searson, *In situ study of the growth kinetics of individual island electrodeposition of copper.* J Phys Chem B 2006. **110**(15), 7862–7868.

[104] Nielsen, M.H., D. Li, H. Zhang, S. Aloni, T.Y.-J. Han, C. Frandsen, J. Seto, J.F. Banfield, H. Cölfen, and J.J.D. Yoreo, *Investigating Processes of Nanocrystal Formation and Transformation via Liquid Cell TEM.* Microscopy and Microanalysis, 2014. **20**, 425–436.

[105] Yoreo, J.D., *Crystal nucleation: more than one pathway.* Nat. Mater. , 2013. **12**, 284–285.

[106] Grogan, J.M., N.M. Schneider, F.M. Ross, and H.H. Bau, *Bubble and pattern formation in liquid induced by an electron beam.* Nano Lett, 2014. **14**(1), 359-64.

[107] Chee, S.W., S.H. Pratt, K. Hattar, D. Duquette, F.M. Rossc, and R. Hulla, *Studying localized corrosion using liquid cell transmission electron microscopy.* Chem. Commun., 2015. **51**, 168-171.

[108] Jiang, Y., G. Zhu, F. Lin, H. Zhang, C. Jin, J. Yuan, D. Yang, and Z. Zhang, *In situ study of oxidative etching of palladium nanocrystals by liquid cell electron microscopy.* Nano Lett, 2014. **14**(7), 3761-3765.

[109] Liao, H.G., L. Cui, S. Whitelam, and H. Zheng, *Real-time imaging of Pt_3Fe nanorod growth in solution.* Science 2012. **336**, 1011-1014.

[110] Woehl, T.J., J.E. Evans, I. Arslan, W.D. Ristenpart, and N.D. Browning, *Direct in Situ Determination of the Mechanisms Controlling Nanoparticle Nucleation and Growth.* ACS Nano, 2012. **6** (10), 8599–8610.

[111] Abellan, P., T.H. Moser, I.T. Lucas, J.W. Grate, J.E. Evans, and N.D. Browning, *The formation of cerium(iii) hydroxide nanoparticles by a radiation mediated increase in local pH.* RSC Adv., 2017. **7**(7), 3831-3837.

[112] Nielsen, M.H., S. Aloni, and J.J. De Yoreo, *In situ TEM imaging of CaCO3 nucleation reveals coexistence of direct and indirect pathways.* Science, 2014. **345**(6201), 1158-1162.
[113] Liu, J., Z. Wang, A. Sheng, F. Liu, F. Qin, and Z.L. Wang, *In situ observation of hematite nanoparticle aggregates using liquid cell transmission electron microscopy.* Environ. Sci. Technol., 2016. **50**, 5606-5613.
[114] Verch, A., M. Pfaff, and N.d. Jonge, *Exceptionally slow movement of gold nanoparticles at a solid/liquid interface investigated by scanning transmission electron microscopy.* Langmuir, 2015. **31**(25), 6956-6964.
[115] Yoreo, J.J.D. and P.G. Vekilov, *Principles of Crystal Nucleation and Growth.* Reviews in Mineralogy and Geochemistry, 2003. **54**(1), 57-93.
[116] Reed-Hill, R.E., *Physical metallurgy principles*. Van Nostrand: 920.
[117] Knoll, M. and E. Ruska, *The electron microscope* Z. Phys., 1932. **78**, 319-339.
[118] Goodhew, P.J., J. Humphreys, and R. Beanland, *Electron microscopy and analysis*, 3rd ed. 2001, Taylor and Francis.
[119] Williams, D.B. and C.B. Carte, *Transmission electron microscopy a textbook for materials science*. 2009, Springer.
[120] Reimer, L. and H. Kohl, *Transmission electron microscopy physics of image formation* 2008 Springer.
[121] Protochips, I., *Poseidon P500 user manual*, in *liquid and electrical control within the microscope*, P. Inc., Editor. 2013: Raleigh. 1-53.
[122] Ring, E.A. and N.d. Jonge, *Microfluidic system for transmission electron microscopy.* Microsc. Microanal. , 2010. **16**, 622-629.
[123] De Jonge, N., N. Poirier-Demers, H. Demers, D.B. Peckys, and D. Drouin, *Nanometer-resolution electron microscopy through micrometers-thick water layers.* Ultramicroscopy, 2010. **110**(9), 1114-1119.
[124] Takeda, S. and H. Yoshida, *Atomic-resolution environmental TEM for quantitative in-situ microscopy in materials science.* Microscopy, 2013. **62**(1), 193–203.
[125] Egerton, R.F., *Physical principles of electron microscopy*. 2005, Springer, United States of America.
[126] Buck, E.C. and J.A. Fortner, *Detecting low levels of transuranics with electron energy loss spectroscopy.* Ultramicroscopy, 1997. **67** 69-75.
[127] Fortner, J.A. and E.C. Buck, *The chemistry of the light rare-earth elements as determined by electron energy loss spectroscopy.* Appl. Phys. Lett., 1996. **68**(26), 3817-3819.
[128] Sayle, T.X.T., M. Molinari, S. Das, U.M. Bhatta, G. Möbus, S.C. Parker, S. Sealc, and Dean C. Sayle, *Environment-mediated structure, surface redox activity and reactivity of ceria nanoparticles.* Nanoscale, 2013. **5**, 6063-6073.
[129] Virot, M., T. Chave, D. Horlait, N. Clavier, N. Dacheux, J. Ravaux, and S.I. Nikitenk, *Catalytic dissolution of ceria under mild conditions.* J. Mater. Chem., 2012. **22**, 14734–14740.
[130] Beaudoux, X., M. Virot, T. Chave, G. Leturcq, N. Clavier, N. Dacheux, and S.I. Nikitenko, *Catalytic dissolution of ceria–lanthanide mixed oxides provides environmentally friendly partitioning of lanthanides and platinum,.* Hydrometallurgy, 2015. **151**, 107–115.
[131] Claparede, L., N. Clavier, N. Dacheux, P. Moisy, R. Podor, and J. Ravaux, *Influence of crystallization state and microstructure on the chemical durability of cerium neodymium mixed oxides.* Inorg. Chem., 2011. **50**, 9059–9072.

[132] Park, J.H., N.M. Schneider, J.M. Grogan, M.C. Reuter, H.H. Bau, S. Kodambaka, and F.M. Ross, *Control of electron beam-induced Au nanocrystal growth kinetics through solution chemistry.* Nano Lett., 2015. **15**(8), 5314-20.

[133] Abellan, P., B.L. Mehdi, L.R. Parent, M. Gu, C. Park, W. Xu, Y. Zhang, I. Arslan, J.G. Zhang, C.M. Wang, J.E. Evans, and N.D. Browning, *Probing the degradation mechanisms in electrolyte solutions for Li-ion batteries by in situ transmission electron microscopy.* Nano Lett, 2014. **14**(3), 1293-9.

[134] Anand, U., J. Lu, D. Loh, Z. Aabdin, and U. Mirsaidov, *Hydration layer-mediated pairwise interaction of nanoparticles.* Nano Lett., 2016. **16**(786-790).

[135] Min, Y., M. Akbulut, K. Kristiansen, Y. Golan, and J. Israelachvili, *The role of interparticle and external forces in nanoparticle assembly.* Nature Materials 2008. **7**, 527-538.

[136] Cho, K.-S., D.V. Talapin, W. Gaschler, and C.B. Murray, *Designing PbSe nanowires and nanorings through oriented attachment of nanoparticles.* J. Am. Chem. Soc. , 2005. **127**, 7140-7147.

[137] Prevo, B.G., D.M. Kuncicky, and O.D. Velev, *Engineered deposition of coatings from nano- and micro-particles: A brief review of convective assembly at high volume fraction.* Colloids and Surfaces A, 2007. **311**(1-3), 2-10.

[138] Gnanavel, T., S. Kumar, and G. Möbus, *In-situ fabrication of three dimensional nickel nanobeads by electron beam induced transformation.* Journal of Nanoscience and Nanotechnology, 2011. **11**(2), 1019-1024.

[139] Gnanavel, T. and G. Möbus, *In-situ cobalt nanocrystal synthesis by intense electron beams in TEM.* Journal of Physics: Conference Series 2012. **371**, 1-5.

[140] Arul, N.S., N. Ponpandian , D. Mangalaraj, P. Meena, P.C. Chen, and Y. Masuda, *Enhanced photocatalytic activity of cobalt-doped CeO2 nanorods.* J Sol-Gel Sci Technol 2012. **64**, 515-523.

[141] Arai, S., S. Muto, T. Sasaki, K. Tatsumi, Y. Ukyo, K. Kuroda, and H. Saka, *Novel valence state of cerium in Ce2Zr2O7.5 elucidated by electron energy-loss spectroscopy under electron channeling conditions.* Solid State Communications 2005. **135**, 664–667.

[142] Bhatta, U.M., D.L. Reid, T. Sakthivel, T.X.T. Sayle, D.C. Sayle, M. Molinari, S.C. Parker, I.M. Ross, S. Seal, and G.n. Möbus, *Morphology and surface analysis of pure and doped cuboidal ceria nanoparticles.* J. Phys. Chem. C 2013. **117**, 24561-24569.

[143] Long, N.j. and a.k. Petford-long, *Combined HREM and EELS studies of the electron beam induced reduction of maximal-valence transition-metal oxides.* Mat. Res. Soc. Symp. Proc. , 1987. **74**, 299-304.

[144] Du, N., H. Zhang, B. Chen, X.a. Ma, and D. Yang, *Ligand-free self-assembly of ceria nanocrystals into nanorods by oriented attachment at low temperature.* J. Phys. Chem. C 2007. **111**, 12677-12680.

[145] Xu, Q., W. Lei, X. Li, X. Qi, J. Yu, G. Liu, J.a. Wang, and P. Zhang, *Efficient removal of formaldehyde by nanosized gold on well defined CeO2 nanorods at room temperature.* Environ. Sci. Technol. American Chemical Society, 2014. **48**, 9702−9708.

[146] Bhatta, U.M., F. Karounis, A. Stringfellow, and G. Möbus, *Perforation and carbon ablation experiments on nano-ceria by electron irradiation.* MRS Proceedings, 2013. **1552**, 125-130.

[147] Karakoti, A.S., S.V.N.T. Kuchibhatla, K.S. Babu, and S. Seal, *Direct synthesis of nanoceria in aqueous polyhydroxyl solutions.* J. Phys. Chem. C, 2007. **111**, 17232-17240.

[148] Han, W.-Q., L. Wu, and Y. Zhu, *Formation and oxidation state of CeO2-x nanotubes.* J. AM. Chem. Soc., 2005. **127**, 12814-12815.